

**MOLECULAR MIMETIC SELF-ASSEMBLY OF NOBLE  
METAL NANOCCLUSERS**

**YAO QIAOFENG**

**NATIONAL UNIVERSITY OF SINGAPORE**

**2014**

**MOLECULAR MIMETIC SELF-ASSEMBLY  
OF NOBLE METAL NANOCCLUSERS**

**YAO QIAOFENG**

*(B. Sci., University of Science and Technology of China)*

**A THESIS SUBMITTED**

**FOR THE DEGREE OF DOCTOR OF PHILOSOPHY**

**DEPARTMENT OF CHEMICAL & BIOMOLECULAR ENGINEERING**

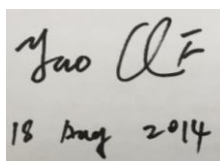
**NATIONAL UNIVERSITY OF SINGAPORE**

**2014**

## DECLARATION

I hereby declare that the thesis is my original work and it has been written by me in its entirety. I have duly acknowledged all the sources of information which have been used in the thesis.

This thesis has also not been submitted for any degree in any university previously.



Yao QF  
18 Aug 2014

---

Yao Qiaofeng

18 August 2014

## ACKNOWLEDGEMENT

First and foremost, I am sincerely grateful to my main supervisor Prof. Lee Jim Yang, and my co-supervisor Dr. Xie Jianping, for their constant guidance, help, and support. This thesis would not have been completed without their continuous encouragement. Their enthusiasm for research has always been contagious and motivational for me. In particular, I would like to thank Prof. Lee not only for shaping the direction of my research, but also for the latitude and trust he has given to me in this study. He has guided me to think in a scientific and creative way, which will definitely benefit my entire career limitlessly. I also profoundly appreciate Dr. Xie Jianping for his timely advices, in-depth discussion, and meticulous attention to details, which not only sharpen my thoughts but also greatly improve the scientific content of my work.

I would like to express my sincere thanks to all my friends and colleagues in the research group, in particular, Dr. Yu Yue, Dr. Yu Yong, Mr. Yuan Xun, Mr. Luo Zhentao, Ms. Dou Xinyue, Dr. Zhang Chao, Dr. Zhang Qingbo, Dr. Ji Ge, Dr. Fang Chunliu, Dr. Chen Dongyun, Dr. Zhao Tingting, Dr. Qu Jianglan, Dr. Liu Bo, Dr. Ma Yue, Dr. Yang Shiliu, Dr. Li Jingfa, Mr. Ding Bo, Ms. Zheng Kaiyuan, Mr. Li Jingguo, Mr. Nirmal Goswami, Mr. Zhan Yi, Mr. Yang Liuqing, Mr. Qu Baihua, Ms. Liu Qing and Mr. Jiang Xi. I thank them for their valuable suggestions and stimulating discussions.

I am indebted to the technical staff in the department especially Mr. Boey Kok Hong, Mr. Chia Phai Ann, Dr. Yuan Zeliang, Mr. Mao Ning, Ms. Lee Chai Keng, Mr. Liu Zhicheng, Ms. Lim Kwee Mei, Mr. Lim You Kang, Ms. Fam Samantha, Dr. Yang liming, Mr. Qin Zhen, Ms. Lin Huey Yi, Mr. Tan Evan Stephen, Ms. Khoh Sandy

Leng Khim, Mr. Chan Alistair Chuin Mun, Ms. Teo Ai Peng, and Mr. Toh Keng Chee. Their superb technical service and support are essential for the timely completion of this study.

Last but not least, I'd like to thank the continuous support, understanding and love from my family members.

The financial supports by the way of Research Scholarship from the National University of Singapore (NUS) are greatly acknowledged.

# TABLE OF CONTENT

ACKNOWLEDGEMENT .....	I
TABLE OF CONTENT .....	III
SUMMARY .....	VIII
LIST OF TABLES .....	XII
LIST OF FIGURES .....	XIII
LIST OF ABBREVIATIONS .....	XX
CHAPTER 1 INTRODUCTION .....	1
1.1 Background .....	1
1.2 Objectives and Scope .....	5
1.3 Thesis Organization .....	8
CHAPTER 2 LITERATURE REVIEW .....	9
2.1 Fundamentals of $M_n(SR)_m$ NCs .....	9
2.1.1 The Electronic Structure of $M_n(SR)_m$ NCs.....	10
2.1.1.1 Metal Core: The Origin of Strong Quantum Confinement Effect....	10
2.1.1.2 Thiolate Ligand Shell: the Modifier of Electronic Structure.....	13
2.1.2 Molecule-Like Properties and Potential Applications of $M_n(SR)_m$ NCs	16
2.1.2.1 Molecule-Like UV-vis Absorption and Applications as	
Photosensitizers .....	18
2.1.2.2 Strong Luminescence and Applications as Optical Probes .....	19
2.1.2.3 Molecule-Like Redox Charging and Applications as Catalysts.....	20
2.2 Synthesis of Monodisperse Atomically Precise $M_n(SR)_m$ NCs .....	25
2.2.1 Physical Separation Approaches .....	26
2.2.1.1 Solubility Based Fractionation .....	27
2.2.1.2 Electrophoresis .....	28

---

2.2.1.3	Liquid Chromatography .....	29
2.2.2	Chemical Selection Techniques .....	31
2.2.2.1	Size-Dependent Stability of $M_n(\text{SR})_m$ NCs: The Foundation of “Size-Focusing” .....	31
2.2.2.2	Size Distribution of Starting $M_n(\text{SR})_m$ NCs: A Determining Factor for the Size of Final Product.....	35
2.3	Self-Assembly of $M_n(\text{SR})_m$ NCs.....	36
2.3.1	Template-Assisted Self-Assembly .....	37
2.3.2	Template-Free Self-Assembly .....	40
2.3.2.1	Crystallization Approaches .....	40
2.3.2.2	Interactions Promoting the Crystallization of $M_n(\text{SR})_m$ NCs.....	43
<b>CHAPTER 3 SYNTHESIS OF BUILDING BLOCKS WITH ATOMIC PRECISION:</b>		
<b>THE CASE OF <math>\text{Au}_{15}(\text{SR})_{13}</math> AND <math>\text{Au}_{18}(\text{SR})_{14}</math> NANOCCLUSERS....</b>		
3.1	Introduction.....	48
3.2	Experimental Section .....	50
3.2.1	Materials.....	50
3.2.2	Synthesis of Au NCs .....	50
3.2.2.1	Synthesis of $\text{Au}_{15}(\text{SR})_{13}$ NCs.....	50
3.2.2.2	Synthesis of $\text{Au}_{18}(\text{SR})_{14}$ NCs.....	51
3.2.3	Control Experiments .....	51
3.2.3.1	Synthesis of Au(0) Nanocrystals .....	51
3.2.3.2	Synthesis of Au NCs by $\text{NaBH}_4$ .....	52
3.2.3.3	One-Phase Synthesis of Au NCs .....	52
3.2.3.4	Synthesis of NCs at pH ~ 10.0 .....	52
3.2.4	Characterization .....	52

---

3.3	Results and Discussion .....	53
3.3.1	Synthesis of Au <sub>15</sub> (SR) <sub>13</sub> NCs.....	54
3.3.2	Synthesis of Au <sub>18</sub> (SR) <sub>14</sub> NCs.....	58
3.3.3	Au Oxidation State and Photoluminescence of As-Synthesized Au <sub>15</sub> (SR) <sub>13</sub> and Au <sub>18</sub> (SR) <sub>14</sub> NCs .....	60
3.3.4	Origin of the High Monodispersity and Size-tunability .....	62
3.4	Conclusion .....	66
CHAPTER 4 SELF-ASSEMBLY OF SUPRAMOLECULAR IONS VIA ELECTROSTATIC INTERACTIONS: ION-LIKE BEHAVIOR OF CHARGED NOBLE METAL NANOCCLUSERS .....		68
4.1	Introduction.....	68
4.2	Experimental Section .....	70
4.2.1	Materials.....	70
4.2.2	Synthesis of M <sub>n</sub> (SR) <sub>m</sub> NCs .....	70
4.2.2.1	Synthesis of Orange-Emitting Au <sub>29-43</sub> (SG) <sub>27-37</sub> NCs .....	70
4.2.2.2	Synthesis of Red-Emitting Au <sub>15</sub> (SG) <sub>13</sub> NCs.....	70
4.2.2.3	Synthesis of Red-Emitting Ag <sub>16</sub> (SG) <sub>9</sub> NCs.....	71
4.2.3	Ion-Induced Self-Assembly of M <sub>n</sub> (SR) <sub>m</sub> NCs.....	72
4.2.3.1	Ion-Induced Self-Assembly of Orange-Emitting Au <sub>29-43</sub> (SG) <sub>27-37</sub> NCs .....	72
4.2.3.2	Ion-Induced Self-Assembly of Red-Emitting Au <sub>15</sub> (SG) <sub>13</sub> NCs.....	72
4.2.3.3	Ion-Induced Assembly of Red-Emitting Ag <sub>16</sub> (SG) <sub>9</sub> NCs.....	72
4.2.4	Characterization .....	73
4.3	Results and Discussion .....	74
4.3.1	Zn <sup>2+</sup> -Induced Self-Assembly of Orange-Emitting Au <sub>29-43</sub> (SG) <sub>27-37</sub> NCs .....	74



---

4.3.2	Ion-Like Self-Assembly Behavior of o-Au NCs.....	80
4.3.3	Origin of Ion-Like Assembly Behavior of o-Au NCs.....	81
4.3.3.1	Bridging Effect of Zn <sup>2+</sup> Dictated Self-Assembly .....	81
4.3.3.2	Ionic Strength Dependence of Self-Assembly .....	83
4.3.3.3	pH Dependence of Self-Assembly .....	85
4.3.4	Self-Assembly Induced Photoluminescent Enhancement.....	86
4.3.5	Versatility of Ion-Induced Self-Assembly Approach.....	88
4.4	Conclusion .....	90
CHAPTER 5 INTRODUCING AMPHIPHILICITY TO NOBLE METAL NANOCLUSTERS VIA PHASE-TRANSFER DRIVEN ION- PAIRING REACTION: SYNTHESIS AND SELF-ASSEMBLY OF AMPHIPHILIC NOBLE METAL NANOCLUSTERS.....		
5.1	Introduction.....	91
5.2	Experimental Section .....	93
5.2.1	Materials.....	93
5.2.2	Synthesis of Au <sub>25</sub> (MHA) <sub>18</sub> NCs.....	94
5.2.3	Synthesis of CTA <sup>+</sup> Coated Au <sub>25</sub> (MHA) <sub>18</sub> NCs (Au <sub>25</sub> (MHA) <sub>18</sub> @xCTA NCs) .....	94
5.2.3.1	Synthesis of Phase-Transferred Au <sub>25</sub> (MHA) <sub>18</sub> @xCTA NCs .....	94
5.2.3.2	Synthesis of Intermediate-Phase-Transferred and Non-Phase- Transferred Au <sub>25</sub> (MHA) <sub>18</sub> @xCTA NCs .....	95
5.2.4	Self-Assembly of Au <sub>25</sub> (MHA) <sub>18</sub> @xCTA NCs (x = 6-9) .....	95
5.2.5	Characterization .....	95
5.3	Results and Discussion .....	96
5.3.1	Synthesis of Amphiphilic Au <sub>25</sub> (MHA) <sub>18</sub> @xCTA NCs (x = 6-9).....	96

---

5.3.2	Amphiphilicity of Au <sub>25</sub> (MHA) <sub>18</sub> @ <i>x</i> CTA NCs ( <i>x</i> = 6-9).....	104
5.3.3	Enhanced Stability of Au <sub>25</sub> (MHA) <sub>18</sub> @ <i>x</i> CTA NCs ( <i>x</i> = 6-9).....	111
5.4	Conclusion .....	114
CHAPTER 6 SHAPE-TAILORABLE CRYSTALLIZATION OF SUPRAMOLECULAR ATOMS: COUNTERION-ASSISTED SHAPING OF Ag <sub>44</sub> ( <i>P</i> -MBA) <sub>30</sub> NC SUPRACRYSTALS.....		
6.1	Introduction.....	116
6.2	Experimental Section .....	118
6.2.1	Materials.....	118
6.2.2	Synthesis of Ag <sub>44</sub> ( <i>p</i> -MBA) <sub>30</sub> NCs.....	118
6.2.3	Crystallization of Ag <sub>44</sub> ( <i>p</i> -MBA) <sub>30</sub> NCs .....	119
6.2.4	Characterization .....	119
6.3	Results and Discussion .....	120
6.3.1	Fabrication of Octahedral Ag <sub>44</sub> ( <i>p</i> -MBA) <sub>30</sub> NC-SCs.....	120
6.3.2	Fabrication of Concave-Octahedral Ag <sub>44</sub> ( <i>p</i> -MBA) <sub>30</sub> NC-SCs.....	126
6.3.3	The Operating Regions of Shape-Tailorable Crystallization of Ag <sub>44</sub> ( <i>p</i> -MBA) <sub>30</sub> NCs.....	130
6.4	Conclusion .....	138
CHAPTER 7 CONCLUSIONS AND RECOMMENDATIONS .....		
7.1	Conclusions.....	139
7.2	Recommendations for Future Work.....	142
REFERENCES .....		
PUBLICATIONS .....		

## SUMMARY

Noble metal nanoclusters (NM-NCs) are ultras-small particles with a core size of 2 nm or lower. They can be denoted as  $M_n(L)_m$  where  $n$  and  $m$  are respectively the number of metal atoms and ligands (*e.g.*, thiolate ligand (SR)). Particles in this size range exhibit strong quantum confinement effects and molecule-like properties such as strong luminescence and enhanced catalytic activity. Hence noble metal NCs could add to the diversity of functional materials for biomedical and catalytic applications. The self-assembly of NM-NCs is an area of increasing interest in both basic and applied research. It is important to basic research because it provides a means to form NM-NC single crystals (*i.e.*, crystallization of NM-NCs) where the precise cluster structure may be determined by X-ray crystallography; a necessary first step in establishing reliable structure-property relationships. The self-assembly of NM-NCs into hierarchical nanostructures also contributes to applied research by providing a means to further customize the cluster properties for the application of interest (*e.g.* via the coupling effects between neighboring NM-NCs).

This thesis project aims to develop a systematic approach to the self-assembly of NM-NCs by leveraging on molecule-like features of NM-NCs (*e.g.*, small size and uniformity of structure). NM-NCs are thus treated like molecule analogs (or supramolecules), and their molecule-like properties are used to regulate the assembly process. Orderliness of assembly is the special emphasis of this research since high structural orders (*i.e.*, long-range crystalline order) are preferred in cluster structure analysis.

The thesis began with the construction of basic building blocks (*e.g.*, monodisperse atomically precise Au NCs) especially in the small size range (*e.g.*  $n < 20$ ) where good synthesis methods are still lacking. A one-pot two-phase method was developed which

could produce small and monodisperse  $\text{Au}_{15}(\text{SR})_{13}$  and  $\text{Au}_{18}(\text{SR})_{14}$  NCs in atomic precision. In this new method a mild reducing agent, borane tert-butylamine (TBAB), and two equilibrium conditions were used in tandem to provide a constant reaction environment conducive for the formation of small and monodisperse NCs. A mild and unvarying reducing power was maintained throughout the reaction by the equilibrium partition of a mild reducing agent between an organic solvent and the aqueous solution. At the same time a slow and constant release of the Au precursor was made possible by the aggregation-dissociation equilibrium between free and aggregated Au(I)-SR complexes. The pH sensitivity of the aggregation-dissociation equilibrium was then used to manipulate the cluster size. This work addresses the current synthesis gap in the preparation of atomically precise Au NCs in the small size range ( $n < 20$ ), and increases the diversity of building blocks that can be used for assembly investigations.

A facile and general method based on the electrostatic interaction between oppositely-charged species was then developed to assemble charged NM-NCs in water. Thiolate-capped NM-NCs (*e.g.*,  $\text{Au}_{29-43}(\text{SG})_{27-37}$ ,  $\text{Au}_{15}(\text{SG})_{13}$ , and  $\text{Ag}_{16}(\text{SG})_9$  NCs, where SG denotes glutathione), which are negatively charged, were bridged by divalent counter cations such as  $\text{Zn}^{2+}$  and  $\text{Cd}^{2+}$  into monodisperse spherical assemblies. Small NM-NCs may be regarded as supramolecular ions in view of their uniformity of structure, ultrasmall size and high charge density. Indeed they exhibited step-like assembly behavior analogous to solid formation when its solubility product is exceeded. The assembly also caused a significant increase of the photoluminescent intensity of NM-NCs, suggesting that the interaction between closely packed NM-NCs may be used to customize cluster properties. However, it should be pointed out that these spherical NM-NC assemblies still lack a long-range crystalline order (no regular packing spacing  $d$  was observed).

On the other hand, the amphiphilic NM-NCs, as supramolecular amphiphiles, could be formed by phase-transfer (PT) driven ion-pairing reaction between hydrophobic cations (*e.g.*, cetyltrimethylammonium,  $\text{CTA}^+$ ) and anionic surface functionality (*e.g.*,  $-\text{COO}^-$ ) of hydrophilic NM-NCs. Amphiphilic  $\text{Au}_{25}(\text{MHA})_{18}@x\text{CTA}$  NCs with  $x$  (number of  $\text{CTA}^+$  per cluster) = 6-9, where MHA is hydrophilic 6-mercaptohexanoic acid ligand, were synthesized this way. Due to coexistence of flexible hydrophilic MHA and hydrophobic  $\text{MHA}\cdots\text{CTA}$  ligands in comparable quantity on NC surface,  $\text{Au}_{25}(\text{MHA})_{18}@x\text{CTA}$  NCs ( $x = 6-9$ ) possessed good amphiphilicity; which not only rendered them well-soluble in a broad range of solvent with distinctly different polarities, but also imparted them with molecule-amphiphile-like self-assembly behavior. The amphiphilic  $\text{Au}_{25}(\text{MHA})_{18}@x\text{CTA}$  NCs ( $x = 6-9$ ) could self-organize into bilayer-based lamellar structures at liquid-air interface, resembling the formation of lamellar phase of common surfactants. It is worth mentioning that the lamellar assemblies exhibited regular interlayer packing spacing. However, 3D crystalline order was still absent in these assemblies.

3D structural order could be achieved by self-arrangement of fully deprotonated  $\text{Ag}_{44}(p\text{-MBA})_{30}$  NCs ( $p\text{-MBA} = p\text{-mercaptobenzoic acid}$ ) into single-crystalline supracrystals (SCs). By changing the counterion of  $p\text{-MBA}$  ligand from  $\text{H}^+$  to  $\text{Cs}^+$  suppressing the formation of directional hydrogen-bonds between NCs, a non-directional bonding habit could be imparted to  $\text{Ag}_{44}(p\text{-MBA})_{30}$  NCs. Owing to the non-directional bonding habit, together with uniform size, *pseudo*-spherical geometry and rigid surface (resulting from rigidity of  $p\text{-MBA}$  ligands);  $\text{Cs}^+$ -deprotonated  $\text{Ag}_{44}(p\text{-MBA})_{30}$  NCs could be regarded as hard-sphere-like supramolecular atoms. By mimicking the packing behavior of hard spheres (*e.g.*, entropic effect driven formation of closest-packed crystals),  $\text{Cs}^+$ -deprotonated  $\text{Ag}_{44}(p\text{-MBA})_{30}$  NCs self-organized into

*f.c.c.* single-crystalline SCs with octahedral morphology. We also found the crystallization of  $\text{Ag}_{44}(\text{p-MBA})_{30}$  NCs followed a  $\text{Cs}^+$ -assisted nucleation and growth mechanism, which offered a good opportunity for tailoring SC shape. Simply by bringing up the concentration of  $\text{Cs}^+$ , the SCs could be selectively shaped into concave-octahedron by a fast nucleation and slow growth kinetics.

## LIST OF TABLES

<b>Table 2.1</b>	Catalytic performances of “ligand-on” type $M_n(SR)_m$ NC catalysts in selected reactions. ....	23
<b>Table 2.2</b>	Catalytic performances of “ligand-off” type $M_n(SR)_m$ NC catalysts in selected reactions. ....	24
<b>Table 2.3</b>	Summary of successful crystallization of $M_n(SR)_m$ NCs ( $M = Au$ or $Ag$ ). The crystallization method, and the shape and space group of $M_n(SR)_m$ NC-SCs are given in this Table. ....	39

# LIST OF FIGURES

- Figure 2.1** Illustration of the core-shell construction of  $M_n(SR)_m$  NCs. .... 10
- Figure 2.2** Illustration comparing the size of noble metal atoms, noble metal nanoclusters ( $M_n(SR)_m$  NCs), noble metal nanoparticles and bulk noble metal..... 11
- Figure 2.3** Kohn-Sham molecular orbital energy level diagram of  $Au_{25}(SR)_{18}$  NCs. Each orbital is drawn to show the relative contributions (as line lengths of different colors) of the atomic orbitals of Au(6sp) (green), Au(5d) (blue), S(3p) (yellow), and others (unspecified atomic orbitals with <1 % contribution each) (grey). The left column of the orbitals shows the orbital symmetry (g or u) and degeneracy (in parenthesis); the right column shows the HOMO and LUMO sets. SR was taken to be SH for computational expediency. Adopted from Ref.<sup>(25)</sup> with the permission of the American Chemical Society. .... 14
- Figure 2.4** Size-dependent molecule-like properties of  $M_n(SR)_m$  NCs. (a) UV-vis absorption spectra of  $Au_n(SG)_m$  NCs in various sizes: (n m) = (10 10), (15 13), (18 14), (22 16), (22 17), (25 18), (29 20), (33 22), and (39 24); the black and red arrows indicate the onset and maximum of UV-vis absorption, respectively. (b) Emission (excitation wavelength  $\lambda_{ex} = 520$  nm) spectra of  $Au_{22}(SG)_{18}$  NCs (red, right side) and  $Au_{25}(SG)_{18}$  NCs (blue); the excitation (emission wavelength  $\lambda_{em} = 665$  nm) spectrum of  $Au_{22}(SG)_{18}$  NCs is also shown (red, left side); the insets are representative digital images of  $Au_{22}(SG)_{18}$  NC (No. 1) and  $Au_{25}(SG)_{18}$  NC (No. 2) aqueous solutions taken under UV irradiation ( $\lambda = 365$  nm). (c) Differential pulse voltammograms (DPV) of  $Au_n(SC_6H_{13})_m$  NCs as a function of core size; core sizes were measured in terms of the  $Au_nS_m$  core mass and labeled in each voltammogram; the DVP analysis was carried out in a toluene/acetonitrile (2/1 v:v) solution of 0.05 M tetrahexylammonium perchlorate, using a  $9.5 \times 10^{-3}$  cm<sup>2</sup> Pt electrode, a direct current (DC) 50 mV pulse and a scan rate of 10 mV/s. (d) The turn-over-frequency (TOF) of cyclohexane in cyclohexane oxidation catalyzed by hydroxyapatite (HAP) supported  $Au_n$  NCs with different core sizes (n = 10, 18, 29, 39, and 85); the inset is a schematic illustration of the catalytic reaction. (a, b, d) were adopted from Refs.<sup>(8)</sup>, <sup>(12)</sup>, and <sup>(90)</sup> respectively with the permission of the American Chemical Society; and (c) was adopted from Ref.<sup>(14)</sup> with the permission of the American Association for the Advancement of Science (AAAS)..... 17
- Figure 2.5** Schematic illustration of the processes for monodisperse  $M_n(SR)_m$  NC synthesis..... 27
- Figure 2.6** MALDI-TOF-MS spectra of  $Au_n(SR)_m$  NCs mixtures in the “size-focusing” (thiol-etching) synthesis of (a)  $Au_{25}(SR)_{18}$ , (b)  $Au_{38}(SR)_{24}$  and (c)  $Au_{144}(SR)_{60}$  NCs at different reaction times. The asterisked peaks in (a) and (b) indicate fragments of  $Au_{25}(SR)_{18}$  and  $Au_{38}(SR)_{24}$



- NCs, respectively. (a-c) were adopted from Refs.<sup>(88)</sup>, <sup>(79)</sup>, and <sup>(89)</sup> respectively with the permission of the American Chemical Society. . 34
- Figure 2.7** Schematic illustration of the working principle of the “size-focusing” approach to the synthesis of monodisperse  $M_n(SR)_m$  NCs.  $Au_n(SR)_m$  NCs were used as examples. Adopted from Ref.<sup>(131)</sup> with the permission of the American Chemical Society..... 35
- Figure 2.8** (a-b)  $\pi$ - $\pi$  stacking interactions and (c-d) H-bonding in  $M_n(SR)_m$  NC-SCs. (a) Crystal structure of packed  $Au_{102}(p\text{-MBA})_{40}(p\text{-BBT})_4$  NCs. (b) Expanded view of the boxed area in (a), showing the  $\pi$ - $\pi$  stacking interactions between neighboring  $Au_{102}(p\text{-MBA})_{40}(p\text{-BBT})_4$  NCs; a ball-and-stick model is used to show the  $p$ -BBT ligands in the boxed area (dark red = Br, red = O, grey = C, white = H, green = S, and yellow = Au). (c) Crystal structure of packed  $Ag_{44}(p\text{-MBA})_{30}$  NCs; the arrows indicate the unit cell vectors  $\mathbf{a}$  and  $1/2\mathbf{c}$  of triclinic  $Ag_{44}(p\text{-MBA})_{30}$  NC-SCs. (d) Expanded view of the boxed area in (c), showing the formation of H-bonds between neighboring  $Ag_{44}(p\text{-MBA})_{30}$  NCs (orange = O, grey = C, and dark grey = H). (a-b) were adopted from Ref.<sup>(153)</sup> with the permission of the American Chemical Society; and (c-d) were adopted from Ref.<sup>(64)</sup> with the permission of the Nature Publishing Group. .... 44
- Figure 3.1** Schematic illustration of the two-phase synthesis of high purity  $Au_{15}(SG)_{13}$  and  $Au_{18}(SG)_{14}$  NCs..... 53
- Figure 3.2** Digital photos of Au(I)-SG complexes formed at different pH: pH ~2.0 (no. 1), 2.7 (no. 2) and 10.0 (no. 3)..... 54
- Figure 3.3** UV-vis spectrum (a) and ESI spectra (in negative ion mode; b-d) of as-synthesized  $Au_{15}$  NCs. The inset of (a) shows a digital photo (no. 1) and the PAGE analysis (no. 2) of the crude product. The dotted line in (a) shows the zero of optical absorbance of as-synthesized  $Au_{15}(SG)_{13}$  NCs. The red line in (d) is the simulated isotope pattern of  $[Au_{15}(SG)_{13} - 4H]^4-$  ..... 55
- Figure 3.4** UV-vis spectra of as-synthesized  $Au_{15}$  NCs after passing through a PD-10 column: freshly prepared (solid line) and after 4 months’ storage at 4 °C (dotted line). The inset shows the enlarged view of the boxed area.56
- Figure 3.5** Detailed assignment of the fragments in the ESI spectrum of as-synthesized  $Au_{15}$  in Figure 3.3b. L denotes the SG ligand. .... 58
- Figure 3.6** UV-vis spectrum (a) and ESI spectra (in negative ion mode; b-d) of as-synthesized  $Au_{18}$  NCs. The inset in (a) shows the digital photo of the crude product. The dotted line in (a) shows the zero of optical absorbance of as-synthesized  $Au_{18}$  NCs. Peaks #1 - #6 in (c) are assigned to  $[Au_{18}(SG)_{14} - 4H]^4-$ ,  $[Au_{18}(SG)_{14} - 5H + Na]^4-$ ,  $[Au_{18}(SG)_{14} - 5H + K]^4-$ ,  $[Au_{18}(SG)_{14} - 6H + 2Na]^4-$ ,  $[Au_{18}(SG)_{14} - 6H + Na + K]^4-$ , and  $[Au_{18}(SG)_{14} - 6H + 2K]^4-$  respectively. The dotted line in (d) is the simulated isotope pattern of  $[Au_{18}(SG)_{14} - 4H]^4-$  ..... 59

- Figure 3.7** Au(4f) XPS spectra of as-synthesized Au<sub>15</sub> NCs (blue), Au<sub>18</sub> NCs (red), freshly prepared Au(0) nanocrystals (pink) and Au(I)-SG complexes (black). The Au(I)-SG complexes were prepared by the direct mixing of GSH and HAuCl<sub>4</sub> and the Au(0) nanocrystals were synthesized by the reduction of HAuCl<sub>4</sub> in excess NaBH<sub>4</sub> without any protecting agent. . 61
- Figure 3.8** Photoemission (solid lines) and photoexcitation (dotted lines) spectra of as-synthesized (a) Au<sub>15</sub>(SG)<sub>13</sub> and (b) Au<sub>18</sub>(SG)<sub>14</sub>. The  $\lambda_{\text{ex}}$  for photoemission spectra were 370 and 570 nm for Au<sub>15</sub>(SG)<sub>13</sub> and Au<sub>18</sub>(SG)<sub>14</sub>, respectively. The  $\lambda_{\text{em}}$  for the photoexcitation spectra was 920 nm for both Au<sub>15</sub>(SG)<sub>13</sub> and Au<sub>18</sub>(SG)<sub>14</sub>. The insets show the corresponding digital photos taken under UV illumination ( $\lambda = 365$  nm). ..... 61
- Figure 3.9** UV-vis spectra of the NC products by NaBH<sub>4</sub> reduction (no.1) and one-phase TBAB reduction (no.2). ..... 63
- Figure 3.10** Molecular structure and protonation/deprotonation processes of GSH, where  $\text{pK}_{\text{a}1} = 2.12$ ,  $\text{pK}_{\text{a}2} = 3.53$ , and  $\text{pK}_{\text{a}3} = 8.66$ .  $\text{pK}_{\text{a}4} = 9.62$ . ..... 64
- Figure 3.11** UV-vis spectrum of the as-prepared NC product at pH ~10.0. .... 65
- Figure 3.12** UV-vis spectrum of Au<sub>15</sub>(SG)<sub>13</sub> produced in a scaled-up synthesis. The inset shows the digital photo of the Au<sub>15</sub>(SG)<sub>13</sub> solution in a 250 mL flask after centrifugation. For the scaled-up synthesis the reaction volume was increased from 10 to 150 mL, and all other reaction conditions remained the same as that in §3.2.2.1. .... 66
- Figure 4.1** (a-d) TEM images of o-Au NCs assembled in different Zn<sup>2+</sup> concentrations:  $R_{[\text{Zn}^{2+}]/[\text{-SG}]} = 0$  (a), 0.3 (b), 0.6 (c), and 0.9 (d); the insets in (c) and (d) show the corresponding HR-TEM images (scale bar = 20 nm). (e) DLS analysis of o-Au NCs assembled at  $R_{[\text{Zn}^{2+}]/[\text{-SG}]} = 0$  (black), 0.3 (red), 0.6 (blue), and 0.9 (green); the inset in (e) shows the dependence of the hydrodynamic diameter of the assembly on  $R_{[\text{Zn}^{2+}]/[\text{-SG}]}$ . ..... 75
- Figure 4.2** pH dependence of the  $\zeta$ -potential of o-Au NCs. The isoelectric point (IEP) of the o-Au NCs was estimated to be 3.23. .... 76
- Figure 4.3** UV-vis absorption spectra of o-Au NCs assembled at different  $R_{[\text{Zn}^{2+}]/[\text{-SG}]}$  values; the inset shows the absorbance at 400 nm as a function of  $R_{[\text{Zn}^{2+}]/[\text{-SG}]}$ . ..... 78
- Figure 4.4** (a) Scanning transmission electron microscopy (STEM) image of a representative o-Au NC colloidal sphere assembled at  $R_{[\text{Zn}^{2+}]/[\text{-SG}]} = 0.6$ . (b-c) EDX elemental maps of the circular region in (a) in terms of Au (b), and Zn (c). The insets of (b) and (c) show respectively the Au and Zn signals in the EDX line scan across the yellow line in (a). .... 79
- Figure 4.5** Proposed mechanism for Zn<sup>2+</sup>-induced assembly of o-Au NCs. .... 81

- Figure 4.6**  $\zeta$ -potential of o-Au NCs assembled under different  $R_{[Zn^{2+}]/[-SG]}$  values. The  $\zeta$ -potential at  $R_{[Zn^{2+}]/[-SG]} = 0$  was arbitrarily set at -1 for ease of comparison. .... 83
- Figure 4.7** Measured hydrodynamic diameters of assembled/disassembled o-Au NCs at different pH and in the presence of different ions. The assembly with  $Zn^{2+}$  was carried out at  $R_{[Zn^{2+}]/[-SG]} = 0.6$ . .... 84
- Figure 4.8** Effects of pH cycling on the hydrodynamic diameters (a) and photoemission spectra (b, excited at 365 nm) of o-Au NCs assembled by  $Zn^{2+}$ . The o-Au NCs were initially assembled at pH ~6.5 (#1), and then pH was varied in the sequence of ~2.7 (#5) -- 6.5 (#2) -- 2.7 (#6) -- 6.5 (#3) -- 2.7 (#7) -- 6.5 (#4). In a separate experiment, solution #7 was dialyzed overnight followed by reassembly with  $Zn^{2+}$  at pH 6.5. The hydrodynamic diameter of the reassembled “refreshed” o-Au NCs was recorded as the red dot in (a). The inset of (b) shows the expanded view of the circled area. All self-assemblies were carried out at  $R_{[Zn^{2+}]/[-SG]} = 0.6$ . .... 86
- Figure 4.9** (a) Digital photos of o-Au NCs assembled at various  $R_{[Zn^{2+}]/[-SG]}$  values: 0 (#1 and #5), 0.3 (#2 and #6), 0.6 (#3 and #7), and 0.9 (#4 and #8); #1~4 were taken under normal light while #5~8 were taken under UV illumination (365 nm); (b) Photoemission spectra (excited at 365 nm) of o-Au NCs assembled under different  $R_{[Zn^{2+}]/[-SG]}$  values: 0 (black), 0.3 (red), 0.6 (blue), and 0.9 (purple); the inset shows the emission intensity maximum as a function of  $R_{[Zn^{2+}]/[-SG]}$ . .... 88
- Figure 4.10** Emission spectra of o-Au NC (a, after excitation at 365 nm),  $Au_{15}(SG)_{13}$  NC (b, after excitation at 370 nm) and  $Ag_{16}(SG)_9$  NC (c, after excitation at 440 nm) before (black line) and after (red lines) self-assembly in presence of divalent cations ( $Cd^{2+}$  for (a) and  $Zn^{2+}$  for (b) and (c)). Corresponding TEM images of assembled NCs are shown in the insets. .... 89
- Figure 5.1** (a) UV-vis absorption spectra of  $Au_{25}(MHA)_{18}$  (black line) and phase-transferred  $Au_{25}(MHA)_{18}@xCTA$  (red line) NCs; the insets in (a) are the digital images of freshly prepared  $Au_{25}(MHA)_{18}$  NCs in aqueous solution (#1) and phase-transferred  $Au_{25}(MHA)_{18}@xCTA$  NCs in the organic phase (#2). (b) Negative-ion mode ESI-MS spectrum of  $Au_{25}(MHA)_{18}$  NCs; inset #1 in (b) is the zoomed-in spectrum of ionized  $Au_{25}(MHA)_{18}$  NCs with 5- charge, with the number of coordinated  $Na^+$  shown above each peak; inset #2 in (b) shows the experimental (black line) and simulated (red line) isotope patterns of  $[Au_{25}(MHA)_{18} + 6Na - 11H]^{5-}$ . (c) Negative-ion mode ESI-MS spectrum of phase-transferred  $Au_{25}(MHA)_{18}@xCTA$  NCs, with the value of  $x^z$  (the apparent number of  $CTA^+$  in each NC with charge  $z$ ) shown in red above each peak; the inset in (c) is the experimental (black line) and simulated (red line) isotope pattern of  $[Au_{25}(MHA)_{18}@2CTA - 7H]^{5-}$ . .... 98
- Figure 5.2** Schematic illustration of the synthesis of  $Au_{25}(MHA)_{18}@xCTA$  NCs ( $x = 6-9$ ) and their self-assembly. .... 101

- Figure 5.3** Comparison of ESI-MS spectra (in negative-ion mode) of non-phase-transferred (i), intermediate-phase-transferred (ii), and phase-transferred (iii)  $\text{Au}_{25}(\text{MHA})_{18}@x\text{CTA}$  NCs prepared with  $f_{\text{EtOH}} = 0, 0.20$  and  $0.33$  respectively. (a) Spectra in the broad 1500-4000  $m/z$  region; the insets in (a) show corresponding digital images of  $\text{Au}_{25}(\text{MHA})_{18}@x\text{CTA}$  NCs, where the blue arrow in (ii) indicates the intermediate-phase-transferred  $\text{Au}_{25}(\text{MHA})_{18}@x\text{CTA}$  NCs agglomerating at the aqueous-organic interface. (b) Zoomed-in spectra of NC species with 3- charge. (c) Zoomed-in spectra of representative peaks in (b). (d) Isotope patterns of the most pronounced peak in (c), where (i) corresponds to  $[\text{Au}_{25}(\text{MHA})_{18} - 3\text{H}]^{3-}$  and (ii-iii) correspond to  $[\text{Au}_{25}(\text{MHA})_{18}@4\text{CTA} - 7\text{H}]^{3-}$ ; the black and red lines in (d) are the experimental and simulated isotope patterns respectively..... 103
- Figure 5.4** Schematic illustration showing the sizes of the Au core, MHA and  $\text{CTA}^+$  cations in  $\text{Au}_{25}(\text{MHA})_{18}@x\text{CTA}$  NCs ( $x = 6-9$ ). The size of the  $\text{Au}_{25}$  core is taken from the literature,<sup>17,70</sup> and the lengths of MHA and  $\text{CTA}^+$  are estimated by CS ChemOffice Ultra 4.5..... 105
- Figure 5.5** (a) UV-vis absorption spectra and (b-f) TEM images of  $\text{Au}_{25}(\text{MHA})_{18}@x\text{CTA}$  NCs ( $x = 6-9$ ) in different media: (a(i), b) ethanol/hexane = 10/90 v/v,  $\epsilon_r = 4.15$ ; (a(ii), c) ethanol/hexane = 40/60 v/v,  $\epsilon_r = 10.97$ ; (a(iii), d) ethanol/hexane = 70/30 v/v,  $\epsilon_r = 17.78$ ; (a(iv), e) ethanol,  $\epsilon_r = 24.60$ ; and (a(v), f) ethanol/water = 70/30 v/v,  $\epsilon_r = 41.25$ . The superimposed black and red lines in (a) are respectively the UV-vis absorption spectra of freshly prepared and centrifuged (at 10,000 rpm for 10 min) NC solutions. The insets in (a) are the digital images of freshly prepared NC solutions. The insets in (b-f) are corresponding HR-TEM images of the NCs, where the scale bars are 20 nm. .... 106
- Figure 5.6** UV-vis absorption spectrum, (d) XRD pattern, (b-c) FESEM and (e-f) TEM images of  $\text{Au}_{25}(\text{MHA})_{18}@x\text{CTA}$  NCs ( $x = 6-9$ ) assembled at the liquid-air interface. The insets in (a) are the digital images of  $\text{Au}_{25}(\text{MHA})_{18}@x\text{CTA}$  NCs before (#1) and after (#2) self-assembly; the top view of the circled area of #2 is also shown to the right of #2. The inset in (d) shows a schematic illustration of the lamellar assembly formed by the NC bilayers..... 108
- Figure 5.7** UV-vis spectra of (a)  $\text{Au}_{25}(\text{MHA})_{18}$  NCs and (b)  $\text{Au}_{25}(\text{MHA})_{18}@x\text{CTA}$  NCs ( $x = 6-9$ ) over a period of 1 week at the ambient condition (298 K and 1 atm). The insets show the enlarged spectra in the 550-800 nm spectral region. The absorption peak at  $\sim 672$  nm of  $\text{Au}_{25}(\text{MHA})_{18}$  NCs was significantly broadened after 3 d, while the absorption peak of  $\text{Au}_{25}(\text{MHA})_{18}@x\text{CTA}$  NCs ( $x = 6-9$ ) did not show any broadening over 7 d; indicating the good stability of the latter. .... 113
- Figure 5.8** UV-vis absorption spectra of assembled  $\text{Au}_{25}(\text{MHA})_{18}@x\text{CTA}$  NCs ( $x = 6-9$ ) after heating at 393 K for 3 d in air (black line) and in vacuum ( $\sim 20$  mbar, blue line)..... 114

- Figure 6.1** UV-vis absorption spectrum (a) and TEM image (b) of freshly prepared  $\text{Ag}_{44}(\text{p-MBA})_{30}$  NCs. Inset in (a) schematically illustrates the structure of a  $\text{Ag}_{44}(\text{p-MBA})_{30}$  NC (drawn according to the crystal structure reported by Desireddy *et al.*<sup>27</sup>) where red dots are O atoms, dark grey dots are C atoms, yellow dots are S atoms, and light grey dots are Ag atoms. H atoms are omitted in the illustration for a cleaner representation. .... 121
- Figure 6.2** (a) SEM image, (b) UV-vis absorption spectrum, and (c) EDX elemental analysis of octahedral supracrystals grown at  $[\text{Cs}^+] = 33$  mM and  $f_{\text{DMSO}} = 0.5$ ; and (d) UV-vis absorbance at  $\lambda = 645$  nm ( $I$ ) of the crystallization solution before (black line) and after (red line) centrifugation plotted against evaporation time ( $t$ ). The top inset in (a) shows the size histogram of supracrystals, while the bottom insets in (a) show the FESEM images and the schematic illustrations of supracrystals viewed from 3 different directions. Upper and lower panels in (c) are the elemental maps and EDX spectrum, respectively. Insets #1-2 in (d) show the FESEM images of supracrystals harvested at different  $t$ , and inset #3 shows the fit of a kinetic model for the precipitation reaction of  $\text{Ag}_{44}(\text{p-MBA})_{30}$  NCs, where  $t_{\text{nuc}} = 12$  h was used in the fitting. All scale bars in the EM images are 10  $\mu\text{m}$  unless indicated otherwise. .... 122
- Figure 6.3** Powder XRD pattern of octahedral  $\text{Ag}_{44}(\text{p-MBA})_{30}$  NC-SCs grown in a solution of  $f_{\text{DMSO}} = 0.5$  and  $[\text{Cs}^+] = 33$  mM. The peak at  $2\theta = 4.19^\circ$  was assigned to *f.c.c.* (111)<sub>SC</sub> facets. Theoretical  $2\theta$  corresponding to *f.c.c.* (111)<sub>SC</sub> could be estimated based on the reported packing diameter ( $D = 2.58$  nm) of  $\text{Ag}_{44}(\text{p-MBA})_{30}$  NCs in the SCs.<sup>27</sup> The  $D$  was transcribed into the lattice parameter  $a$  of a *f.c.c.* SC via the equation  $a = \sqrt{2}D$ . Since the X-ray source was Cu  $K_\alpha$  radiation ( $\lambda = 1.5405$  Å),  $2\theta$  corresponding to *f.c.c.* (111)<sub>SC</sub> was calculated to be  $4.20^\circ$ , in good agreement with the measured value ( $2\theta = 4.19^\circ$ ). .... 124
- Figure 6.4** Schematic illustration of the formation of octahedral (Route I) and concave-octahedral (Route II)  $\text{Ag}_{44}(\text{p-MBA})_{30}$  NC supracrystals. .... 126
- Figure 6.5** SEM image, (b) UV-vis absorption spectrum, and (c) EDX elemental analysis of concave-octahedral supracrystals grown at  $[\text{Cs}^+] = 66$  mM and  $f_{\text{DMSO}} = 0.5$ ; and (d) UV-vis absorbance at  $\lambda = 645$  nm ( $I$ ) of the crystallization solution before (black line) and after (blue line) centrifugation plotted against  $t$ . The top inset in (a) shows the size histogram of supracrystals, while the bottom insets in (a) show the FESEM images and schematic illustrations of supracrystals viewed from 3 different directions. The upper and lower panels in (c) are elemental maps and EDX spectrum, respectively. Insets #1-2 in (d) show the FESEM images of supracrystals obtained at different  $t$ , and inset #3 shows the fit of a kinetic model for the precipitation reaction of  $\text{Ag}_{44}(\text{p-MBA})_{30}$  NCs, where  $t_{\text{nuc}} = 10$  h was used in the fitting. All scale bars in the EM images are 10  $\mu\text{m}$  unless indicated otherwise. .... 128

- Figure 6.6** SEM images of assembled/crystallized  $\text{Ag}_{44}(\text{p-MBA})_{30}$  NCs at  $f_{\text{DMSO}} = 0.6$  and  $[\text{Cs}^+] = 8.25$  mM (a, e), 16.5 mM (b, f), 33 mM (c, g), 66 mM (d, h), 82.5 mM (i, l), 99 mM (j, m) and 132 mM (k, n). (a-d, i-k) and (e-h, l-n) are low and high magnification views, respectively..... 131
- Figure 6.7** UV-vis absorption spectra of a typical amorphous film (black line) and a typical rod-like assembly (blue line) redispersed in 66 mM CsOH aqueous solution. .... 132
- Figure 6.8** STEM image (a) and elemental maps of Ag (b), S (c), and (d) Cs in the rod-like assembly..... 132
- Figure 6.9** UV-vis absorption spectra of  $\text{Ag}_{44}(\text{p-MBA})_{30}$  NCs in 1 wt.% CsOH ( $[\text{CsOH}] = 66$  mM) aqueous solution (black line), in ultrapure water (red line), and in 1 wt.% HOAc aqueous solution (blue line). The fading of the absorption features of pure  $\text{Ag}_{44}(\text{p-MBA})_{30}$  NCs from the top to the bottom panels suggests the decreased stability of as-prepared  $\text{Ag}_{44}(\text{p-MBA})_{30}$  NCs in progressively more acidic solutions. .... 134
- Figure 6.10** The operating regions of shape-tailorable crystallization of  $\text{Ag}_{44}(\text{p-MBA})_{30}$  NCs in mixtures of DMSO/water with varied  $f_{\text{DMSO}}$  and  $[\text{Cs}^+]$ . .... 135
- Figure 6.11** SEM images of assembled/crystallized  $\text{Ag}_{44}(\text{p-MBA})_{30}$  NCs at  $f_{\text{DMSO}} = 0.7$  (a-b, d-e) and 0.8 (c, f).  $[\text{Cs}^+] = 0$  mM in (a, d) and 33 mM in (b-c, e-f) respectively. (a-c) and (d-f) are low and high magnification views, respectively. .... 136
- Figure 6.12** SEM images of assembled/crystallized  $\text{Ag}_{44}(\text{p-MBA})_{30}$  NCs at  $f_{\text{DMSO}} = 0.5$  and at  $[\text{Cs}^+] = 13.2$  mM (a, d), 26.4 mM (b, e), 39.6 mM (c, f), 52.8 mM (g, j), 99 mM (h, k) and 132 mM (i, l). (a-c, g-i) and (d-f, j-l) are low and high magnification views, respectively..... 136
- Figure 6.13** SEM images of assembled/crystallized  $\text{Ag}_{44}(\text{p-MBA})_{30}$  NCs at  $f_{\text{DMSO}} = 0.4$  and  $[\text{Cs}^+] = 33$  mM (a, d), 66 mM (b, e), and 99 mM (c, f). (a-c) and (d-f) are low and high magnification views, respectively. .... 137
- Figure 6.14** SEM images of assembled/crystallized  $\text{Ag}_{44}(\text{p-MBA})_{30}$  NCs at  $f_{\text{DMSO}} = 0.3$  and  $[\text{Cs}^+] = 26.4$  mM (a, c) and 33 mM (b, d). (a-b) and (c-d) are low and high magnification views, respectively..... 137
- Figure 6.15** SEM images of assembled/crystallized  $\text{Ag}_{44}(\text{p-MBA})_{30}$  NCs at  $f_{\text{DMSO}} = 0.2$  and  $[\text{Cs}^+] = 33$  mM (a, c) and 66 mM (b, d). (a-b) and (c-d) are low and high magnification views, respectively..... 137

# LIST OF ABBREVIATIONS

(FE)SEM	(Field Emission) Scanning Electron Microscopy
(HR-)TEM	(High Resolution) Transmission Electron Microscopy
[NC] <sub>s</sub>	Solubility of Nanocluster
2D	2-Dimensional
3D	3-Dimensional
BSA	Bovine Serum Albumin
CNT	Carbon Nanotube
CTA(B)	Cetyltrimethylammonium (Bromide)
<i>d</i>	Interlayer Spacing
<i>D</i>	Packing Diameter of Nanocluster in Supracrystals
DE	Dibenzyl Ether
DFT	Density Functional Theory
DLS	Dynamic Light Scattering
DMF	Dimethylformamide
DMSO	Dimethylsulfoxide

DPV	Differential Pulse Voltammetry
EDX	Energy-Dispersive X-Ray Spectroscopy
$E_F$	Fermi Energy
ELS	Electrophoresis Light Scattering
ESI	Electrospray Ionization
<i>f.c.c.</i>	Face-Centered-Cubic
$f_A$	Volume Fraction of Solvent A in a Hybrid Solvent System
HAP	Hydroxyapatite
HD	Hydrodynamic Diameter
HOMO	Highest Occupied Molecular Orbital
HPLC	High Performance Liquid Chromatography
H-SG or GSH	Glutathione
H-SR	Thiol Ligand
<i>I</i>	Optical Absorbance at 645 nm
ICP	Inductively Coupled Plasma
IEP	Isoelectric Point



$I_{\text{ion}}$	Ionic Strength
<i>intra-</i> or <i>inter</i> -EL	Inter- or Intra-Cluster Electrostatic Linkage
$k_B$	Boltzmann Constant
$K_{\text{sp}}$	Solubility Product
LDI	Laser Desorption/Ionization
LOD	Limit of Detection
LP	Liquid Paraffin
LUMO	Lowest Unoccupied Molecular Orbital
MALDI	Matrix Assisted Laser Desorption/Ionization
MHA	6-Mercaptohexanoic Acid
MO	Molecular Orbitals
MS	Mass Spectrometry
MWCO	Molecular Weight Cut-Off
$N_A$	Total Valence Electron Count of a Nanocluster
NC	Nanocluster
NM	Noble Metal
NP	Nanoparticle

o-Au NCs	Orange-Emitting Au <sub>29-43</sub> (SG) <sub>27-37</sub> NCs
ODE	Octadecane
PAGE	Polyacrylamide Gel Electrophoresis
PL	Photoluminescence
<i>p</i> -MBA	<i>p</i> -Mercaptobenzoic Acid
PT	Phase Transfer
QY	Quantum Yield
R <sub>[H-SR]/[M]</sub>	Thiol-to-Metal Ratio
R <sup>2</sup>	Coefficient of Determination
S	Supersaturation
SAd	1-Adamantanethiolate
SC	Supracrystal
S <sub>cri</sub>	Critical Supersaturation
SEC	Size Exclusion Chromatography
SF	Solubility Based Fractionation
SPR	Surface Plasmon Resonance
STEM	Scanning Transmission Electron Microscopy

T	Temperature
t	Time
TBAB	Borane <i>tert</i> -Butylamine Complex
$t_{\text{nuc}}$	Nucleation Time
TOF	Time of Flight
UV-vis	Ultraviolet-visible
$V_A$	Number of Valence Electrons per Nanocluster
XPS	X-Ray Photoelectron Spectroscopy
XRD	X-Ray Diffraction
z	Net Charged of a Nanocluster
$\Delta_{\text{HL}}$	HOMO-LUMO Energy Gap
$\epsilon_r$	Relative Permittivity
$\lambda_{\text{em}}$	Emission Wavelength
$\lambda_{\text{ex}}$	Excitation Wavelength

# CHAPTER 1 INTRODUCTION

## 1.1 Background

Ligand (*e.g.*, thiolate or phosphine)-protected noble metal (*e.g.*, Au or Ag) nanoclusters (NM-NCs) are ultrasmall nanoparticles below 2 nm in size containing typically several to a few hundreds of metal atoms.<sup>1-6</sup> Among them, thiolate-protected NM-NCs, generally representable by the “molecular formula”  $M_n(SR)_m$  (where  $n$  and  $m$  are the numbers of metal atoms ( $M = Au$  or  $Ag$ ) and thiolate ligands per cluster respectively), have drawn increasing interest because of the outstanding stability derived from a strong thiolate-metal interaction.<sup>1-2,5</sup> Due to the strong quantum confinement effect in the sub-2-nm regime, the  $M_n(SR)_m$  NCs display discrete, rather than the continuous or semi-continuous electronic structure of bulk noble metal (bulk-NM) and noble metal nanoparticles (NM-NPs,  $>2$  nm) respectively.<sup>2,7</sup> Properties which are uniquely bulk-NM (*e.g.*, surface luster) or NM-NPs (*e.g.*, surface plasmon resonance, SPR) are therefore absent in  $M_n(SR)_m$  NCs. The discrete electronic structure instead introduced a variety of size-dependent molecule-like properties (*e.g.*, HOMO-LUMO transition, strong luminescence, quantized charging, and high catalytic activity).<sup>2,8-17</sup> These molecule-like properties can add to the diversity in the use of  $M_n(SR)_m$  NCs for energy conversion, biomedicine, environmental monitoring, catalysis, and etc.<sup>9,16-20</sup> These newfound properties of the  $M_n(SR)_m$  NCs have stimulated strong research interest in the last two decades to establish reliable structure-property relations, and to design NC properties for technology deployment.<sup>2-</sup>

4,9,20-22

Aside from their unique molecule-like properties,  $M_n(SR)_m$  NCs also display unprecedented atomic packing structures (“crystal” structures).<sup>21,23-28</sup> It is now known that the atomic packing in  $M_n(SR)_m$  NCs, like their physicochemical properties, varies greatly with size, and may deviate strongly from the face-centered-cubic (*f.c.c.*) structure adopted by most crystalline NM-NPs.<sup>24-29</sup> For example, Kornberg and co-workers have shown that  $Au_{102}(SR)_{44}$  NCs consist of a 79-Au-atom ( $Au_{79}$ ) core with *pseudo*  $D_{5h}$  symmetry, capped by 19 monomeric SR-Au-SR and 2 dimeric SR-(Au-SR)<sub>2</sub> motifs.<sup>24</sup> It should be noted that  $D_{5h}$  is a forbidden symmetry in *f.c.c.* structures. There is a need to establish the “laws” behind properties and atomic packing unique to the NCs, in order to understand the structural origin of the NC properties and to rationalize the tailoring of NC properties.<sup>21,23</sup> The uncovering of structure-property evolutions with NC size also answers the basic questions in cluster and nanoparticle research, such as at what size and in what atomic packing structure do SPR properties begin to appear.<sup>21,30-31</sup> As a result of such great importance, the correlation of the size-dependent properties of NCs with size-dependent structures has been the centerpiece in the basic research on  $M_n(SR)_m$  NCs.<sup>2,21,23,25-29,32-33</sup>

Property tailoring is another focused area of NC research. Different applications require different specific performances of the  $M_n(SR)_m$  NCs.<sup>3,9,17,20</sup> For example, the  $M_n(SR)_m$  NCs for *in vivo* bio-imaging materials are required to have strong luminescence (*e.g.*, quantum yield (QY) >1 %), good biocompatibility, and an appropriate renal clearance period.<sup>20</sup> Due to the dependence of the properties of  $M_n(SR)_m$  NCs on size (*i.e.*, (n m)) and composition (*i.e.*, M and SR), the desired properties may be achieved by a size- and composition-controlled synthesis or by post-synthesis modifications (*e.g.*, post-synthesis surface functionalization).<sup>4,8,34-36</sup> A great variety of  $M_n(SR)_m$  NCs with different sizes (*e.g.*, from  $Au_{10}(SR)_{10}$  to

$\text{Au}_{187}(\text{SR})_{68}$ ),<sup>8,37-41</sup> core compositions (*e.g.*, monometallic  $\text{Au}_{25}(\text{SR})_{18}$  to bimetallic  $\text{Au}_{25-x}\text{Ag}_x(\text{SR})_{18}$  NCs),<sup>34,42</sup> ligand combinations (*e.g.*,  $\text{Au}_{25}(\text{SR}_1)_{18-x}(\text{SR}_2)_x$  where  $x = 0-18$  and  $\text{SR}_1$  and  $\text{SR}_2$  denotes two different types of thiolate ligands)<sup>36,43-44</sup> have been produced in the last two decades, giving rise to a wide spectrum of physical (*e.g.*, optical and electronic) and chemical (*e.g.*, electrochemical and catalytic) properties. More details about the synthesis and properties of  $\text{M}_n(\text{SR})_m$  NCs can be found in Chapter 2.

Self-assembly is a process in which building blocks (*e.g.*, molecules, nanoscopic and microscopic objects), prompted by specific interactions between the building blocks or between the building blocks and a template, spontaneously organize themselves into higher hierarchy structures.<sup>45-46</sup> The self-assembly of  $\text{M}_n(\text{SR})_m$  NCs is of fundamental importance to both basic and applied research alike. For the former it is used to confirm the NC structure and for the latter, it is a tool to further modify the properties of  $\text{M}_n(\text{SR})_m$  NCs. Reliable structure-property relations are predicated upon accurate crystal structure information. The determination of the  $\text{M}_n(\text{SR})_m$  NC crystal structure is commonly based on high precision diffraction techniques (*e.g.*, X-ray crystallography), which require perfect single-crystalline samples.<sup>2</sup> Advances in structure-property investigations therefore depend on the successful assembly (or crystallization) of  $\text{M}_n(\text{SR})_m$  NCs into single-crystalline supracrystals (SCs). In application explorations, self-assembly offers an added avenue to modify the NC properties without changing the size and composition of individual NCs. In a majority of cases proximal interactions or coupling effects between neighboring NCs of an assembly can lead to property changes. The NP (>2 nm) literature is replete with examples of enhanced and/or new NP properties by assembling the NPs into close-packed structures.<sup>47-51</sup> For example, Lee *et al.* showed that the electromagnetic

coupling between co-assembled Au NPs and CdTe nanowires could lead to a 5-fold enhancement of the luminescent intensity of CdTe nanowires (emission maximum at 660 nm,  $\lambda_{\text{ex}} = 420$  nm).<sup>50</sup> In a different study, Courty *et al.* reported the narrowing of the Stokes-anti-Stokes shift in the Raman spectrum of *f.c.c.* SCs of Ag NPs (diameter =  $\sim 5$  nm).<sup>51</sup> The new Raman response was attributed to the coherent vibrations of Ag NPs in the SCs due to the interactions between regularly- and closely-packed Ag NPs under laser excitation. It is plausible to expect that similar interactions or coupling effects in closely-packed NCs may also be useful for varying the properties of  $M_n(\text{SR})_m$  NCs.

Contrary to the self-assembly of NM-NPs, which is relatively well-established with numerous reports of unary, binary, ternary SCs,<sup>45,49,52-54</sup> the self-assembly of  $M_n(\text{SR})_m$  NCs is at a very early stage of development, and hence there is limited literature on the structural determination and structure-property exploration of NCs. There are two reasons for the lack of progress. First, self-assembly of NCs is a recent discovery which was hitherto unknown until the successful crystallization of  $\text{Au}_{102}(\text{SR})_{44}$  NCs by Kornberg and coworkers in 2007.<sup>24</sup> By comparison the self-assembly of NM-NPs has been investigated for several decades.<sup>47,55-56</sup> Second and more importantly, the self-assembly (especially crystallization) of  $M_n(\text{SR})_m$  NCs is technically challenging.<sup>2</sup> Despite the considerable activities in the last few years on the self-assembly (primarily crystallization) of  $M_n(\text{SR})_m$  NCs, success remains limited. Up to date, crystallization of  $M_n(\text{SR})_m$  NCs was only successful for 8 discrete sizes (*e.g.*,  $(n\ m) = (23\ 16)$ ,<sup>57</sup>  $(25\ 18)$ ,<sup>25-26,58</sup>  $(28\ 20)$ ,<sup>59</sup>  $(30\ 18)$ ,<sup>33</sup>  $(36\ 24)$ ,<sup>29</sup>  $(38\ 24)$ ,<sup>60</sup>  $(44\ 30)$ <sup>27-28</sup> and  $(102\ 44)$ <sup>24,61</sup>). There were also a few report on the self-assembly of  $M_n(\text{SR})_m$  NCs into less ordered 2-dimensional (2D) structures.<sup>62-63</sup> The limited success was partly due to the fragility of the NCs, but more importantly, due to a lack of understanding of the governing

principles for NC self-assembly which may be different from NP self-assembly. For example, uniform orientation of individual NCs is required for packing them into SCs, while preferential crystal orientation was rarely observed in spherical NPs packed into SCs.<sup>24,64-65</sup> The self-assembly of  $M_n(SR)_m$  NCs can definitely benefit from a more systematic approach to method development.

## 1.2 Objectives and Scope

This PhD thesis study is an exploration on the self-assembly of  $M_n(SR)_m$  NCs with the primary objective in developing a general approach to produce  $M_n(SR)_m$  NC assemblies with the desired structural orderliness. This was accomplished by a molecular (or atomic/ionic) mimetic strategy, where  $M_n(SR)_m$  NCs were regarded as supramolecules (or supramolecular atoms/ions) to mimic the ways nature arranges molecules (or atoms/ions) into disordered (amorphous) or/and ordered (crystalline) structures. The molecular (or atomic/ionic) mimetic approach to assembly is based on several unique but generic molecule- (or atom-/ion-) like structural features (*e.g.*, well-defined sizes and uniform structures), which are generally applicable to  $M_n(SR)_m$  NCs in a broad spectrum of sizes. Structural orderliness is a special emphasis of this PhD study, since a high structural order is necessary for post-assembly investigations (*e.g.*, crystal structure determination). However, due to limited time and resources, these post-assembly investigations were not carried out in this project. The specific research activities which were completed in this PhD project include the following:

- 1) This project began with the preparation of monodisperse and atomically precise  $M_n(SR)_m$  NCs as the high quality building blocks for self-assembly. Small  $Au_{15}(SG)_{13}$  and  $Au_{18}(SG)_{14}$  NCs, where SG is glutathione ligand, were



synthesized by a two-phase one-pot method which achieved size and monodispersity control through the kinetic control of NC formation. The NCs so produced (*e.g.*, Au<sub>15</sub>(SR)<sub>13</sub> and Au<sub>18</sub>(SR)<sub>14</sub> NCs) also filled the current lack of monodisperse NCs in the small and metastable size range ( $n < 20$ ), which could contribute to understanding the size-dependence of cluster stability and other physiochemical properties.

- 2) Charged M<sub>n</sub>(SR)<sub>m</sub> NCs were used to form hierarchical assemblies by mimicking the way ionic crystals are formed in nature. Specifically negatively charged M<sub>n</sub>(SR)<sub>m</sub> NCs (*e.g.*, supramolecular ions of Au<sub>29-43</sub>(SG)<sub>27-37</sub>, Au<sub>15</sub>(SG)<sub>13</sub>, and Ag<sub>16</sub>(SG)<sub>9</sub> NCs) were assembled into monodisperse colloidal spheres by electrostatic cross-linking with divalent cations (*e.g.*, Zn<sup>2+</sup> and Cd<sup>2+</sup>). Several ion-like behaviors, most notably a step-like assembly controlled by solubility product ( $k_{sp}$ ), were experimentally observed. However, long-range structural order (*e.g.*, constant spacing in the packing,  $d$ ) was not observed in the assemblies formed this way.
- 3) The use of amphiphilic chemistry for self-assembly was then explored. Amphiphilicity was introduced to sub-2-nm NCs by patching hydrophilic M<sub>n</sub>(SR)<sub>m</sub> NCs (*e.g.*, Au<sub>25</sub>(MHA)<sub>18</sub> NCs, where MHA is 6-mercaptohexanoic acid, with hydrophobic cations (*e.g.*, cetyltrimethylammonium, CTA<sup>+</sup>) to about half of a monolayer coverage. Amphiphilic Au<sub>25</sub>(MHA)<sub>18</sub>@<sub>x</sub>CTA NCs ( $x = 6-9$ , where  $x$  is the number of CTA<sup>+</sup> per NC), as supramolecular amphiphiles, were prepared by a phase-transfer (PT) driven ion-pairing reaction between CTA<sup>+</sup> and –COO<sup>–</sup> (derived from the deprotonation of MHA terminal carboxyl group). The self-assembly characteristics of amphiphilic Au<sub>25</sub>(MHA)<sub>18</sub>@<sub>x</sub>CTA NCs ( $x = 6-9$ ) was then investigated in a dual-solvent system of dimethylsulfoxide (DMSO, poor

solvent) and ethanol (good solvent). Slow- and selective-evaporation of ethanol self-assembled the amphiphilic NCs into a bilayer-based structure at the liquid-air interface, resembling the formation of the lamellar phase (the liquid crystal phase) of molecular amphiphiles. Regular *interlayer* packing (as evidenced by a constant *d*-spacing) was observed in these bilayers of amphiphilic NCs, but 3D crystalline order was still absent.

- 4) 3D long-range crystalline order was then achieved in NC assemblies by packing hard-sphere-like NCs by depletion forces (*i.e.*, entropic effects). Cs<sup>+</sup>-deprotonated Ag<sub>44</sub>(*p*-MBA)<sub>30</sub> NCs, where the *p*-mercaptobenzoic acid (*p*-MBA) ligands were fully deprotonated by reaction with CsOH, were used as supramolecular atoms and assembled into *f.c.c.* octahedral SCs, mimicking crystal formation by hard-sphere-like atoms. The self-assembly (or crystallization) was conducted, similar to the self-assembly of amphiphilic NCs mentioned before, in a water/DMSO dual-solvent system by the slow and selective evaporation of water (good solvent). The kinetics of SC growth was investigated by monitoring the depletion rate of discrete Ag<sub>44</sub>(*p*-MBA)<sub>30</sub> NCs in the crystallization solution. The insights from the kinetics study enabled us to vary the shape of Ag<sub>44</sub>(*p*-MBA)<sub>30</sub> NC-SCs by adjusting the concentration of the counter cations, Cs<sup>+</sup>. At high Cs<sup>+</sup> concentrations, concave-octahedral Ag<sub>44</sub>(*p*-MBA)<sub>30</sub> NC-SCs were selectively formed.

### 1.3 Thesis Organization

This thesis is organized into 7 chapters. After this introductory chapter, a brief review of the current research most relevant to the self-assembly of  $M_n(SR)_m$  NCs is presented (Chapter 2). Chapter 3 details the synthesis of monodisperse and atomically precise  $Au_{15}(SG)_{13}$  and  $Au_{18}(SG)_{14}$  NCs, as a demonstration of monodispersity control and size tuning of  $M_n(SR)_m$  NCs. Chapters 4, 5 and 6 describe, respectively, the self-assembly of negatively charged  $Au_{29-43}(SG)_{27-37}$ ,  $Au_{15}(SG)_{13}$ , and  $Ag_{16}(SG)_9$  NCs (supramolecular ions); of amphiphilic  $Au_{25}(MHA)_{18}@xCTA$  NCs where  $x = 6-9$  (supramolecular amphiphiles); and of  $Cs^+$ -deprotonated  $Ag_{44}(p-MBA)_{30}$  NCs (supramolecular atoms). The thesis concludes with Chapter 7 together with several suggestions for future work.

## CHAPTER 2 LITERATURE REVIEW

This chapter provides a succinct but up-to-date account of the major topics in understanding the self-assembly of thiolate-protected noble metal nanoclusters (NM-NCs), or  $M_n(\text{SR})_m$  NCs ( $M = \text{Au}$  or  $\text{Ag}$ ) for short. Since the self-assembly (and other related processes such as synthesis and device fabrication) are based on the molecule-like properties of  $M_n(\text{SR})_m$  NCs, the chapter begins with the discussion of the molecule-like properties, their origin, size-dependence and potential applications (§ 2.1). This is followed by a review of the major methods for synthesizing high quality building blocks for the self-assembly, *i.e.* monodisperse  $M_n(\text{SR})_m$  NCs, in § 2.2. Current progress in the self-assembly chemistry of  $M_n(\text{SR})_m$  NCs then round up the remaining of the chapter (§ 2.3).

### 2.1 Fundamentals of $M_n(\text{SR})_m$ NCs

$M_n(\text{SR})_m$  NCs have drawn significant research interest in the last two decades, primarily due to their size-dependent molecule-like properties (*e.g.*, molecule-like UV-vis absorption<sup>2-3,8,66</sup> and redox properties,<sup>14,67</sup> strong luminescence,<sup>9,11-12,20,68-69</sup> high catalytic activity<sup>16-17,70-72</sup>) which may find applications in a diversity of technology areas (*e.g.*, photosensitizers,<sup>18-19,73</sup> optical probes,<sup>9,20,74-75</sup> and catalysts<sup>16-17,71,76</sup>). This thesis study is an effort to promote the acceptance of  $M_n(\text{SR})_m$  NCs as a new family of functional materials through the discovery of more structure-property relations and property engineering. The research builds upon the current understanding of the molecule-like properties, their origin and their targeted applications given in the survey below.

### 2.1.1 The Electronic Structure of $M_n(SR)_m$ NCs

The molecule-like properties of  $M_n(SR)_m$  NCs are the direct consequence of their discrete electronic energy levels,<sup>2,7,17,69</sup> the first topic of our discussion.  $M_n(SR)_m$  NCs are invariably core-shell structured containing a sub-2-nm metal core and a thiolate ligand shell (Figure 2.1). The very small size of the metal core elicits a strong quantum confinement effect which results in discrete electronic energy levels. The thiolate ligands further modify the discrete electronic structure of  $M_n(SR)_m$  NCs through strong metal-thiolate interaction. It is worth noting that the metal-core@ligand-shell model is a simplified first order structural model for  $M_n(SR)_m$  NCs.

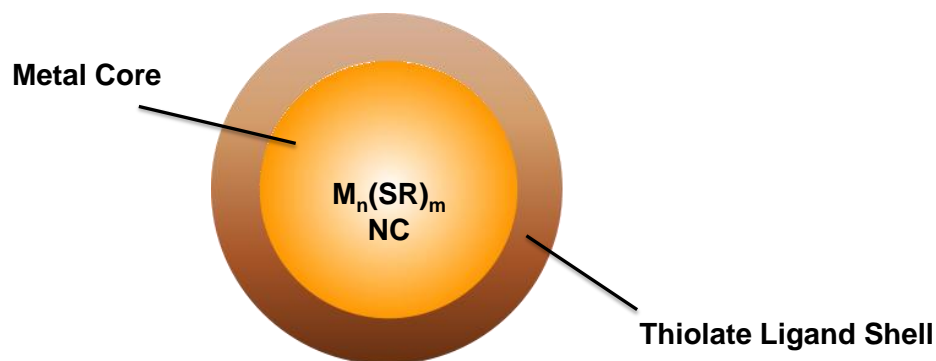


**Figure 2.1** Illustration of the core-shell construction of  $M_n(SR)_m$  NCs.

#### 2.1.1.1 Metal Core: The Origin of Strong Quantum Confinement Effect

The small metal core in  $M_n(SR)_m$  NCs having a size smaller than 2 nm (Figure 2.2) is fundamental to the size transition from discrete noble metal atoms to large noble metal nanoparticles (NM-NPs, >2 nm).<sup>1-2,4,77</sup> Such a small core is not able to support continuous (*i.e.* bulk metal) or semi-continuous (NM-NPs) electronic states. It elicits

strong quantum confinement effect leading to the quantization of electronic energy levels in  $M_n(\text{SR})_m \text{NCs}$ .<sup>2,7,21</sup>

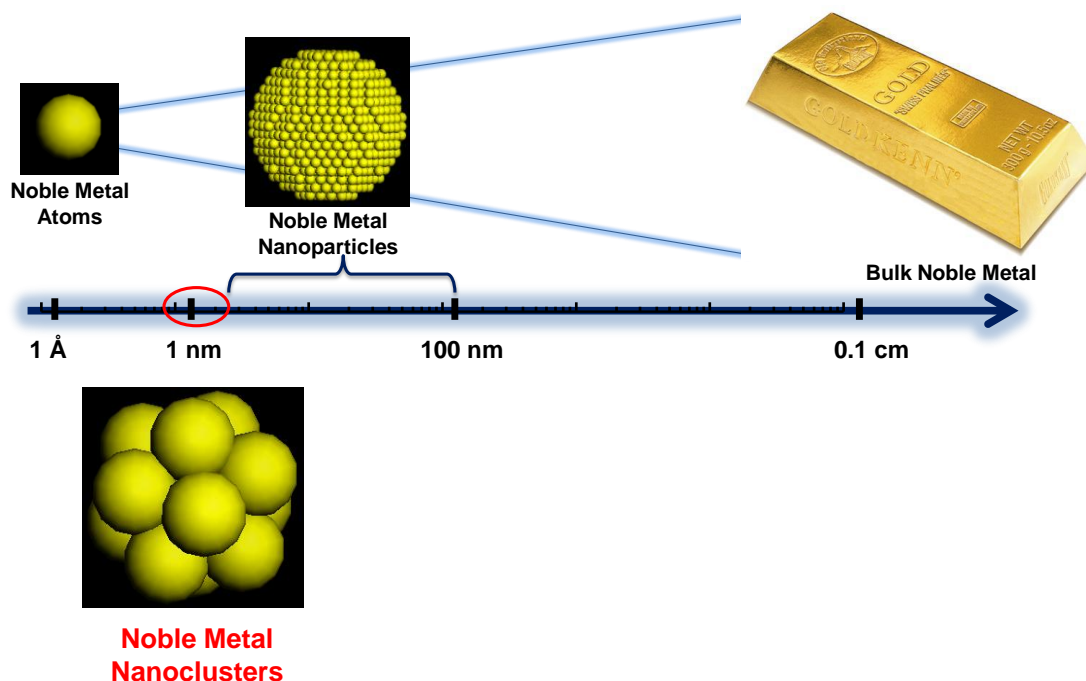


**Figure 2.2** Illustration comparing the size of noble metal atoms, noble metal nanoclusters ( $M_n(\text{SR})_m \text{NCs}$ ), noble metal nanoparticles and bulk noble metal.

The quantization of the electronic energy levels in this sub-2-nm regime could be understood in terms of the free-electron model, as suggested by Jin.<sup>2</sup> In the free-electron model of Au, for example, the single-electron Schrödinger equation can be applied to describe the 6s electron of Au atom if electron-electron and electron-nucleus interactions are negligible.<sup>78</sup>

The solution of the single electron Schrödinger equation yields the eigenvalues and consequently the energy level (E) of the electron

$$E = \frac{\pi^2 \hbar^2}{2m_e a^2} n_e^2 \quad (2.1)$$

where  $m_e$  is the mass of electron,  $\hbar$  is the Plank constant,  $n_e$  is the principal quantum number, and  $a^3$  is an approximation of the metal core volume of  $M_n(\text{SR})_m$  NCs. The  $E \sim n_e^2$  correlation means equal distribution of the electronic energy states on a spherical surface with the characteristic radius of  $n_e$ . Given that  $n_e^2 = n_{ex}^2 + n_{ey}^2 + n_{ez}^2$  in a 3-dimensional (3D) Cartesian coordinate system, and that  $n_{ex}$ ,  $n_{ey}$ , and  $n_{ez}$  could only assume positive integers (*i.e.*, in the positive octant of the 3D Cartesian space), the number of energy states (N) with an energy up to E could be described as

$$N = \frac{1}{8} \left( \frac{4}{3} \pi n_e^3 \right) \quad (2.2)$$

Substitution of Equation 2.1 into Equation 2.2 gives

$$N = \frac{\pi}{6} \left( \frac{2m_e a^2}{\pi^2 \hbar^2} \right)^{\frac{3}{2}} E^{\frac{3}{2}} \quad (2.3)$$

The density of energy states is obtained by differentiating Equation 2.3 with E

$$\frac{dN}{dE} = \frac{a^3}{4\pi^2} \left( \frac{2m_e}{\hbar^2} \right)^{\frac{3}{2}} E^{\frac{1}{2}} \quad (2.4)$$

The spacing of energy states ( $\delta$ ) could be approximated by the reciprocal of the density of energy states.

$$\delta = \frac{4\pi^2}{a^3} \left( \frac{\hbar^2}{2m_e} \right)^{\frac{3}{2}} E^{-\frac{1}{2}} \quad (2.5)$$

Discrete electronic states are noticeable at a certain temperature (T) if the spacing of energy states is larger than the thermal energy ( $k_B T$ , where  $k_B$  is the Boltzmann constant). *i.e.*,

$$\delta \geq k_B T \quad (2.6)$$

Assuming  $T = 278$  K (room temperature), and using the Fermi energy of Au ( $E_F = 5.5$  eV) as E, the critical core size of  $Au_n(\text{SR})_m$  NCs to show discrete electronic states is  $a$

= ~1.7 nm. Hence, based on the free-electron model, the quantization of electronic states is significant for  $\text{Au}_n(\text{SR})_m$  NCs in the sub-2-nm metal core region.

Equation 2.5 also provides a first order view on the size-dependence of the electronic structure of  $\text{M}_n(\text{SR})_m$  NCs. In Equation 2.5, the spacing of energy states is inversely proportional to the metal core volume of  $\text{M}_n(\text{SR})_m$  NCs as  $\delta \sim (1/a^3)$ . Hence the spacing of energy states is more significant in smaller NCs. This is consistent with the trend of increasing HOMO-LUMO energy gap ( $\Delta_{\text{HL}}$ ) with decreasing metal core size observed for the  $\text{Au}_n(\text{SR})_m$  NCs.<sup>8</sup> It should, however, be emphasized that the free-electron model is a highly simplified model of a complex structure (due to the omission of several important interactions, *e.g.*, electron-electron and electron-nucleus interactions), and is not expected to provide precise predictions. For example, the free-electron model predicts an evenly distributed  $\delta$  in  $\text{M}_n(\text{SR})_m$  NCs with fixed metal core size, which is not the case in real world  $\text{M}_n(\text{SR})_m$  NCs.<sup>25,79</sup>

### 2.1.1.2 Thiolate Ligand Shell: the Modifier of Electronic Structure

The free-electron model not only leaves out electron-electron or electron-nucleus interactions, but also neglects the effects of the thiolate ligand shell. The generally strong metal-thiolate interaction and high surface-to-volume ratio should lead to significant modifications of the  $\text{M}_n(\text{SR})_m$  NC electronic structure.<sup>80</sup> Current advances in the synthesis and crystal structural determination of  $\text{M}_n(\text{SR})_m$  NCs have unambiguously confirmed the inference.<sup>25,29,59-60,81-83</sup>

The thiolate ligands could modify the electronic structure of the noble metal nanoclusters by involving themselves in the formation of the of  $\text{M}_n(\text{SR})_m$  NCs molecular orbitals (MOs). For example, Zhu *et al.* calculated the Kohn-Sham MO (*i.e.*, MO calculations based on Kohn-Sham equation) energy levels of  $\text{Au}_{25}(\text{SR})_{18}$  NCs via



the density functional theory (DFT) based on the crystal structure of  $\text{Au}_{25}(\text{SC}_2\text{H}_4\text{Ph})_{18}$  NCs ( $\text{SC}_2\text{H}_4\text{Ph} = 2\text{-phenylethanethiolate}$  ligands).<sup>25</sup> The results of the calculation, which are reproduced in Figure 2.3, show a considerable contribution from the S(3p) orbital in the HOMO and LUMO orbital sets of  $\text{Au}_{25}(\text{SR})_{18}$  NCs, evincing the direct involvement of the thiolate ligands in construction of the  $\text{Au}_{25}(\text{SR})_{18}$  NC MOs. The direct involvement of thiolate ligands in the electronic structure of metal nanoclusters via the S(3p) orbital have also been reported for other types of  $\text{M}_n(\text{SR})_m$  NCs.<sup>27-29,33,59-60,79</sup>

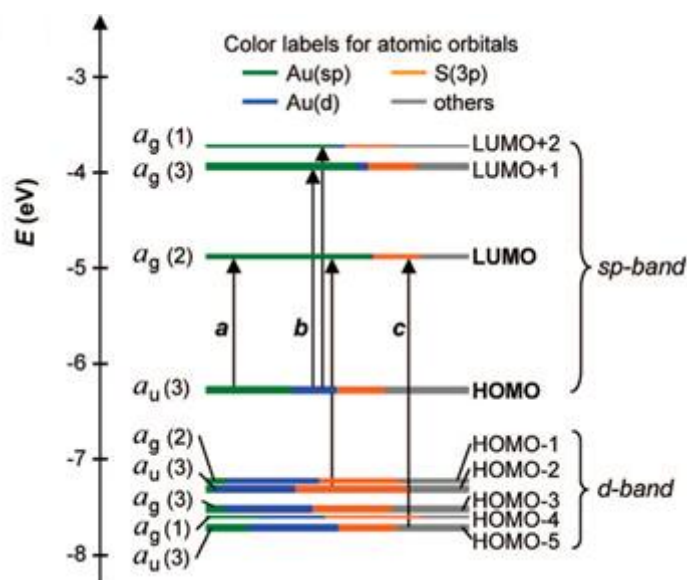


**Figure 2.3** Kohn-Sham molecular orbital energy level diagram of  $\text{Au}_{25}(\text{SR})_{18}$  NCs. Each orbital is drawn to show the relative contributions (as line lengths of different colors) of the atomic orbitals of Au(6sp) (green), Au(5d) (blue), S(3p) (yellow), and others (unspecified atomic orbitals with <1 % contribution each) (grey). The left column of the orbitals shows the orbital symmetry (g or u) and degeneracy (in parenthesis); the right column shows the HOMO and LUMO sets. SR was taken to be SH for computational expediency. Adopted from Ref.<sup>(25)</sup> with the permission of the American Chemical Society.

In addition to their direct involvement in the construction of the  $\text{M}_n(\text{SR})_m$  NC MOs, the thiolate ligands could also influence the  $\text{M}_n(\text{SR})_m$  NC electronic behavior by rendering certain metal core sizes more stable than others. It has been experimentally

found that stable  $M_n(SR)_m$  NCs could only be formed in certain metal core sizes.<sup>8,84-85</sup> Recently, Krommenhoek *et al.*<sup>81</sup> and Zeng *et al.*<sup>29,59,86</sup> suggested that the stable metal core is strongly dependent on the steric hindrance and/or electronic conjugation effects of the thiolate ligands. By using various bulky thiolate ligands (*e.g.*, cyclohexanethiolate (S-*c*-C<sub>6</sub>H<sub>11</sub>) and 1-adamantanethiolate (SAd)) in their synthesis, Krommenhoek *et al.* obtained a series of stable  $Au_n(SR)_m$  NCs with unprecedented metal core sizes (*e.g.*, Au<sub>30</sub>(SAd)<sub>18</sub>, Au<sub>39</sub>(SAd)<sub>23</sub>, Au<sub>65</sub>(S-*c*-C<sub>6</sub>H<sub>11</sub>)<sub>30</sub> and Au<sub>67</sub>(S-*c*-C<sub>6</sub>H<sub>11</sub>)<sub>30</sub>),<sup>81</sup> which are distinctively different from the stable products (*e.g.*, Au<sub>25</sub>(SR)<sub>18</sub>, Au<sub>38</sub>(SR)<sub>24</sub>, and Au<sub>144</sub>(SR)<sub>60</sub>) in the synthesis of  $Au_n(SR)_m$  NCs using conventional thiolate ligands (*e.g.*, SC<sub>2</sub>H<sub>4</sub>Ph).<sup>79,87-89</sup> This is a lucid demonstration of the steric hindrance effects of thiolate ligands on the stable core size of  $M_n(SR)_m$  NCs. In another work, Zeng *et al.* reacted 4-*tert*-butylbenzenethiolate (SPh-*t*-Bu) with Au<sub>25</sub>(SC<sub>2</sub>H<sub>4</sub>Ph)<sub>18</sub> and Au<sub>38</sub>(SC<sub>2</sub>H<sub>4</sub>Ph)<sub>24</sub> NCs, which are stable species in the  $Au_m(SC_2H_4Ph)_n$  NC system, to form monodisperse Au<sub>28</sub>(SPh-*t*-Bu)<sub>20</sub> and Au<sub>36</sub>(SPh-*t*-Bu)<sub>24</sub> NCs respectively.<sup>29,59,86</sup> The authors attributed the transformation of stable metal core size (Au<sub>25</sub> → Au<sub>28</sub> and Au<sub>38</sub> → Au<sub>36</sub>) to the steric hindrance and electron conjugation effects of the SPh-*t*-Bu ligand. It should be noted that the SPh-*t*-Bu ligand is bulkier than the SC<sub>2</sub>H<sub>4</sub>Ph ligand; and S is directly conjugated to the phenyl ring in the SPh-*t*-Bu ligand, which could result in a strong inductive effect between the phenyl ring and the Au core.<sup>29</sup>

### 2.1.2 Molecule-Like Properties and Potential Applications of $M_n(SR)_m$ NCs

The discrete electronic structure of  $M_n(SR)_m$  NCs determined by the metal core and the thiolate ligand shell can give rise to very diverse molecule-like physicochemical properties such as molecule-like UV-vis absorption, strong luminescence, molecule-like redox charging and high catalytic activity.<sup>2-3,9,14,16-17</sup> All of these physicochemical properties display a strong dependence on the NC size.<sup>8-9,13-14,16-17</sup> The strong size dependence of properties is consequential upon the strong quantum confinement effect and strong metal-thiolate interaction in  $M_n(SR)_m$  NCs, where the addition or removal of even a single metal atom or a thiolate ligand could lead to significant changes in the electronic structure of  $M_n(SR)_m$  NCs.<sup>2,4</sup> Based on this argument, we opine that (n m), which is usually deduced from mass spectrometry analysis, is a better measure of the size of  $M_n(SR)_m$  NCs, in comparison to diameter measured by conventional electron microscopy (EM, less effective in <1 nm size range). Hence the (n m) designation will be used to refer to the NC size hereafter unless stated otherwise.

These unique size-dependent molecule-like properties make the  $M_n(SR)_m$  NCs potentially useful as solar cell photosensitizers, sensor optical probes and catalysts.<sup>9,16-18</sup> The following sections will sample some of the size-dependent molecule-like properties of  $M_n(SR)_m$  NCs and their potential applications.

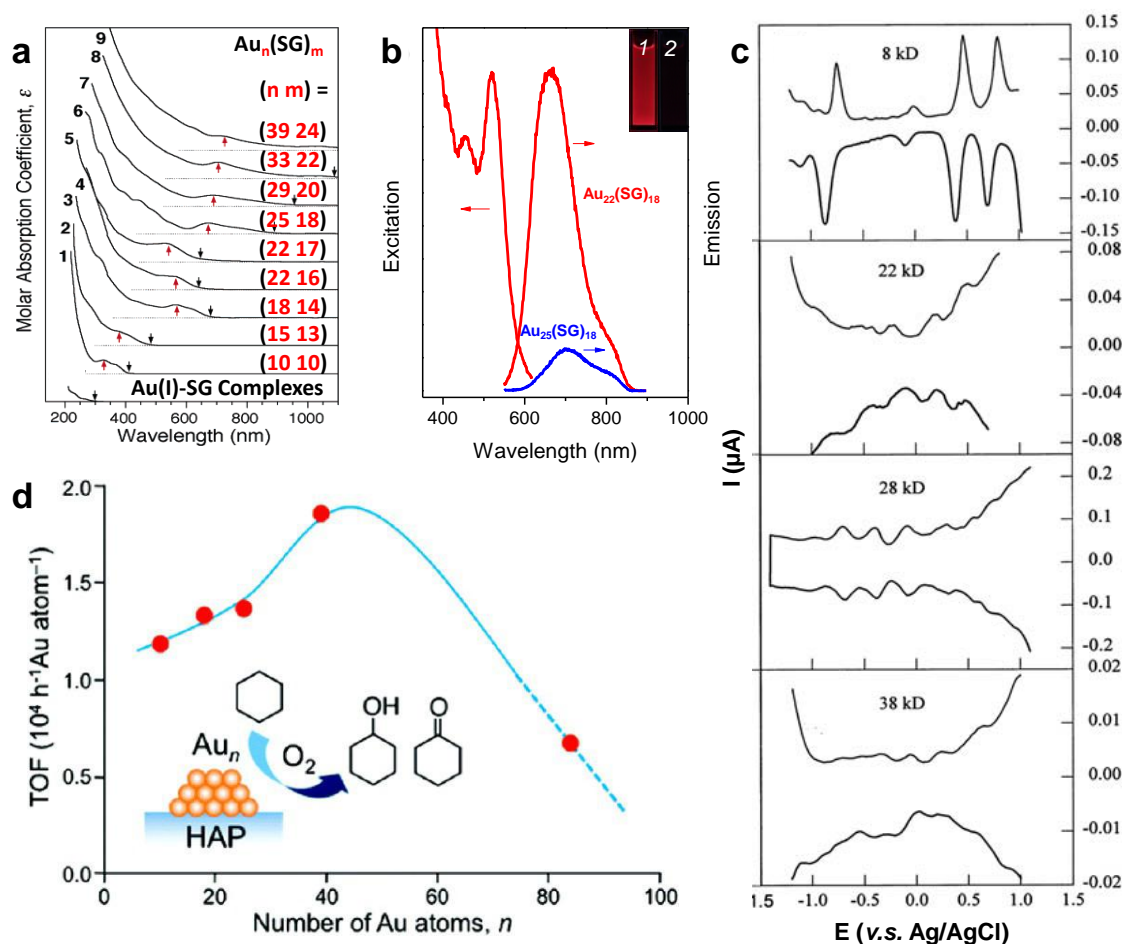


**Figure 2.4** Size-dependent molecule-like properties of  $M_n(SR)_m$  NCs. (a) UV-vis absorption spectra of  $Au_n(SG)_m$  NCs in various sizes:  $(n m) = (10 10)$ ,  $(15 13)$ ,  $(18 14)$ ,  $(22 16)$ ,  $(22 17)$ ,  $(25 18)$ ,  $(29 20)$ ,  $(33 22)$ , and  $(39 24)$ ; the black and red arrows indicate the onset and maximum of UV-vis absorption, respectively. (b) Emission (excitation wavelength  $\lambda_{ex} = 520$  nm) spectra of  $Au_{22}(SG)_{18}$  NCs (red, right side) and  $Au_{25}(SG)_{18}$  NCs (blue); the excitation (emission wavelength  $\lambda_{em} = 665$  nm) spectrum of  $Au_{22}(SG)_{18}$  NCs is also shown (red, left side); the insets are representative digital images of  $Au_{22}(SG)_{18}$  NC (No. 1) and  $Au_{25}(SG)_{18}$  NC (No. 2) aqueous solutions taken under UV irradiation ( $\lambda = 365$  nm). (c) Differential pulse voltammograms (DPV) of  $Au_n(SC_6H_{13})_m$  NCs as a function of core size; core sizes were measured in terms of the  $Au_nS_m$  core mass and labeled in each voltammogram; the DVP analysis was carried out in a toluene/acetonitrile (2/1 v:v) solution of 0.05 M tetrahexylammonium perchlorate, using a  $9.5 \times 10^{-3} \text{ cm}^2$  Pt electrode, a direct current (DC) 50 mV pulse and a scan rate of 10 mV/s. (d) The turn-over-frequency (TOF) of cyclohexane in cyclohexane oxidation catalyzed by hydroxyapatite (HAP) supported  $Au_n$  NCs with different core sizes ( $n = 10, 18, 29, 39,$  and  $85$ ); the inset is a schematic illustration of the catalytic reaction. (a, b, d) were adopted from Refs.<sup>(8)</sup>, <sup>(12)</sup>, and <sup>(90)</sup> respectively with the permission of the American Chemical Society; and (c) was adopted from Ref.<sup>(14)</sup> with the permission of the American Association for the Advancement of Science (AAAS).

### 2.1.2.1 Molecule-Like UV-vis Absorption and Applications as Photosensitizers

Since UV-vis absorption spectrum is a direct reflection of the electronic structure, the discrete electronic structure of  $M_n(\text{SR})_m$  NCs gives rise to molecule-like absorption features which are distinctively difference from the surface plasmon resonance (SPR, arising from a semi-continuous electronic structure) induced absorption of NM-NPs (>2 nm).<sup>8,21,91</sup> Figure 2.4a shows the UV-vis spectra of a series of glutathione (H-SG or GSH) protected Au NCs in different sizes; (n m) = (10 10), (15 13), (18 14), (22 16), (22 17), (25 18), (29 20), (33 22) and (39 24).<sup>8</sup> These UV-vis spectra are distinctively different from those of large Au NPs (>2 nm), which generally display an unimodal broad peak at ~520 nm due to SPR.<sup>92</sup> This is indication that  $M_n(\text{SR})_m$  NCs are more similar to molecules (with discrete electronic states) than NM-NPs (>2 nm). In addition to the lack of a SPR induced absorption, the UV-vis absorption of  $M_n(\text{SR})_m$  NCs also shows strong size-dependence. Figure 2.4a shows that the UV-vis absorption spectra of  $\text{Au}_n(\text{SG})_m$  NCs vary significantly with the NC size (*i.e.*, (n m)), with no shared common features among them. An approximate trend (with the exceptions of (n m) = (22 16) and (22 17)) of increasing  $\Delta_{\text{HL}}$  (measured by the absorption onset, the black arrows in Figure 2.4a) with decreasing NC size may be generalized from these UV-vis absorption spectra. The trend is consistent with the prediction of the free-electron model in §2.1.1.1.

The molecule-like UV-vis absorption, and a relatively high LUMO level, make the  $M_n(\text{SR})_m$  NCs useful as a new family of high performance photosensitizers.<sup>18-19,73</sup> In the development of solar cells or water splitting catalysts, the visible light photoactivity of large bandgap semiconductors (*e.g.*,  $\text{TiO}_2$ ) can be augmented by a photosensitizer.<sup>93</sup> A good photosensitizer should be able to absorb visible light efficiently and deliver the absorbed energy to the large bandgap semiconductor.<sup>93</sup> The

molecule-like absorption of most  $M_n(\text{SR})_m$  NCs occurs mostly in the visible light region, and the high LUMO level of  $M_n(\text{SR})_m$  NCs could facilitate the transfer of the excited electron to the semiconductor. These make  $M_n(\text{SR})_m$  NCs a contender for photosensitizers. The Kamat group was the first to explore  $M_n(\text{SR})_m$  NCs as photosensitizers.<sup>18-19</sup> They used the  $\text{Au}_{29-43}(\text{SG})_{27-37}$  NCs of Luo *et al.* (with strong absorption in the 400-525 nm region)<sup>11</sup> as the photosensitizer for a  $\text{TiO}_2$  solar cell. The as-fabricated  $M_n(\text{SR})_m$  NC sensitized solar cell could generate a stable photocurrent density of  $3.96 \text{ mA/cm}^2$  at a power conversion efficiency ( $\eta$ ) of  $\sim 2.3 \%$  under visible-light irradiations (provided by a AM 1.5 solar simulator), which is comparable in performance with a typical quantum dot sensitized solar cells.<sup>94</sup>

### 2.1.2.2 Strong Luminescence and Applications as Optical Probes

The discrete electronic structure of  $M_n(\text{SR})_m$  NCs can also result in strong luminescence. A good example is the extensively-investigated  $\text{Au}_{25}(\text{SG})_{18}$  NCs which exhibit a emission peak at  $\sim 700 \text{ nm}$  under excitation by  $\lambda_{\text{ex}} = 520 \text{ nm}$  (Figure 2.4b, blue line).<sup>12,95</sup> The quantum yield (QY) of  $\text{Au}_{25}(\text{SG})_{18}$  NCs was calculated to be  $\sim 0.2 \%$ , which is more than 7 orders of magnitude higher than that of bulk gold (QY =  $\sim 10^{-10}$ ).<sup>8</sup> Yu *et al.* recently reported highly luminescent  $\text{Au}_{22}(\text{SG})_{18}$  NCs (Figure 2.4b, inset #1). While the emission maximum was similar, at  $\sim 665 \text{ nm}$  ( $\lambda_{\text{ex}} = 520 \text{ nm}$ ), the QY was a much higher  $\sim 8 \%$  (Figure 2.4b, red curve to the right).<sup>12</sup> This significant emission enhancement brought about by the deletion of 3 Au atoms ( $\text{Au}_{22}(\text{SG})_{18}$  *v.s.*  $\text{Au}_{25}(\text{SG})_{18}$ ) is a good demonstration of the strong size-sensitivity of the luminescence of  $M_n(\text{SR})_m$  NCs. Other thiolate protected  $M_n(\text{SR})_m$  NCs with strong luminescence have also been reported by the Xie and coworkers,<sup>10-11,96-98</sup> Zheng and coworkers,<sup>99-100</sup>

Pradeep and coworkers,<sup>22,95,101-102</sup> and Nienhaus and coworkers<sup>13,103</sup>. A state of art QY, at 15%, was reported by Luo *et al.*<sup>11</sup>

The strong luminescence, together with other features such as low toxicity, small size and good optical stability, suggests that  $M_n(\text{SR})_m$  NCs may be suitable as the optical probes for sensors.<sup>9-10</sup> There are two ways to use the  $M_n(\text{SR})_m$  NCs in an optics-based sensor: 1) as a “turn-on” sensor, where the presence of an analyte induces or enhances the luminescence of  $M_n(\text{SR})_m$  NCs,<sup>104-105</sup> and 2) as a “turn-off” sensor where the luminescence of  $M_n(\text{SR})_m$  NCs is quenched or diminished by the specific interaction between the analyte and NCs.<sup>74-75,106-107</sup> For example, Wu *et al.* found that  $\text{Ag}^+$  could interact strongly with the Au(0) in the core of  $\text{Au}_{25}(\text{SG})_{18}$  NCs resulting in luminescent enhancement.<sup>105</sup> A “turn-on” sensor for  $\text{Ag}^+$  detection with a limit of detection (LOD) of 200 nM was developed based on this principle.<sup>105</sup> In sharp contrast to the  $\text{Ag}^+\cdots\text{Au}(0)$  interaction-enhanced luminescence, the strong metallophilic interaction between  $\text{Hg}^{2+}$  and Au(I) or Ag(I) (such oxidized metal species are often present on the  $M_n(\text{SR})_m$  NC surface to coordinate the metal atoms to the thiolate ligands) could quench the luminescence of  $M_n(\text{SR})_m$  NCs.<sup>106-107</sup> The latter principle was used by the Xie group to develop two prototype “turn-off” optical sensors for  $\text{Hg}^{2+}$  detection (LOD < 0.5 nM in both cases) using  $\text{Ag}_{12}(\text{SG})_{10}$  NCs (emission maximum at 435 nm under  $\lambda_{\text{ex}} = 350$  nm)<sup>107</sup> and  $\text{Au}_{25}(\text{BAS})$  NCs (emission maximum at 640 nm under  $\lambda_{\text{ex}} = 480$  nm)<sup>106</sup> where BSA denotes bovine serum albumin (a thiol-group containing protein).

### 2.1.2.3 Molecule-Like Redox Charging and Applications as Catalysts

Molecule-like redox charging is another important property of small  $M_n(\text{SR})_m$  NCs due to their large  $\Delta_{\text{HL}}$ . The molecule-like redox charging of  $M_n(\text{SR})_m$  NCs was first

demonstrated by Chen *et al.* in 1998.<sup>14</sup> The authors carried out differential pulse voltammetry (DPV) on a family of different-sized  $\text{Au}_n(\text{SC}_6\text{H}_{13})_m$  NCs, where  $\text{SC}_6\text{H}_{13}$  is hexanethiolate. The size of  $\text{Au}_n(\text{SC}_6\text{H}_{13})_m$  NCs in the study was expressed in terms of the mass of the  $\text{Au}_n\text{S}_m$  core from laser desorption/ionization mass spectrometry (LDI-MS) analysis. As the  $\text{Au}_n\text{S}_m$  core mass decreased from  $\sim 38$  kDa ( $\sim \text{Au}_{200}$  NCs) to  $\sim 8$  kDa ( $\sim \text{Au}_{38}$  NCs),<sup>108</sup> the electrochemical behavior of the  $\text{Au}_n(\text{SC}_6\text{H}_{13})_m$  NCs deviated from the typical metal-like double layer charging to molecule-like redox charging. Figure 2.4c shows that, for a  $\text{Au}_n\text{S}_m$  core mass of  $\sim 22$  kDa ( $\sim \text{Au}_{102}$  NCs)<sup>40</sup> or higher, the voltage difference between two neighboring current peaks ( $\Delta V$ ) in the voltammograms of  $\text{Au}_n(\text{SC}_6\text{H}_{13})_m$  NCs were regularly spaced, as expected from the quantized charging of a dielectric film (*e.g.*, thiolate monolayer coated Au(111) surface;  $\Delta V = e/C = \text{constant}$ , where  $e$  is electronic charge, and  $C$  is the capacitance of thiolate monolayer covered Au surface).<sup>109</sup> On the contrary, in  $\text{Au}_n(\text{SC}_6\text{H}_{13})_m$  NCs with a  $\text{Au}_n\text{S}_m$  core mass of  $\sim 8$  kDa, the  $\Delta V$  was no longer regularly spaced, and a large voltage gap was present between the first positive and negative current peaks. The large central  $\Delta V$  ( $\Delta V$  between the first positive and negative current peaks) could not be explained by classical metal-like double layer charging, but could be ascribed to the large  $\Delta_{\text{HL}}$  of small  $\text{Au}_n(\text{SC}_6\text{H}_{13})_m$  NCs.<sup>14</sup> Therefore, the first positive and negative current peaks of  $\sim 8$  kDa NC species could be assigned to NC redox peaks corresponding to changing the NC charge state from 0/+1 and 0/-1 respectively.<sup>79</sup>

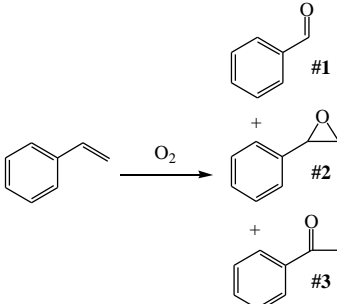
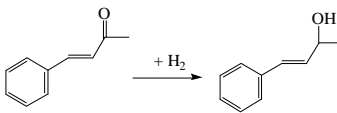
The molecule-like redox charging was also found in other small-sized  $\text{M}_n(\text{SR})_m$  NCs, with mostly reversible conversion of the NC charge state.<sup>110-111</sup> For example, the charge states of  $[\text{Au}_{25}(\text{SR})_{18}]^z$  (where  $z = -1, 0$  and  $+1$  is the net charge of the NC) could be facily switched by reversible oxidization and reduction.<sup>112-113</sup> The reversible conversion of the charge states qualifies the  $\text{M}_n(\text{SR})_m$  NCs as good electron



transfer mediators in redox reactions. The ability to mediate electron transfer, together with an under-coordinated noble metal surface (which facilitates reactant adsorption), imparts the  $M_n(SR)_m$  NCs with catalytic activity in a number of redox reactions.<sup>17</sup> Based on this simple concept, a variety of “ligand-on” (thiolate ligands not removed) and “ligand-off” (thiolate ligands removed, typically by heat-treatment) type  $M_n(SR)_m$  NCs catalysts were developed, and used with and without a catalyst support (*e.g.*, oxides, and carbon nanotubes (CNTs)).<sup>70,76,90,114-118</sup> Some representative applications of “ligand-on” and “ligand-off”  $M_n(SR)_m$  NC catalysts in redox reactions are listed in Tables 2.1 and 2.2 respectively. In addition to the reversible charge state conversion, the catalytically active bare metal surface may contribute (perhaps dominantly but this is still under debate)<sup>17,76,116</sup> to the catalytic activity of the “ligand-off” type of  $M_n(SR)_m$  NCs catalysts.<sup>16,76</sup>

Similar to other molecule-like properties, the catalytic activity of  $M_n(SR)_m$  NCs is also highly size-dependent. For example, Liu *et al.* reported a volcano-shaped activity-size relationship (Figure 2.4d) for their hydroxyapatite (HAP) supported  $Au_n$  NC ( $Au_n/HAP$ ) catalysts, which were used to catalyze the selective oxidation of cyclohexane into KA-oil (cyclohexanol/cyclohexanone mixture).<sup>90</sup> The origin of the volcano-shaped activity-size relationship has yet to be well understood.

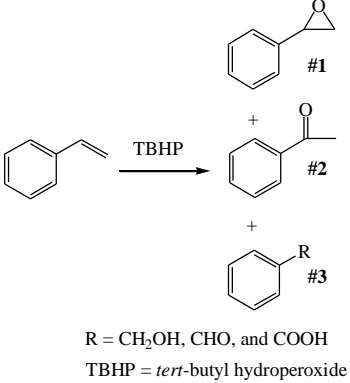
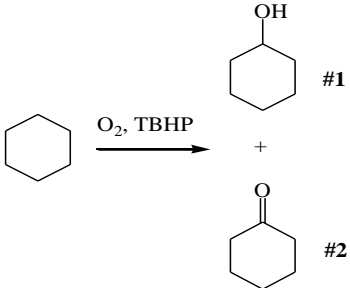
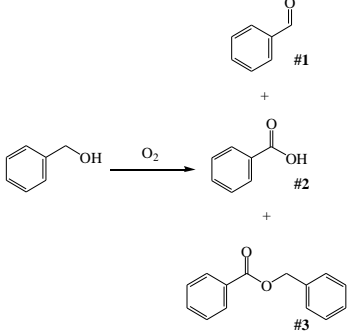
**Table 2.1** Catalytic performances of “ligand-on” type  $M_n(SR)_m$  NC catalysts in selected reactions.

No.	Catalyst*	Reaction	Conversion (%)	Selectivity (%)	Reaction Conditions	Ref.
1	$Au_{25}(SR)_{18}$	Styrene Oxidation: 	27	#1: 70 #2: 24	373 K, 24 h, under 1 MPa $O_2$ .	114
2	$Au_{38}(SR)_{24}$		14	#1: 72 #2: 24		
3	$Au_{144}(SR)_{60}$		12	#1: 80 #2: 20		
4	$Au_{25}(SR)_{18}/SiO_2$		18	#1: 80 #2: N.A.	353 K, 12 h, under 1 MPa $O_2$ .	115
5	$Au_{38}(SR)_{24}/SiO_2$		8	#1: 79 #2: N.A.		
6	$Au_{144}(SR)_{60}/SiO_2$		8	#1: 85 #2: N.A.		
7	$Au_{25}(SR)_{18}/HAP^{**}$		22	#1: 55 #2: N.A.		
8	$Au_{38}(SR)_{24}/HAP$		14	#1: 59 #2: N.A.		
9	$Au_{144}(SR)_{60}/HAP$		14	#1: 62 #2: N.A.		
10	$Au_{25}(SR)_{18}/CeO_2$	CO Oxidation: $CO \xrightarrow{O_2} CO_2$	100	100	373 K, 0.5 h, $CO/O_2 = 1/2$ v/v.	76
11	$Au_{25}(SR)_{18}$	Benzalacetone Hydrogenation: 	22	100	273 K, 3 h, under 1 MPa $H_2$ .	70
12	$Au_{25}(SR)_{18}/Fe_2O_3$		43	100		
13	$Au_{25}(SR)_{18}/TiO_2$		40	100		
14	$Au_{25}(SR)_{18}/SiO_2$		19	100		

\* Supported “ligand-on” type  $M_n(SR)_m$  NC catalysts are denoted as  $M_n(SR)_m$ /support;

\*\* HAP denotes hydroxyapatite.

**Table 2.2** Catalytic performances of “ligand-off” type  $M_n(SR)_m$  NC catalysts in selected reactions.

No.	Catalyst*	Reaction	Conversion (%)	Selectivity (%)	Reaction Conditions	Ref.
1	Au <sub>25</sub> /HAP**	Styrene Oxidation:  R = CH <sub>2</sub> OH, CHO, and COOH TBHP = <i>tert</i> -butyl hydroperoxide	90	#1: 92 #2: N.A.	353 K, 12 h.	<sup>118</sup>
2	Au <sub>25</sub> /HAP		100	#1: 100		<sup>115</sup>
3	Au <sub>38</sub> /HAP		100	#1: 100		
4	Au <sub>144</sub> /HAP		100	#1: 100		
5	Au <sub>25</sub> /SiO <sub>2</sub>		90	#1: 92 #2: N.A.		
6	Au <sub>38</sub> /SiO <sub>2</sub>		95	#1: 95 #2: N.A.		
7	Au <sub>144</sub> /SiO <sub>2</sub>		100	#1: 100		
8	Au <sub>10</sub> /HAP	Cyclohexane Oxidation: 	11.6	#1: 58 #2: 41	423 K, 0.5 h, under 1 MPa O <sub>2</sub> .	<sup>90</sup>
9	Au <sub>18</sub> /HAP		12.9	#1: 49 #2: 50		
10	Au <sub>25</sub> /HAP		14.2	#1: 50 #2: 49		
11	Au <sub>39</sub> /HAP		14.9	#1: 50 #2: 49		
12	Au <sub>85</sub> /HAP		6.9	#1: 53 #2: 41		
13	Au <sub>25</sub> /CNTs	Benzyl Alcohol Oxidation: 	22	#1: 37 #2: 29 #3: 34	303 K, 6 h, under 1 MPa O <sub>2</sub> .	<sup>117</sup>

\* Supported “ligand-off” type  $M_n(SR)_m$  NC catalysts are denoted as  $M_n$ /support;

\*\* HAP denotes hydroxyapatite.

## 2.2 Synthesis of Monodisperse Atomically Precise $M_n(SR)_m$ NCs

Since the electronic structure and physiochemical properties of  $M_n(SR)_m$  NCs are strongly size dependent. The ability to synthesize monodisperse  $M_n(SR)_m$  NCs in atomic precision (*i.e.*, with narrow deviations from the defined (n m)) is a prerequisite for establishing unambiguous size-property relationships, and for obtaining reliable performance from  $M_n(SR)_m$  NC based functional materials.<sup>4</sup> In addition, a successful self-assembly of  $M_n(SR)_m$  NCs also depends on the availability of high quality building blocks, *i.e.*, monodisperse  $M_n(SR)_m$  NCs. This is especially important for the assembly of  $M_n(SR)_m$  NCs into a 3D ordered crystalline structure (*i.e.*,  $M_n(SR)_m$  NC supracrystals or  $M_n(SR)_m$  NC-SCs) for crystal structure determination, and for collective property investigation. This is because the long-range order of the assembly is more demanding of the monodispersity of the building blocks.<sup>25,52</sup>

The synthesis of  $M_n(SR)_m$  NCs could be dated date back to the early 1990s, when Brust *et al.* reported their seminal work on the preparation of small-sized thiolate protected Au NPs (2-5 nm).<sup>119</sup> The preparation was based on two primary reactions:

- 1) The reduction of Au(III) (*e.g.*, from  $HAuCl_4$ ) by the thiol ligand (H-SR) to form Au(I)-SR complexes:

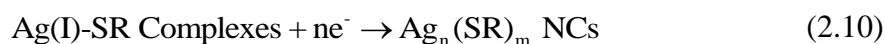


- 2) The reductive decomposition of Au(I)-SR complexes in presence of a strong reductant (*e.g.*,  $NaBH_4$ ) to form Au NPs:



Based on these two reactions, the groups of Whetten and Murray were able to produce  $Au_n(SR)_m$  NCs with sizes smaller than 2 nm by varying the thiol-to-Au ratio  $R_{[H-SR]/[Au]}$  (modified Brust method or Brust-like method). For example, by increasing

the  $R_{[H-SR]/[Au]}$  from  $\sim 1$  (the value used by Brust *et al.*) to 2, Whetten *et al.* synthesized  $\sim 1.5$  nm  $Au_n(SR)_m$  NCs, with a core mass (as  $Au_nS_m$ ) of  $\sim 28$  kDa according to LDI-MS analysis<sup>1</sup> (the later work by Chaki *et al.*<sup>108</sup> and Qian *et al.*<sup>79</sup> suggested that this  $\sim 28$  kDa NC species could be  $Au_{144}(SR)_{60}$ ). A further reduction of the NC size (down to a  $Au_nS_m$  core mass of  $\sim 8$  kDa) could be obtained by increasing  $R_{[SR]/[Au]}$  to 3, as shown by the follow-up studies from the same group.<sup>84,120</sup> Murray and coworkers also reported the preparation of  $\sim 1.5$  nm  $Au_n(SR)_m$  NCs via a similar Brust-like method.<sup>121</sup>  $Ag_n(SR)_m$  NCs could also be prepared by the Brust-like methods but with Equations 2.7 and 2.8 replaced by Equations 2.9 and 2.10 respectively.<sup>122-124</sup>



However, the strong reducing power of  $NaBH_4$  typically produces  $M_n(SR)_m$  NCs with a broad size distribution in a Brust-like method.<sup>84,121-122</sup> For the preparation of monodisperse  $M_n(SR)_m$  NCs with atomic precision, the as-synthesized polydisperse  $M_n(SR)_m$  NCs have to be size-refined by either physical separation (Route I in Figure 2.5) or chemical selection means (“size-focusing” reaction, Route II in Figure 2.5).

### 2.2.1 Physical Separation Approaches

In a typical physical separation, polydisperse  $M_n(SR)_m$  NCs are fractionated into monodisperse  $M_n(SR)_m$  NCs by post-synthesis high resolution separation techniques. The most common separation or isolation of monodisperse  $M_n(SR)_m$  NCs techniques include solubility-based fractionation (SF), electrophoresis, and liquid chromatography.

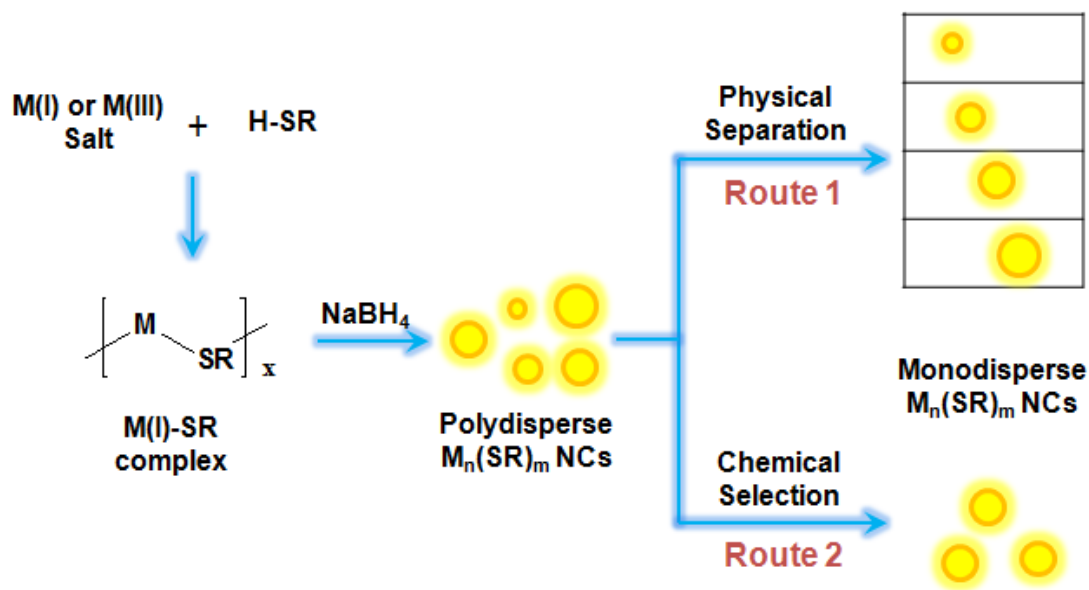


**Figure 2.5** Schematic illustration of the processes for monodisperse  $M_n(SR)_m$  NC synthesis.

### 2.2.1.1 Solubility Based Fractionation

Solubility based fractionation (SF) is a separation technique that leverages the size-dependent solubility of  $M_n(SR)_m$  NCs.<sup>1,84,120</sup> In a typical SF process, the solvent polarity is fine-tuned by introducing a certain amount of poor solvent into the  $M_n(SR)_m$  NC solution to induce the precipitation of  $M_n(SR)_m$  NCs in a given size range (usually centrifugation is applied to facilitate precipitation). Soluble and insoluble fractions are then separated, and the fractionation procedure is repeated until the desired monodispersity in the fractionated  $M_n(SR)_m$  NCs is obtained.

The SF method was pioneered by the Whetten group and demonstrated for the preparation of monodisperse  $M_n(SR)_m$  NCs. In the late 1990s they succeeded in fractionating a mixture  $Au_n(SR)_m$  NCs of different sizes prepared by a Brust-like method, into a series of discrete-sized  $Au_n(SR)_m$  NCs.<sup>84,120</sup> Core sizes (expressed by the  $Au_nS_m$  core mass) of these  $Au_n(SR)_m$  NCs based on LDI-MS measurements were

~8, 14, 22, and 29 kDa. The precise assignment of molecular formula for these  $\text{Au}_n(\text{SR})_m$  NC species was not possible at that time due to the lack of advanced characterization techniques (*e.g.*, high resolution electrospray ionization mass spectrometry, ESI-MS). In subsequent studies, several other groups have reproduced these  $\text{Au}_n(\text{SR})_m$  NC species by SF methods which were modifications of the original Whetten method, and successfully assigned molecular formulas of  $\text{Au}_{38}(\text{SR})_{24}$ ,  $\text{Au}_{68}(\text{SR})_{34}$ ,  $\text{Au}_{102}(\text{SR})_{44}$ , and  $\text{Au}_{144}(\text{SR})_{60}$  to the ~8, 14, 22, and 29 kDa NC species respectively.<sup>38,40,89,108</sup>

### 2.2.1.2 Electrophoresis

Polyacrylamide gel electrophoresis (PAGE) is the most widely used electrophoresis technique for the separation of  $\text{M}_n(\text{SR})_m$  NCs.<sup>8,11,122,125</sup> It is able to differentiate between water-soluble charged  $\text{M}_n(\text{SR})_m$  NCs based on their size-dependent mobility in polyacrylamide gel under an external electric field. By using a properly condensed polyacrylamide gel, PAGE can produce atomically precise monodispersity in each fraction.<sup>8,72</sup>

The use of PAGE for the fractionation of  $\text{M}_n(\text{SR})_m$  NCs first appeared in the seminal work of Schaaff *et al.* in 1998, where  $\text{Au}_n(\text{SR})_m$  NCs in a mixture of sizes prepared by a Brust-like method were separated into 4 fractions by PAGE.<sup>125</sup> The most predominant fraction showed a relatively clean (ESI-MS) spectrum (implying high monodispersity), which allowed the authors to assign a molecular formula of  $\text{Au}_{28}(\text{SG})_{16}$  (corrected later by Negishi *et al.*<sup>3</sup> to be  $\text{Au}_{25}(\text{SG})_{18}$ ). Using improved sampling and electrophoresis methods, Negishi *et al.* were able to isolate 9 fractions from a similar mixture of differently sized  $\text{Au}_n(\text{SG})_m$  NCs prepared by a Brust-like method.<sup>8</sup> A careful ESI-MS analysis disclosed these 9 fractions as monodisperse

$\text{Au}_n(\text{SR})_m$  with  $(n\ m) = (10\ 10), (15\ 13), (18\ 14), (22\ 16), (22\ 17), (25\ 18), (29\ 20), (33\ 22)$  and  $(39\ 24)$ . Very recently, Yu *et al.* also applied PAGE to isolate a highly luminescent (emission maximum at 665 nm with a QY of ~8%,  $\lambda_{\text{ex}} = 520$  nm)  $\text{Au}_n(\text{SG})_m$  NC species from a mixture of  $\text{Au}_n(\text{SG})_m$  NCs produced by the CO-reduction of Au(I)-SG complexes.<sup>12</sup> The high monodispersity of the isolated highly luminescent  $\text{Au}_n(\text{SG})_m$  NC species allowed the authors to assign a molecular formula of  $\text{Au}_{22}(\text{SG})_{18}$  by ESI-MS. Likewise monodisperse  $\text{Ag}_n(\text{SR})_m$  NCs could also be isolated by PAGE. The monodisperse  $\text{Ag}_{32}(\text{SG})_{19}$  NCs of Guo *et al.*<sup>90</sup> are one such example.

### 2.2.1.3 Liquid Chromatography

Despite the success of PAGE in the separation of charged  $\text{M}_n(\text{SR})_m$  NCs in aqueous solution, the use of PAGE for separating  $\text{M}_n(\text{SR})_m$  NCs in organic solution can be limited by compatibility issues between the polyacrylamide gel and organic solvents.<sup>72</sup> Liquid chromatography, which is extensively used in the purification of organic compounds, would be a good alternative in this case. Size exclusion chromatography (SEC) and high performance liquid chromatography (HPLC) are two common liquid chromatography techniques used for the separation of organic soluble  $\text{M}_n(\text{SR})_m$  NCs.<sup>41,44,85,126-128</sup>

SEC separates  $\text{M}_n(\text{SR})_m$  NCs based on their sizes, where larger  $\text{M}_n(\text{SR})_m$  NCs are eluted before the smaller ones. The resolution of SEC can be significantly improved by cycling the SEC procedure, where  $\text{M}_n(\text{SR})_m$  NC fractions are allowed to repeatedly pass through the SEC column.<sup>72</sup> The cycling-SEC technique was used by Tsunoyama *et al.* to successfully isolate a series of  $\text{Au}_n(\text{SC}_{18}\text{H}_{35})_m$  NCs (where  $\text{SC}_{18}\text{H}_{35}$  is 1-octadecanethiolate) into discrete core masses (as  $\text{Au}_n\text{S}_m$ ) of ~8, 11, 21, and 26 kDa.<sup>85</sup>



$\text{Au}_n(\text{SR})_m$  NCs with a  $\text{Au}_n\text{S}_m$  core mass of  $\sim 11$  kDa were also isolated by Qian *et al.* using a similar cycling-SEC method.<sup>128</sup> Qian *et al.* further characterized this  $\text{Au}_n(\text{SR})_m$  NC species by ESI-MS and assigned a molecular formula of  $\text{Au}_{55}(\text{SR})_{31}$ .<sup>128</sup> Qian *et al.* also demonstrated the capability of SEC to isolate  $\text{Au}_{40}(\text{SC}_2\text{H}_4\text{Ph})_{24}$  NCs from a mixture of closely-sized  $\text{Au}_{38}(\text{SC}_2\text{H}_4\text{Ph})_{24}$  and  $\text{Au}_{40}(\text{SC}_2\text{H}_4\text{Ph})_{24}$  NCs.<sup>127</sup> Very recently, SEC was used by Crasto *et al.* to purify  $\text{Au}_{30}(\text{S-}t\text{-Bu})_{18}$  NCs (where S-*t*-Bu denotes *tert*-butanethiolate) to a level high enough for the crystallization of  $\text{Au}_{30}(\text{S-}t\text{-Bu})_{18}$  NCs.<sup>33</sup>

HPLC could differentiate  $\text{M}_n(\text{SR})_m$  NCs not only by size but also by the polarity of the ligand shell. It should be noted that the polarity of  $\text{Au}_n(\text{SR})_m$  NCs is also dependent on the NC size.<sup>1,84,129</sup> Based on the size-sensitive polarity, Negishi *et al.*<sup>97</sup> isolated  $\text{Au}_{130}(\text{SC}_{12}\text{H}_{25})_{50}$  and  $\text{Au}_{187}(\text{SC}_{12}\text{H}_{25})_{68}$  NCs (where  $\text{SC}_{12}\text{H}_{25}$  is 1-dodecanethiolate) from a mixture of  $\text{Au}_n(\text{SC}_{12}\text{H}_{25})_m$  NCs (containing mostly  $\text{Au}_{102}(\text{SC}_{12}\text{H}_{25})_{44}$ ,  $\text{Au}_{130}(\text{SC}_{12}\text{H}_{25})_{50}$ ,  $\text{Au}_{144}(\text{SC}_{12}\text{H}_{25})_{60}$  and  $\text{Au}_{187}(\text{SC}_{12}\text{H}_{25})_{68}$  NCs) in a reverse-phase HPLC column based on the size of the  $\text{Au}_n(\text{SR})_m$  NCs. The polarity difference caused by the heterogeneity of thiolate ligands in the shell of mixed-thiolate protected  $\text{M}_n(\text{SR})_m$  NCs could be sufficient to drive HPLC separation. For example, Niihori *et al.* prepared  $\text{Au}_{25}(\text{SC}_{12}\text{H}_{25})_{18-x}(\text{SC}_2\text{H}_4\text{Ph})_x$  and  $\text{Au}_{38}(\text{SC}_{12}\text{H}_{25})_{24-x}(\text{SC}_2\text{H}_4\text{Ph})_x$  NCs by the ligand exchange reactions of  $\text{Au}_{25}(\text{SC}_{12}\text{H}_{25})_{18}$  and  $\text{Au}_{38}(\text{SC}_{12}\text{H}_{25})_{24}$  respectively with 2-phenylethanethiol ( $\text{H-SC}_2\text{H}_4\text{Ph}$ ).<sup>44</sup> The mixed-thiolate protected  $\text{Au}_{25}$  and  $\text{Au}_{38}$  NCs were then separated by reverse phase HPLC where monodisperse NCs in all possible ligand combinations (*i.e.*,  $x = 1-18$  for  $\text{Au}_{25}(\text{SC}_{12}\text{H}_{25})_{18-x}(\text{SC}_2\text{H}_4\text{Ph})_x$  NCs, and  $x = 1-24$  for  $\text{Au}_{38}(\text{SC}_{12}\text{H}_{25})_{24-x}(\text{SC}_2\text{H}_4\text{Ph})_x$ ) were isolated as products.

## 2.2.2 Chemical Selection Techniques

Although physical separation methods are able to refine  $M_n(\text{SR})_m$  NCs to a sufficiently high monodispersity, the laboriousness of the separation procedures inevitably leads to a low production rate.<sup>4,130</sup> Such drawbacks can be largely avoided by using a chemical selection approach (Route II in Figure 2.5). In a chemical selection approach, ligands that can strongly coordinate to the metal atoms (typically known as the etchants, *e.g.*, thiol) are used to etch a population of polydisperse  $M_n(\text{SR})_m$  NCs. The etching reaction introduces natural size selection based on the size-dependent reactivity of the polydisperse  $M_n(\text{SR})_m$  NCs, where the less stable sizes are eliminated and the more stable sizes survive.<sup>131</sup> Since such etching reactions typically result in a very narrow size distribution (ideally to a lone survivor) for the  $M_n(\text{SR})_m$  NCs, they are also frequently referred to as “size-focusing” reactions.<sup>131</sup>

### 2.2.2.1 Size-Dependent Stability of $M_n(\text{SR})_m$ NCs: The Foundation of “Size-Focusing”

The size-dependent stability of  $M_n(\text{SR})_m$  NCs, the basis of “size-focusing” reactions, has long been recognized experimentally. Several sizes of  $\text{Au}_n(\text{SR})_m$  (*e.g.*,  $(n, m) = (25, 18)$ ,<sup>88,132</sup>  $(38, 24)$ ,<sup>79,133</sup>  $(102, 44)$ <sup>24,40</sup> and  $(144, 60)$ <sup>89,134</sup>) and  $\text{Ag}_n(\text{SR})_m$  (*e.g.*,  $(n, m) = (32, 19)$ ,<sup>123,135</sup>  $(44, 30)$ <sup>27</sup> and  $(152, 60)$ <sup>136</sup>) NCs have shown unparalleled stability over other homologues. For example, the exceptional stability of  $\text{Au}_{25}(\text{SR})_{18}$  NCs has been reported by various groups in the last two decades. The observation of Schaaff *et al.* in 1998 on the predominance of  $\text{Au}_{25}(\text{SG})_{18}$  NCs in a mixture of  $\text{Au}_n(\text{SG})_m$  NCs produced by the  $\text{NaBH}_4$  reduction of  $\text{Au}(\text{I})\text{-SG}$  complexes (Brust-like method), is one of the early indications of the high stability of  $\text{Au}_{25}(\text{SR})_{18}$  NCs.<sup>125</sup> Negishi *et al.* in

2007 provided a more direct experimental evidence for the stability of  $\text{Au}_{25}(\text{SR})_{18}$  NCs.<sup>132</sup> They evaluated the stability of different sizes of  $\text{Au}_n(\text{SG})_m$  NCs ( $n = 10-39$ ) by reacting them with excess GSH at elevated temperature (328 K) for 3 h. Their results showed that all  $\text{Au}_n(\text{SG})_m$  with  $n > 25$  were converted to  $\text{Au}_{25}(\text{SG})_{18}$  NCs while those with  $n < 25$  decomposed into Au(I)-SG complexes by the aggressive thiol-etching reaction. The stability of  $\text{Au}_{25}(\text{SG})_{18}$  NCs over other sizes of  $\text{Au}_n(\text{SG})_m$  NCs was also demonstrated by other groups; such as the works of Pradeep<sup>95</sup> and Dass<sup>88</sup>.

Although the size-dependent stability of  $\text{M}_n(\text{SR})_m$  NCs has been known in the research community for a long time, the origin of the size-dependent stability is still under debate. Walter *et al.* suggested that the stability of  $\text{M}_n(\text{SR})_m$  NCs could be predicted by the “superatom electronic theory” based on their valence electron count (electronic effect).<sup>137</sup> The total valence electron count ( $N_A$ ) of a NC species  $[\text{M}_n(\text{SR})_m]^z$  could be calculated by the equation

$$N_A = n \times V_A - m - z \quad (2.11)$$

where  $V_A$  is the number of valence electrons per metal atom ( $V_A = 1$  for Au and Ag), and  $z$  is the net charge of the NC. According to the “superatom electronic theory”, the valence electrons of  $\text{M}_n(\text{SR})_m$  NCs are delocalized and filled the superatom electronic orbitals (S, P, D, F...) via an appropriate aufbau rule, *i.e.*  $1S^2|1P^6|1D^{10}|2S^2|1F^{14}|...$   $\text{M}_n(\text{SR})_m$  NCs with  $N_A$  corresponding to a shell-closing electronic structure (*i.e.*,  $N_A = 2, 8, 18, 34...$ ) are expected to be stable. The “superatom electronic theory” has been proven to be successful in explaining the unique stability of a number of  $\text{M}_n(\text{SR})_m$  NCs. These  $\text{M}_n(\text{SR})_m$  NCs include  $\text{Au}_n(\text{SR})_m$  NCs:  $[\text{Au}_{25}(\text{SR})_{18}]^-$  (18 e-), and  $[\text{Au}_{102}(\text{SR})_{44}]^0$  (58 e-); and  $\text{Ag}_n(\text{SR})_m$  NCs:  $[\text{Ag}_{44}(\text{SR})_{30}]^{4+}$  (18 e-) and  $[\text{Ag}_{152}(\text{SR})_{60}]^0$  (92 e-).

However, the “superatom electronic theory” alone could not rationalize the good stability of some  $M_n(\text{SR})_m$  NCs with a non-shell-closing  $N_A$  (e.g.,  $\text{Au}_n(\text{SR})_m$  NCs:  $[\text{Au}_{25}(\text{SR})_{18}]^0$  (17 e-),  $[\text{Au}_{25}(\text{SR})_{18}]^{+1}$  (16 e-),  $[\text{Au}_{38}(\text{SR})_{24}]^0$  (14 e-), and  $[\text{Au}_{144}(\text{SR})_{60}]^0$  (84 e-); and  $\text{Ag}_n(\text{SR})_m$  NCs:  $[\text{Ag}_{32}(\text{SR})_{19}]^0$  (13 e-)). The most striking finding is the comparable stability of  $[\text{Au}_{25}(\text{SR})_{18}]^z$  NCs with  $z = +1, 0,$  and  $-1$ , corresponding to  $N_A = 16, 17$  and  $18$  respectively.<sup>112</sup> Based on these observations, Tsukuda and coworkers suggested that structural factors, in addition to electronic effect, also contributed to the stability of  $M_n(\text{SR})_m$  NCs.<sup>112</sup> They reasoned that the structural anisotropy of  $M_n(\text{SR})_m$  NCs could cause deviations from the “superatom electronic theory” which is based on a spherical shell assumption.<sup>138</sup>

Although the origin of NC stability is still unclear, the size-dependent stability of  $M_n(\text{SR})_m$  NCs can be used to narrow the size distribution of a polydisperse sample by presenting an aggressive chemical environment (e.g., thiol-etching reaction). This stability-based principle (chemical selection) was first used in the synthesis of  $\text{Au}_{25}(\text{SR})_{18}$  NCs. Zhu *et al.*, aged mixed sizes of  $\text{Au}_n(\text{SC}_2\text{H}_4\text{Ph})_m$  NCs in excess of  $\text{H-SC}_2\text{H}_4\text{Ph}$  overnight at room temperature.  $\text{Au}_{25}(\text{SC}_2\text{H}_4\text{Ph})_{18}$  NCs were the dominant species in the product (judging from the UV-vis spectrum of the final product where the characteristics of  $\text{Au}_{25}(\text{SR})_{18}$  NCs were shown).<sup>87</sup> The authors also found that the purity of  $\text{Au}_{25}(\text{SC}_2\text{H}_4\text{Ph})_{18}$  NCs could be further improved (evidenced by more distinct UV-vis absorption features of  $\text{Au}_{25}(\text{SR})_{18}$  NCs) by prolonging the aging time in thiol and optimizing the solvent polarity.<sup>139</sup> As an attempt to gain some insights on the predominance of  $\text{Au}_{25}(\text{SC}_2\text{H}_4\text{Ph})_{18}$  NCs in the thiol-etching reaction, Dharmaratne *et al.* followed the evolution of mixed sizes of  $\text{Au}_n(\text{SC}_2\text{H}_4\text{Ph})_m$  to monodisperse  $\text{Au}_{25}(\text{SC}_2\text{H}_4\text{Ph})_{18}$  NCs in excess thiol with time by matrix assisted laser desorption/ionization mass spectrometry (MALDI-TOF-MS).<sup>88</sup> The occurrence of a

“size-focusing” process was confirmed (Figure 2.6a) where  $\text{Au}_n(\text{SC}_2\text{H}_4\text{Ph})_m$  NCs with a broad size distribution ( $n = 25\text{-}102$ , top line in Figure 2.6a) slowly transformed into monodisperse  $\text{Au}_{25}(\text{SC}_2\text{H}_4\text{Ph})_{18}$  NCs (bottom line in Figure 2.6a) over a course of 3 d of etching in excess thiol. A similar “size-focusing” approach was also used by Muhammed *et al.* for the synthesis of monodisperse water soluble  $\text{Au}_{25}(\text{SG})_{18}$  NCs.<sup>95</sup>

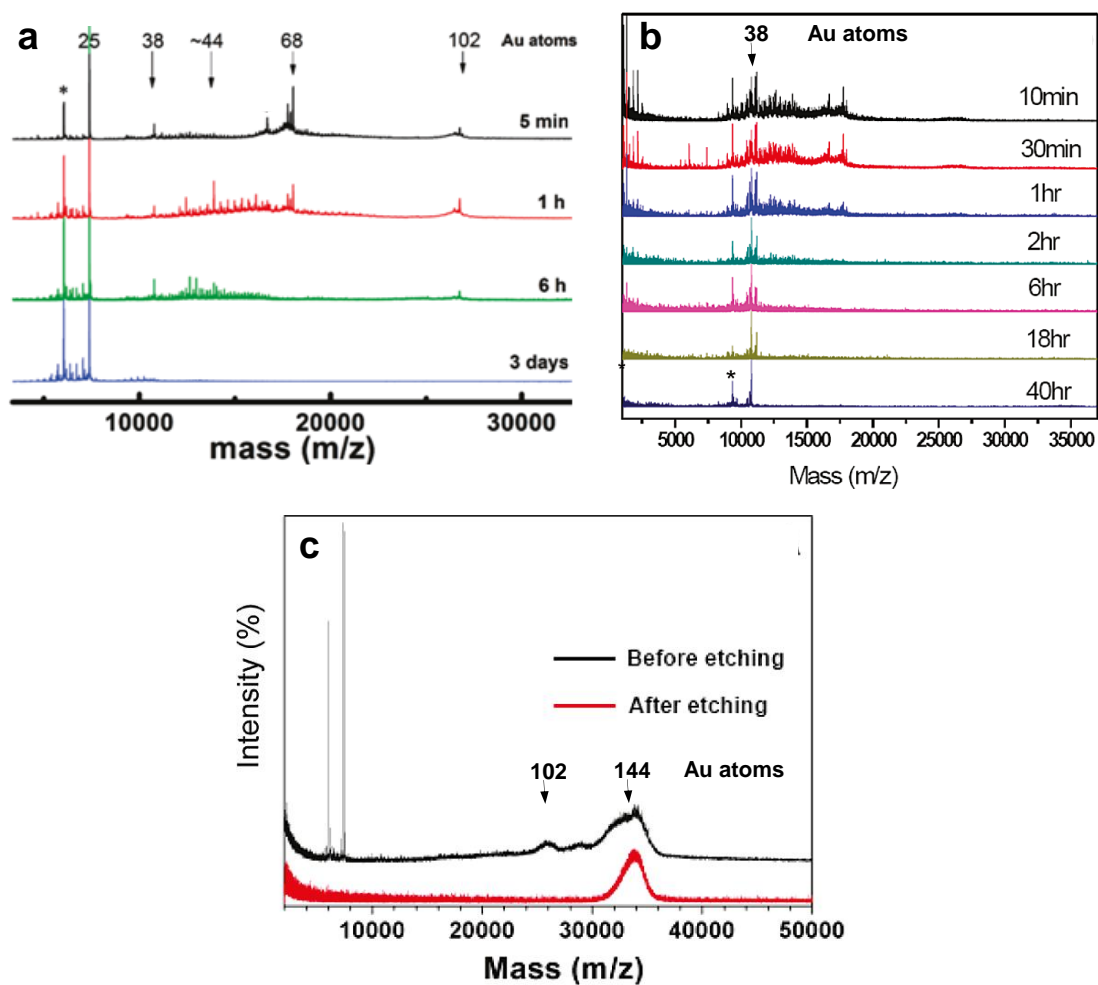


**Figure 2.6** MALDI-TOF-MS spectra of  $\text{Au}_n(\text{SR})_m$  NCs mixtures in the “size-focusing” (thiol-etching) synthesis of (a)  $\text{Au}_{25}(\text{SR})_{18}$ , (b)  $\text{Au}_{38}(\text{SR})_{24}$  and (c)  $\text{Au}_{144}(\text{SR})_{60}$  NCs at different reaction times. The asterisked peaks in (a) and (b) indicate fragments of  $\text{Au}_{25}(\text{SR})_{18}$  and  $\text{Au}_{38}(\text{SR})_{24}$  NCs, respectively. (a-c) were adopted from Refs.<sup>(88)</sup>, <sup>(79)</sup>, and <sup>(89)</sup> respectively with the permission of the American Chemical Society.

### 2.2.2.2 Size Distribution of Starting $M_n(\text{SR})_m$ NCs: A Determining Factor for the Size of Final Product

An appealing feature of the “size-focusing” approach is its size-tunability. For example, stable  $\text{Au}_n(\text{SR})_m$  NCs in other sizes (*v.s.*  $\text{Au}_{25}(\text{SR})_{18}$  NCs) could be synthesized in atomic precision monodispersity, by controlling the size distribution of the starting polydisperse  $\text{Au}_n(\text{SR})_m$  NCs. Figure 2.7 shows how this can be done. In essence the starting polydisperse  $\text{Au}_n(\text{SR})_m$  NCs needs to be in a size range where only one stable size prevails. The thiol-etching reaction can then be applied to narrow the size distribution to that stable size. Based on this principle, Jin and coworkers succeeded in applying “size-focusing” to the synthesis of  $\text{Au}_{38}(\text{SR})_{24}$ <sup>79,140</sup> and  $\text{Au}_{144}(\text{SR})_{60}$ <sup>89,134</sup> NCs. They controlled the size distribution of the starting polydisperse  $\text{Au}_n(\text{SR})_m$  NCs to fall within a proper range ( $25 < n \leq 102$ , top line of Figure 2.6b) by manipulating the solvent polarity, and successfully converted the polydisperse  $\text{Au}_n(\text{SR})_m$  NCs into  $\text{Au}_{38}(\text{SR})_{24}$  NCs via thiol-etching reaction in 40 h (bottom line in Figure 2.6b).<sup>79</sup> If polydisperse  $\text{Au}_n(\text{SR})_m$  NCs with high initial sizes ( $n \geq 102$ , top line in Figure 2.6c) were used as the starting material, the “size-focusing” thiol-etching produced monodisperse  $\text{Au}_{144}(\text{SR})_{60}$  NCs (bottom line in Figure 2.6c) instead.<sup>89</sup>

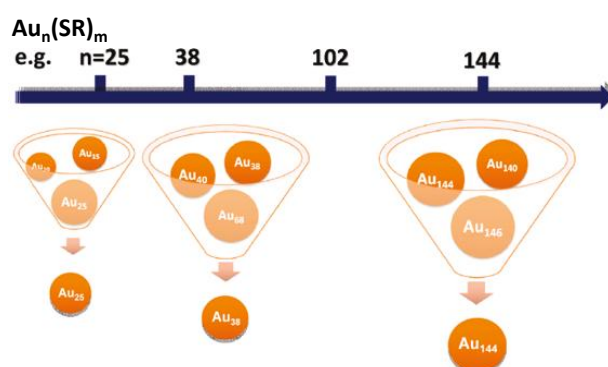


**Figure 2.7** Schematic illustration of the working principle of the “size-focusing” approach to the synthesis of monodisperse  $M_n(\text{SR})_m$  NCs.  $\text{Au}_n(\text{SR})_m$  NCs were used as examples. Adopted from Ref.<sup>(131)</sup> with the permission of the American Chemical Society.

Equipped with the above knowledge, researchers were capable to synthesize a series of monodisperse  $M_n(SR)_m$  NCs in atomic precision, through the deliberate control of the conditions for the starting polydisperse  $M_n(SR)_m$  NC formation and the thiol-etching reaction (*e.g.*, reaction temperature, stirring rate, solvent polarity, type and quantity of reductant, and type and quantity of thiol). Monodisperse  $M_n(SR)_m$  NCs which have been prepared this way include:  $Au_n(SR)_m$  NCs:  $(n\ m) = (19\ 13)$ ,<sup>141</sup>  $(20\ 16)$ ,<sup>142</sup>  $(23\ 16)$ ,<sup>57</sup>  $(24\ 20)$ ,<sup>143</sup>  $(25\ 18)$ ,<sup>37,87,95</sup>  $(30\ 18)$ ,<sup>83</sup>  $(36\ 24)$ ,<sup>29,86</sup>  $(38\ 24)$ ,<sup>39,79,140</sup>  $(64\ 32)$ <sup>144</sup>,  $(99\ 42)$ <sup>145</sup> and  $(144\ 60)$ <sup>89</sup>; and  $Ag_n(SR)_m$  NCs:  $(n\ m) = (7\ 4)$ ,<sup>146</sup>  $(9\ 6)$ ,<sup>98</sup>  $(16\ 9)$ <sup>98</sup> and  $(280\ 120)$ <sup>147</sup>.

### 2.3 Self-Assembly of $M_n(SR)_m$ NCs

The self-assembly of  $M_n(SR)_m$  NCs is of interest to both basic and applied research of NCs. For basic research, the ability to assimilate  $M_n(SR)_m$  NCs into 3D ordered structures ( $M_n(SR)_m$  NC supracrystals or  $M_n(SR)_m$  NC-SCs) could facilitate the crystal structure determination of  $M_n(SR)_m$  NCs by X-ray crystallography, an essential first step in the establishment of reliable structure-property relations.<sup>21,24-28</sup> For applied research, the self-assembly of  $M_n(SR)_m$  NCs into hierarchical structures could offer a means for customizing the NC properties, via the coupling effects between neighboring  $M_n(SR)_m$  NCs.<sup>49-50,52</sup> Despite these motivations, the self-assembly of  $M_n(SR)_m$  NCs is still in the very early stages of development. Only limited successes have been reported to date on the self-assembly of  $M_n(SR)_m$  NCs. The successful attempts were based primarily on two categories of methods: 1) template-assisted self-assembly, and 2) template-free self-assembly. In the review below, we will focus on the structural orderliness of  $M_n(SR)_m$  NC assemblies prepared by these methods; since

the structural orderliness of  $M_n(SR)_m$  NC assemblies is critical to post-assembly investigations (especially to crystal structure determination of  $M_n(SR)_m$  NCs).<sup>24-28</sup>

### 2.3.1 Template-Assisted Self-Assembly

Soft-templates, which are easy to remove after the assembly, are often used in template-assisted self-assembly to create ordered free-standing  $M_n(SR)_m$  NC-SCs.<sup>62-63</sup> Liquid-liquid interface is the most common soft template used to guide the self-assembly of  $M_n(SR)_m$  NCs.<sup>62-63</sup>

Wang *et al.* reported the *in-situ* formation and self-assembly of  $Au_n(SC_{12}H_{25})_m$  NCs at water/octadecane (ODE) interface.<sup>62</sup> In their method, organic-soluble Au(III)- $SC_{12}H_{25}$  complexes (the +3 oxidation state of Au was inferred from the X-ray photoelectron spectrum (XPS) of the authors) were reduced by a weak water-soluble reductant (formaldehyde) at the water/ODE interface to  $Au_n(SC_{12}H_{25})_m$  NCs. The core diameter of the NCs was  $1.8 \pm 0.3$  nm according to transmission electron microscopy (TEM). The authors, however, did not attempt a precise determination of the (n m) values. The *in-situ* generated  $Au_n(SC_{12}H_{25})_m$  NCs were found to spontaneously organize into ribbon-like assemblies (~50-100 nm in width and ~20-30  $\mu$ m in length) at the water/ODE interface. High resolution TEM (HR-TEM) images suggest that the  $Au_n(SC_{12}H_{25})_m$  NCs were orderly aligned in the ribbon-like assemblies with an inter-NC spacing of 3.3 nm. The ordered arrangement of  $Au_n(SC_{12}H_{25})_m$  NCs was confirmed by X-ray diffraction (XRD) analysis, where a regular inter-layer spacing ( $d$ ) of 3.2 nm (consistent with the 3.3 nm in TEM measurements) could be calculated. It is worth noting that these ordered assemblies of  $Au_n(SC_{12}H_{25})_m$  NCs exhibited enhanced emission maximum at 598 nm (QY = 13.3 %,  $\lambda_{ex}$  = 360 nm), which was different from



randomly aggregated  $\text{Au}_n(\text{SC}_{12}\text{H}_{25})_m$  NCs (QY = 6.7 %,  $\lambda_{\text{ex}} = 360$  nm). The cause for the structural-orderliness-induced luminescence enhancement has yet to be understood.

The templating effect of the liquid-liquid interface was also put to good use by Wu *et al.* to arrange  $\text{Au}_n(\text{SC}_{12}\text{H}_{25})_m$  NCs (core diameter =  $1.5 \pm 0.3$  nm) into sheet-like structures.<sup>63</sup> The liquid-liquid interface used in their study was formed by the micro-phase-separation of two miscible nonvolatile solvents (*e.g.*, dibenzyl ether (DE) and liquid paraffin (LP)) at high temperature (*e.g.*, 413 K). Heating a DE/LP (88/12 v/v) solution of  $\text{Au}_n(\text{SC}_{12}\text{H}_{25})_m$  NCs at 413 K for 1 h led to the formation of a single-NC-thick sheet-like structure ( $\sim 300$  nm in width and  $\sim 200$ -1000 nm in length). TEM analysis revealed a semi-ordered arrangement of  $\text{Au}_n(\text{SC}_{12}\text{H}_{25})_m$  NCs in the sheet-like structure with both ordered and disordered packing domains in each sheet. The authors suggested that the self-assembly of  $\text{Au}_n(\text{SC}_{12}\text{H}_{25})_m$  NCs at the DE/LP interface was a result of surface energy minimization, and the generation of ordered domains in the sheet-like assembly was thermodynamically favored and kinetically promoted by the heat treatment. Since the luminescent property of the  $\text{Au}_n(\text{SC}_{12}\text{H}_{25})_m$  NCs (emission maximum at 600 nm under  $\lambda_{\text{ex}} = 320$  nm) was largely retained after self-assembly, the single-NC-thick sheet-like  $\text{Au}_n(\text{SC}_{12}\text{H}_{25})_m$  NC assembly was said to be useful for the construction of ultra-thin optical devices for real world applications.

While the liquid-liquid interface is a good template to align  $\text{M}_n(\text{SR})_m$  NCs into ordered 2-dimensional (2D) structures, the inherent lack of a third dimension in any liquid-liquid interface suggests that such a soft template is not suitable for the growth of 3D ordered  $\text{M}_n(\text{SR})_m$  NC assemblies. Given that there are very few 3D templates for self-assembly and the inherent disadvantages of 3D templates (*e.g.* added complexity to the assembly system and hard to remove after assembly),<sup>45</sup> one may

have to rely on template free approaches to assemble  $M_n(SR)_m$  NC into free-standing 3D ordered structures.

**Table 2.3** Summary of successful crystallization of  $M_n(SR)_m$  NCs ( $M = Au$  or  $Ag$ ). The crystallization method, and the shape and space group of  $M_n(SR)_m$  NC-SCs are given in this Table.

No.	$M_n(SR)_m$ NCs*	$M_n(SR)_m$ NC-SCs		Ref.
		Shape (Space Group)	Crystallization Method	
1	$Au_{102}(p-MBA)_{44}$	Needle-like (C2/c)	Protein-like crystallization	24,40
2	$Au_{102}(p-MBA)_{40}(p-BBT)_4$	N.A. (C2/c)	Protein-like crystallization	61
3	$Au_{38}(SC_2H_4Ph)_{24}$	N.A. (P-1)	Liquid-liquid diffusion	60
4	$Au_{36}(SPh-t-Bu)_{24}$	Rhombic-shaped (C2/c)	Liquid-liquid diffusion	29
5	$Au_{30}S(S-t-Bu)_{18}$	Rhombic-shaped (P-1)	Vapor-liquid diffusion	33
6	$Au_{28}(SPh-t-Bu)_{20}$	Rhombic-shaped (P-1)	Liquid-liquid diffusion	59
7	$Au_{18.3}Ag_{6.7}(SC_2H_4Ph)_{18}$	N.A. (P-1)	Vapor-liquid diffusion	58
8	$Au_{25}(SC_2H_4Ph)_{18}$	Needle-like (P-1)	Liquid-liquid diffusion	25-26
9	$Au_{23}(S-c-C_6H_{11})_{16}$	N.A. (Ccca)	Vapor-liquid diffusion	57
10	$Ag_{44}(p-MBA)_{30}$	Rhombic-shaped (R-3c)	Slow evaporation	27
11-12	$Ag_{44}(SPhF_x)_{30}$ , $x = 1$ or $2$	Rhombic-shaped (P-1)	Liquid-liquid diffusion	28
13	$Ag_{44}(SPhCF_3)_{30}$	N.A. (P21/n)	Liquid-liquid diffusion	28
14-15	$Au_{12}Ag_{30}(SPhF_x)_{30}$ , $x = 1$ or $2$	N.A. (P-1)	Liquid-liquid diffusion	28
16	$Au_{12}Ag_{30}(SPhCF_3)_{30}$	N.A. (P21/n)	Liquid-liquid diffusion	28

\*  $p$ -BBT =  $p$ -bromobenzene thiolate, SPhF = 4-fluorothiophenolate, SPhF<sub>2</sub> = 3,4-difluorothiophenolate, and SPhCF<sub>3</sub> = 4-(trifluoromethyl)thiophenolate.

## 2.3.2 Template-Free Self-Assembly

Many of the template-free self-assembly approaches demonstrated in the past decade were based on the crystallization of monodisperse  $M_n(\text{SR})_m$  NCs.<sup>24-28</sup> While the topic has drawn a significant amount of interest and research activities, the crystallization of  $M_n(\text{SR})_m$  NCs remains to be a great challenge and only a limited number of successful attempts were reported. A summary of the successful crystallization of  $M_n(\text{SR})_m$  NCs to date is given in Table 2.3.

### 2.3.2.1 Crystallization Approaches

Based on the information in Table 2.3,  $M_n(\text{SR})_m$  NCs could be crystallized by mainly 4 approaches: 1) liquid-liquid diffusion, 2) vapor-liquid diffusion, 3) slow evaporation, and 4) protein-like crystallization.

The liquid-liquid diffusion method involves the slow diffusion of a poor solvent (in the liquid state) to the  $M_n(\text{SR})_m$  NC solution, gently altering the polarity of the  $M_n(\text{SR})_m$  NC solution to induce the formation of  $M_n(\text{SR})_m$  NC-SCs. Yang *et al.*, for example, were able to grow 6 different single-crystalline  $M_{12}\text{Ag}_{30}(\text{SR})_{30}$  NC-SCs, where  $M = \text{Ag}$  or  $\text{Au}$ , and  $\text{SR} = \text{SPhF}$  (4-fluorothiophenolate),  $\text{SPhF}_2$  (3,4-difluorothiophenolate), or  $\text{SPhCF}_3$  (4-(trifluoromethyl)thiophenolate) ( $6 = 2 \times 3$ , see No. 11-16 in Table 2.3) by this method.<sup>28</sup> In the growth of  $\text{Ag}_{44}(\text{SPhF})_{30}$  NC-SCs, the authors infused a poor solvent (hexane) into a dichloromethane (DCM) solution of  $\text{Ag}_{44}(\text{SPhF})_{30}$  NCs at a reduced temperature (277 K, for a slow diffusion rate) to induce crystallization.<sup>28</sup> Single-crystalline rhombic-shaped  $\text{Ag}_{44}(\text{SPhF})_{30}$  NC-SCs (P-1 space group) were obtained after a slow SC growth lasting for 10 d. Other  $M_{12}\text{Ag}_{32}(\text{SR})_{30}$  NC-SCs were grown similarly (layering hexane into DCM solutions of

NCs).<sup>28</sup> The liquid-liquid diffusion approach was also used by Jin and coworkers for the crystallization of selected  $Au_n(SR)_m$  NCs (*i.e.*,  $Au_{38}(SC_2H_4Ph)_{24}$ ,<sup>60</sup>  $Au_{36}(SPh-t-Bu)_{24}$ ,<sup>29</sup>  $Au_{28}(SPh-t-Bu)_{20}$ ,<sup>59</sup> and  $Au_{25}(SC_2H_4Ph)_{18}$  NCs,<sup>25</sup> No. 3, 4, 6 and 8 respectively in Table 2.3). In these works, ethanol (poor solvent) was mixed with a DCM or toluene (good solvent) solution of monodisperse  $Au_n(SR)_m$  NCs. Single-crystalline  $Au_n(SR)_m$  NC-SCs could be formed after 1-5 d of still incubation at ambient conditions (298 K and 1 atm). Crystallization was made possible by the slow diffusion of ethanol into the DCM or toluene solvation layer of  $Au_n(SR)_m$  NCs, which caused the de-solvation of  $Au_n(SR)_m$  NCs from DCM or toluene to induce crystallization. The de-solvation induced crystallization approach was also used by Heaven *et al.* for the crystallization of  $Au_{25}(SC_2H_4Ph)_{18}$  NCs (No. 8 in Table 2.3).<sup>26</sup>

The vapor-liquid diffusion approach is similar to liquid-liquid diffusion, except that the poor solvent (a volatile liquid) is introduced to the  $M_n(SR)_m$  NC solutions in vapor form. Das *et al.* slowly diffused pentane (a poor solvent) vapor into a DCM solution of  $Au_{23}(S-c-C_6H_{11})_{16}$  NCs over a period of 1-2 d under ambient conditions, and reported the formation of single-crystalline  $Au_{23}(S-c-C_6H_{11})_{16}$  NC-SCs (Ccca space group, No. 9 in Table 2.3).<sup>57</sup> Crasto *et al.* obtained single-crystalline rhombic-shaped  $Au_{30}S(S-t-Bu)_{18}$  NC-SCs (P-1 space group, No. 5 in Table 2.3) via the slow diffusion of ethanol vapor into a toluene solution of  $Au_{30}(S-t-Bu)_{18}$  NCs over a period of 7-10 d.<sup>33</sup> Interesting an additional S atom was added to the  $Au_{30}(S-t-Bu)_{18}$  NC during crystallization, giving rise to  $Au_{30}S(S-t-Bu)_{18}$  NC-SCs instead of  $Au_{30}(S-t-Bu)_{18}$  NC-SCs. The mechanism for the crystallization-induced transformation of  $Au_{30}(S-t-Bu)_{18}$  NCs to  $Au_{30}S(S-t-Bu)_{18}$  NCs is not known to date. The diffusion of ethanol vapor into toluene solution of  $M_n(SR)_m$  NCs was also used by Kumara *et al.* to produce single-crystalline SCs (P-1 space group, No. 7 in Table 2.3) of  $Au_{25-x}Ag_x(SC_2H_4Ph)_{18}$  NCs

with heterogeneous cores of different alloy compositions (the statistical molecular formula was  $\text{Au}_{18.3}\text{Ag}_{6.7}(\text{SC}_2\text{H}_4\text{Ph})_{18}$  based on their X-ray crystallography data).<sup>58</sup> The successful co-crystallization of  $\text{Au}_{25-x}\text{Ag}_x(\text{SC}_2\text{H}_4\text{Ph})_{18}$  NCs despite variations in core compositions could be attributed to the similar sizes of Au and Ag atoms,<sup>148</sup> which allowed the retention of geometry and size uniformity in the variously constituted  $\text{Au}_{25-y}\text{Ag}_y(\text{SC}_2\text{H}_4\text{Ph})_{18}$  NCs.

In addition to changing the solvent polarity, as in the case of liquid-liquid or vapor-liquid diffusion, the crystallization of  $\text{M}_n(\text{SR})_m$  NCs could also be induced by the slow evaporation of solvent. This method was demonstrated by the Bigioni group for crystallizing  $\text{Ag}_{44}(p\text{-MBA})_{30}$  NC-SCs (where *p*-MBA is *p*-mercaptobenzoic acid)<sup>27</sup> from the dimethylformamide (DMF) solution of  $\text{Ag}_{44}(p\text{-MBA})_{30}$  NCs. Single-crystalline rhombic-like  $\text{Ag}_{44}(p\text{-MBA})_{30}$  NC-SCs (R-3c space group, No. 10 in Table 2.3) were formed after the slow evaporation of DMF by bubbling Ar for 1-3 d. The bubbling of Ar was critical to this protocol, since DMF is a nonvolatile solvent hard to evaporate at ambient conditions. It is worth noting that the *p*-MBA ligands (each *p*-MBA ligand carries a carboxyl group) of  $\text{Ag}_{44}(p\text{-MBA})_{30}$  NCs need to be fully protonated before  $\text{Ag}_{44}(p\text{-MBA})_{30}$  NCs could be dissolved in DMF, and the hydrogen bonds (H-bonds) thus developed between the protonated *p*-MBA ligands promoted the crystallization of  $\text{Ag}_{44}(p\text{-MBA})_{30}$  NCs (more discussion later in § 2.3.2.2).<sup>64</sup>

$\text{M}_n(\text{SR})_m$  NCs with amino acid like surface functionalities (*e.g.*, carboxyl group) may be crystallized in ways similar to proteins, given the comparable size between  $\text{M}_n(\text{SR})_m$  NCs and proteins. The first successful crystallization of  $\text{M}_n(\text{SR})_m$  NCs by a protein-like crystallization method was in 2007, by Jadzinsky *et al.*<sup>24</sup> Jadzinsky and coworkers dissolved  $\text{Au}_{102}(p\text{-MBA})_{44}$  NCs in a water/methanol (54/46 v/v) mixture, followed by slowly “salting out” the dissolved  $\text{Au}_{102}(p\text{-MBA})_{44}$  NCs at high ionic

strengths (by adding sodium chloride and sodium acetate to the solution to final concentrations of 300 mM and 100 mM respectively) at a target pH (~2.5).<sup>24</sup> Single-crystalline needle-like  $\text{Au}_{102}(\textit{p}\text{-MBA})_{44}$  NC-SCs (C2/c space group, No. 1 in Table 2.3) were formed after “salting out” the NC solution for 1-3 d. A similar protein-like crystallization method was also used by Heinecke *et al.* for the growth of single-crystalline  $\text{Au}_{102}(\textit{p}\text{-MBA})_{40}(\textit{p}\text{-BBT})_4$  NC-SCs (C2/c space group, No. 2 in Table 2.3, where *p*-BBT is *p*-bromobenzene thiolate).<sup>61</sup> The  $\text{Au}_{102}(\textit{p}\text{-MBA})_{40}(\textit{p}\text{-BBT})_4$  NCs were prepared by partially displacing the MBA ligands with the *p*-BBT ligands in the ligand exchange reaction of  $\text{Au}_{102}(\textit{p}\text{-MBA})_{44}$  NCs with *p*-BBT.<sup>61</sup>

### 2.3.2.2 Interactions Promoting the Crystallization of $\text{M}_n(\text{SR})_m$ NCs

Different from the template-assisted methods where the organization of  $\text{M}_n(\text{SR})_m$  NCs is guided by the template, the self-assembly or crystallization of  $\text{M}_n(\text{SR})_m$  NCs in template-free methods is driven by the affinity interactions between  $\text{M}_n(\text{SR})_m$  NCs. Thus an analysis on the inter-NC interactions which promote the crystallization of  $\text{M}_n(\text{SR})_m$  NCs, will be useful for understanding the genesis of ordered structures in  $\text{M}_n(\text{SR})_m$  NC-SCs.

First of all, depletion forces (entropic effect) is an important consideration in the crystallization of  $\text{M}_n(\text{SR})_m$  NCs. Depletion forces are well represented by the hard-sphere model where the building blocks are treated as impenetrable spheres.<sup>53,149-150</sup> According to the hard sphere model, the system entropy is maximized by organizing the hard spheres into closest-packed structures, suggesting that the crystallization of hard-sphere-like building blocks is thermodynamically favorable. It is worth noting that all  $\text{M}_n(\text{SR})_m$  NCs that have been successfully crystallized were protected by rigid thiolate ligands containing either an aromatic ring (*e.g.*,  $\text{SC}_2\text{H}_4\text{Ph}$ ,  $\text{SPh-}t\text{-Bu}$ ,  $\text{SPhF}_x$  (x

= 1-2), SPhCF<sub>3</sub> and *p*-MBA) or a short but bulky alkyl group (e.g., *S-t*-Bu and *S-c*-C<sub>6</sub>H<sub>11</sub>). These rigid thiolate ligands could impart a rigid surface to the M<sub>n</sub>(SR)<sub>m</sub> NCs. The rigid surface, together with the uniform size and *pseudo*-spherical geometry of the NCs, suggest that the M<sub>n</sub>(SR)<sub>m</sub> NCs can be approximated well by hard spheres. Therefore, depletion forces should contribute, at least partially, to the crystallization of the M<sub>n</sub>(SR)<sub>m</sub> NCs. The entropic effect has been used extensively in the construction of NP-SCs. For example, Murray and co-workers have prepared 15 different NP-SCs based on depletion forces.<sup>151-152</sup>

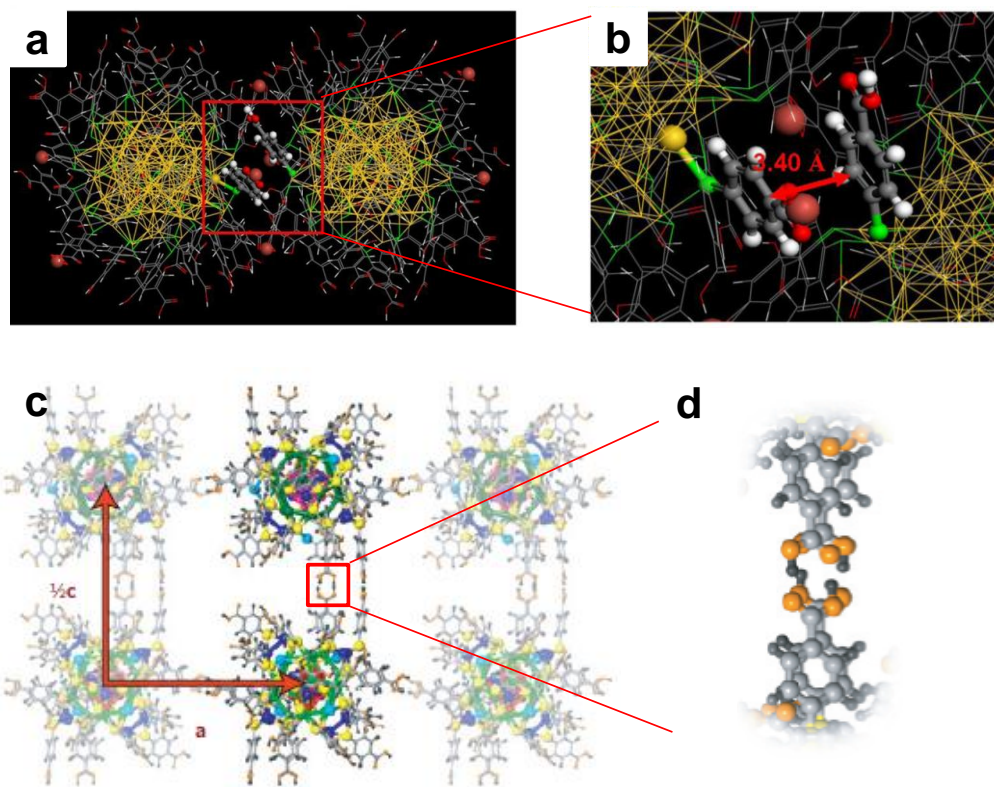


**Figure 2.8** (a-b)  $\pi$ - $\pi$  stacking interactions and (c-d) H-bonding in M<sub>n</sub>(SR)<sub>m</sub> NC-SCs. (a) Crystal structure of packed Au<sub>102</sub>(*p*-MBA)<sub>40</sub>(*p*-BBT)<sub>4</sub> NCs. (b) Expanded view of the boxed area in (a), showing the  $\pi$ - $\pi$  stacking interactions between neighboring Au<sub>102</sub>(*p*-MBA)<sub>40</sub>(*p*-BBT)<sub>4</sub> NCs; a ball-and-stick model is used to show the *p*-BBT ligands in the boxed area (dark red = Br, red = O, grey = C, white = H, green = S, and yellow = Au). (c) Crystal structure of packed Ag<sub>44</sub>(*p*-MBA)<sub>30</sub> NCs; the arrows indicate the unit cell vectors **a** and  $\frac{1}{2}c$  of triclinic Ag<sub>44</sub>(*p*-MBA)<sub>30</sub> NC-SCs. (d) Expanded view of the boxed area in (c), showing the formation of H-bonds between neighboring Ag<sub>44</sub>(*p*-MBA)<sub>30</sub> NCs (orange = O, grey = C, and dark grey = H). (a-b) were adopted from Ref.<sup>(153)</sup> with the permission of the American Chemical Society; and (c-d) were adopted from Ref.<sup>(64)</sup> with the permission of the Nature Publishing Group.

In addition to depletion forces, the interactions between  $M_n(\text{SR})_m$  NC surfaces due to the intermolecular bonding of the thiolate ligands (*e.g.*,  $\pi$ - $\pi$  stacking interaction and hydrogen bonding), could also influence the crystallization behavior of  $M_n(\text{SR})_m$  NCs. While each intermolecular bond is weak (*e.g.*,  $\sim k_B T$  at  $T = 298$  K),<sup>53,154-155</sup> the multitude of such intermolecular bonds between two surfaces can result in strong surface interactions. This is especially so when the surface-to-volume ratio is high, as in the case of  $M_n(\text{SR})_m$  NCs.

$\pi$ - $\pi$  stacking interaction is a prevalent attractive interaction in all  $\pi$  systems. The binding energy (B.E.) arising from the  $\pi$ - $\pi$  stacking interaction is typically  $\sim 0.08$ - $0.14$  eV at room temperature ( $\sim 3.2$ - $5.6$   $k_B T$  at  $T = 298$  K).<sup>154,156</sup> It has been well documented that  $\pi$ - $\pi$  stacking interaction is the origin of molecular recognition chemistry and drives the self-assembly of DNAs, proteins and other molecules with aromatic rings.<sup>157-159</sup> Since phenyl group is a common surface functionality among the  $M_n(\text{SR})_m$  NCs which have been successfully crystallized,  $\pi$ - $\pi$  stacking interaction is likely to be a contributor, if not a significant one. This inference has been supported by the DFT calculation of Gao *et al.*<sup>153</sup> who simulated the packing behavior of  $\text{Au}_{102}(\text{p-MBA})_{40}(\text{p-BBT})_4$  NCs based on the crystal structure of  $\text{Au}_{102}(\text{p-MBA})_{40}(\text{p-BBT})_4$  NCs reported by Heinecke *et al.*<sup>61</sup> As shown in Figure 2.8a-b, the spacing between the phenyl rings of *p*-BBT ligands on two neighboring NCs is about  $3.40$  Å (calculated value), which is the typical distance for  $\pi$ - $\pi$  stacking interaction.<sup>153-154</sup> The authors further demonstrated (via DFT calculations) that the formation of  $\pi$ - $\pi$  stacking interaction could reduce the total energy of  $\text{Au}_{102}(\text{p-MBA})_{40}(\text{p-BBT})_4$  NC-SCs and thus stabilize the NC-SCs.<sup>153</sup>

H-bond formation is an attractive interaction which occurs between two highly electronegative centers (*e.g.*, N, O and F atoms) and a bridging hydrogen atom



between them. The B.E. of H-bonds at room temperature could vary from  $\sim 0.1$ - $0.4$  eV ( $\sim 4.0$ - $16$   $k_B T$  at  $T = 298$  K).<sup>53,155</sup> The involvement of H-bonds in molecular crystal engineering has been quite extensively investigated and reported.<sup>155,160-161</sup> H-bonds were likely involved in the formation of  $\text{Ag}_{44}(\text{p-MBA})_{30}$  and  $\text{Au}_{102}(\text{p-MBA})_{44}$  NC-SCs since they could be easily established between the carboxyl groups of *p*-MBA ligands. This was especially so in the case of  $\text{Ag}_{44}(\text{p-MBA})_{30}$  NC-SCs which were built from the fully protonated form of *p*-MBA ligands.<sup>27</sup> The involvement of H-bonds in  $\text{Ag}_{44}(\text{p-MBA})_{30}$  NC-SCs was proven in a very recent publication of Yoon *et al.*, which showed all of the 30 *p*-MBA ligands per NC formed intermolecular H-bonds with the *p*-MBA ligands from neighboring NCs (Figure 2.8c).<sup>64</sup> Figure 2.8d shows that each pair of *p*-MBA ligands could form two H-bonds in  $\text{Ag}_{44}(\text{p-MBA})_{30}$  NC-SCs, suggesting that each NC bonds to the neighboring NCs via 60 H-bonds. A elaborate H-bond network is thus formed which should be strong enough to keep the  $\text{Ag}_{44}(\text{p-MBA})_{30}$  NCs together in the SCs. This corollary was confirmed by comparing the calculated H-bond energy with the cohesive energy of the  $\text{Ag}_{44}(\text{p-MBA})_{30}$  NC-SCs. The comparison showed that the H-bond energy dominated the cohesive energy of  $\text{Ag}_{44}(\text{p-MBA})_{30}$  NC-SCs with only trace contributions from other interactions.<sup>64</sup>

In summary, the assembly of  $\text{M}_n(\text{SR})_m$  NC-SCs into a long-range 3D ordered structures can be based on depletion forces, intermolecular forces, or both. Depletion force assembly is promoted by the use of high quality hard-sphere-like building block NCs; and this requires the NCs to be prepared with high monodisperse of size and structure, and protected by thiol ligands to provide a rigid surface. Since intermolecular interactions (*e.g.*,  $\pi$ - $\pi$  stacking interaction and H-bonds) are mostly surface forces; the deliberate control of the  $\text{M}_n(\text{SR})_m$  NCs surface chemistry (*e.g.* via post-synthesis modification through ligand exchange reactions) should also be

considered to promote self-assembly. In extreme cases as has been shown in previous work, the latter may even dominate the crystallization of  $M_n(SR)_m$  NCs.

---

# CHAPTER 3 SYNTHESIS OF BUILDING BLOCKS WITH ATOMIC PRECISION: THE CASE OF $\text{Au}_{15}(\text{SR})_{13}$ AND $\text{Au}_{18}(\text{SR})_{14}$ NANOCLUSTERS

## 3.1 Introduction

It is current interest to use NC assembly for structural determination and for diversifying the application potential of  $\text{M}_n(\text{SR})_m$  NCs.<sup>24-27,64</sup> As extensively demonstrated in precedent chapters, NC size has a determining influence on the structure and properties of the  $\text{M}_n(\text{SR})_m$  NCs, and a high size monodispersity could technically facilitate the self-assembly process. Thereby, the development of size-property relationships and property engineering principles can be made more comprehensive if the building blocks (*i.e.*,  $\text{M}_n(\text{SR})_m$  NCs) are available in a wide range of sizes (*e.g.*,  $n =$  several to a few hundred), with atomic precision size monodispersity and in sufficiently large quantities.

In this chapter  $\text{Au}_n(\text{SR})_m$  NCs are used as the model system to demonstrate atomically precise size monodispersity control and size tuning in NC synthesis. In the earlier days of NC synthesis,  $\text{Au}_n(\text{SR})_m$  NCs were often produced in a mixture of sizes and then size-sorted by various high resolution separation technique such as solubility based fractionation,<sup>40,84,108,120</sup> gel electrophoresis<sup>8,11,125,162-163</sup> and liquid chromatography<sup>33,85,126,128</sup>. Stable  $\text{Au}_n(\text{SR})_m$  NCs with core sizes of  $n = 15, 18, 25, 30, 38, 55, 68, 102, 130, 144,$  and  $187$  were obtained this way.<sup>8,33,108,112,120,128</sup> The last two

decades have witnessed the growth in the use of direct synthesis approaches to circumvent the laborious post-synthesis size sorting process. “Size-focusing” is one such direct synthesis method. In a typical “size-focusing” synthesis,  $\text{Au}_n(\text{SR})_m$  NCs (typically in a broad size distribution) are formed by reacting Au(I)-SR precursor complexes with a strong reducing agent (*e.g.*,  $\text{NaBH}_4$ ). This is followed by a thermodynamically driven “size-focusing” process where excess thiol ligands are used to gradually decompose the metastable NC species.<sup>79,87,89,131,144-145</sup> Only the thermodynamically stable NCs survive through the “size-focusing” process to appear in the final product. The “size-focusing” method has been successful for the preparation of medium and large ( $n = 19, 25, 38, 64, 99$  and  $144$ )<sup>79,87,89,141,144-145</sup>  $\text{Au}_n(\text{SR})_m$  NCs.

In comparison to  $\text{Au}_{25}$ ,  $\text{Au}_{38}$  and  $\text{Au}_{144}$  NCs, smaller  $\text{Au}_n$  NCs (*e.g.*,  $n \leq 18$ ) are less stable and readily decomposed to Au(I)-SR complexes in “size-focusing” step.<sup>132</sup> The metastability of these small NCs, on the one hand, suggests their critical role in understanding the origin of cluster stability; but on the other hand, makes “size-focusing” method less effective in preparation of these NCs. A possible strategy is to kinetically trap Au NCs into well-defined small sizes (kinetic trapping). Since the formation of NCs in well-defined sizes is in principle achievable through a deliberate control of the kinetics of precursor reduction and NC growth, we posit that a relatively weak reducing agent and suitably low concentrations of the reducing agent and Au(I)-SR complexes would provide a mild reaction environment and hence more controllability in the formation of small Au NCs in high monodispersity.

The work in this chapter aims to fill the current technology gap in the synthesis of monodisperse  $\text{Au}_n(\text{SR})_m$  NCs in the small size range ( $n \leq 18$ ). Specifically a one-pot two-phase strategy was developed for the preparation of Au NCs as  $\text{Au}_{15}(\text{SR})_{13}$  and

$\text{Au}_{18}(\text{SR})_{14}$  species with atomic precision. A mild reductant (borane *tert*-butylamine complex or TBAB), the equilibrium partition of TBAB between water and an organic phase, and the aggregation-dissociation equilibrium of Au(I)-SR complexes were used in tandem to create an unvarying mild reaction environment most conducive for the creation of  $\text{Au}_{15}(\text{SR})_{13}$  and  $\text{Au}_{18}(\text{SR})_{14}$  NCs in aqueous solution in high purity.

## 3.2 Experimental Section

### 3.2.1 Materials

Hydrogen tetrachloroaurate(III) trihydrate ( $\text{HAuCl}_4 \cdot 3\text{H}_2\text{O}$ ) from Alfa Aesar; L-glutathione reduced form (GSH), borane *tert*-butylamine complex (TBAB) and sodium borohydride ( $\text{NaBH}_4$ ) from Sigma Aldrich; nitric acid ( $\text{HNO}_3$ ) from J. T. Baker; ethanol and sodium hydroxide ( $\text{NaOH}$ ) from Merck; and toluene from Tedia were used as received without further purification. Ultrapure Millipore water (18.2 M $\Omega$ ) was used for the preparation of all aqueous solutions. All glassware was washed with *aqua regia* and rinsed with ethanol and ultrapure water before use.

### 3.2.2 Synthesis of Au NCs

#### 3.2.2.1 Synthesis of $\text{Au}_{15}(\text{SR})_{13}$ NCs

Stock aqueous solutions of GSH (20 mM) and  $\text{HAuCl}_4$  (10 mM) were prepared in ultrapure water. A 10 mM TBAB solution in toluene was freshly prepared by dissolving 34.8 mg TBAB in 40 mL of toluene. 0.75 mL of the GSH stock solution and 0.5 mL of the  $\text{HAuCl}_4$  stock solution were added to 3.75 mL of ultrapure water. The pH of the mixture was then adjusted to  $\sim 2.0$  by adding 1 M  $\text{HNO}_3$  until the target

pH was reached. The mixture was then incubated for 5 min for the Au(I)-SG complexes to form. A semi-translucent dispersion (Figure 3.2, no. 1) was obtained. 5 mL of the 10 mM TBAB solution in toluene was then added to the Au(I)-SG complex dispersion. The growth of NCs occurred for 4 h under vigorous stirring (1000 rpm). The light-yellow solution obtained at the end of the procedure was centrifuged at 5000 rpm for 5 min to remove the insoluble species. The resulting supernatant was purified by a PD-10 desalting column into a light-yellow effluent (the final product).

### **3.2.2.2 Synthesis of Au<sub>18</sub>(SR)<sub>14</sub> NCs**

The procedure was similar to the preparation of the Au<sub>15</sub>(SR)<sub>13</sub> NCs except for some minor changes. The pH of the aqueous solution was increased to ~2.7 (by adding 1 M NaOH) where a cloudy dispersion of Au(I)-SG complexes was formed (Figure 3.2, no. 2). The TBAB reduction time was increased to 10 h because of the slower reduction kinetics at this pH (fewer free Au(I)-SG complexes available, see detailed discussion in §3.3). The final product was a light-brown solution after centrifugation and purification by the PD-10 desalting column.

## **3.2.3 Control Experiments**

### **3.2.3.1 Synthesis of Au(0) Nanocrystals**

A fresh NaBH<sub>4</sub> solution was prepared by dissolving 43 mg NaBH<sub>4</sub> in 2 mL of 1 M NaOH, followed by the addition of 8 mL of ultrapure water. 0.125 mL of the 10 mM HAuCl<sub>4</sub> stock solution (same as that in §3.2.2.1) and 0.05 mL of the freshly-prepared NaBH<sub>4</sub> solution were added to 5 mL of ultrapure water. Reaction was completed in 5 min.

### 3.2.3.2 Synthesis of Au NCs by NaBH<sub>4</sub>

1.9 mg NaBH<sub>4</sub> was dissolved in 5 mL of an ethanol-toluene (1:4 v/v) mixture. Ethanol was used here to increase the solubility of NaBH<sub>4</sub> in the mixed solvents. 0.75 mL of 20 mM GSH stock solution (same as that in §3.2.2.1) and 0.5 mL of 10 mM HAuCl<sub>4</sub> stock solution were added to 3.75 mL of ultrapure water. After pH adjustment to ~2.0, the dispersion was incubated for 5 min and then mixed with the NaBH<sub>4</sub> solution in ethanol-toluene mixture. The reaction was completed in 5 min, forming a dark-brown solution with a featureless UV-vis absorption spectrum (Figure 3.9, no. 1).

### 3.2.3.3 One-Phase Synthesis of Au NCs

0.75 mL of 20 mM GSH stock solution and 0.5 mL of 10 mM HAuCl<sub>4</sub> stock solution were added to 3.75 mL of ultrapure water. The pH of the mixed solution was adjusted to ~2.0. After 5 min of incubation, 4.3 mg TBAB solid was added. The mixture was vigorously stirred for 4 h and the crude product was collected after the removal of the insoluble species by centrifugation (5000 rpm for 5 min).

### 3.2.3.4 Synthesis of NCs at pH ~ 10.0

Similar procedure as that in §3.2.2.1 except that the pH of the aqueous solution was ~10.0.

## 3.2.4 Characterization

pH was monitored by a Mettler Toledo FE 20 pH-meter. Crude products were centrifuged by an Eppendorf Centrifuge 5424. PD-10 desalting columns with a molecular weight cut-off (MWCO) of 5000 Da were purchased from GE Healthcare. The yield of products was determined by inductively coupled plasma mass

spectroscopy (ICP-MS) on an Agilent 7500A. UV-vis spectra were recorded on a Shimadzu UV-1800 spectrometer. Photoluminescent (PL) spectra were recorded by a Fluorolog spectrofluorometer. Electrospray ionization mass spectrometry (ESI-MS) analysis was conducted on a Bruker microTOF-Q system in the negative ion mode. X-ray photoelectron spectroscopy (XPS) was performed on a VG ESCALAB MKII spectrometer operating at 25.0 KV. All binding energies were referenced to the C(1s) carbon peak at 284.6 eV. Polyacrylamide gel electrophoresis (PAGE) was carried out on a 5-lane BIO-RAD Mini-Protean unit. The acrylamide monomer contents in the stacking and resolving gels were 3 wt% and 30 wt% (acrylamide/bis(acrylamide)) = 94 : 6) respectively. The eluting buffer contained 192 mM glycine and 25 mM tris(hydroxymethylamine). The as-synthesized Au NCs were dissolved in 5% (v/v) glycerol-water. 0.1 mL of the sample was loaded and allowed for elution at 150 V for 6 h.

### 3.3 Results and Discussion

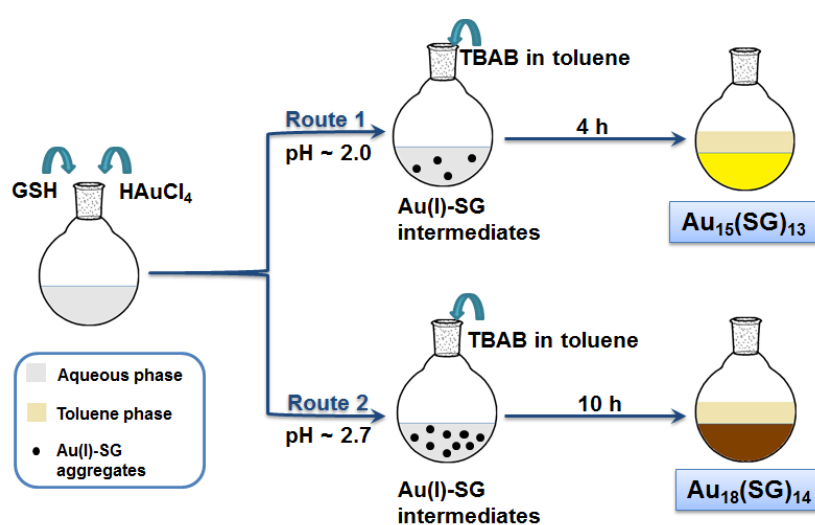


**Figure 3.1** Schematic illustration of the two-phase synthesis of high purity Au<sub>15</sub>(SG)<sub>13</sub> and Au<sub>18</sub>(SG)<sub>14</sub> NCs.



### 3.3.1 Synthesis of Au<sub>15</sub>(SR)<sub>13</sub>NCs

Glutathione (GSH or H-SG), a natural tripeptide, was the thiolate ligand in the synthesis. The protocol as illustrated in Figure 3.1 consists of two steps. For example, in the synthesis of SG-protected Au<sub>15</sub> NCs, aqueous solutions of HAuCl<sub>4</sub> (0.5 mL, 10 mM) and GSH (4.5 mL, 3.33 mM) were vigorously mixed by stirring. The solution pH was adjusted to ~2.0 where Au(I)-SG complexes could be quickly formed in water to yield a semi-translucent dispersion (Figure 3.2, no. 1). TBAB (5 mL, 10 mM) in toluene was then added to this aqueous dispersion and the mixture was vigorously stirred (1000 rpm) at room temperature for 4 h (route 1 in Figure 3.1). The color of the aqueous solution turned to light-yellow after 4 h while no color change was noticed for toluene. An insoluble species, most likely large aggregates of Au(I)-SG complexes,<sup>133</sup> was removed by centrifugation. The resulting light-yellow supernatant was collected as a crude product (inset no. 1 of Figure 3.3a). The typical yield of Au<sub>15</sub> NCs based on the amount of Au atoms in the starting mixture was ~44% according to inductively coupled plasma mass spectrometric (ICP-MS) measurements.

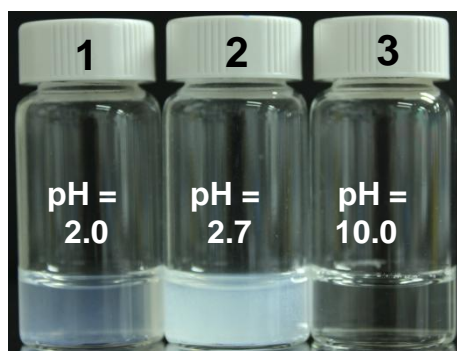


**Figure 3.2** Digital photos of Au(I)-SG complexes formed at different pH: pH ~2.0 (no. 1), 2.7 (no. 2) and 10.0 (no. 3).

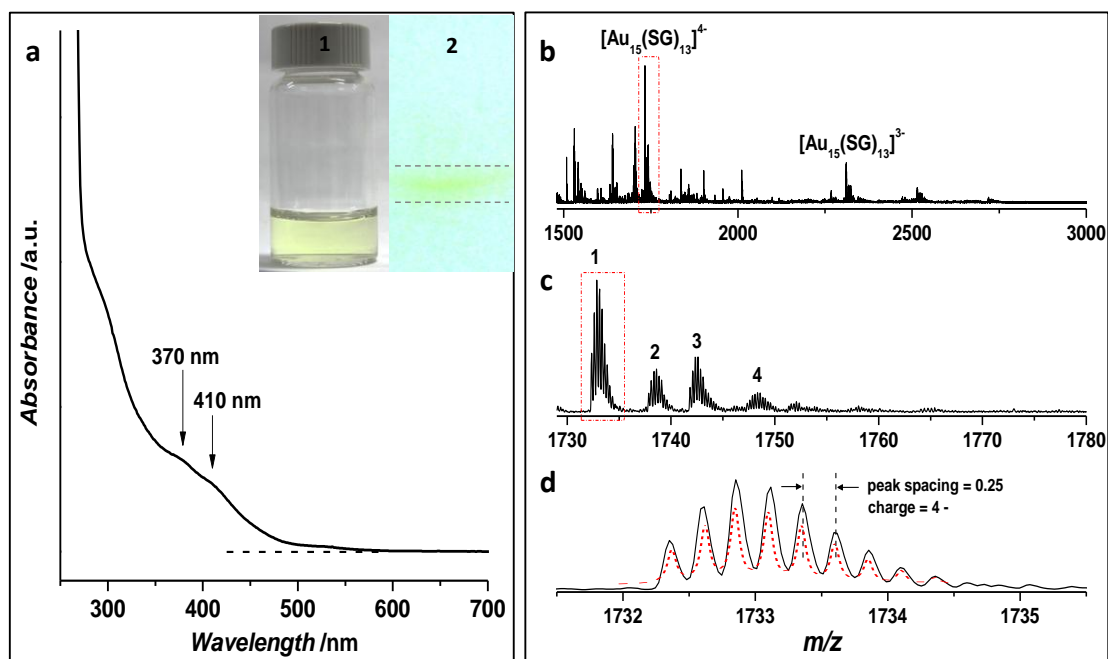


**Figure 3.3** UV-vis spectrum (a) and ESI spectra (in negative ion mode; b-d) of as-synthesized  $\text{Au}_{15}$  NCs. The inset of (a) shows a digital photo (no. 1) and the PAGE analysis (no. 2) of the crude product. The dotted line in (a) shows the zero of optical absorbance of as-synthesized  $\text{Au}_{15}(\text{SG})_{13}$  NCs. The red line in (d) is the simulated isotope pattern of  $[\text{Au}_{15}(\text{SG})_{13} - 4\text{H}]^{4-}$ .

UV-vis spectroscopy was used to characterize the crude product. The as-synthesized  $\text{Au}_{15}$  NCs showed two absorption features at 370 and 410 nm (Figure 3.3a) which correspond well with the characteristic absorption of  $\text{Au}_{15}(\text{SG})_{13}$  NCs reported by Negishi *et al.*<sup>8</sup> The distinct absorption spectrum suggests a high monodispersity of  $\text{Au}_{15}$  NCs in the crude product. The absorption spectrum of the crude product after passing through a desalting column (PD-10, GE healthcare) with 5000 Da molecular weight cut-off (MWCO) was almost the same (Figure 3.4, solid line), confirming the high monodispersity of Au NCs in the crude product. Further supporting evidence was also provided by the PAGE analysis of as-synthesized Au NCs where only a single band was found (inset no.2 of Figure 3.3a). It should be mentioned that the as-

synthesized Au<sub>15</sub> NCs had excellent stability in water. The loss of the optical intensity at 370 nm was < 15% after storage at 4 °C for 4 months (Figure 3.4, dotted line).

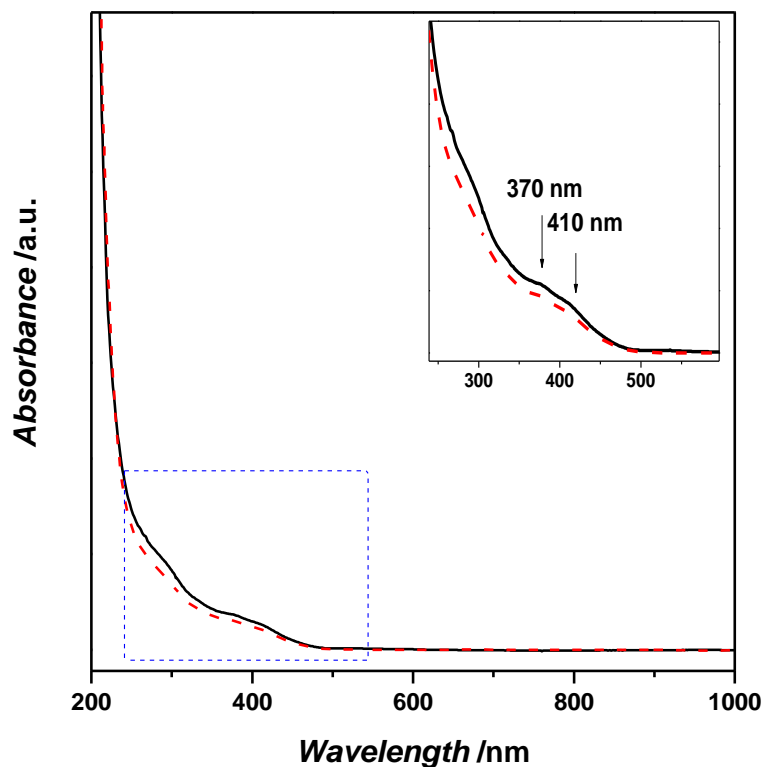


**Figure 3.4** UV-vis spectra of as-synthesized Au<sub>15</sub> NCs after passing through a PD-10 column: freshly prepared (solid line) and after 4 months' storage at 4 °C (dotted line). The inset shows the enlarged view of the boxed area.

ESI-MS was then used to determine the NC formula.<sup>43,125,163</sup> Several intense peaks were present in the  $m/z$  1500 – 3000 range of the ESI-MS spectrum (Figure 3.3b). The two most pronounced peaks at  $m/z$  ~1732 and 2312 could be assigned to  $[\text{Au}_{15}(\text{SG})_{13} - 4\text{H}]^{4-}$  and  $[\text{Au}_{15}(\text{SG})_{13} - 3\text{H}]^{3-}$  respectively while other identifiable peaks could be assigned to small fragmented species such as  $[\text{Au}_3(\text{SG})_4]^-$ ,  $[\text{Au}_5(\text{SG})_3]^-$  and  $[\text{Au}_4(\text{SG})_4]^-$  (see Figure 3.5 for the detailed assignment).<sup>125,164</sup> The base peak at  $m/z$  1732.86 (#1, Figure 3.3c) was accompanied by a series of less-intense but similar-looking peaks (#2 - #4) with two distinct spacings: 5.5  $m/z$  (#1 to #2, #3 to #4) and 9.5

$m/z$  (#1 to #3). Isotope pattern analysis (Figure 3.3d, solid line) of the 1732.86 peak (#1) indicates that the ionized NCs carried four units of negative charge (isotope peak spacing = 0.25). Hence the molecular weight of the NCs was 6931.44 Da ( $1732.86 \times 4$ ) which is consistent with the molecular formula of  $[\text{Au}_{15}(\text{SG})_{13} - 4\text{H}]^{4-}$  (the simulated molecular weight is 6931.4; see the simulated isotope pattern in Figure 3.3d, dotted line). The 5.5 or 9.5  $m/z$  spacing between the ionized species in Figure 3.3c is equal to 22 Da ( $5.5 \times 4$ ) or 38 Da ( $9.5 \times 4$ ) respectively, which is typical of the mass difference caused by  $\text{H}^+$  dissociation and  $\text{Na}^+$  or  $\text{K}^+$  coordination (*i.e.*,  $[-\text{H} + \text{Na}]$  or  $[-\text{H} + \text{K}]$ ).<sup>125,165</sup> Therefore the other ionized species in Figure 3.3c could be identified as  $[\text{Au}_{15}(\text{SG})_{13} - 5\text{H} + \text{Na}]^{4-}$  (#2),  $[\text{Au}_{15}(\text{SG})_{13} - 5\text{H} + \text{K}]^{4-}$  (#3) and  $[\text{Au}_{15}(\text{SG})_{13} - 6\text{H} + \text{Na} + \text{K}]^{4-}$  (#4). As an important corollary of the above ESI-MS analysis, the as-synthesized  $\text{Au}_{15}(\text{SG})_{13}$  was charge neutral with a total valence electron count of 2 (The total valence electron count  $N_A$  of  $[\text{Au}_n(\text{SR})_m]^z$  was calculated by Equation 2.11). It has been well-documented that  $\text{Au}_n(\text{SR})_m$  NCs with a shell-closing electron count ( $N_A = 2, 8, 18, 34 \dots$ ) are stable in solution.<sup>137</sup> The  $\text{Au}_{15}(\text{SG})_{13}$  NCs in this study contained 2 valence electrons, which could contribute to their good stability in solution.

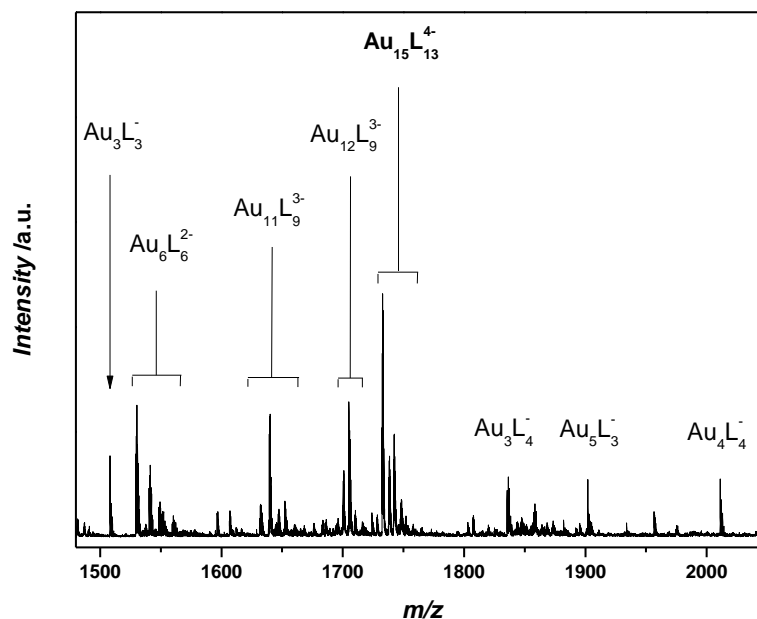


**Figure 3.5** Detailed assignment of the fragments in the ESI spectrum of as-synthesized Au<sub>15</sub> in Figure 3.3b. L denotes the SG ligand.

### 3.3.2 Synthesis of Au<sub>18</sub>(SR)<sub>14</sub> NCs

The most useful feature of this new preparation method is its size tailorability. Monodisperse SG-protected Au<sub>18</sub> NCs were synthesized by this method by simply adjusting the pH of the Au(I)-SG complex solution to ~2.7 (route 2 in Figure 3.1) while keeping other reaction conditions intact. More large aggregates of Au(I)-SG complexes were formed at pH ~2.7, as indicated by the increased turbidity of the dispersion (Figure 3.2, no. 2). The addition of the same amount of TBAB in toluene to the aqueous solution of Au(I)-SG complexes, followed by 10 h of incubation at room temperature turned the white turbid solution into a light-brown solution after centrifugation (inset in Figure 3.6a). The as-synthesized Au NCs were purified by a PD-10 column with a MWCO of 5000 Da. The typical yield of Au<sub>18</sub> NCs based on the amount of Au atoms in the starting mixture was ~58% as determined by ICP-MS. The stability of as-synthesized Au<sub>18</sub> NCs was similar to that of Au<sub>15</sub> NCs.

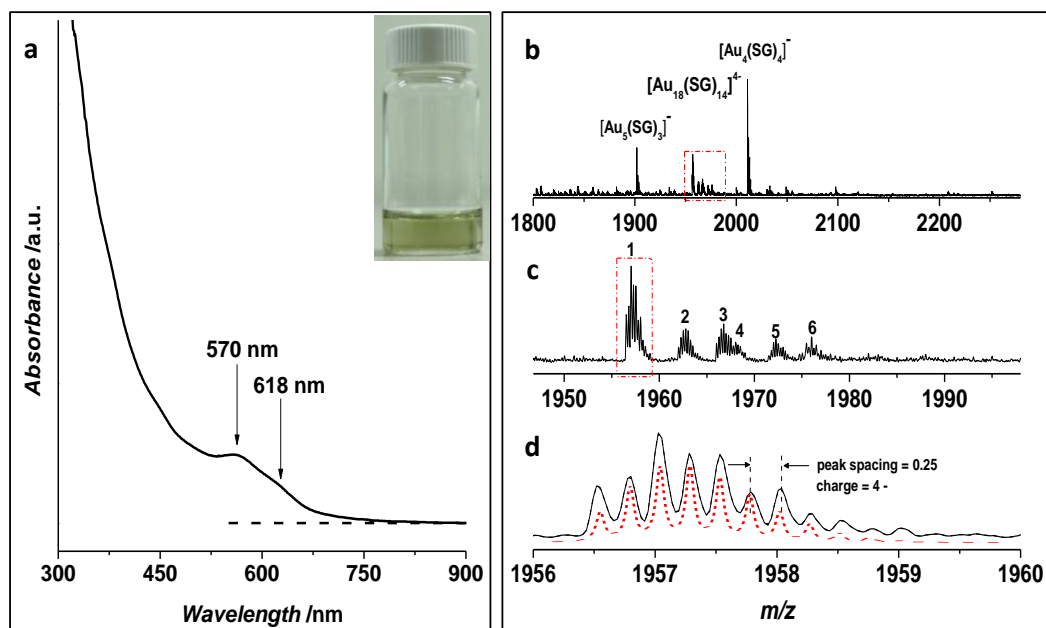


**Figure 3.6** UV-vis spectrum (a) and ESI spectra (in negative ion mode; b-d) of as-synthesized Au<sub>18</sub> NCs. The inset in (a) shows the digital photo of the crude product. The dotted line in (a) shows the zero of optical absorbance of as-synthesized Au<sub>18</sub> NCs. Peaks #1 - #6 in (c) are assigned to [Au<sub>18</sub>(SG)<sub>14</sub> - 4H]<sup>4+</sup>, [Au<sub>18</sub>(SG)<sub>14</sub> - 5H + Na]<sup>4+</sup>, [Au<sub>18</sub>(SG)<sub>14</sub> - 5H + K]<sup>4+</sup>, [Au<sub>18</sub>(SG)<sub>14</sub> - 6H + 2Na]<sup>4+</sup>, [Au<sub>18</sub>(SG)<sub>14</sub> - 6H + Na + K]<sup>4+</sup>, and [Au<sub>18</sub>(SG)<sub>14</sub> - 6H + 2K]<sup>4+</sup> respectively. The dotted line in (d) is the simulated isotope pattern of [Au<sub>18</sub>(SG)<sub>14</sub> - 4H]<sup>4+</sup>.

The as-synthesized Au<sub>18</sub> NCs were similarly analyzed by UV-vis spectroscopy and ESI-MS. The absorption spectrum in Figure 3.6a shows the characteristic absorption of Au<sub>18</sub>(SG)<sub>14</sub> at 570 and 618 nm.<sup>8</sup> The absence of other absorption features suggests high monodispersity of the Au<sub>18</sub> NCs in the product. A molecular formula for the Au<sub>18</sub> NCs could be deduced from ESI-MS measurements. The three intense peaks at *m/z* ~1902, 1957, and 2011 in Figure 3.6b could be attributed to [Au<sub>5</sub>(SG)<sub>3</sub>]<sup>-</sup>, [Au<sub>18</sub>(SG)<sub>14</sub> - 4H]<sup>4+</sup> (see the isotope pattern in Figure 3.6d) and [Au<sub>4</sub>(SG)<sub>4</sub>]<sup>-</sup> respectively. Hence on the basis of UV-vis and ESI-MS analysis, a molecular formula of Au<sub>18</sub>(SG)<sub>14</sub> may be proposed. The total valence electron count of Au<sub>18</sub>(SG)<sub>14</sub> NCs is 4 ( $N_A = 18 \times 1 - 14 - 0$  based on Equation 2.11), which is not a shell-closing electron count predicted by the "superatom electronic theory" (based on the spherical shell

assumption). The good stability of Au<sub>18</sub>(SG)<sub>14</sub> NCs, however, could be understood from a non-spherical shell model. Recent DFT simulations have predicted a stable cluster structure for Au<sub>18</sub>(SR)<sub>14</sub> containing a prolate (non-spherical) Au<sub>8</sub> core covered with two dimeric SR-(Au-SR)<sub>2</sub> and two trimeric SR-(Au-SR)<sub>3</sub> staple-like motifs.<sup>166-167</sup> Similar observations of good solution stability of thiolate-protected NCs with a total valence electron count of 4 have also been reported for other NC systems both in theory and experiments.<sup>142,146,168</sup>

### 3.3.3 Au Oxidation State and Photoluminescence of As-Synthesized Au<sub>15</sub>(SR)<sub>13</sub> and Au<sub>18</sub>(SR)<sub>14</sub> NCs

The oxidation states of Au in Au<sub>15</sub>(SG)<sub>13</sub> and Au<sub>18</sub>(SG)<sub>14</sub> were determined by X-ray photoelectron spectroscopy (XPS). The Au 4f<sub>7/2</sub> binding energies (B.E.) of Au<sub>15</sub>(SG)<sub>13</sub> (Figure 3.7, blue line) and Au<sub>18</sub>(SG)<sub>14</sub> (Figure 3.7, red line) were intermediate between those of Au(I)-SG complexes (prepared by mixing HAuCl<sub>4</sub> with GSH, Figure 3.7, black line) and large Au(0) nanocrystals (> 3 nm, prepared by the NaBH<sub>4</sub> reduction of HAuCl<sub>4</sub> without any protecting agent, Figure 3.7, pink line), thereby suggesting mixtures of Au(I) and Au(0) in Au<sub>15</sub> and Au<sub>18</sub> NCs. The Au 4f<sub>7/2</sub> B.E. of Au<sub>18</sub>(SG)<sub>14</sub> were closer to large Au(0) nanocrystals than Au<sub>15</sub>(SG)<sub>13</sub>. Hence there should be a relatively higher content of Au(0) in Au<sub>18</sub> NCs than in Au<sub>15</sub> NCs, agreeing well with the lower thiolate-to-Au ratio in Au<sub>18</sub> NCs.<sup>8</sup> Both Au<sub>15</sub>(SG)<sub>13</sub> and Au<sub>18</sub>(SG)<sub>14</sub> NCs showed weak luminescence with an emission wavelength ( $\lambda_{em}$ ) of ~920 nm (or 1.35 eV, Figure 3.8), similar to the  $\lambda_{em}$  reported in other studies (~1.5 eV).<sup>8</sup> The small wavelength difference could be due to solvent effects and the variation in the charge of ligand.<sup>110-111,169-170</sup>

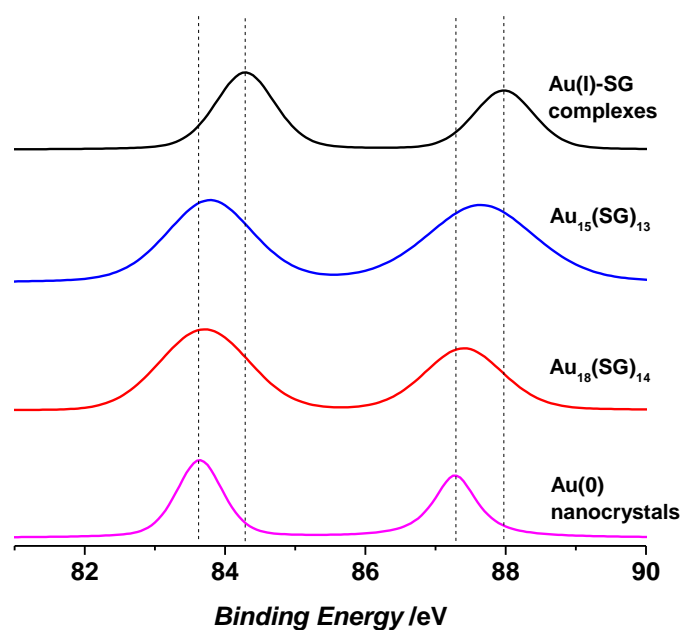


**Figure 3.7** Au(4f) XPS spectra of as-synthesized Au<sub>15</sub> NCs (blue), Au<sub>18</sub> NCs (red), freshly prepared Au(0) nanocrystals (pink) and Au(I)-SG complexes (black). The Au(I)-SG complexes were prepared by the direct mixing of GSH and HAuCl<sub>4</sub> and the Au(0) nanocrystals were synthesized by the reduction of HAuCl<sub>4</sub> in excess NaBH<sub>4</sub> without any protecting agent.

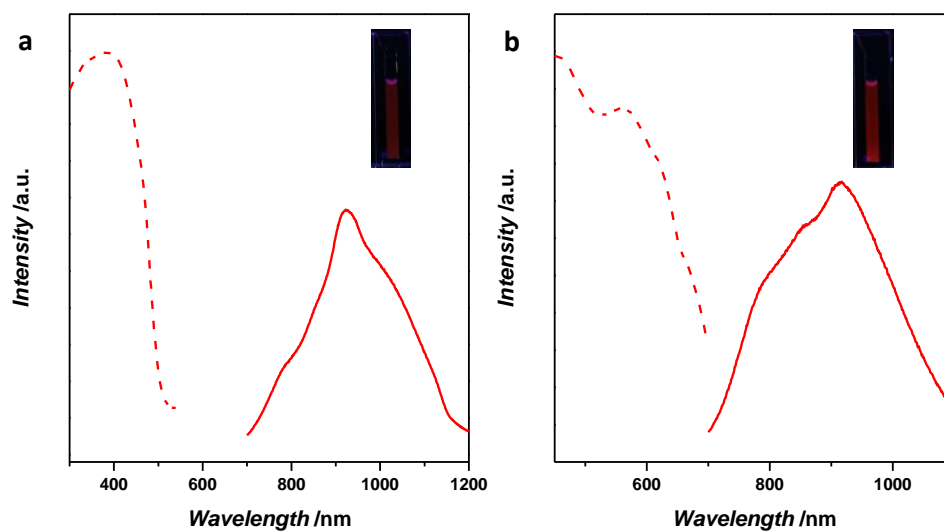


**Figure 3.8** Photoemission (solid lines) and photoexcitation (dotted lines) spectra of as-synthesized (a) Au<sub>15</sub>(SG)<sub>13</sub> and (b) Au<sub>18</sub>(SG)<sub>14</sub>. The  $\lambda_{\text{ex}}$  for photoemission spectra were 370 and 570 nm for Au<sub>15</sub>(SG)<sub>13</sub> and Au<sub>18</sub>(SG)<sub>14</sub>, respectively. The  $\lambda_{\text{em}}$  for the photoexcitation spectra was 920 nm for both Au<sub>15</sub>(SG)<sub>13</sub> and Au<sub>18</sub>(SG)<sub>14</sub>. The insets show the corresponding digital photos taken under UV illumination ( $\lambda = 365$  nm).



### 3.3.4 Origin of the High Monodispersity and Size-tunability

An unvarying gentle reduction environment for Au NC formation, made possible by the controlled release of the mild reductant TBAB and free Au(I)-SG complexes, was essential for the synthesis of high purity Au<sub>15</sub> and Au<sub>18</sub> NCs. TBAB,<sup>141,171-172</sup> a milder reductant than the commonly used strong reducing agent NaBH<sub>4</sub>, was chosen for this study. The weak reducing power of TBAB gave rise to a slower reduction kinetics and hence more controllability of the reduction environment. The opposite result of a fast and uncontrollable reduction was demonstrated by replacing TBAB with NaBH<sub>4</sub> which formed only polydispersed Au NCs in water, as evinced by the featureless absorption spectrum (Figure 3.9, no. 1).<sup>173</sup> The two-phase design is another important element of this synthesis of small Au<sub>15</sub>(SR)<sub>13</sub> and Au<sub>18</sub>(SR)<sub>13</sub> NCs. The direct addition of TBAB into an aqueous solution of Au(I)-SG complexes (a typical one-phase synthesis) also resulted in a mixture of different sizes of Au NCs and hence a featureless absorption spectrum (Figure 3.9, no. 2). The equilibrium partition of TBAB between organic and aqueous phases provided the mechanism to release TBAB into the aqueous solution as replenishment of the TBAB consumed by NC formation and growth. The combination of a weak reducing agent and the two-phase design was able to maintain a low and constant reducing power in the aqueous solution for the conversion of Au(I)-SG complexes into Au NCs.

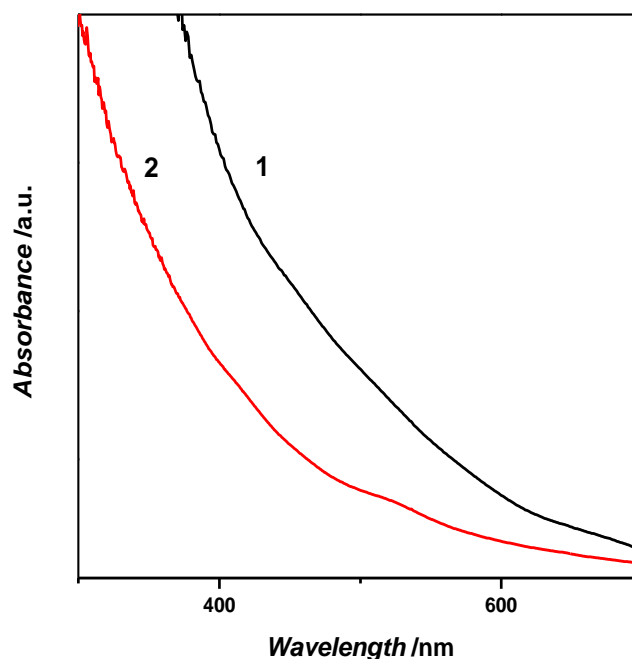


**Figure 3.9** UV-vis spectra of the NC products by  $\text{NaBH}_4$  reduction (no.1) and one-phase TBAB reduction (no.2).

Another equally important factor was the aggregation-dissociation equilibrium between aggregated and free Au(I)-SG complexes in the aqueous solution. Aggregated Au(I)-SG complexes had to be dissociated into free Au(I)-SG complexes before reduction could occur. It is reasonable to expect that the thiolates in the Au(I)-SG complexes would affect the aggregation-dissociation equilibrium. The thiol used in this study, GSH, has two carboxyl, one amine and one thiol groups (resulting in four  $\text{pK}_a$  values:  $\text{pK}_{a1} = 2.12$ ,  $\text{pK}_{a2} = 3.53$ ,  $\text{pK}_{a3} = 8.66$ , and  $\text{pK}_{a4} = 9.62$ , see Figure 3.10 for details),<sup>174</sup> providing the means to vary the surface charge on Au(I)-SG complexes and consequently their extent of aggregation through pH adjustments (Figure 3.2). At low pH (*e.g.*, pH  $\sim 2$  and 2.7), the SG ligand in Au(I)-SG complexes is either singly positively charged (pH  $\sim 2 < \text{pK}_{a1}$ ) or neutral ( $\text{pK}_{a1} < \text{pH} \sim 2.7 < \text{pK}_{a2}$ ). The limited electrostatic repulsion between the Au(I)-SG complexes promoted the formation of Au(I)-SG aggregates (Figure 3.2, no. 1 and 2) and established the equilibrium between

aggregation and dissociation. The concentration of free Au(I)-SG complexes could then be kept at a constant and low level in the aqueous solution for TBAB reduction. The combination of constant reducing power and constant free complex concentration stabilized the chemical kinetics for Au NC formation, and consequently monodispersity of the product in well-defined sizes. A low and constant concentration of free Au(I)-GSH complexes in water was maintained by the controlled release of free Au(I)-SG complexes according to the aggregation-dissociation equilibrium. A control experiment using an alkaline pH ( $\sim 10.0$ ) to disrupt the aggregation-dissociation equilibrium resulted in a mixture of Au NCs in different sizes as shown by a featureless absorption spectrum (Figure 3.11). At pH  $\sim 10.0$  ( $> pK_{a4} = 9.62$  of GSH), the SG ligand in the Au(I)-SG complexes was completely deprotonated into doubly charged anions. The electrostatic repulsion in this case was strong enough to inhibit aggregation. Free Au(I)-SG complexes were abundant as shown by the high clarity of the solution (Figure 3.2, no. 3). The relatively high concentration of free Au(I)-SG complexes at this pH ( $\sim 10.0$ ) created an uncontrollable reaction environment, leading to the formation of Au NCs in mixed sizes.

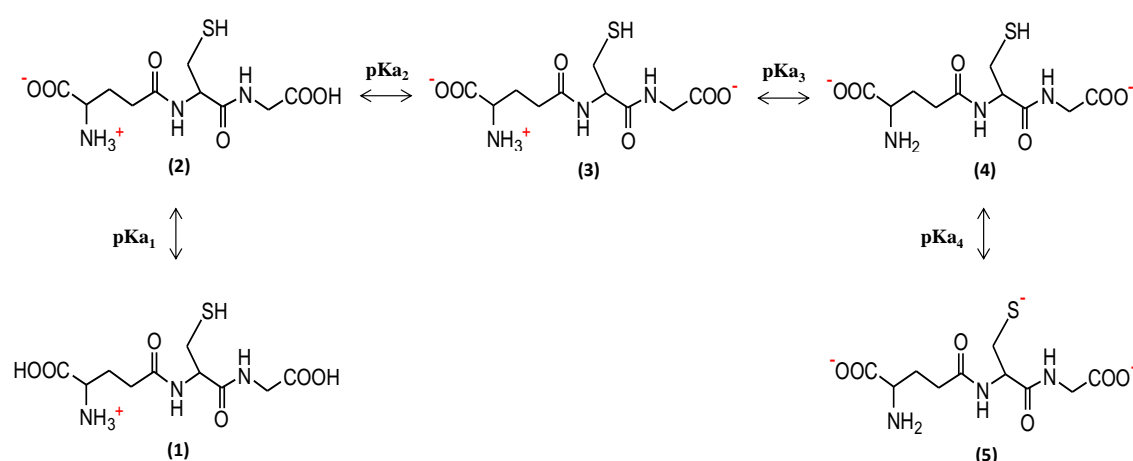


**Figure 3.10** Molecular structure and protonation/deprotonation processes of GSH, where  $pK_{a1} = 2.12$ ,  $pK_{a2} = 3.53$ , and  $pK_{a3} = 8.66$ .  $pK_{a4} = 9.62$ .

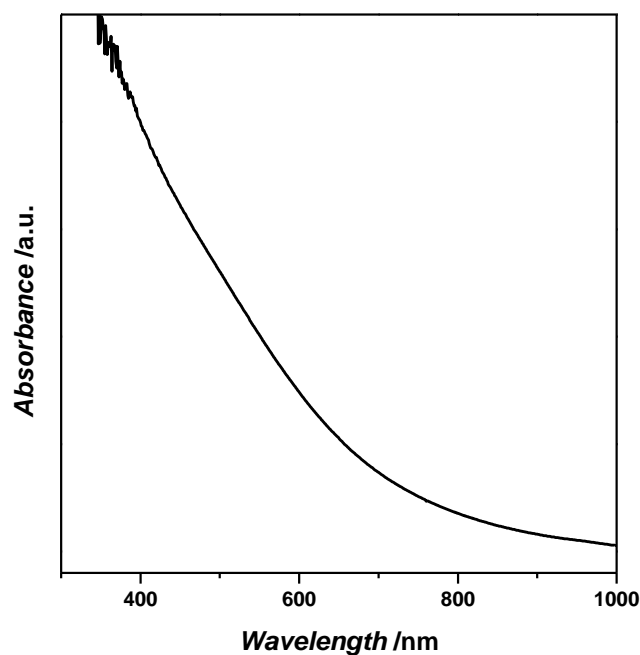


**Figure 3.11** UV-vis spectrum of the as-prepared NC product at pH ~10.0.

The aggregation-dissociation equilibrium could be used to advantage to produce Au NCs in fixed but different sizes. The only difference between the conditions for routes 1 and 2 of Figure 3.1 was the pH of the Au(I)-SG complex solution. The aggregation-dissociation equilibrium is strongly pH dependent due to the progressive ionization of different functional groups in GSH. Route 1 was carried out at pH lower than  $pK_{a1}$  (2.12) and hence the SG ligands in Au(I)-SG complexes were singly charged. When the pH was increased slightly to ~2.7 (route 2), which is between  $pK_{a1}$  (2.12) and  $pK_{a2}$  (3.53) of GSH, the SG ligands in the Au(I)-SG complexes were neutral. Hence there should be more aggregation of Au(I)-SG complexes at pH ~2.7 (Figure 3.2, no. 2) than at pH ~2.0 (Figure 3.2, no. 1); and consequently a lower concentration of free Au(I)-SG complexes in the aqueous solution for TBAB reduction. This could result in more difficult nucleation and hence larger NCs ( $Au_{18}$ ) were formed.<sup>65</sup> Therefore, our synthesis method provides a facile strategy to tailor the cluster size (precise number of atoms) simply by varying the reaction pH.

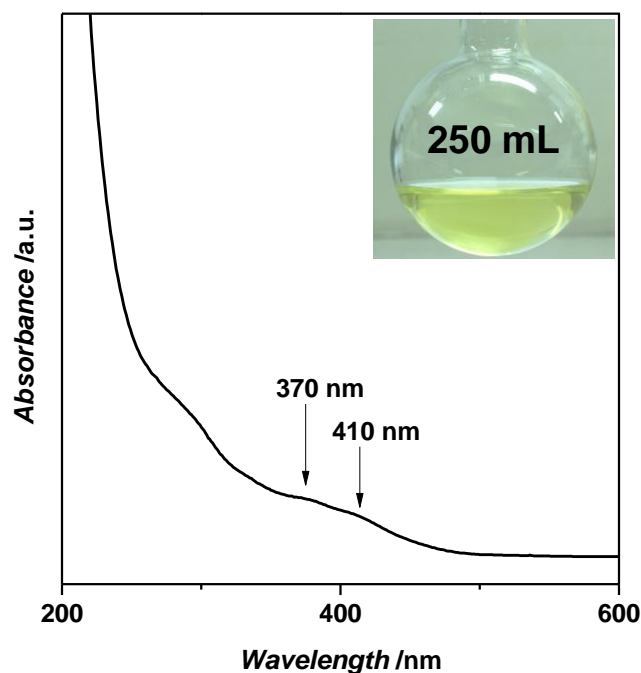


**Figure 3.12** UV-vis spectrum of Au<sub>15</sub>(SG)<sub>13</sub> produced in a scaled-up synthesis. The inset shows the digital photo of the Au<sub>15</sub>(SG)<sub>13</sub> solution in a 250 mL flask after centrifugation. For the scaled-up synthesis the reaction volume was increased from 10 to 150 mL, and all other reaction conditions remained the same as that in §3.2.2.1.

### 3.4 Conclusion

In summary, we have developed a simple one-pot two-phase method for the synthesis of small NCs (Au<sub>15</sub>(SG)<sub>13</sub> and Au<sub>18</sub>(SG)<sub>14</sub>) in atomic precision monodispersity. The method can be easily scaled up for volume production (*e.g.*, to 150 mL, see Figure 3.12). A constant and gentle reduction environment, made possible by the combined use of a weak reducing agent (TBAB), the equilibrium partition of TBAB between organic and aqueous phases, and pH dependent aggregation-dissociation between aggregated and free Au(I)-SG complexes, facilitated the formation of NCs in well-defined sizes. The two equilibriums could be fine-tuned to vary the reduction kinetics of Au(I)-SG complexes to form Au NCs in different sizes

(*e.g.*, Au<sub>15</sub> and Au<sub>18</sub> were synthesized by changing the pH only). The products and the synthesis approach demonstrated in this study are of interest not only because they provide the convenience of a one-pot method for the preparation of high quality small Au<sub>15</sub>(SR)<sub>13</sub> and Au<sub>18</sub>(SR)<sub>14</sub> NCs, but also because they exemplify the use of equilibrium partition and aggregation-dissociation equilibrium to regulate the supply of reactants and to create a mild and more controllable reaction kinetics for the formation of NCs in customizable sizes. Based on the synthesis method developed in this chapter as well as those documented in cluster literature, we now have the tools of high quality building blocks (*e.g.*, atomically precise Au NCs over a wide size spectrum) for self- or directed-assembly. In the coming chapters, several specific interactions (*e.g.*, attractive electrostatic forces, amphiphilicity, and depletion forces), which are used by nature for creating ionic/molecular/atomic crystals, will be exploited for the assembly of atomically precise metal NCs. Since water-soluble metal NCs (of which the GSH-protected NCs synthesized in this chapter are a good example) are easy to acquire negative charges by deprotonation at neutral or high pH, electrostatically induced self-assembly will be discussed first in Chapter 4.

---

# CHAPTER 4 SELF-ASSEMBLY OF SUPRAMOLECULAR IONS VIA ELECTROSTATIC INTERACTIONS: ION- LIKE BEHAVIOR OF CHARGED NOBLE METAL NANOCCLUSERS

## 4.1 Introduction

Despite its essential importance to both basic (*e.g.*, NC crystal structure determination) and applied (*e.g.*, NC property tailoring) research, self-assembly of thiolate-protected noble metal (Au or Ag) nanoclusters ( $M_n(SR)_m$  NCs) is still at its infant stage of development. Only a few  $M_n(SR)_m$  NC species (most of them are protected by aromatic thiolate) have been assembled in organic solvents or semi-aqueous phase (methanol/water mixture) to date.<sup>24-29,33,57,59-60</sup> There are still no reports on the self-assembly of hydrophilic metal NCs in aqueous solution. The hydrophilic thiolate ligands on the NC surface do not contain the rigid aromatic rings which could effectively drive the self-assembly of  $M_n(SR)_m$  NCs in organic solution through strong  $\pi$ - $\pi$  interactions.

On the other hand the hydrophilic thiolate ligands on the NC surface may contain functionalities such as the carboxyl group ( $-\text{COOH}$ ) which, upon deprotonation, can impart the NCs with a negative charge in aqueous solution.<sup>10,175-176</sup> Due to a very high ligand-to-metal ratio ( $\sim 0.4$  to 1 typically)<sup>8,41</sup> and an ultras-small size ( $< 2$  nm), a high charge density can be developed on the surface of the NCs. The high charge density,

together with well-defined (atomically precise) size and highly symmetric *pseudo*-spherical geometry qualify the hydrophilic metal NCs as a new family of ion mimics (“supramolecular ions”) in the aqueous phase. We hypothesize that the ion-like features (high charge density, well-defined size and *pseudo*-spherical morphology) could promote strong electrostatic interactions between the hydrophilic  $M_n(SR)_m$  NCs and counter cations, in ways similar to the formation of ionic crystals from real ions.

Herein, we report a facile method to self-assemble negatively charged  $M_n(SR)_m$  NCs in water via the electrostatic interactions between the dissociated carboxyl groups on the NC surface and divalent counter cations (*e.g.*,  $Zn^{2+}$  and  $Cd^{2+}$ ) which are introduced to the solution. The divalent metal cations are used to electrostatically cross-link the negatively charged NCs into large assemblies. An interesting ion-like behavior of the charged NCs was observed, where the self-assembly of NCs occurred in a step fashion and only when the counter-cation ( $M_c$ )-to-thiolate-ligand ratio (denoted as  $R_{[M_c]/[L-SR]}$ ) exceeded specific threshold values. The NC assemblies formed as such were spherical and monodisperse in shape and size. The difference from the random aggregation of large colloidal NPs by counter ions is distinct and also suggests a high order of regularity in the assembly structure which is more akin to the formation of ionic crystals from real ions in solution. More interestingly, photoluminescence (PL) of the NCs was significantly enhanced after assembly, implying the existence of strong synergistic effects between the close-packed NC building blocks.



## 4.2 Experimental Section

### 4.2.1 Materials

Hydrogen tetrachloroaurate(III) trihydrate ( $\text{HAuCl}_4 \cdot 3\text{H}_2\text{O}$ ), L-glutathione reduced form (GSH), borane tert-butylamine (TBAB) and sodium borohydride ( $\text{NaBH}_4$ ) from Sigma Aldrich; hydrochloric acid (HCl) and nitric acid ( $\text{HNO}_3$ ) from J. T. Baker; zinc chloride ( $\text{ZnCl}_2$ ), silver nitrate ( $\text{AgNO}_3$ ) and sodium hydroxide (NaOH) from Merck; and cadmium chloride ( $\text{CdCl}_2$ ) from Strem were used as received without further purification. Ultrapure Milipore water (18.2 M $\Omega$ ) was used in the preparation of all aqueous solutions. All glassware was washed with *aqua regia* and rinsed with ethanol and ultrapure water before use.

### 4.2.2 Synthesis of $\text{M}_n(\text{SR})_m$ NCs

#### 4.2.2.1 Synthesis of Orange-Emitting $\text{Au}_{29-43}(\text{SG})_{27-37}$ NCs

The synthesis of orange-emitting  $\text{Au}_{29-43}(\text{SG})_{27-37}$  NCs (o-Au NCs) was conducted following a previously-reported procedure.<sup>11</sup> Briefly, 0.5 mL of 20 mM  $\text{HAuCl}_4$  and 0.2 mL of 100 mM GSH aqueous solutions were mixed with 4.35 mL of ultrapure water at room temperature (298 K). After incubation under gentle stirring (500 rpm) at 343 K for 24 h, o-Au NCs were formed. As suggested by the ESI-MS in the original work, the o-Au NCs consist of mainly 5 sizes of  $\text{Au}_n(\text{SG})_m$  NCs, *i.e.*,  $(n, m) = (29, 27)$ ,  $(30, 28)$ ,  $(36, 32)$ ,  $(39, 35)$ , and  $(43, 37)$ .<sup>11</sup>

#### 4.2.2.2 Synthesis of Red-Emitting $\text{Au}_{15}(\text{SG})_{13}$ NCs

The detailed synthesis of  $\text{Au}_{15}(\text{SG})_{13}$  NCs can be found in Chapter 3. Briefly, 0.75 mL of GSH aqueous solution and 0.5 mL of  $\text{HAuCl}_4$  aqueous solution were added to

3.75 mL of ultrapure water. The pH of the mixed solution was adjusted to  $\sim 2.0$  by adding 1 M  $\text{HNO}_3$  until the target pH was reached. The mixture was then incubated for 5 min for the Au(I)-SG complexes to form. A semi-translucent dispersion was obtained. 5 mL of 10 mM TBAB solution in toluene was then added to the Au(I)-SG dispersion. The growth of NCs occurred over a period of 4 h under vigorous stirring (1000 rpm). The light-yellow  $\text{Au}_{15}(\text{SG})_{13}$  solution obtained at the end of the procedure was centrifuged at 5000 rpm for 5 min to remove the insoluble byproducts.

#### 4.2.2.3 Synthesis of Red-Emitting $\text{Ag}_{16}(\text{SG})_9$ NCs

$\text{Ag}_{16}(\text{SG})_9$  NCs were prepared by a cyclic reduction-decomposition method detailed elsewhere.<sup>98</sup> Briefly, 125  $\mu\text{L}$  of 20 mM  $\text{AgNO}_3$  and 150  $\mu\text{L}$  of 50 mM GSH aqueous solutions were added to 4.85 mL of ultrapure water under vigorous stirring ( $\sim 1200$  rpm) to form Ag(I)-SG complexes. 50  $\mu\text{L}$  of 112 mM  $\text{NaBH}_4$  aqueous solution was then introduced to reduce the Ag(I)-SG complexes, giving rise to a deep-red solution of Ag NCs within 5 min. The As-formed Ag NC solution (deep-red) was allowed to decompose to Ag(I)-SG complexes (colorless) after  $\sim 3$  h of incubation at room temperature (298 K). 50  $\mu\text{L}$  of 112 mM  $\text{NaBH}_4$  aqueous solution was then added to this colorless solution under vigorous stirring ( $\sim 1200$  rpm). The color of solution turned from colorless to light-brown within 15 min. This light-brown Ag NC solution was allowed to stand (without stirring) at room temperature (298 K) for 8 h to form  $\text{Ag}_{16}(\text{SG})_9$  NCs in aqueous solution.

### 4.2.3 Ion-Induced Self-Assembly of $M_n(SR)_m$ NCs

#### 4.2.3.1 Ion-Induced Self-Assembly of Orange-Emitting $Au_{29-43}(SG)_{27-37}$ NCs

$ZnCl_2$  and  $CdCl_2$  aqueous solutions in specific concentrations were freshly prepared by dissolving calculated amounts of  $ZnCl_2$  and  $CdCl_2$  in ultrapure water respectively. The pH of each metal salt solution was adjusted to  $\sim 6.5$  by adding 0.1 M NaOH. The as-prepared o-Au NC aqueous solution was diluted 4 times ( $4\times$  diluted) and the pH was adjusted to  $\sim 6.5$  before use. In a typical self-assembly (taking  $R_{[Zn^{2+}]/[-SG]} = 0.6$  as an example), 0.25 mL of 1 mM  $ZnCl_2$  was quickly added to 1 mL of the diluted o-Au NC solution, followed by mixing on a vortex mixer (1500 rpm for 30 s). The pH of the mixture was maintained at  $\sim 6.5$ . Subsequently, the mixture was kept still at room temperature (298 K) for 15 min to allow the self-assembly to complete. Self-assembly of o-Au NCs by  $Zn^{2+}$  in other concentrations and by  $Cd^{2+}$  solution were also carried out likewise, using different metal salt solutions before mixing.

#### 4.2.3.2 Ion-Induced Self-Assembly of Red-Emitting $Au_{15}(SG)_{13}$ NCs

The pH of  $Au_{15}(SG)_{13}$  NC as well as 3 mM  $ZnCl_2$  aqueous solution was brought to  $\sim 6.5$  before use. Similar to the  $Zn^{2+}$  induced assembly of o-Au NCs, 1 mL of  $Au_{15}(SG)_{13}$  NC and 0.25 mL of 3 mM  $ZnCl_2$  aqueous solutions were mixed while pH was maintained at  $\sim 6.5$ , followed by still incubation at room temperature (298 K) for 15 min.

#### 4.2.3.3 Ion-Induced Assembly of Red-Emitting $Ag_{16}(SG)_9$ NCs

The pH of  $Ag_{16}(SG)_9$  NC as well as 2 mM  $ZnCl_2$  aqueous solution was brought to  $\sim 6.5$  before use. Similar to the  $Zn^{2+}$  induced assembly of o-Au NCs, 1 mL of

$\text{Ag}_{16}(\text{SG})_9$  NC and 0.25 mL of 2 mM  $\text{ZnCl}_2$  aqueous solutions were mixed while pH was maintained at ~6.5, followed by still incubation at room temperature (298 K) for 15 min.

#### 4.2.4 Characterization

pH was monitored by a Mettler Toledo FE 20 pH-meter. UV-vis absorption and PL spectra were recorded by a Shimadzu UV-1800 spectrometer and a PerkinElmer LS-55 fluorescence spectrometer respectively. TEM, scanning transmission electron microscopy (STEM), and energy-dispersive X-ray spectroscopy (EDX) elemental analysis were performed on a JEOL JEM 2010 microscope operating at 200 kV. The size and  $\zeta$ -potential of NCs before and after assembly were measured by dynamic light scattering (DLS) and electrophoresis light scattering (ELS) on a Malvern Zetasizer Nano ZS, respectively. The samples were centrifuged on an Eppendorf Centrifuge 5424. NC solutions were dialyzed by sealing 5 mL of NC solution in a semipermeable bag (MWCO = 3500 Da; Spectra/Por<sup>®</sup>), followed by immersion into 5 L of ultrapure water under moderate stirring (1000 rpm) overnight. The Au and Zn contents in the samples were analyzed by ICP-MS measurement on an Agilent 7500A. The GSH and carboxyl group contents were calculated based on the Au content via the relation Au : GSH : COOH = 1 : 0.84 : 1.68.<sup>11</sup> The ionic strength of NaCl or  $\text{ZnCl}_2$  solution was calculated by the equation

$$I_{\text{ion}} = 0.5 \sum c_i z_i^2 \quad (4.1)$$

where  $I_{\text{ion}}$  is the ionic strength,  $c_i$  is the concentration of a specific ion, and  $z_i$  is the specific charge number of the ion.

## 4.3 Results and Discussion

### 4.3.1 Zn<sup>2+</sup>-Induced Self-Assembly of Orange-Emitting Au<sub>29-43</sub>(SG)<sub>27-37</sub> NCs

As a proof-of-concept, highly luminescent SG-protected Au NCs reported by some of us<sup>11</sup> were chosen as the model supramolecular ions. The Au NCs synthesized as such showed strong orange emission which peaked at a wavelength of ~610 nm with a state of art QY at ~15 %, <sup>11</sup> which could be used to monitor the self-assembly process. As shown in Figure 4.1a, these orange emitting Au NCs (o-Au NCs) were small spheres with a core size below 2 nm, and may be described by the molecular formula of Au<sub>29-43</sub>(SG)<sub>27-37</sub> NCs as suggested by the ESI-MS analysis in the original work<sup>11</sup>. The as-synthesized o-Au NCs had a high SG content on the NC surface (the SG-to-Au-atom ratio was ~0.84 as reported in the original study).<sup>11</sup> The GSH ligands are likely to be present as oligomeric GS-(Au(I)-SG)<sub>n</sub> motifs<sup>11</sup> on the NC surface and determine the charge and surface properties of the o-Au NCs. Each GSH moiety carries two carboxyl groups with pK<sub>a</sub> below 4.<sup>174</sup> Hence at the near neutral condition of pH 6.5 in our experiments, all of the carboxyl groups on the NC surface were deprotonated to give rise to a negative charge on the o-Au NCs. The ζ-potential plot in Figure 4.2 illustrates the pH dependence of the charge on the o-Au NCs.

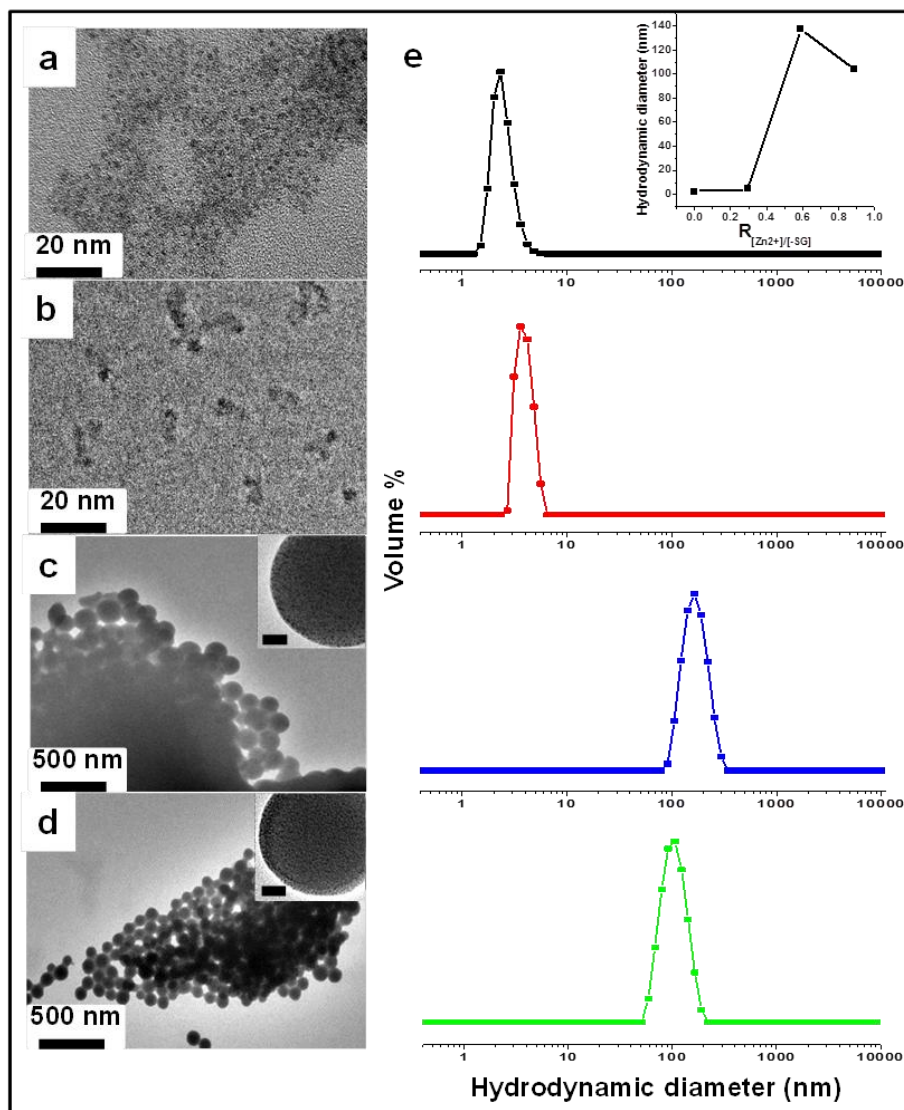


**Figure 4.1** (a-d) TEM images of o-Au NCs assembled in different  $Zn^{2+}$  concentrations:  $R_{[Zn^{2+}]/[L-SG]} = 0$  (a), 0.3 (b), 0.6 (c), and 0.9 (d); the insets in (c) and (d) show the corresponding HR-TEM images (scale bar = 20 nm). (e) DLS analysis of o-Au NCs assembled at  $R_{[Zn^{2+}]/[L-SG]} = 0$  (black), 0.3 (red), 0.6 (blue), and 0.9 (green); the inset in (e) shows the dependence of the hydrodynamic diameter of the assembly on  $R_{[Zn^{2+}]/[L-SG]}$ .

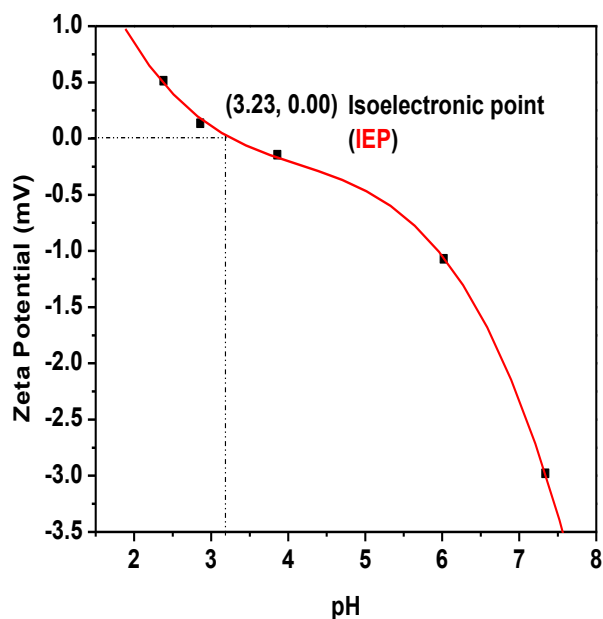


**Figure 4.2** pH dependence of the  $\zeta$ -potential of o-Au NCs. The isoelectric point (IEP) of the o-Au NCs was estimated to be 3.23.

$\text{Zn}^{2+}$  was the counter cation used in this study.  $\text{Zn}^{2+}$  carries two positive charge and can electrostatically bind to two monovalent anionic  $-\text{COO}^-$  groups. Therefore,  $\text{Zn}^{2+}$  can be used as a bifunctional cross-linker to electrostatically bridge between two negatively charged o-Au NCs to build large NC assemblies. In a typical  $\text{Zn}^{2+}$ -induced NC assembly, 1 mL of o-Au NCs at an optimized concentration of 0.46 mM (on Au atom basis as determined by ICP-MS) was mixed with 0.25 mL of  $\text{ZnCl}_2$  solution at a given concentration. The pH of the mixture was brought to  $\sim 6.5$  by the addition of 0.1 M NaOH. The solution was well-mixed in a vortex mixer (1500 rpm, 30 s) and kept at room temperature for  $\sim 15$  min to allow the reaction to complete. The procedure was repeated by using different concentrations of  $\text{ZnCl}_2$  while keeping the concentration of the o-Au NCs constant.

The size of the assembled NCs formed with different concentrations of  $\text{Zn}^{2+}$  was analyzed by TEM and dynamic light scattering (DLS). The degree of assembly was determined by the ratio of divalent cations ( $\text{Zn}^{2+}$ ) to negatively charged NCs (poly-

anions). Since the latter depends on the SG ligands on the NC surface, a controllable experimental variable would be the ratio of divalent cation ( $\text{Zn}^{2+}$ ) to SG on the o-Au NC surface (taking into account that there are two anionic carboxylate groups in one SG moiety), termed as  $\text{Zn}^{2+}$ -to-SG ratio or  $R_{[\text{Zn}^{2+}]/[\text{-SG}]}$ . If no  $\text{Zn}^{2+}$  ions were added to the o-Au NC solution (or  $R_{[\text{Zn}^{2+}]/[\text{-SG}]} = 0$ ), the o-Au NCs were well-dispersed in water and remained separated, as shown in the TEM image (Figure 4.1a). The discrete nature of the o-Au NCs was also supported by DLS measurements, where a hydrodynamic diameter (HD) of  $\sim 2.7$  nm was calculated (Figure 4.1e, black line). When  $R_{[\text{Zn}^{2+}]/[\text{-SG}]}$  was increased to 0.3, some small and irregularly-shaped NC assemblies began to appear in the TEM image (Figure 4.1b). The slight increase in HD in the DLS measurements (Figure 4.1e, red line) is consistent with the formation of small NC assemblies. The small amount of counter cations introduced to the NC solution at a low  $R_{[\text{Zn}^{2+}]/[\text{-SG}]}$  value (0.3) could only induce controlled aggregation of the negatively charged NCs to a limited extent; and only NC assemblies smaller than 10 nm were formed (Figure 4.1b). The small size of the NC assemblies was also corroborated by UV-vis spectroscopy (Figure 4.3) where scattering intensity increase (indication of a significant particle size increase)<sup>11</sup> was not found relative to the discrete o-Au NCs.

Fractal-like spheres displaying limited self-similarity<sup>177</sup> (spherical supramolecular ion to spherical colloidal assembly at the scale of  $\sim 1$  and 100 nm, respectively) were present in the TEM image when  $R_{[\text{Zn}^{2+}]/[\text{-SG}]}$  was increased to 0.6 (Figure 4.1c). The spherical assemblies had a uniform core size of 136.2 nm (100 colloidal spheres counted) and a HD of  $\sim 137.6$  nm (Figure 4.1e, blue line). The assembled structure at a higher  $R_{[\text{Zn}^{2+}]/[\text{-SG}]}$  value of 0.9 was visually similar (Figure 4.1d). The diameter of the NC assemblies was however smaller, at  $\sim 92.8$  nm (100 colloidal spheres counted) and likewise the measured HD decreased to  $\sim 93.5$  nm (Figure 4.1e, green line). An



increase in the scattering intensity of the NC assemblies was noted when  $R_{[Zn^{2+}]/[-SG]}$  was increased from 0.6 to 0.9 (Figure 4.3). This is an indication of the increase in the number of NC assemblies at  $R_{[Zn^{2+}]/[-SG]}$  of 0.9. Hence at the higher  $R_{[Zn^{2+}]/[-SG]}$  value of 0.9, there were more NC assemblies formed but the size was smaller (vs  $R_{[Zn^{2+}]/[-SG]} = 0.6$ ). This finding can be understood based on the common nucleation-growth mechanism.<sup>178</sup> At a higher  $R_{[Zn^{2+}]/[-SG]}$  (0.9), more  $Zn^{2+}$  ions were available as electrostatic cross-linkers, leading to a faster formation of “assembly nuclei”. More “nucleation sites” were available for growth through continuous assembly of NCs. Consequently smaller NC assemblies were formed when the same NC concentration was used. The dependence of the NC assembly size on the concentration of the counter cations ( $Zn^{2+}$ ) is summarized in the inset of Figure 4.1e, where the maximum in the size of the NC assemblies was found to be around  $\sim 137.6$  nm.

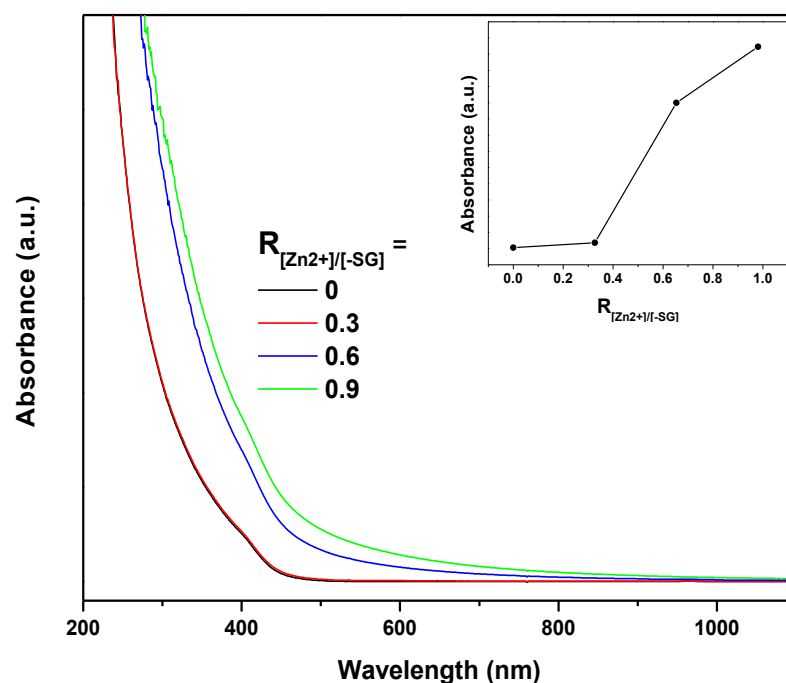


**Figure 4.3** UV-vis absorption spectra of o-Au NCs assembled at different  $R_{[Zn^{2+}]/[-SG]}$  values; the inset shows the absorbance at 400 nm as a function of  $R_{[Zn^{2+}]/[-SG]}$ .

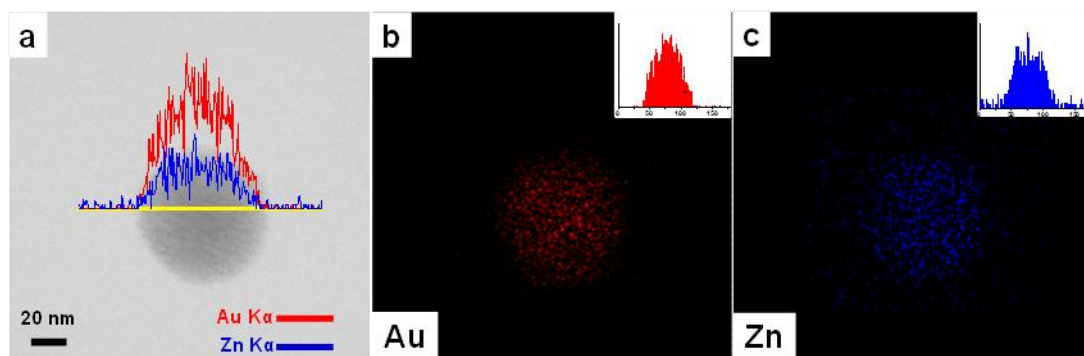


**Figure 4.4** (a) Scanning transmission electron microscopy (STEM) image of a representative o-Au NC colloidal sphere assembled at  $R_{[Zn^{2+}]/[-SG]} = 0.6$ . (b-c) EDX elemental maps of the circular region in (a) in terms of Au (b), and Zn (c). The insets of (b) and (c) show respectively the Au and Zn signals in the EDX line scan across the yellow line in (a).

The structure and composition of fractal-like NC assemblies assimilated by  $Zn^{2+}$  were also examined by HR-TEM. The HR-TEM images of assemblies formed at  $R_{[Zn^{2+}]/[-SG]}$  of 0.6 and 0.9 are shown as insets in Figure 4.1c and d respectively, where NCs smaller than 2 nm are clearly visible within the assembly. UV-vis spectroscopy also provided supporting evidence for the assimilation of primary NCs (Figure 4.3). The characteristic absorption peak of isolated (primary) o-Au NCs at  $\sim 400$  nm was mostly retained in the UV-vis spectra of the NC assemblies. The surface plasmon resonance (SPR) of large spherical Au NPs, which absorbs at  $\sim 520$  nm (for  $\sim 50$  nm Au NPs)<sup>92</sup> was conspicuously absent, suggesting that the size and structure of the o-Au NC building blocks were preserved in the assemblies. No increase in the size of the NC building blocks was detected in the assemblies, confirming that the ion-induced NC self-assembly is a soft approach. The relatively weak electrostatic interaction between the NCs and the counter ions was unable to alter the size and structure of the NC building blocks. The chemical composition of the NC assemblies was analyzed by energy dispersion X-ray spectroscopy (EDX). Line scan analysis across the diameter of a representative assembly (Figure 4.4a) and the elemental maps of the latter confirm

the uniform distribution of Au (Figure 4.4b) and Zn (Figure 4.4c) throughout the colloidal sphere, suggesting that the spherical assembly was formed by the assimilation of o-Au NCs by  $\text{Zn}^{2+}$  ions.

### 4.3.2 Ion-Like Self-Assembly Behavior of o-Au NCs

The self-assembly of negatively charged o-Au NCs (supramolecular ions) exhibited an intriguing ion-like behavior, where a step-wise dependence on the concentration of counter cations ( $\text{Zn}^{2+}$ ) was observed, as shown in the insets of Figure 4.1e and Figure 4.3. The negatively charged NCs were initially inert to the addition of a small amount of  $\text{Zn}^{2+}$  up to a threshold value of  $R_{[\text{Zn}^{2+}]/[\text{-SG}]}$  ( $\sim 0.3$ ). Increase in the  $R_{[\text{Zn}^{2+}]/[\text{-SG}]}$  value beyond this threshold value (e.g.,  $0.3 < R_{[\text{Zn}^{2+}]/[\text{-SG}]} < 0.6$ ) triggered the formation of spherical NC assemblies, similar to the formation of precipitates beyond the solubility limit defined by the solubility product  $K_{\text{sp}}$ . In precipitation, taking  $\text{A}^+ + \text{B}^- = \text{AB}\downarrow$  as an example, the ionic product  $Q = [\text{A}^+][\text{B}^-]$  is always a constant ( $K_{\text{sp}}$ ) in a solution saturated with the precipitate AB. Similarly, a constant  $Q$  value ( $= [\text{COO}^-]^2[\text{Zn}^{2+}]$  considering the formation of  $-\text{COO}^- \cdots \text{Zn}^{2+} \cdots \text{OOC}-$  ion pairs) was also observed in the “saturated solutions” of negatively charged NCs and counter cations ( $\text{Zn}^{2+}$ ). The  $Q$  values (determined by ICP-MS) obtained in  $R_{[\text{Zn}^{2+}]/[\text{-SG}]}$  of 0.6 and 0.9 were  $3.31 \times 10^{-11}$  and  $3.35 \times 10^{-11} \text{ M}^3$  respectively. The  $K_{\text{sp}}$  was therefore estimated to be  $3.33 \times 10^{-11} \text{ M}^3$ . The high ligand-to-metal ratio (the SG-to-Au ratio is  $\sim 0.84$ ), the high symmetry of *pseudo*-spherical geometry and the uniform size of the o-Au NCs are key contributors to their ion-like properties (step-like assembly). The possession of ion-like structural features in the o-Au NCs not only made it possible for the step-like assembly, but also produced an ordered structure mimicking the formation of ionic crystalline compounds. In nature oppositely charged ions are often packaged into crystalline ionic compounds

with long-range order. Similarly, the NC assemblies here adopted a fractal-like spherical geometry (Figure 4.1c and d). It should be reiterated that such fractal-like assembly was different from the counter-ion-induced assembly of large NPs (> 3 nm) where the aggregates display only a low symmetry.<sup>179-180</sup> However, it should be noted that the spherical NC assemblies did not exhibit long-range crystalline order. This could be attributed to the relatively large difference in size between the negatively charged NCs and the counter cations ( $\text{Zn}^{2+}$ ). Due to the relatively large diameter (~1.5 nm), surface charge was localized at the surface carboxylate groups of o-Au NCs, rather than delocalized over the whole cluster; a behavior substantially different from common anions. The uneven distribution of surface charge due to the largeness of o-Au NCs could be the major factor for the deviation from the assembly habit of common ions (*e.g.*, the lack of a long-range structural order).

### 4.3.3 Origin of Ion-Like Assembly Behavior of o-Au NCs

#### 4.3.3.1 Bridging Effect of $\text{Zn}^{2+}$ Dictated Self-Assembly

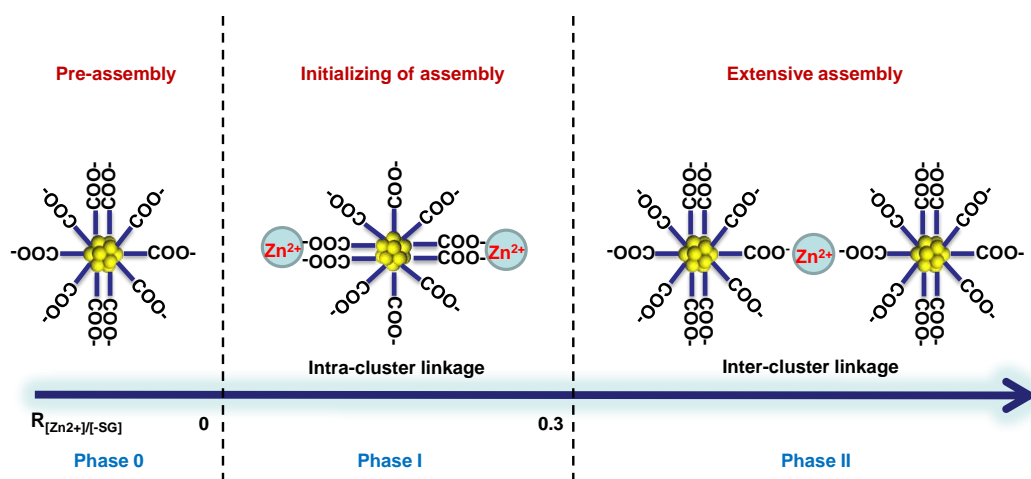


**Figure 4.5** Proposed mechanism for  $\text{Zn}^{2+}$ -induced assembly of o-Au NCs

The counter cations  $\text{Zn}^{2+}$  exerted their influence on the self-assembly of negatively-charged o-Au NCs through principally two effects. The first was the screening effect where  $\text{Zn}^{2+}$  reduced the negative charge on the o-Au NC surface through the formation of *intra*-cluster  $-\text{COO}^- \cdots \text{Zn}^{2+} \cdots \text{OOC}-$  electrostatic linkage (referred to henceforth as *intra*-EL). The second was the bridging effect forming *inter*-cluster  $-\text{COO}^- \cdots \text{Zn}^{2+} \cdots \text{OOC}-$  electrostatic linkages (*inter*-EL). The bridging effect brought two separate NCs together while *intra*-EL did not bring about NC self-assembly *per se*. These two effects are illustrated schematically in Figure 4.5.

At low  $R_{[\text{Zn}^{2+}]/[\text{-SG}]}$  ( $\sim 0.3$ ), the amount of  $\text{Zn}^{2+}$  in the NC solution was small and  $\text{Zn}^{2+}$  tended to bind to anionic carboxylate group on the same NC, thus leading to the formation of *intra*-ELs. This was the phase I stage in the self-assembly of NCs. Charge screening effect was dominant in this stage, as evidenced by the rapid increase in the  $\zeta$ -potential of the NCs with the increase in the  $\text{Zn}^{2+}$  concentration ( $R_{[\text{Zn}^{2+}]/[\text{-SG}]}$  from 0 to 0.3, Figure 4.6). The formation of *intra*-ELs gradually approached saturation with the continuing increase in  $\text{Zn}^{2+}$  concentration. At the threshold value of  $R_{[\text{Zn}^{2+}]/[\text{-SG}]}$  (determined to be  $\sim 0.3$  in this study), *inter*-ELs began to form resulting in the formation of small and irregularly-shaped NC assemblies due to partial bridging effect (Figure 4.1b). Further increase in the  $\text{Zn}^{2+}$  concentration increased the extent of *inter*-ELs (ionic cross-linking) until the step-like assembly of the o-Au NCs occurred, the inception of which is identified as phase II in Figure 4.5. For example, at  $R_{[\text{Zn}^{2+}]/[\text{-SG}]} = 0.6$ , the o-Au NCs were extensively assimilated into colloidal spheres (Figure 4.1c). However, the  $\zeta$ -potential of the NCs (Figure 4.6) was nearly unchanged when  $R_{[\text{Zn}^{2+}]/[\text{-SG}]}$  was increased from 0.3 to 0.6. This observation suggests that in the concentration range of  $0.3 < R_{[\text{Zn}^{2+}]/[\text{-SG}]} < 0.6$ , the charge screening of  $\text{Zn}^{2+}$  was nearly constant and the bridging effect of  $\text{Zn}^{2+}$  was more important than the screening effect. A further

increase in the  $\text{Zn}^{2+}$  concentration from  $R_{[\text{Zn}^{2+}]/[-\text{SG}]} = 0.6$  to 0.9 led to the gradual depletion of o-Au NCs in the solution, and the completion of the NC assembly process. The gradual depletion of NCs was accompanied by the accumulation of excess  $\text{Zn}^{2+}$  through adsorption on the surface of NC assemblies, which resulted in a second series of  $\zeta$ -potential increase of the NC solution (Figure 4.6).

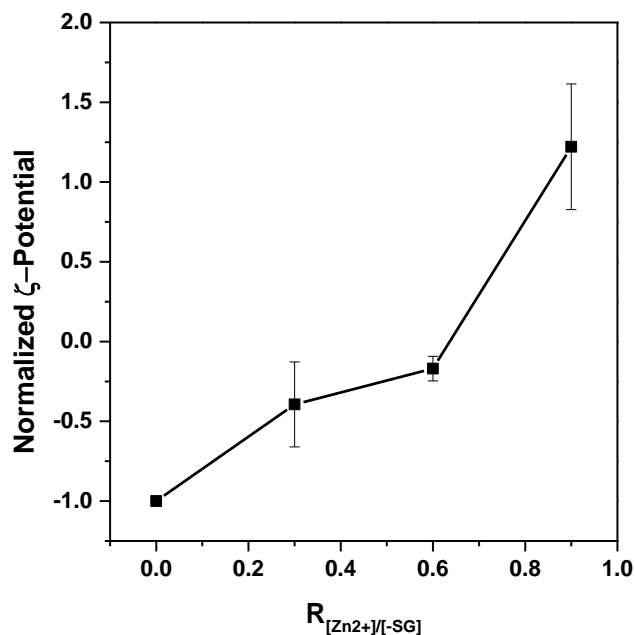


**Figure 4.6**  $\zeta$ -potential of o-Au NCs assembled under different  $R_{[\text{Zn}^{2+}]/[-\text{SG}]}$  values. The  $\zeta$ -potential at  $R_{[\text{Zn}^{2+}]/[-\text{SG}]} = 0$  was arbitrarily set at -1 for ease of comparison.

#### 4.3.3.2 Ionic Strength Dependence of Self-Assembly

Several independent measurements also suggest the bridging effect of divalent  $\text{Zn}^{2+}$  ions as the primary factor in the self-assembly of o-Au NCs. First, common monovalent cations such as  $\text{Na}^+$  ions (from dissolved NaCl), which could also screen the surface charge of o-Au NCs, were unable to cause a similar assembly of the o-Au NCs. o-Au NCs remained separate in 0.6 mM NaCl solution (same ionic strength as the 0.2 mM  $\text{ZnCl}_2$  used to provide  $R_{[\text{Zn}^{2+}]/[-\text{SG}]} = 0.6$ , please refer to the section §4.2.4.2

for the details of the ionic strength calculation). The HD measurement in Figure 4.7 (second column) indicated likewise. A further increase in the ionic strength of the NaCl solution (*e.g.*, by increasing the NaCl concentration to 0.5 M) also did not help to bring about the assembly of o-Au NCs (Figure 4.7, third column). Hence the screening effect of cations on the surface charge of the NCs is not critical to the self-assembly of NCs. The increase in the solution ionic strength could however disrupt the electrostatic interaction between  $\text{Zn}^{2+}$  and anionic carboxylate groups. The presence of NaCl in large excess in the o-Au NC solution ( $\sim 0.5$  M in the final reaction mixture) prior to  $\text{ZnCl}_2$  addition could suppress the assembly to a great extent. The HD of the NCs in the presence of both  $\text{Na}^+$  and  $\text{Zn}^{2+}$  was also the same as that of discrete NCs, thereby suggesting no significant assembly of the o-Au NCs (Figure 4.7, fifth column).

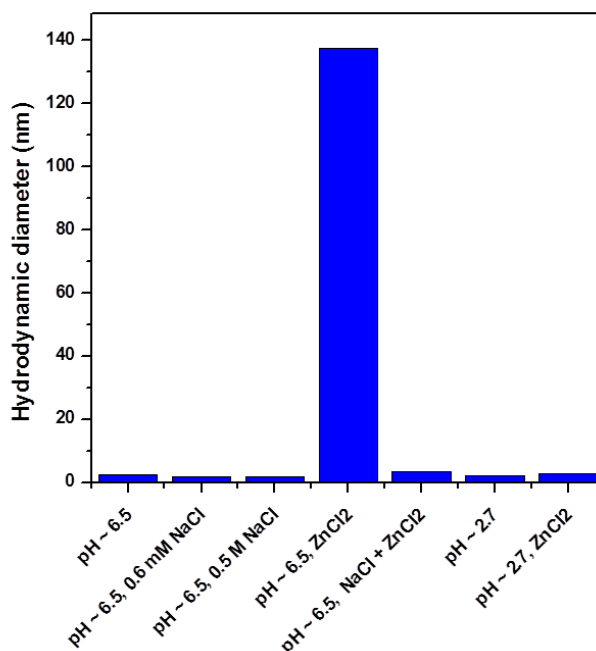


**Figure 4.7** Measured hydrodynamic diameters of assembled/disassembled o-Au NCs at different pH and in the presence of different ions. The assembly with  $\text{Zn}^{2+}$  was carried out at  $R_{[\text{Zn}^{2+}]/[\text{1-SG}]} = 0.6$ .

### 4.3.3.3 pH Dependence of Self-Assembly

Excess  $H^+$  had the same effect as  $Na^+$  in disrupting the self-assembly of NCs by  $Zn^{2+}$ . For example, by adjusting the pH of the NC solution to  $\sim 2.7$  (a value lower than the isoelectric point of o-Au NCs, Figure 4.2), the self-assembly of o-Au NCs was significantly inhibited, as shown by the nearly invariant HD of the NCs in the presence and absence of  $Zn^{2+}$  at pH  $\sim 2.7$  (Figure 4.7, the last two columns). More interestingly, the assembly and disassembly of the o-Au NCs could be reversed by cycling the pH of the solution between 6.5 and 2.7. The zigzag changes in the HD of the o-Au NCs under pH cycling (Figure 4.8a) indicate that the o-Au NCs could undergo repeated assembly and disassembly at pH 6.5 and 2.7 respectively.

There was irreversibility shown, however, as the HD of the o-Au NCs at pH 6.5 gradually decreased with the increase in the cycle number. This trend could be attributed to the slow accumulation of ionic strength due to the way pH cycling was implemented: The pH of the solution was adjusted by the addition of a given amount of 0.1 M HCl or 0.1 M NaOH, leading to the gradual buildup of ionic strength with the increase in the cycle number. A higher ionic strength of the solution increased the screening effect on the electrostatic interactions between  $Zn^{2+}$  and negatively-charged NCs, thus leading to a smaller degree of assembly (decreasing size of the NC assemblies). The ionic-strength-induced irreversibility could be eliminated by removing the excess small ions. We "refreshed" the o-Au NC solution at the lower pH of cycle 3 (corresponding to point 7 in Figure 4.8a) by dialysis, where a semipermeable membrane with a MWCO of 3500 Da was used to filter away the small ions (*e.g.*,  $H^+$ ,  $Na^+$ ,  $Zn^{2+}$  and  $Cl^-$ ). After pH adjustment to 6.5 and  $Zn^{2+}$  addition, a HD of 124.4 nm (the red dot in Figure 4.8a) could be obtained from the "refreshed" o-Au NC solution, similar to the HD assembled at pH = 6.5 in cycle 1 from a fresh o-Au NC



solution (137.6 nm, point 1 in Figure 4.8a). This observation led us to conclude that the reversibility of assembly and disassembly could be greatly improved through the control of the ionic strength.

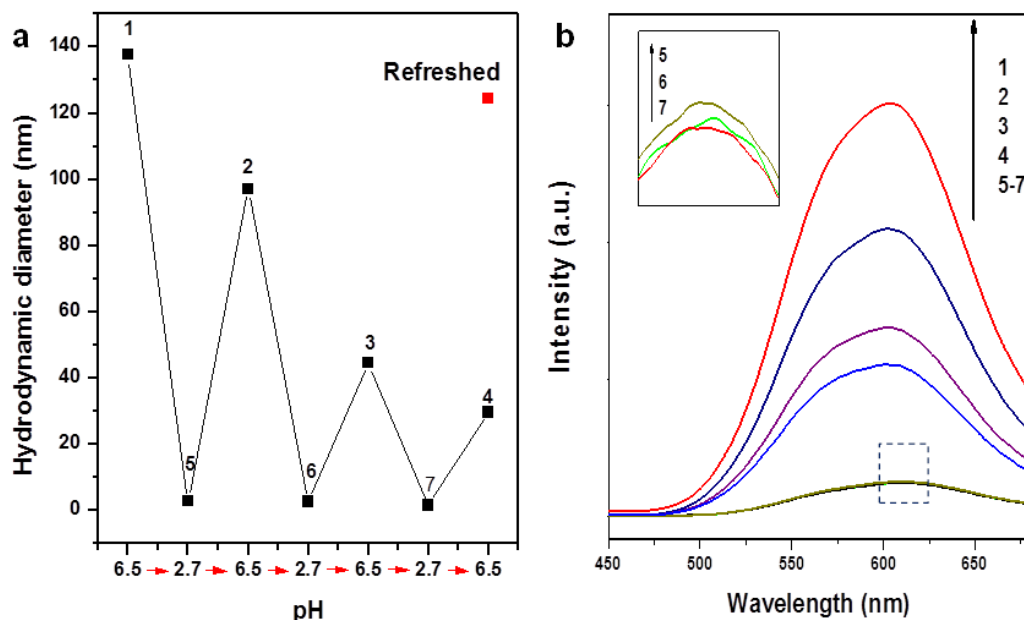


**Figure 4.8** Effects of pH cycling on the hydrodynamic diameters (a) and photoemission spectra (b, excited at 365 nm) of o-Au NCs assembled by  $\text{Zn}^{2+}$ . The o-Au NCs were initially assembled at pH ~6.5 (#1), and then pH was varied in the sequence of ~2.7 (#5) -- 6.5 (#2) -- 2.7 (#6) -- 6.5 (#3) -- 2.7 (#7) -- 6.5 (#4). In a separate experiment, solution #7 was dialyzed overnight followed by reassembly with  $\text{Zn}^{2+}$  at pH 6.5. The hydrodynamic diameter of the reassembled “refreshed” o-Au NCs was recorded as the red dot in (a). The inset of (b) shows the expanded view of the circled area. All self-assemblies were carried out at  $R_{[\text{Zn}^{2+}]/[\text{I-SG}]} = 0.6$ .

#### 4.3.4 Self-Assembly Induced Photoluminescent Enhancement

The physical and chemical properties of the Au NCs could be altered by proximity effects in an ionically cross-linked close-packed structure. One most interesting property of the Au NCs is their strong optical luminescence, as shown in Figure 4.9 (black line). The as-synthesized o-Au NCs had a unique Au(0)@Au(I)-thiolate core-

shell structure, where the *intra*-cluster aurophilic interaction (Au(I)-Au(I)) contributed to the PL of the NCs.<sup>11,181-182</sup> The distance between the o-Au NCs could be significantly shortened after self-assembly to promote *inter*-cluster aurophilic interaction. The increase in *inter*-cluster aurophilic interaction could increase the PL of the NCs. The assembly of o-Au NCs could also reduce non-irradiative relaxation of excited electrons, which also enhances the PL of the NCs.<sup>183-184</sup> For example, the bridging  $Zn^{2+}$  between neighboring anionic carboxylate groups (via either an *intra*- or *inter*-EL) could inhibit the vibration or rotation of the thiolate ligands, which is one of the non-irradiative relaxation pathways.<sup>8</sup> Experimentally the PL (at 610 nm) of the NC assemblies (Figure 4.9) was significantly higher than that of discrete o-Au NCs. In order to rule out the possibility of PL enhancement through the formation of  $Zn^{2+}$ -thiolate (SG) complexes, a control experiment was carried out by mixing  $Zn^{2+}$  and GSH in water. The resultant Zn-SG complexes did not exhibit any luminescence (data not shown). Two other experimental observations also provided supporting evidence on proximity-induced properties in the NC assemblies. First, as shown in the inset of Figure 4.9b, the PL enhancement effect also displayed a similar step-like trend with the increase of the  $Zn^{2+}$  concentration, which corresponds well with the step-like assembly of the o-Au NCs. Second, the PL enhancement could also be turned on or off corresponding to the assembly or disassembly of o-Au NCs in pH cycling (Figure 4.8b).

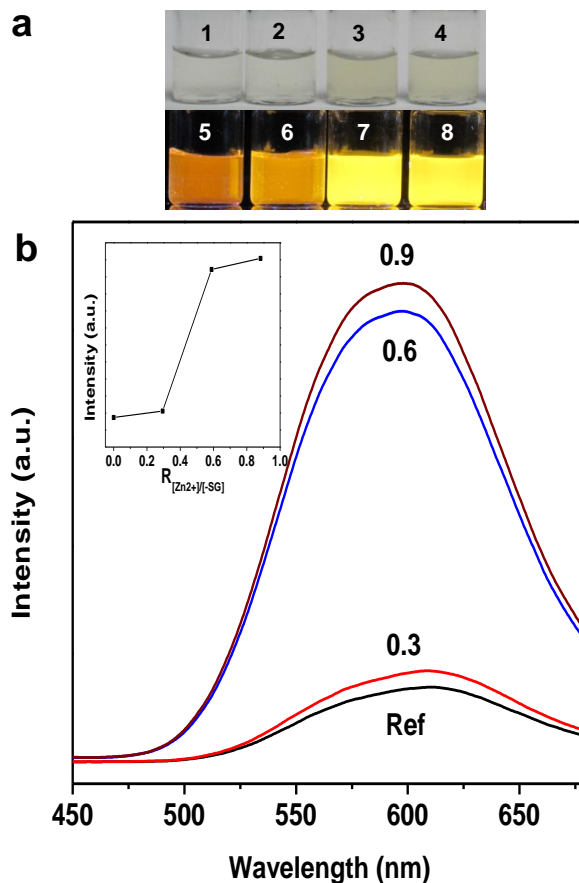


**Figure 4.9** (a) Digital photos of o-Au NCs assembled at various  $R_{[Zn^{2+}]/[L-SG]}$  values: 0 (#1 and #5), 0.3 (#2 and #6), 0.6 (#3 and #7), and 0.9 (#4 and #8); #1~4 were taken under normal light while #5~8 were taken under UV illumination (365 nm); (b) Photoemission spectra (exited at 365 nm) of o-Au NCs assembled under different  $R_{[Zn^{2+}]/[L-SG]}$  values: 0 (black), 0.3 (red), 0.6 (blue), and 0.9 (purple); the inset shows the emission intensity maximum as a function of  $R_{[Zn^{2+}]/[L-SG]}$ .

#### 4.3.5 Versatility of Ion-Induced Self-Assembly Approach

Since the self-assembly process only depends on the electrostatic interaction between bivalent cation and negatively charged NC surface, the ion-induced assembly of NCs developed in this study is expected to be generic, and hence should be applicable to other charged  $M_n(SR)_m$  NCs and divalent counter ions. For example, other divalent cations, such as  $Cd^{2+}$ , may be used to substitute for  $Zn^{2+}$ . Similar

spherical NC assemblies were indeed obtained by using  $\text{Cd}^{2+}$  as the counter cations (inset of Figure 4.10a). Similarly, the PL intensity of the NCs assimilated by  $\text{Cd}^{2+}$  was also significantly higher than that of discrete o-Au NCs (Figure 4.10a). The ion-induced assembly of NCs could also be extended to SG-protected Au NCs in other sizes; *e.g.*,  $\text{Au}_{15}(\text{SG})_{13}$  NCs which exhibited weak red-emission.<sup>175</sup> As shown in the inset of Figure 4.10b, the addition of  $\text{Zn}^{2+}$  to the  $\text{Au}_{15}(\text{SG})_{13}$  NC solution also assembled  $\text{Au}_{15}(\text{SG})_{13}$  NCs into spherical NC assemblies. Enhanced PL in the visible light range was also detected for the  $\text{Au}_{15}(\text{SG})_{13}$  NC assemblies (Figure 4.10b). In addition to NC size, the ion-induced assembly approach is also tolerant to the change in the chemical composition of the NC core. A red-emitting Ag NC, whose formula was characterized as  $\text{Ag}_{16}(\text{SG})_9$  in the original work,<sup>98</sup> could also be assembled into colloidal spheres via the bridging effect of  $\text{Zn}^{2+}$  (inset of Figure 4.10c). The assembly in this case again resulted in a significant enhancement of the PL of  $\text{Ag}_{16}(\text{SG})_9$  NCs (Figure 4.10c).

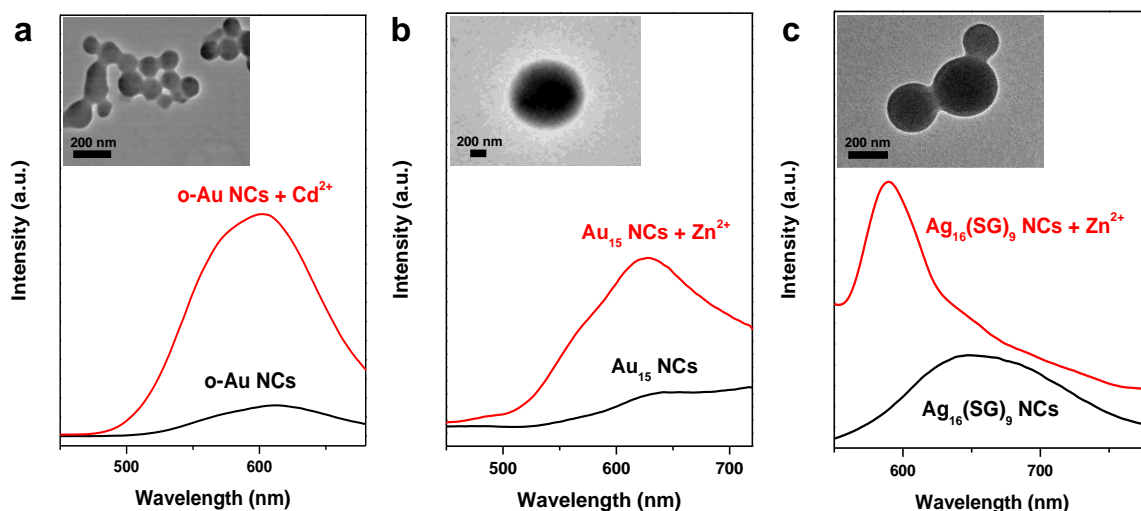


**Figure 4.10** Emission spectra of o-Au NC (a, after excitation at 365 nm),  $\text{Au}_{15}(\text{SG})_{13}$  NC (b, after excitation at 370 nm) and  $\text{Ag}_{16}(\text{SG})_9$  NC (c, after excitation at 440 nm) before (black line) and after (red lines) self-assembly in presence of divalent cations ( $\text{Cd}^{2+}$  for (a) and  $\text{Zn}^{2+}$  for (b) and (c)). Corresponding TEM images of assembled NCs are shown in the insets.

## 4.4 Conclusion

In summary, we have developed a facile and general ionic mimetic method to assemble charged  $M_n(SR)_m$  NCs in water based on the electrostatic interaction between oppositely-charged entities. Negatively-charged o-Au NCs were assembled into monodisperse and spherical assemblies by divalent counter cations such as  $Zn^{2+}$  and  $Cd^{2+}$ , via the formation of *inter*-cluster electrostatic linkages (*inter*-EL) of the type  $-COO^- \cdots M^{2+} \cdots ^-OOC-$ . Owing to their high charge density, uniformity of size, and *pseudo*-spherical geometry, the o-Au NCs may be regarded as an ion-mimic nanomaterials (supramolecular ions), exhibiting ion-like properties of step-like assembly dictated by  $K_{sp}$  and a high structural order in the assembly. The bridging effect of the divalent cations is essential to the formation of NC assemblies. A strong synergy between the NCs due to the close-packed order in the assembly resulting in the PL enhancement of NCs was also demonstrated in this study. The NC assemblies and the self-assembly methods in this study are of interest not only because they provide a simple and general method to generate a suprastructure of functional  $M_n(SR)_m$  NCs, which is of interest to both basic and applied research; but also because they exemplify a NC surface with charged hydrophilic ligands as three-dimensional supramolecular ions, with the potential to mimic some of the useful behavior of real ions in various practical settings. However, long-range crystalline order was absent in these NC assemblies formed by the electrostatic interaction between negatively charged NCs and small divalent cations. Further work is still needed to improve the symmetry order in the NC assembly, and Chapter 5 will demonstrate the use of amphiphilicity to accomplish that.

---

# CHAPTER 5 INTRODUCING AMPHIPHILICITY TO NOBLE METAL NANOCLUSTERS VIA PHASE-TRANSFER DRIVEN ION-PAIRING REACTION: SYNTHESIS AND SELF-ASSEMBLY OF AMPHIPHILIC NOBLE METAL NANOCLUSTERS

## 5.1 Introduction

Thiolate-protected noble metal (*e.g.*, Au or Ag) nanoclusters (NM-NCs) or  $M_n(SR)_m$  exhibit strong size-dependent properties (*e.g.*, HOMO-LUMO transition, intense photoluminescence, and high catalytic activity).<sup>8,10-12,16-17,25,67,97,185</sup> Surface engineering is yet another approach to vary their properties. For example, the electronic and optical properties of NCs are modifiable by tailoring the ligand environment; and the decisive role of NC surface on the recognition chemistry of NCs is well-known.<sup>10-12,35-36,43-44,111,170,186-187</sup> Amphiphilicity is a desirable NC surface property, but it has yet to be explored to date. This is because an amphiphilic surface can impart to NCs good solubility in a wide range of solvents with markedly different polarities, thereby extending their usability in both basic and applied research.<sup>188-190</sup> It may also introduce molecular-amphiphile-like self-assembly properties (formation of

spherical, cylindrical or disk-shaped micelles,<sup>191-198</sup> vesicles<sup>199-201</sup> and bilayers<sup>202</sup>) for packing the NCs into higher hierarchy structures with the desired geometry, symmetry and structural order for NC structural determination and property tuning.<sup>24-28,33,203-204</sup> Amphiphilic NCs, as supramolecular amphiphiles, make it easier to study the difference between discrete and assembled NCs.

In principle, a good NC amphiphile (or amphiphilic NC) should possess a comparable number of hydrophilic and hydrophobic moieties on its surface.<sup>188,198,205</sup> Such amphiphilic NCs can be formed by two methods: 1) ligand-exchange reaction,<sup>36,43,79,130,206-207</sup> and 2) partial modification of a uniform surface.<sup>208</sup> However, in the first approach where the creation of amphiphilicity relies on the exchange reaction between ligands with very different polarities, the perturbation of the metal core is often observed resulting in random changes to the NC optical and catalytic properties.<sup>79,101,130</sup> Thus, the alternative of a “soft” surface modification without perturbation of the metal core is the center of attention here. Partial patching of hydrophilic NCs with hydrophobic moieties is an appealing approach since hydrophilic NCs often contain functionalities (*e.g.*, carboxyl (-COOH) and sulfonic (-SO<sub>3</sub>H) groups),<sup>9,97,175,187</sup> which are useful for the surface modification reactions. Hydrophobic NCs, quite on the contrary, lack such functionalities. In addition, since most of these hydrophilic functionalities can readily deprotonate at neutral pH or above and thus acquire negative charges, electrostatic interaction can be a means to drive the surface modification of hydrophilic NCs.<sup>10-11,165,204</sup>

Herein, we demonstrate the preparation of amphiphilic NCs by coating hydrophilic NCs with hydrophobic cations to about half of a monolayer coverage. This was made possible by the phase-transfer (PT) driven ion-pairing reaction between hydrophobic cations (*e.g.*, cetyltrimethylammonium, CTA<sup>+</sup>) and anionic surface functionalities of

hydrophilic NCs (*e.g.*, carboxylate,  $-\text{COO}^-$ ). A *moderately-polar* organic medium was used to selectively extract similarly *moderately-polar* hydrophilic NCs coated with about half a monolayer of hydrophobic cations (*i.e.*, amphiphilic NCs) from the aqueous phase, driving the ion-pairing reaction in the aqueous phase to continuously regenerate these amphiphilic NCs. The amphiphilic NCs produced as such were readily soluble in many organic media covering a wide range of relative dielectric constants ( $\epsilon_r = 4.15\text{-}42.5$ ). More interestingly, the amphiphilic NCs (or supramolecular amphiphiles) could be self-assembled into bilayer-based structures at the liquid-air interface, similar to the formation of the lamellar liquid crystal phase<sup>209-210</sup> of molecular amphiphiles.

## 5.2 Experimental Section

### 5.2.1 Materials

Hydrogen tetrachloroaurate(III) trihydrate ( $\text{HAuCl}_4 \cdot 3\text{H}_2\text{O}$ ), 6-mercaptopentanoic acid (MPA), cetyltrimethylammonium bromide (CTAB) and sodium borohydride ( $\text{NaBH}_4$ ) from Sigma Aldrich; acetone, acetonitrile, dichloromethane ( $\text{CH}_2\text{Cl}_2$ ), and sodium hydroxide ( $\text{NaOH}$ ) from Merck; ethanol ( $\text{EtOH}$ ) and hexane from Fisher; methanol ( $\text{MeOH}$ ) from J. T. Baker and dimethylsulfoxide (DMSO) from Tedia were all used as received. All aqueous solutions were prepared in Ultrapure Milipore water (18.2 M $\Omega$ ). All glassware was washed with *aqua regia* and rinsed with ethanol and ultrapure water before use.



## 5.2.2 Synthesis of Au<sub>25</sub>(MHA)<sub>18</sub> NCs

The synthesis of Au<sub>25</sub>(MHA)<sub>18</sub> followed a reported procedure with several minor modifications.<sup>186</sup> Briefly, 29.7 µg MHA and 5 mL 20 mM HAuCl<sub>4</sub> aqueous solution were mixed in 100 mL ultrapure water to form yellowish Au(I)-MHA complexes. 4 mL 1 M NaOH aqueous solution was then added to bring the pH of the solution to ~10, followed by the drop-wise addition of 2 mL 112 mM NaBH<sub>4</sub> in 0.2 M NaOH aqueous solution. After vigorously stirring (at 1,000 rpm) for 3 h, a brownish aqueous solution of Au<sub>25</sub>(MHA)<sub>18</sub> NCs was collected as the raw product.

## 5.2.3 Synthesis of CTA<sup>+</sup> Coated Au<sub>25</sub>(MHA)<sub>18</sub> NCs (Au<sub>25</sub>(MHA)<sub>18</sub>@xCTA NCs)

### 5.2.3.1 Synthesis of Phase-Transferred Au<sub>25</sub>(MHA)<sub>18</sub>@xCTA NCs

The raw product (Au<sub>25</sub>(MHA)<sub>18</sub> NCs) were used for surface modification without further purification. 80 mL of the Au<sub>25</sub>(MHA)<sub>18</sub> NC aqueous solution was mixed with 80 mL 100 mM CTAB solution in ethanol under vigorous stirring (1,000 rpm), followed by the addition of 80 mL toluene. The mixture was stirred for another 5 min, and then kept still for 10 min to allow phase-transfer to complete. At the end of this procedure, phase-transferred Au<sub>25</sub>(MHA)<sub>18</sub>@xCTA NC raw product could be collected from the organic phase.

Raw phase-transferred Au<sub>25</sub>(MHA)<sub>18</sub>@xCTA NCs were precipitated by centrifugation (8,000 rpm, 5 min) after mixing with 2 equivalent volumes of hexane (*i.e.*, 200 mL hexane for every 100 mL of NC solution). The precipitate was recovered and washed by acetone-dichloromethane-dichloromethane-acetone (in that sequence) to remove residual CTAB and other impurities. The cleaned phase-transferred Au<sub>25</sub>(MHA)<sub>18</sub>@xCTA NCs were then dissolved in 2 mL ethanol and kept for further

use. ESI-MS analysis suggests  $x = 6-9$  in the cleaned phase-transferred  $\text{Au}_{25}(\text{MHA})_{18}@x\text{CTA}$  NCs (see §5.3.1 for details on ESI-MS analysis).

### 5.2.3.2 Synthesis of Intermediate-Phase-Transferred and Non-Phase-Transferred $\text{Au}_{25}(\text{MHA})_{18}@x\text{CTA}$ NCs

The intermediate-phase-transferred and non-phase-transferred  $\text{Au}_{25}(\text{MHA})_{18}@x\text{CTA}$  NCs were similarly prepared; but with some revision of the amount of ethanol used in the synthesis. In the preparation of intermediate-phase-transferred  $\text{Au}_{25}(\text{MHA})_{18}@x\text{CTA}$  NCs, 80 mL of  $\text{Au}_{25}(\text{MHA})_{18}$  NC aqueous solution was added with 40 mL of 200 mM CTAB ethanol solution (instead of 80 mL 100 mM CTAB ethanol solution). In the preparation of non-phase-transferred  $\text{Au}_{25}(\text{MHA})_{18}@x\text{CTA}$  NCs, 80 mL of  $\text{Au}_{25}(\text{MHA})_{18}$  NC aqueous solution was added in an amount equal to that of solid CTAB (8 mmol). The raw products of intermediate-phase-transferred and non-phase-transferred  $\text{Au}_{25}(\text{MHA})_{18}@x\text{CTA}$  NCs were collected at the aqueous-organic interface and from the aqueous phase, respectively.

### 5.2.4 Self-Assembly of $\text{Au}_{25}(\text{MHA})_{18}@x\text{CTA}$ NCs ( $x = 6-9$ )

The phase-transferred  $\text{Au}_{25}(\text{MHA})_{18}@x\text{CTA}$  NCs ( $x = 6-9$ ) after cleaning were dissolved in a DMSO/ethanol mixture (50/50 v/v) to a final NC concentration ([NC]) of 0.53 mM. The solvent was then evaporated at the ambient condition (298 K and 1 atm). The self-assembly was allowed to progress for 3 d. A brownish-black film was collected at the air-liquid interface as the self-assembly product.

### 5.2.5 Characterization

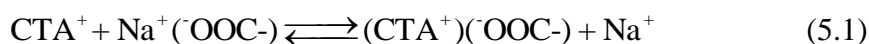
UV-vis absorption spectra were recorded by a Shimadzu UV-1800 spectrometer. The molecular formulas of  $\text{Au}_{25}$  NCs were deduced by ESI-MS on a Bruker

microTOF-Q system operating in negative-ion mode. The ESI-MS samples of  $\text{Au}_{25}(\text{MHA})_{18}$  NCs and non-phase-transferred  $\text{Au}_{25}(\text{MHA})_{18}@x\text{CTA}$  NCs were prepared in ultrapure water, while those of intermediate-phase-transferred and phase-transferred  $\text{Au}_{25}(\text{MHA})_{18}@x\text{CTA}$  were prepared in an acetonitrile/methanol mixture (75/25 v/v). The XRD patterns of assembled  $\text{Au}_{25}(\text{MHA})_{18}@x\text{CTA}$  NCs ( $x = 6-9$ ) were recorded by a Bruker D8 advance X-ray diffractometer using a  $\text{Cu K}_\alpha$  source ( $\lambda = 1.5405 \text{ \AA}$ ). TEM and field emission scanning electron microscopy (FESEM) were performed on a JEOL JEM 2010 microscope operating at 200 kV, and a JEOL JSM-6700F microscope operating at 5 kV respectively. TEM and FESEM samples of the solution product were typically prepared by dispensing a drop of the solution onto a copper grid, following by overnight drying at the ambient condition (298 K and 1 atm). The FESEM sample of the assembled film was prepared by slicing a piece of film from the air-liquid, followed by drying in a Binder VD-23 vacuum oven (333 K and ~20 mbar) overnight.

### 5.3 Results and Discussion

#### 5.3.1 Synthesis of Amphiphilic $\text{Au}_{25}(\text{MHA})_{18}@x\text{CTA}$ NCs ( $x = 6-9$ )

$\text{Au}_{25}(\text{MHA})_{18}$  NCs where MHA is 6-mercaptohexanoic acid, and  $\text{CTA}^+$ , were the model hydrophilic NCs and hydrophobic cations used in this study respectively. The binding of  $\text{CTA}^+$  to the surface of  $\text{Au}_{25}(\text{MHA})_{18}$  NCs was likely to occur via the following ion-pairing reaction:<sup>10,165</sup>



where  $\text{-COO}^-$  was derived from the deprotonation of the  $\text{-COOH}$  group (one  $\text{-COOH}$  group per MHA molecule) and  $\text{Na}^+$  from the ionization of  $\text{NaOH}$  (pH adjuster) in

water. In view of the dynamics of reversible reactions of which the above ion-pairing reaction in aqueous phase is one, the  $\text{CTA}^+$  bound  $\text{Au}_{25}(\text{MHA})_{18}$  NCs (hereafter referred as  $\text{Au}_{25}(\text{MHA})_{18}@x\text{CTA}$  where  $x$  is the number of  $\text{CTA}^+$  per NC) should initially contain a variable number of  $x$  values. It is plausible to expect that  $\text{Au}_{25}(\text{MHA})_{18}@x\text{CTA}$  NCs with  $x$  exceeding certain threshold values were sufficiently hydrophobic to be transferred selectively from the aqueous phase to the organic phase; and the ion-pairing reaction would reform the transferred species in the aqueous phase in an attempt to reestablish equilibrium. We term such regenerative mechanism as “PT driven ion-pairing”. Since the PT was driven by the mutual affinity of  $\text{Au}_{25}(\text{MHA})_{18}@x\text{CTA}$  NCs and the organic medium, it would be most effective when there was a match of polarities of the NCs and the medium. We therefore posit that a deliberate control of the organic medium polarity should allow us to selectively extract  $\text{Au}_{25}(\text{MHA})_{18}@x\text{CTA}$  NCs with the desired polarity or designed  $x$  values from the aqueous phase. In particular,  $\text{Au}_{25}(\text{MHA})_{18}@x\text{CTA}$  NCs with good amphiphilicity and moderate polarity imparted by a moderate  $x$  value (*e.g.*,  $x = \sim 9$ ), should be highly extractable by a *moderately-polar* organic medium to support the volume production of NC amphiphiles by the PT driven ion-pairing mechanism. The following is a detailed account of the experimental demonstration of this hypothesis.

The synthesis of  $\text{Au}_{25}(\text{MHA})_{18}$  NCs was based on a previous procedure with some minor changes.<sup>186</sup> The raw  $\text{Au}_{25}(\text{MHA})_{18}$  NC aqueous solution prepared as such was brown in color (inset #1 of Figure 5.1a) and showed the absorption characteristics of pure  $\text{Au}_{25}(\text{SR})_{18}$  NCs at 440 and 672 nm (Figure 5.1a, black line). The well-defined absorption spectrum suggests the high quality of the  $\text{Au}_{25}(\text{MHA})_{18}$  NCs in the raw product.

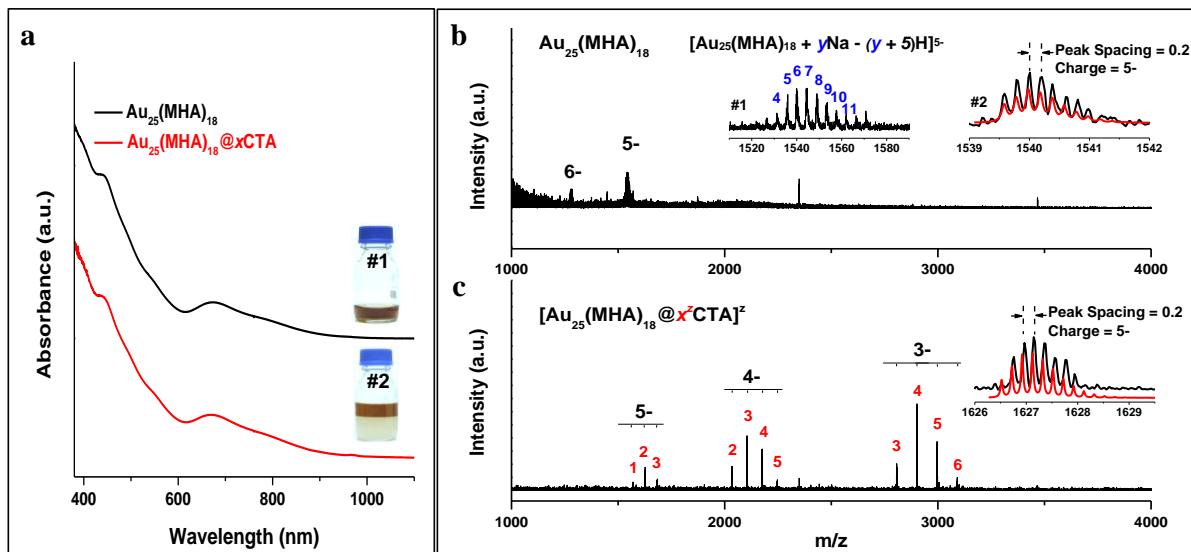


**Figure 5.1** (a) UV-vis absorption spectra of  $\text{Au}_{25}(\text{MHA})_{18}$  (black line) and phase-transferred  $\text{Au}_{25}(\text{MHA})_{18}@x\text{CTA}$  (red line) NCs; the insets in (a) are the digital images of freshly prepared  $\text{Au}_{25}(\text{MHA})_{18}$  NCs in aqueous solution (#1) and phase-transferred  $\text{Au}_{25}(\text{MHA})_{18}@x\text{CTA}$  NCs in the organic phase (#2). (b) Negative-ion mode ESI-MS spectrum of  $\text{Au}_{25}(\text{MHA})_{18}$  NCs; inset #1 in (b) is the zoomed-in spectrum of ionized  $\text{Au}_{25}(\text{MHA})_{18}$  NCs with 5- charge, with the number of coordinated  $\text{Na}^+$  shown above each peak; inset #2 in (b) shows the experimental (black line) and simulated (red line) isotope patterns of  $[\text{Au}_{25}(\text{MHA})_{18} + 6\text{Na} - 11\text{H}]^{5-}$ . (c) Negative-ion mode ESI-MS spectrum of phase-transferred  $\text{Au}_{25}(\text{MHA})_{18}@x\text{CTA}$  NCs, with the value of  $x^z$  (the apparent number of  $\text{CTA}^+$  in each NC with charge  $z$ ) shown in red above each peak; the inset in (c) is the experimental (black line) and simulated (red line) isotope pattern of  $[\text{Au}_{25}(\text{MHA})_{18}@2\text{CTA} - 7\text{H}]^{5-}$ .

The molecular formula of  $\text{Au}_{25}(\text{MHA})_{18}$  NC was determined by ESI-MS analysis operating in the negative-ion mode. In the broad  $m/z$  range of 1000-4000, two sets of intense peaks were found around  $m/z = 1280$  and  $1540$  (Figure 5.1b), which could be assigned to ionized NCs with 6- and 5- charges respectively. The detailed assignment of the ESI-MS spectrum of ionized NCs with 5- charge is given below as an example. The zoomed-in ESI-MS spectrum in the 1510-1590  $m/z$  range (inset #1 in Figure 5.1b) contained a number of peaks with a regular  $m/z$  spacing of 4.4. The isotopic peaks around the most pronounced peak at  $m/z = 1540.01$  (black line in inset #2 in Figure 5.1b) were spaced 0.2  $m/z$  apart, suggesting that the ionized NC species carry a 5- (=

1/0.2) charge. Therefore, the  $m/z = 1540.01$  peak corresponds to a molecular mass of 7700.05 ( $= 1540.01 \times 5$ ) Da, which could be assigned to  $[\text{Au}_{25}(\text{MHA})_{18} + 6\text{Na} - 11\text{H}]^{5-}$ . The simulated isotope pattern of  $[\text{Au}_{25}(\text{MHA})_{18} + 6\text{Na} - 11\text{H}]^{5-}$  (red line in inset #2 in Figure 5.1b) matches well with the experimental measurements (black line in inset of #2 in Figure 5.1b), corroborating the validity of our assignments. The series of peaks in the inset #1 of Figure 5.1b with a  $m/z$  spacing of 4.4 were therefore formed by successive coordination of  $\text{Na}^+$  and dissociation of  $\text{H}^+$  (*i.e.*,  $+ \text{Na} - \text{H}$ , corresponding to a mass change of  $22 = 4.4 \times 5$  Da).

Amphiphilic  $\text{Au}_{25}$  NCs were prepared by the PT driven ion-pairing reaction between  $\text{CTA}^+$  and  $-\text{COO}^-$  on the surface of  $\text{Au}_{25}(\text{MHA})_{18}$  NCs. A *moderately-polar* ethanol/toluene mixture was the organic medium used to selectively extract amphiphilic  $\text{Au}_{25}$  NCs from the aqueous phase. Experimentally, calculated amounts of CTAB and  $\text{Au}_{25}(\text{MHA})_{18}$  NCs (in CTAB : Au mole ratio of 100 : 1) were mixed in a hybrid solvent system consisting of equal volumes of water, ethanol and toluene. The partition of ethanol between water and toluene led to the formation of an organic phase containing ethanol and toluene. The mixture was stirred for 5 min and then kept still for 10 min. The  $\text{Au}_{25}$  NCs could be completely transferred from the aqueous phase to the organic phase (inset #2 in Figure 5.1a), implying that the  $\text{CTA}^+$  ions had successfully bound to the surface of  $\text{Au}_{25}(\text{MHA})_{18}$  NCs. UV-vis spectroscopy was first used to examine the core size of phase-transferred NCs (denoted as PT-NCs). The resulting spectrum, which is shown in Figure 5.1a (red line), is almost identical to the spectrum of the parental  $\text{Au}_{25}(\text{MHA})_{18}$  NCs. This is indication that  $\text{CTA}^+$  binding did not alter the core structure of the parental  $\text{Au}_{25}(\text{MHA})_{18}$  NCs.

ESI-MS (in the negative-ion mode) was then used to examine the extent of  $\text{CTA}^+$  binding on PT-NCs, *i.e.*, the  $x$  value in  $\text{Au}_{25}(\text{MHA})_{18}@x\text{CTA}$  NCs. The ESI-MS

spectrum of PT-NCs in Figure 5.1c shows 3 sets of intense peaks in the broad  $m/z$  range of 1000-4000. They could be assigned to ionized  $\text{Au}_{25}(\text{MHA})_{18}@x\text{CTA}$  NCs with 5- ( $m/z = \sim 1627$ ), 4- ( $m/z = \sim 2105$ ) and 3- ( $m/z = \sim 2902$ ) charges respectively. A representative isotope analysis of  $[\text{Au}_{25}(\text{MHA})_{18}@2\text{CTA} - 7\text{H}]^{5-}$  is appended as the inset in Figure 5.1c. The apparent number of  $\text{CTA}^+$  in each ionized NC species that carried a  $z$  charge (referred as  $x^z$ ) is also labeled in the ESI-MS spectrum (Figure 5.1c) for easy identification. It can be seen that the  $x^{3-}$  species (corresponding to the cluster of peaks at  $m/z = \sim 2902$ ) consisted of a distribution of  $x$  in the range of 3-6 (with a population maximum at 4), while the distributions of  $x^{4-}$  and  $x^{5-}$  contained mostly  $x = 2$ -5 (population maximum at 3) and  $x = 1$ -3 (population maximum at 2) respectively. Despite the variations in peak intensity, the outlines enveloping the peaks of NC species with 3-, 4-, and 5- charges are visually similar, and the peak intensities follow the approximate relation of  $x^{3-} \sim x^{4-} + 1 \sim x^{5-} + 2$ . This suggests that the development of negative charge in these ionized NCs was most likely due to the successive dissociation of  $\text{CTA}^+$ . Observations of bulky hydrophobic cation dissociation in ESI processes before the smaller cations (*e.g.*,  $\text{H}^+$ ) have previously been reported by Lee *et al.*<sup>187</sup> On this basis, the total number of  $\text{CTA}^+$  in the neutral form of individual  $\text{Au}_{25}(\text{MHA})_{18}@x\text{CTA}$  NC (*i.e.*,  $x$ ) can be calculated by the equation

$$x = x^z - z \quad (5.2)$$

Therefore, we infer that there were 6-9 (population maximum at 7)  $\text{CTA}^+$  per  $\text{Au}_{25}(\text{MHA})_{18}$  NC in charge-neutral PT-NCs. Given that each  $\text{Au}_{25}(\text{MHA})_{18}$  contains 18 hydrophilic MHA ligands and the 1 : 1 pairing between MHA and  $\text{CTA}^+$ , the 6-9  $\text{CTA}^+$  per NC would correspond to approximately half a monolayer coverage of hydrophobic moieties on the  $\text{Au}_{25}(\text{MHA})_{18}$  NC surface (see the illustration in Figure 5.2b). This means that  $\text{Au}_{25}(\text{MHA})_{18}@x\text{CTA}$  NCs ( $x = 6$ -9) protected by a comparable

number of hydrophilic MHA and hydrophobic CTA<sup>+</sup>-MHA paired ligands (*i.e.*, MHA⋯CTA where hydrophobicity is imparted by the hydrocarbon chains of CTA<sup>+</sup>), or amphiphilic NCs could be formed in high yield by the PT driven ion-pairing reaction, using a *moderately-polar* ethanol/toluene mixture as the organic medium.

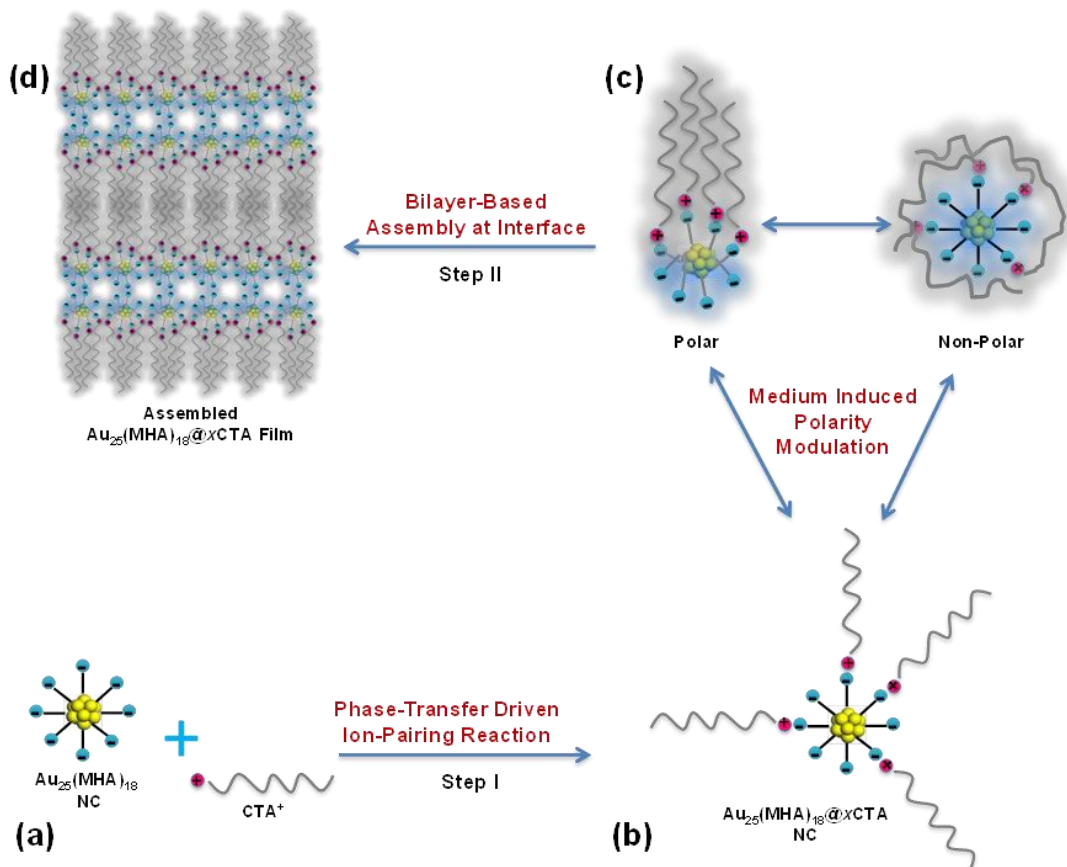


**Figure 5.2** Schematic illustration of the synthesis of Au<sub>25</sub>(MHA)<sub>18</sub>@xCTA NCs ( $x = 6-9$ ) and their self-assembly.

Several control experiments were used to verify the formation of Au<sub>25</sub>(MHA)<sub>18</sub>@xCTA NCs ( $x = 6-9$ ) via the proposed polarity-dependent PT driven ion-pairing mechanism. First, we disabled the PT of Au<sub>25</sub> NCs by tuning the polarity of the organic phase to highly non-polar (CTAB has low solubility in a typical non-polar solvent such as toluene). As shown in the inset of Figure 5.3a(i), the



$\text{Au}_{25}(\text{MHA})_{18}@x\text{CTA}$  NCs were unable to migrate to the organic phase from the aqueous phase when ethanol was eliminated from the tri-solvent system (volume fraction of ethanol,  $f_{\text{EtOH}} = 0$ ). In this case ( $f_{\text{EtOH}} = 0$ ), since no NC species could be transferred to the organic medium, the ion-pairing reaction occurred to the full extent allowable by thermodynamics in the aqueous solution, giving rise to the non-phase-transferred  $\text{Au}_{25}(\text{MHA})_{18}@x\text{CTA}$  NCs ( $x = 3-5$ , with a population maximum at 5, referred as non-PT-NCs hereafter). The  $x$  value was calculated based on the  $x^{3-}$  species in Figure 5.3b(i) according to Equation 5.2. These non-PT-NCs ( $x = 3-5$ ) were much more hydrophilic than those PT-NCs ( $x = 6-9$ , obtained with  $f_{\text{EtOH}} = 0.33$ , the ESI-MS spectra of which are also included in Figure 5.3 (panels (iii)) for ease of comparison). The formation of these much more hydrophilic non-PT-NCs could be attributed to the excess  $\text{Na}^+$  present in the aqueous phase, which could shift the ion-pairing equilibrium (Equation 5.1) significantly to the left, giving rise to a smaller extent of  $\text{CTA}^+$  binding on the  $\text{Au}_{25}(\text{MHA})_{18}$  NC surface. This hypothesis is supported by the extensive presence of  $\text{Na}^+$  as counter cations on the non-PT-NCs, as evidenced by the series of peaks due to  $\text{Na}^+$  coordination in the ESI-MS spectrum (Figure 5.3c(i)). It is worth noting that there were no similar peaks due to  $\text{Na}^+$  coordination in the ESI-MS spectrum of PT-NCs (Figure 5.3c(iii)).

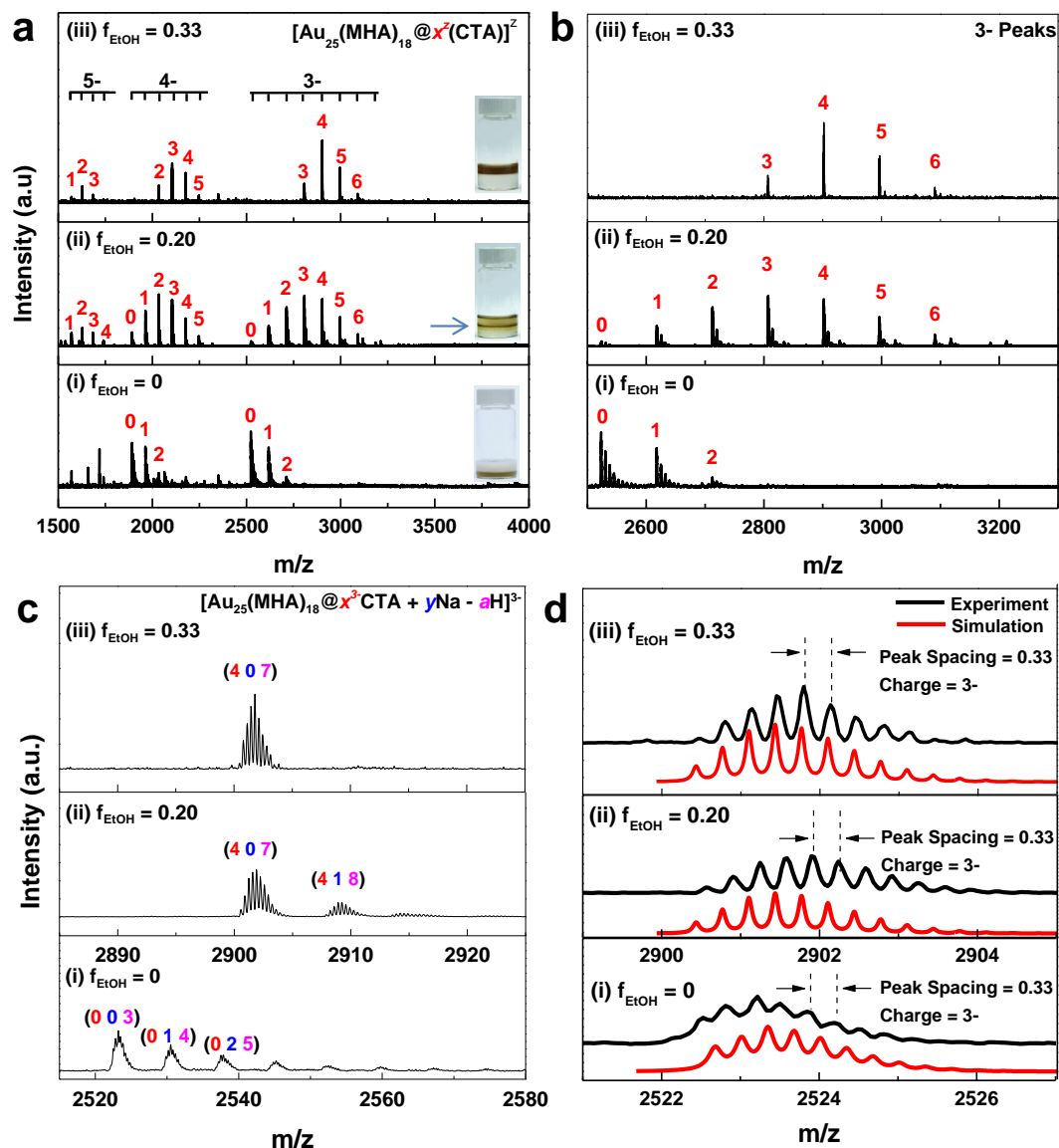


**Figure 5.3** Comparison of ESI-MS spectra (in negative-ion mode) of non-phase-transferred (i), intermediate-phase-transferred (ii), and phase-transferred (iii)  $\text{Au}_{25}(\text{MHA})_{18}@x\text{CTA}$  NCs prepared with  $f_{\text{EtOH}} = 0, 0.20$  and  $0.33$  respectively. (a) Spectra in the broad 1500-4000  $m/z$  region; the insets in (a) show corresponding digital images of  $\text{Au}_{25}(\text{MHA})_{18}@x\text{CTA}$  NCs, where the blue arrow in (ii) indicates the intermediate-phase-transferred  $\text{Au}_{25}(\text{MHA})_{18}@x\text{CTA}$  NCs agglomerating at the aqueous-organic interface. (b) Zoomed-in spectra of NC species with 3- charge. (c) Zoomed-in spectra of representative peaks in (b). (d) Isotope patterns of the most pronounced peak in (c), where (i) corresponds to  $[\text{Au}_{25}(\text{MHA})_{18} - 3\text{H}]^{3-}$  and (ii-iii) correspond to  $[\text{Au}_{25}(\text{MHA})_{18}@4\text{CTA} - 7\text{H}]^{3-}$ ; the black and red lines in (d) are the experimental and simulated isotope patterns respectively.

Using a solvent mixture with an intermediate  $f_{\text{EtOH}}$  ( $= 0.20$ ) and thus intermediate polarity, we were able to control the PT to the extent that  $\text{Au}_{25}(\text{MHA})_{18}@x\text{CTA}$  NCs were agglomerated at the aqueous-organic interface (inset of Figure 5.3a(ii)). These NCs may be referred to as intermediate-PT-NCs. Since the intermediate-PT-NCs were in contact with both aqueous and organic phases, they acquired the surface features of non-PT-NCs and PT-NCs. This is evidenced from the broad distribution of  $x$  values ( $x = 3-9$ , population maximum at 6) in their ESI spectrum. The  $x$  values were calculated based on the  $x^{3-}$  species in Figure 5.3b(ii) according to Equation 5.2. Peaks due to some slight  $\text{Na}^+$  coordination were detected in the ESI-MS spectrum of intermediate-PT-NCs (Figure 5.3c(ii)). All of these observations are consistent with the proposed PT driven ion-pairing mechanism, where polarity-dependent selective PT of certain NC species (*e.g.*,  $\text{Au}_{25}(\text{MHA})_{18}@x\text{CTA}$  NCs with  $x = 6-9$ , obtained by using a *moderately-polar* ethanol/toluene mixture) could drive the ion-pairing reaction to sustain the formation of the extracted NC species. More details about the ESI-MS spectra (including the wide range spectra and representative isotope analyses) of non-PT-NCs, intermediate-PT-NCs and PT-NCs can be found in Figure 5.3.

### 5.3.2 Amphiphilicity of $\text{Au}_{25}(\text{MHA})_{18}@x\text{CTA}$ NCs ( $x = 6-9$ )

Due to the coexistence of hydrophilic MHA and hydrophobic MHA $\cdots$ CTA ligands in comparable quantities on the NC surface, together with the flexible chain structures of these ligands,  $\text{Au}_{25}(\text{MHA})_{18}@x\text{CTA}$  ( $x = 6-9$ ) should be good supramolecular amphiphiles.<sup>188,202</sup> Given that the sizes of the Au core, MHA ligands and  $\text{CTA}^+$  cations are quite comparable ( $\sim 1.0$ ,<sup>17,70</sup> 0.7, and 2.0 nm respectively; see the illustration in Figure 5.4), the polarity of  $\text{Au}_{25}(\text{MHA})_{18}@x\text{CTA}$  ( $x = 6-9$ ) NCs should depend on the way the MHA and MHA $\cdots$ CTA ligands are organized on the NC surface. Therefore,

the flexible hydrocarbon chains of MHA ( $C_6$ -chain) and  $CTA^+$  ( $C_{16}$ -chain), which make the reorganization of these ligands possible, provide a good means to fine-tune the polarity of  $Au_{25}(MHA)_{18}@xCTA$  ( $x = 6-9$ ) NCs according to the polarity of medium to enhance their amphiphilicity. For example, in a polar environment, the hydrophobic MHA $\cdots$ CTA ligands may bunch together at one end and leave the hydrophilic MHA ligands exposed at the opposite end to maximize the NC polarity (the polar configuration illustrated in Figure 5.2c). On the contrary, the hydrophobic MHA $\cdots$ CTA ligands may bend and wrap over the top of hydrophilic MHA ligands to minimize the polarity of the NC in a non-polar medium (the non-polar configuration illustrated in Figure 5.2c). Such a medium-induced polarity modulation mechanism maximizes amphiphilicity by adapting the surface of  $Au_{25}(MHA)_{18}@xCTA$  NCs ( $x = 6-9$ ) to the environment (a “smart” surface of sorts).

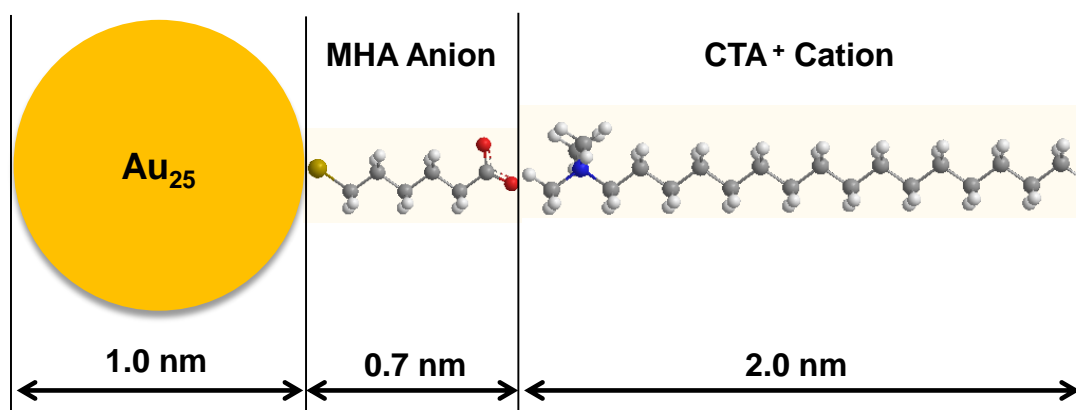


**Figure 5.4** Schematic illustration showing the sizes of the Au core, MHA and  $CTA^+$  cations in  $Au_{25}(MHA)_{18}@xCTA$  NCs ( $x = 6-9$ ). The size of the  $Au_{25}$  core is taken from the literature,<sup>17,70</sup> and the lengths of MHA and  $CTA^+$  are estimated by CS ChemOffice Ultra 4.5.

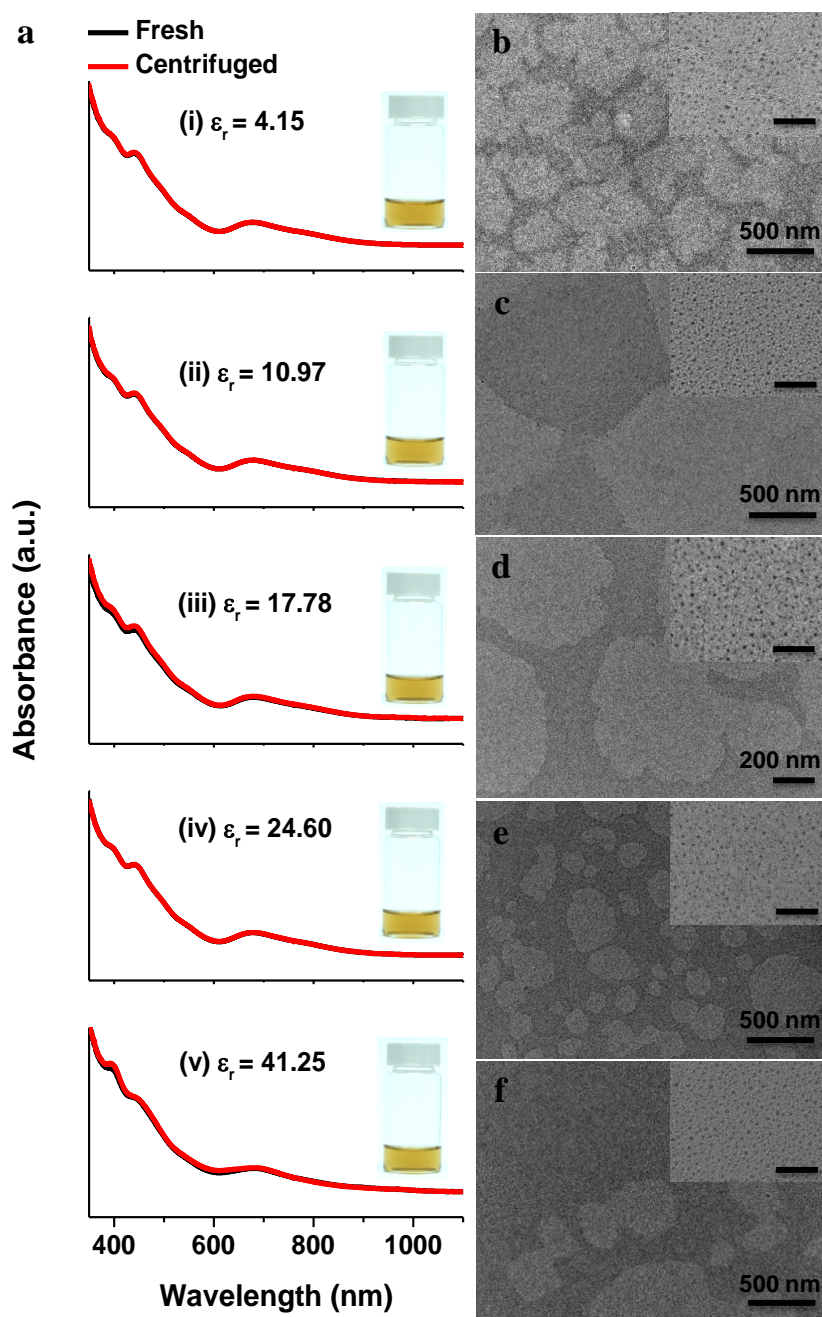


**Figure 5.5** (a) UV-vis absorption spectra and (b-f) TEM images of  $\text{Au}_{25}(\text{MHA})_{18}@x\text{CTA}$  NCs ( $x = 6-9$ ) in different media: (a(i), b) ethanol/hexane = 10/90 v/v,  $\epsilon_r = 4.15$ ; (a(ii), c) ethanol/hexane = 40/60 v/v,  $\epsilon_r = 10.97$ ; (a(iii), d) ethanol/hexane = 70/30 v/v,  $\epsilon_r = 17.78$ ; (a(iv), e) ethanol,  $\epsilon_r = 24.60$ ; and (a(v), f) ethanol/water = 70/30 v/v,  $\epsilon_r = 41.25$ . The superimposed black and red lines in (a) are respectively the UV-vis absorption spectra of freshly prepared and centrifuged (at 10,000 rpm for 10 min) NC solutions. The insets in (a) are the digital images of freshly prepared NC solutions. The insets in (b-f) are corresponding HR-TEM images of the NCs, where the scale bars are 20 nm.

The amphiphilic character of  $\text{Au}_{25}(\text{MHA})_{18}@x\text{CTA}$  NCs ( $x = 6-9$ ) was first demonstrated by their good solubility in a wide range of solvents with very different polarities. The polarity of a solvent is usually measured by its relative dielectric constant,  $\epsilon_r$ . The purified (see §5.2.3.1 for purification procedures)  $\text{Au}_{25}(\text{MHA})_{18}@x\text{CTA}$  NCs ( $x = 6-9$ ) could form homogeneous solutions in mixed solvents over a wide range of  $\epsilon_r$  values from 4.15 (ethanol/hexane = 10/90 v/v) to 41.25 (ethanol/water = 70/30 v/v). These NC solutions ( $[\text{NC}] = 0.02$  mM) were clear (insets of Figure 5.5a) and highly stable to mechanical perturbations. Centrifugation at 10,000 rpm for 10 min would not result in any precipitation, as shown by the superimposable UV-vis absorption spectra of the NC solution before and after centrifugation (Figure 5.5a). TEM images (Figure 5.5b-f) of  $\text{Au}_{25}(\text{MHA})_{18}@x\text{CTA}$  NCs ( $x = 6-9$ ) also confirm their well-dispersed nature in the solutions. No large ( $>3$  nm) aggregates or nanoparticles were found in the TEM images. The high resolution TEM (HR-TEM) images (Figure 5.5b-f insets) also confirm the smallness ( $<2$  nm) and discreteness of the  $\text{Au}_{25}(\text{MHA})_{18}@x\text{CTA}$  NCs ( $x = 6-9$ ) in these media. To the best of our knowledge, the  $\text{Au}_{25}(\text{MHA})_{18}@x\text{CTA}$  NC ( $x = 6-9$ ) could be the NC with the broadest medium polarity window where homogeneous NC solutions may form. However, it should be mentioned that an  $\epsilon_r$  outside of the aforementioned window would render the  $\text{Au}_{25}(\text{MHA})_{18}@x\text{CTA}$  NC ( $x = 6-9$ ) difficult to dissolve. For example, dimethylsulfoxide (DMSO,  $\epsilon_r = 46.70$ ) and hexane ( $\epsilon_r = 1.88$ ) were found to be the non-solvent or poor solvent for  $\text{Au}_{25}(\text{MHA})_{18}@x\text{CTA}$  NCs ( $x = 6-9$ ).

A remarkable feature of molecular amphiphiles is the formation of bilayers and bilayer-based lamellar structures via self-assembly.<sup>194,211</sup> Likewise our NC analog of molecular amphiphiles also exhibited self-assembly properties. The investigation of the self-assembly characteristics of  $\text{Au}_{25}(\text{MHA})_{18}@x\text{CTA}$  NCs ( $x = 6-9$ ) was carried

out in a DMSO/ethanol mixture (50/50 v/v), where the volatile ethanol is a good solvent for  $\text{Au}_{25}(\text{MHA})_{18}@x\text{CTA}$  NCs ( $x = 6-9$ ) and the non-volatile DMSO is a poor solvent. The selective evaporation of ethanol could therefore induce the self-assembly of  $\text{Au}_{25}(\text{MHA})_{18}@x\text{CTA}$  NCs ( $x = 6-9$ ). Experimentally, cleaned  $\text{Au}_{25}(\text{MHA})_{18}@x\text{CTA}$  NCs ( $x = 6-9$ ) were redissolved in a DMSO/ethanol mixture (50/50 v/v) to a final [NC] of 0.53 mM. Solvent evaporation was carried out at the ambient condition (298 K and 1 atm) over a period of 3 d. A brownish black film (inset #2 in Figure 5.6a) was formed at the liquid-air interface at the end of the procedure.

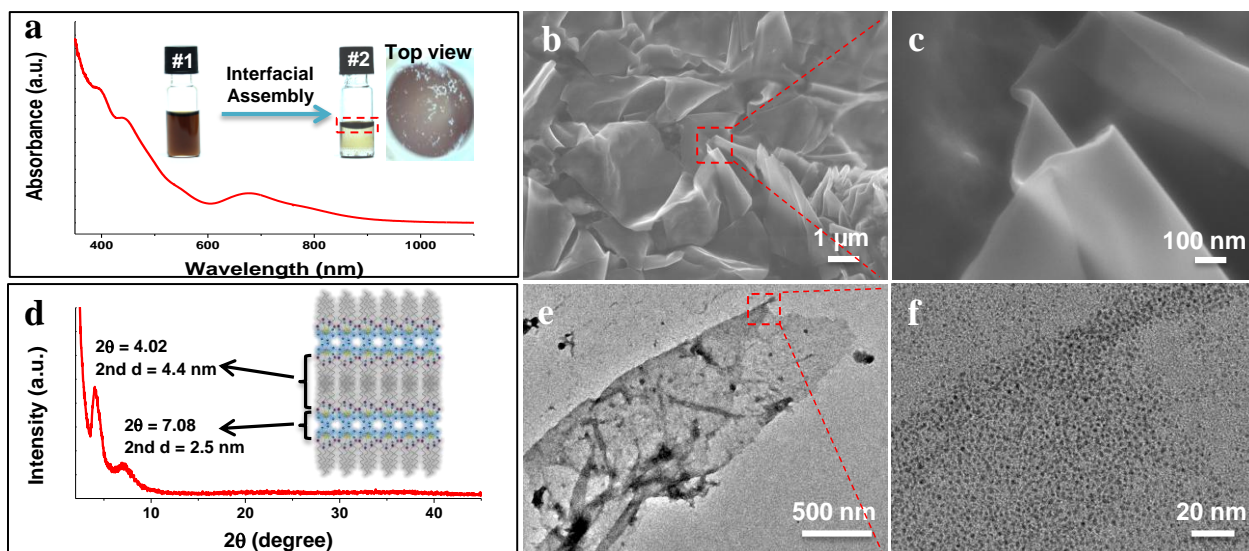


**Figure 5.6** UV-vis absorption spectrum, (d) XRD pattern, (b-c) FESEM and (e-f) TEM images of  $\text{Au}_{25}(\text{MHA})_{18}@x\text{CTA}$  NCs ( $x = 6-9$ ) assembled at the liquid-air interface. The insets in (a) are the digital images of  $\text{Au}_{25}(\text{MHA})_{18}@x\text{CTA}$  NCs before (#1) and after (#2) self-assembly; the top view of the circled area of #2 is also shown to the right of #2. The inset in (d) shows a schematic illustration of the lamellar assembly formed by the NC bilayers.

The brownish-black film was first characterized by UV-vis absorption spectroscopy. The film was redissolvable in ethanol and the ethanol solution of the film could not be differentiated from the ethanol solution of  $\text{Au}_{25}(\text{MHA})_{18}@x\text{CTA}$  NCs ( $x = 6-9$ ) (Figure 5.1a, red line) by UV-vis absorption spectroscopy (Figure 5.6a). This was

possible if the brownish black film was an organized aggregate of the  $\text{Au}_{25}(\text{MHA})_{18}@x\text{CTA}$  NCs ( $x = 6-9$ ). The morphology of these film-like  $\text{Au}_{25}(\text{MHA})_{18}@x\text{CTA}$  NCs ( $x = 6-9$ ) was then examined by FESEM. The FESEM images (Figure 5.6b-c) show a flexible and deformable (evidenced by the presence of creases in Figure 5.6b) sheet-like structure with a typical thickness of  $\sim 15$  nm (see high resolution FESEM image in Figure 5.6c). The XRD pattern of the film (Figure 5.6d) contains two distinctive diffraction peaks at  $2\theta = 4.02^\circ$  and  $7.08^\circ$  respectively. The bimodal XRD pattern is typical of the formation of regularly stacked bilayer structures, where there are two characteristic interlayer distances ( $d$ ) corresponding to hydrophilic-hydrophilic and hydrophobic-hydrophobic aggregation layers respectively (see schematic illustration in the inset of Figure 5.6d). Hence the sheet-like structure in the FESEM images most probably consisted of ordered stacking of bilayers of  $\text{Au}_{25}(\text{MHA})_{18}@x\text{CTA}$  NCs ( $x = 6-9$ ) (Figure 5.2d). Since the thickness of the sheet-like structure ( $\sim 15$  nm) was much larger than the size of a  $\text{Au}_{25}(\text{MHA})_{18}@x\text{CTA}$  NC ( $x = 6-9$ ) (see Figure 5.4 for a schematic illustration), the thin film was a lamellar structure of bilayer stacks of  $\text{Au}_{25}(\text{MHA})_{18}@x\text{CTA}$  NC ( $x = 6-9$ ).

In view of the amphiphilic nature of  $\text{Au}_{25}(\text{MHA})_{18}@x\text{CTA}$  NCs ( $x = 6-9$ ), the lamellar structure was most likely formed by the successive stacking of bilayers of these amphiphilic NCs at the liquid-air interface. With the evaporation of ethanol, the polarity of the DMSO/ethanol mixture gradually increased. In the early stages of evaporation, the “smart” surface of  $\text{Au}_{25}(\text{MHA})_{18}@x\text{CTA}$  NCs ( $x = 6-9$ ) was able to undergo some rearrangement to adapt to the changing polarity of the medium to keep them soluble in the mixed solvent. However, continual evaporation of ethanol would eventually increase the polarity of the DMSO/ethanol mixture to exceed the upper polarity limit of the NCs, resulting in the precipitation of  $\text{Au}_{25}(\text{MHA})_{18}@x\text{CTA}$  NCs



( $x = 6-9$ ) in their most polar configuration. The most polar state of  $\text{Au}_{25}(\text{MHA})_{18}@x\text{CTA}$  NCs ( $x = 6-9$ ) should be a surfactant-like structure with hydrophobic and hydrophilic moieties localized on opposite ends (polar configuration in Figure 5.2c). The surfactant-like NCs aggregated differently at the liquid-air interface and in the bulk of liquid, due to the minimization of surface energy. At the liquid-air interface, the surfactant-like NCs self-assembled into a monolayer with the hydrophobic end facing air, similar to the behavior of a typical surfactant at the liquid-air interface. In the bulk of the liquid (DMSO-rich), the surfactant-like NCs packed into bilayers (or fragments of bilayers) by aggregating the hydrophobic ends, similar to the arrangement of lipids in a cell membrane. Consequently, the bilayer would adhere to the monolayer of surfactant-like NCs via hydrophilic-hydrophilic interaction. A succession of these hydrophilic-hydrophilic induced adhesion would stack the bilayers into the ~15-nm-thick-lamellar structure (Figure 5.2d).

In the above bilayer-based self-assembly, the  $d$ -spacings corresponding to the hydrophobic-hydrophobic and hydrophilic-hydrophilic aggregation layers could be estimated based on the sizes of the Au core (~1.0 nm), MHA ligands (~0.7 nm) and  $\text{CTA}^+$  (~2.0 nm, see Figure 5.4). If the fully extended forms of MHA ligands and  $\text{CTA}^+$  (Au core is considered impenetrable and un-deformable), the  $d$  values corresponding to hydrophilic-hydrophilic and hydrophobic-hydrophobic aggregation layers should be 2.4 ( $= 1.0 + 2 \times 0.7$ ) and 6.4 ( $= 1.0 + 2 \times (2.0 + 0.7)$ ) nm respectively. These estimated  $d$  values are in good agreement with those measured by XRD (Figure 5.6d). If we consider  $2\theta = 4.02^\circ$  and  $7.08^\circ$  peaks as 2<sup>nd</sup> order diffraction peaks (the 1<sup>st</sup> order diffraction peaks were overshadowed by the high background noise at  $2\theta < 2.5^\circ$ ), the 2<sup>nd</sup> order diffraction at  $2\theta = 7.08^\circ$  should correspond to a  $d$  value of 2.5 nm, close to the hydrophilic-hydrophilic aggregation layer (estimated  $d = 2.4$  nm) formed by

fully extended MHA ligands. The  $d$  value corresponding to the 2<sup>nd</sup> order diffraction at  $2\theta = 4.02^\circ$  is 4.4 nm, smaller than the estimated value ( $d = 6.4$  nm) for the hydrophobic-hydrophobic aggregation layer. This could be due to some interdigitation of the hydrocarbon tails of CTA<sup>+</sup>. The interdigitation of long alkyl-chain of CTA<sup>+</sup> in bilayer formation is a rather common phenomenon.<sup>212-215</sup> Based on the above XRD analysis, the number of stacked bilayers in the ~15-nm-thick sheet-like structure was ~2 (*i.e.*  $15 / (4.4 + 2.5) = 2.17$ ).

The layered structure of these Au<sub>25</sub>(MHA)<sub>18</sub>@*x*CTA NC films ( $x = 6-9$ ) was also confirmed by TEM analysis (Figure 5.6e-f). We managed to exfoliate a film in DMSO through a brief ultrasonication (37 kHz, 5 min). A drop of the resultant DMSO solution was dropped onto a TEM copper grid and dried. The TEM image shows a single-NC-thick sheet which was folded in some places (Figure 5.6e). The HR-TEM image (Figure 5.6f) confirms the sheet was composed of NCs <2 nm. There was however no indication of intralayer structural order in individual NC layer (Figure 5.6f), verifying that the peaks in XRD were due to the diffraction from the regularity of interlayer stacking.

### 5.3.3 Enhanced Stability of Au<sub>25</sub>(MHA)<sub>18</sub>@*x*CTA NCs ( $x = 6-9$ )

In addition to introducing amphiphilicity, CTA<sup>+</sup> coating also contributed to improving the stability of Au<sub>25</sub> NCs. This was revealed by comparing the stability of Au<sub>25</sub>(MHA)<sub>18</sub> NCs and Au<sub>25</sub>(MHA)<sub>18</sub>@*x*CTA NCs ( $x = 6-9$ ) at the ambient condition (298 K and 1 atm and mildly oxidizing due to the oxygen in air) over a period of 7 d. The NC stability was assessed by spectral changes in UV-vis spectroscopy (Figure 5.7). The UV-vis absorption spectrum of Au<sub>25</sub>(MHA)<sub>18</sub> NCs after 3 d of ageing showed considerable changes indicative of the decrease in NC quality (Figure 5.7a). In

sharp contrast, the UV-vis absorption spectrum of  $\text{Au}_{25}(\text{MHA})_{18}@x\text{CTA}$  NCs ( $x = 6-9$ ) (Figure 5.7b) underwent little changes even over an extended time period (7 d). The good stability was also retained in the assembled  $\text{Au}_{25}(\text{MHA})_{18}@x\text{CTA}$  NCs ( $x = 6-9$ ). The stability of the latter was evaluated by treating them at an elevated temperature (393 K) either in air or in vacuum for 3 d. The assembled film after the said thermal treatment was redissolved in ethanol for the UV-vis analysis. The results in Figure 5.8 show that the characteristic absorption features of  $\text{Au}_{25}(\text{SR})_{18}$  at 440 and 672 nm were still present in both cases, indicating that the assembled  $\text{Au}_{25}(\text{MHA})_{18}@x\text{CTA}$  NCs ( $x = 6-9$ ) were stable to high temperature (393 K) even in air. These stability tests suggest that the  $\text{CTA}^+$  coating was a competent  $\text{O}_2$  barrier to protect the  $\text{Au}_{25}$  core from oxidative decomposition (a common decomposition pathway for  $\text{Au}_{25}$  NCs).<sup>216-217</sup> It also increased the thermal stability of the NCs by dispersing the thermal energy most probably through  $\text{C}_{16}$ -chain vibrations or rotations; without which the thermal desorption of the thiolate ligands would cause the aggregation of the Au cores to occur.

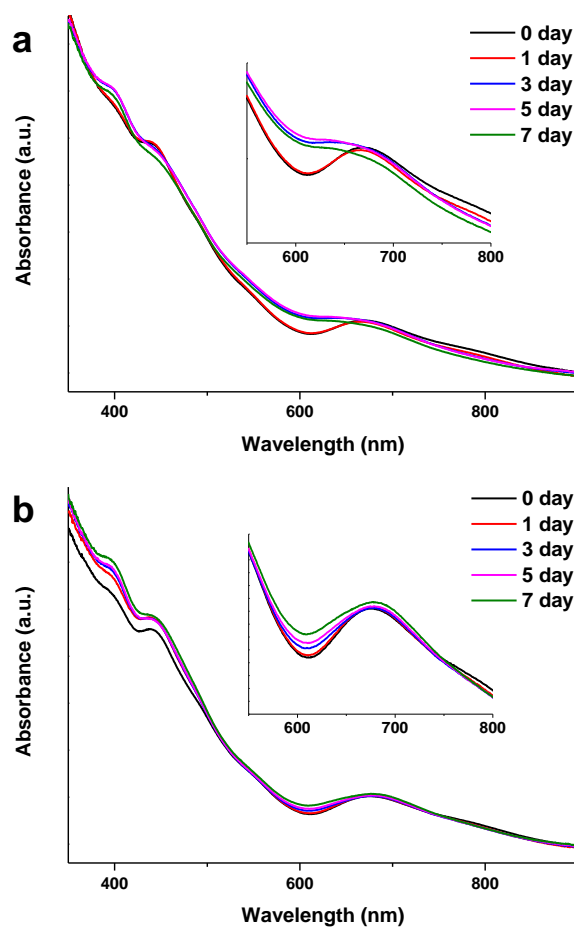


**Figure 5.7** UV-vis spectra of (a)  $\text{Au}_{25}(\text{MHA})_{18}$  NCs and (b)  $\text{Au}_{25}(\text{MHA})_{18}@x\text{CTA}$  NCs ( $x = 6-9$ ) over a period of 1 week at the ambient condition (298 K and 1 atm). The insets show the enlarged spectra in the 550-800 nm spectral region. The absorption peak at  $\sim 672$  nm of  $\text{Au}_{25}(\text{MHA})_{18}$  NCs was significantly broadened after 3 d, while the absorption peak of  $\text{Au}_{25}(\text{MHA})_{18}@x\text{CTA}$  NCs ( $x = 6-9$ ) did not show any broadening over 7 d; indicating the good stability of the latter.

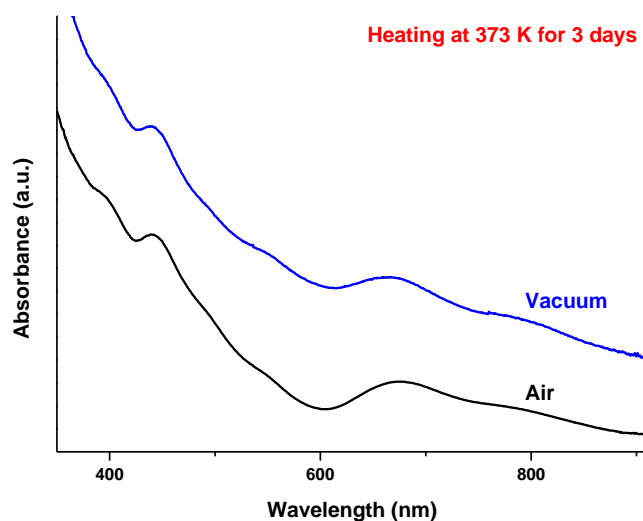


**Figure 5.8** UV-vis absorption spectra of assembled  $\text{Au}_{25}(\text{MHA})_{18}@x\text{CTA}$  NCs ( $x = 6-9$ ) after heating at 393 K for 3 d in air (black line) and in vacuum ( $\sim 20$  mbar, blue line).

## 5.4 Conclusion

In summary we have developed a simple surface modification method for the preparation of amphiphilic NM-NCs. The method is based on a PT driven ion-pairing reaction between hydrophobic cations and anionic surface functionality of the hydrophilic NCs. The reversibility of the ion-pairing reaction is combined with a polarity-dependent PT to selectively extract amphiphilic NCs from the aqueous phase to a *moderately-polar* organic phase, thereby making the preparation of amphiphilic NCs possible. Specifically amphiphilic  $\text{Au}_{25}(\text{MHA})_{18}@x\text{CTA}$  NCs ( $x = 6-9$ ) were prepared by patching the hydrophilic  $\text{Au}_{25}(\text{MHA})_{18}$  NCs partially with  $\text{CTA}^+$  using the hydrocarbon chain of the latter to impart hydrophobicity. Due to a comparable amount of flexible hydrophilic and hydrophobic moieties on the NC surface; the resulting amphiphilic  $\text{Au}_{25}(\text{MHA})_{18}@x\text{CTA}$  NCs ( $x = 6-9$ ) could be regarded as high quality

supramolecular amphiphilicities. These supramolecular amphiphilicities not only possess good solubility in a wide range of medium with distinctly different polarities ( $\epsilon_r$  ranging from 4.15 to 41.25), but also exhibit the self-assembly characteristics of molecular amphiphiles (*e.g.*, formation of stacked bilayers with *regular* interlayer packing at the liquid-air interface). The products and the preparation method demonstrated in this study indicate that amphiphilicity could now be imparted to sub-2-nm particles to increase the versatility of NC-based materials and to regulate the self-assembled structures of the latter. However, 3D crystalline order is not yet obtained in stacked bilayers of NCs although regular interlayer packing is achievable via amphiphilicity driven assembly. Inspired by the packing of hard spheres, we hypothesized that such long-range crystalline order may be achievable through depletion forces, which is the topic of Chapter 6.

---

# CHAPTER 6    SHAPE-TAILORABLE

## CRYSTALLIZATION OF

### SUPRAMOLECULAR ATOMS:

## COUNTERION-ASSISTED SHAPING OF

### AG<sub>44</sub>(P-MBA)<sub>30</sub> NC SUPRACRYSTALS

#### 6.1 Introduction

The crystallization of  $M_n(SR)_m$  ( $M = Au$  and  $Ag$ ) is a central research activity in the development of cluster chemistry.<sup>2,24,27-28</sup> This has been intensely pursued in the last decade because the determination of NC structures depends on the availability of high quality supracrystals (SCs) of NCs.<sup>24-27,29,33,40,57,59-60</sup> Shape also affects the physiochemical (*e.g.*, optical and catalytic) properties of crystalline materials through geometry, symmetry and the exposure of specific crystallographic facets.<sup>77,218-220</sup> The reciprocity between shape and property has been regularly shown by noble metal nanocrystals, and motivates shape engineering as a means to diversify the nanocrystal shape for application explorations.<sup>65,218-219,221-225</sup> The formation of SC with shape control from NC building blocks is however technically challenging. Thus far, only rhombohedral or needle-like NC-SCs with the symmetry of monoclinic, triclinic and orthorhombic crystal systems have been demonstrated.<sup>24-26,28-29,33,40,57,59-60</sup> Thus, the crystallization of NCs into shape-tailorable SCs with structural diversity approaching that of nanocrystals; is clearly of interest to the cluster research community. The ability to perform shape engineering can accelerate NC structural determination by X-

ray crystallography (via the packing of NCs into SCs of high symmetry),<sup>226</sup> and also the development of reliable property-shape relationships for the NC-SCs.<sup>48,150,227-228</sup>

Recently, Desireddy *et al.* reported the synthesis of rhombohedral  $\text{Ag}_{44}(\text{p-MBA})_{30}$  NC-SCs, where *p*-MBA or H-SPhCOOH denotes *p*-mercaptobenzoic acid.<sup>27</sup> Since the SCs were grown from NCs with the protonated form of *p*-MBA ligands, the crystal habit (*e.g.*, the rhombohedral shape of the SCs) is strongly relatable to a bonding environment established by the directional hydrogen bonds (H-bonds) on the component NCs.<sup>64</sup> In this work, we will demonstrate that the shape of  $\text{Ag}_{44}(\text{p-MBA})_{30}$  NC-SCs can be tailored by altering the bonding habit of component NCs. By simply changing the counterions of *p*-MBA ligands from  $\text{H}^+$  to non- $\text{H}^+$  cations (*e.g.*,  $\text{Cs}^+$ ), the formation of directional H-bonds between NCs could be substantially suppressed, thereby promoting non-directional bonding to  $\text{Ag}_{44}(\text{p-MBA})_{30}$  NCs. A non-directional bonding habit, together with several other structural features (*e.g.*, uniform size, *pseudo*-spherical geometry, and rigid ligand shell), imparted the  $\text{Ag}_{44}(\text{p-MBA})_{30}$  NCs with hard-sphere-like atomic properties (supramolecular atoms). Similar to the formation of closest-packed (*e.g.*, *f.c.c.*) crystals by hard-sphere-like atoms, these atom-mimic NCs assembled into octahedral SCs with  $\text{O}_h$  symmetry, in stark contrast to the rhombohedral SCs with lower  $\text{D}_{3d}$  symmetry reported in the literature.<sup>27</sup> Furthermore, the high charge density of  $\text{Ag}_{44}(\text{p-MBA})_{30}$  NCs developed by deprotonating the *p*-MBA ligands offers a means to modify the SC growth kinetics by charge-screening effects, which could be used to alter the faces of octahedral  $\text{Ag}_{44}(\text{p-MBA})_{30}$  NC-SCs to be either convex (octahedron) or concave (concave-octahedron).



## 6.2 Experimental Section

### 6.2.1 Materials

*p*-MBA, NaBH<sub>4</sub>, and cesium hydroxide (CsOH, 50 wt.% solution in water) from Sigma Aldrich; AgNO<sub>3</sub> from Merck; ethanol from Fisher; and DMSO from Tedia were used as received without purification. Ultrapure Milipore water (18.2 MΩ) was used in the preparation of all aqueous solutions. All glassware was washed with *aqua regia* and rinsed with ethanol and ultrapure water before use.

### 6.2.2 Synthesis of Ag<sub>44</sub>(*p*-MBA)<sub>30</sub> NCs

The preparation of Ag<sub>44</sub>(*p*-MBA)<sub>30</sub> NCs followed a previously-reported method with some modifications.<sup>27</sup> 5.25 mL 23.8 mM AgNO<sub>3</sub> aqueous solution was mixed with 3 mL 83 mM *p*-MBA solution in ethanol to form a light-yellow suspension of Ag(I)-(*p*-MBA) complexes. 200 μL 1 wt.% CsOH aqueous solution ([CsOH] = 66 mM) was then introduced to bring up the pH value under vigorous stirring (1,000 rpm). The cloudy suspension turned into a clear solution. 2.25 mL 278 mM NaBH<sub>4</sub> aqueous solution (freshly prepared by adding a calculated amount of NaBH<sub>4</sub> powder in 0.2 M CsOH aqueous solution) was then added drop-wise. The growth of NCs occurred at 323 K for 12 h under vigorous stirring (1,000 rpm). The dark-red solution obtained at the end of this procedure was collected as the raw product.

The raw product was centrifuged at 10,000 rpm for 5 min to remove any likely insoluble impurity (*e.g.*, unreacted Ag(I)-(*p*-MBA) complex). An equal volume of ethanol (*i.e.*, 10 mL ethanol for 10 mL NC solution) was then added to the supernatant, followed by centrifugation at 10,000 rpm for 5 min. The precipitate was recovered and redissolved in 2 mL of 1 wt.% CsOH aqueous solution. After incubation under

moderate stirring (600 rpm) for 10 min, ethanol in double the volume of the NC solution was added, followed by centrifugation at 10,000 rpm for 5 min. The redissolution-centrifugation cycle was repeated for another two rounds to fully deprotonate the carboxyl groups in the *p*-MBA ligands. The precipitate at the end of these procedures was collected as the cleaned product.

### 6.2.3 Crystallization of $\text{Ag}_{44}(\text{p-MBA})_{30}$ NCs

The supracrystals of  $\text{Ag}_{44}(\text{p-MBA})_{30}$  NCs were grown in a dual-solvent system. Cleaned  $\text{Ag}_{44}(\text{p-MBA})_{30}$  NCs were redissolved in a mixture of DMSO/water with a given DMSO content ( $f_{\text{DMSO}}$ , v/v) and CsOH concentration to form the crystallization solution (the target concentration of NC,  $[\text{NC}]$  was 0.73 mM). The crystallization solution was then placed in a vacuum oven at ~20 mbar and 313 K to selectively remove the water in the mixture. The evaporation lasted typically 1-3 days (depending on the  $f_{\text{DMSO}}$ ), and dark-red SCs of  $\text{Ag}_{44}(\text{p-MBA})_{30}$  NCs could be collected from the bottom of crystallization tube at the end of the procedure. For a typical growth of octahedral SCs, a crystallization solution with  $f_{\text{DMSO}} = 0.5$  and  $[\text{CsOH}] = 33$  mM, 1 d of vacuum treatment was sufficient. Increasing to  $[\text{CsOH}] = 66$  mM while keeping other parameters intact formed concave-octahedral SCs from the  $\text{Ag}_{44}(\text{p-MBA})_{30}$  NCs.

### 6.2.4 Characterization

The growth of SCs was performed in a Binder VD-23 vacuum oven maintained at ~20 mbar and 313 K. UV-vis spectra were recorded by a Shimadzu UV-1800 spectrometer. The morphology of discrete  $\text{Ag}_{44}(\text{p-MBA})_{30}$  NCs, NC-SCs or other assemblies was examined by scanning electron microscopy (SEM; on a JEOL JSN-5600lv microscope operating at 15 kV), FESEM (on a JEOL JSM-6700F microscope

operating at 5 kV), TEM (on a JEOL JEM 2010 microscope operating at 200 kV) and STEM (on a JEOL JEM 2010 microscope operating at 200 kV). The composition of SCs was analyzed by energy dispersive X-ray spectroscopy (EDX) on a JEOL JSN-5600lv microscope operating at 15 kV. The composition of rod-like assemblies was determined by EDX on a JEOL JEM 2010 microscope operating at 200 kV. (FE)SEM and TEM samples were prepared by dispensing a drop of the sample dispersion on a copper grid followed by drying in a vacuum oven (Binder VD-23 operating at ~20 mbar and 313 K). XRD pattern was recorded on a Bruker D8 advance X-ray diffractometer using Cu K $\alpha$  radiation ( $\lambda = 1.5405 \text{ \AA}$ ). The centrifugation of samples was performed on an Eppendorf 5810R centrifuge.

## 6.3 Results and Discussion

### 6.3.1 Fabrication of Octahedral Ag<sub>44</sub>(*p*-MBA)<sub>30</sub> NC-SCs

The synthesis of Ag<sub>44</sub>(*p*-MBA)<sub>30</sub> NCs was based on the method of Bigioni *et al.* with several minor changes.<sup>3</sup> The as-synthesized raw Ag<sub>44</sub>(*p*-MBA)<sub>30</sub> NCs showed well-defined absorption peaks at 415, 485, 538, 645 and 835 nm which are identical to the characteristic absorption features of Ag<sub>44</sub>(SR)<sub>30</sub> NCs (Figure 6.1a),<sup>27-28,66,229</sup> an indication of the high purity of the raw product. The TEM image (Figure 6.1b) of the as-synthesized Ag<sub>44</sub>(*p*-MBA)<sub>30</sub> NCs shows that the Ag core size was <2 nm.

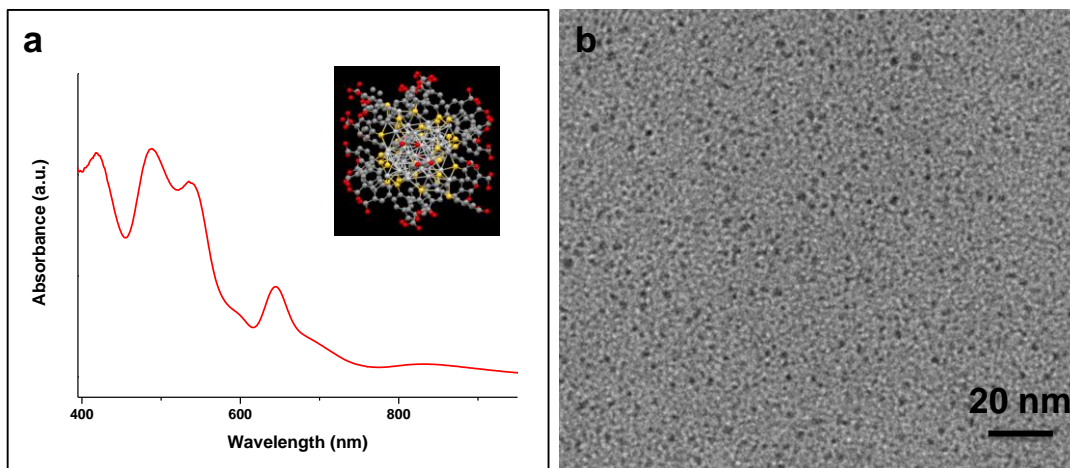


**Figure 6.1** UV-vis absorption spectrum (a) and TEM image (b) of freshly prepared  $\text{Ag}_{44}(\text{p-MBA})_{30}$  NCs. Inset in (a) schematically illustrates the structure of a  $\text{Ag}_{44}(\text{p-MBA})_{30}$  NC (drawn according to the crystal structure reported by Desireddy *et al.*<sup>27</sup>) where red dots are O atoms, dark grey dots are C atoms, yellow dots are S atoms, and light grey dots are Ag atoms. H atoms are omitted in the illustration for a cleaner representation.

Contrary to the crystallization of protonated  $\text{Ag}_{44}(\text{p-MBA})_{44}$  NCs in a single solvent (DMF) system done previously, the crystallization of deprotonated  $\text{Ag}_{44}(\text{p-MBA})_{44}$  NCs (with  $\text{Cs}^+$  counterions) in this study was carried out in a dual-solvent system where a good solvent (*e.g.*, water) was used to increase the solubility of deprotonated  $\text{Ag}_{44}(\text{p-MBA})_{44}$  NCs in a solvent mixture containing a bad solvent (*e.g.*, DMSO). The selection of the good/bad solvent pair was based on vapor pressure differences where the good one should possess a higher vapor pressure (*i.e.*, easier to evaporate) than the bad one. Slow and selective evaporation of the good solvent could then occur to induce the crystallization of  $\text{Ag}_{44}(\text{p-MBA})_{44}$  NCs.

Experimentally, the raw  $\text{Ag}_{44}(\text{p-MBA})_{30}$  NCs were first pelletized by centrifugation in the presence of ethanol, followed by washing with 66 mM CsOH aqueous solution thrice to fully deprotonate the *p*-MBA ligands. The deprotonated  $\text{Ag}_{44}(\text{p-MBA})_{30}$  NCs were redissolved in a DMSO/water mixture ( $[\text{NC}] = 0.73 \text{ mM}$ ) containing a predetermined concentration of  $\text{Cs}^+$  ( $[\text{Cs}^+]$ , from the dissociation of dissolved CsOH).

The solution was then placed in a vacuum oven ( $\sim 20$  mbar and 313 K) to remove the water. After 1-3 days of growth (with duration depending on the volume fraction of DMSO,  $f_{\text{DMSO}}$  in the dual-solvent),  $\text{Ag}_{44}(\text{p-MBA})_{30}$  NC-SCs were recovered as a black-red precipitate at the bottom of the crystallization tube.

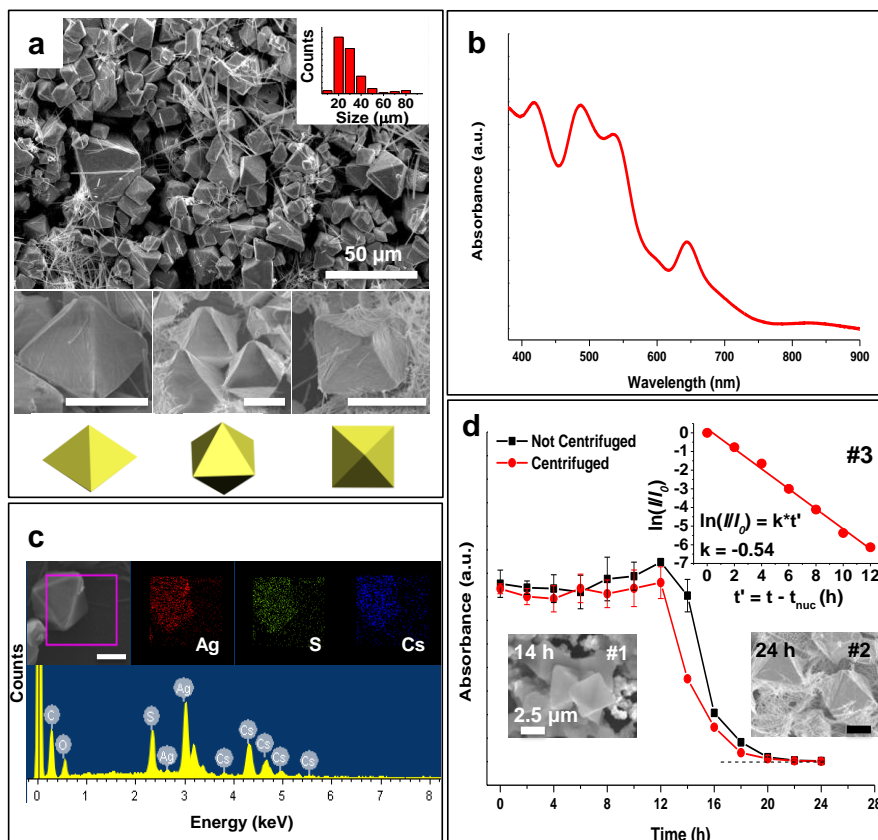


**Figure 6.2** (a) SEM image, (b) UV-vis absorption spectrum, and (c) EDX elemental analysis of octahedral supracrystals grown at  $[\text{Cs}^+] = 33$  mM and  $f_{\text{DMSO}} = 0.5$ ; and (d) UV-vis absorbance at  $\lambda = 645$  nm ( $I$ ) of the crystallization solution before (black line) and after (red line) centrifugation plotted against evaporation time ( $t$ ). The top inset in (a) shows the size histogram of supracrystals, while the bottom insets in (a) show the FESEM images and the schematic illustrations of supracrystals viewed from 3 different directions. Upper and lower panels in (c) are the elemental maps and EDX spectrum, respectively. Insets #1-2 in (d) show the FESEM images of supracrystals harvested at different  $t$ , and inset #3 shows the fit of a kinetic model for the precipitation reaction of  $\text{Ag}_{44}(\text{p-MBA})_{30}$  NCs, where  $t_{\text{nuc}} = 12$  h was used in the fitting. All scale bars in the EM images are 10  $\mu\text{m}$  unless indicated otherwise.

In stark contrast to protonated  $\text{Ag}_{44}(\text{p-MBA})_{30}$  NCs which formed rhombohedral SCs,<sup>27</sup> the  $\text{Cs}^+$ -deprotonated  $\text{Ag}_{44}(\text{p-MBA})_{30}$  NCs were packed into SCs with an

octahedral shape at  $[\text{Cs}^+] = 33 \text{ mM}$  and  $f_{\text{DMSO}} = 0.5$  (Figure 6.2a). The SCs fabricated as such encompassed a broad size distribution (the top inset in Figure 6.2a) with an average value of  $24.48 \text{ }\mu\text{m}$  (from counting  $>100$  SCs). The regular octahedral morphology (bottom insets in Figure 6.2a) of the SCs suggests them to be single-crystalline supracrystals with  $\text{O}_h$  symmetry, symmetry characteristic of the cubic crystal system which is not found in other crystal systems. The octahedral morphology is congruent with *f.c.c.* SCs enclosed by the  $(111)_{\text{SC}}$  facets, as confirmed by a powder X-ray diffraction pattern where the most dominant  $(111)_{\text{SC}}$  peak was located at  $2\theta = \sim 4.19^\circ$  (calculated value =  $4.20^\circ$ , see Figure 6.3 for more calculation details). We posit that the formation of octahedral SCs was thermodynamically driven. After the complete elimination of the directional H-bonds, the interaction between  $\text{Cs}^+$ -deprotonated  $\text{Ag}_{44}(\text{p-MBA})_{30}$  NCs should be non-directional. The non-directional bonding habit, together with uniform size, *pseudo*-spherical geometry, and a rigid surface (brought about by the rigidity of the *p*-MBA ligand); the  $\text{Cs}^+$ -deprotonated  $\text{Ag}_{44}(\text{p-MBA})_{30}$  NCs may be regarded as hard-sphere-like supramolecular atoms, and their packing may be approximated by the classic hard spheres model. The hard spheres model suggests that the depletion force (entropic effect) could drive the packing of spheres into the most condensed pattern (*e.g.*, *f.c.c.* packing).<sup>53,149,230</sup>

Several independent observations confirmed that the octahedral SCs were formed by assimilation of  $\text{Ag}_{44}(\text{p-MBA})_{30}$  NCs in the presence of  $\text{Cs}^+$ . First, after redissolution in water (containing 66 mM CsOH for NC stability considerations, see §6.3.3 for more details), the “SCs” showed identical UV-vis absorption spectrum (Figure 6.2b) as that of discrete  $\text{Ag}_{44}(\text{p-MBA})_{30}$  NCs (Figure 6.1a), suggesting that the size and structure of  $\text{Ag}_{44}(\text{p-MBA})_{30}$  NCs were preserved in the SCs. Additional supporting evidence also came from energy-dispersive X-ray spectroscopy (EDX)

analysis. First, all of the elements identified in the EDX spectrum (Figure 6.2c, down panel) were those of  $\text{Ag}_{44}(\text{p-MBA})_{30}$  NCs and  $\text{Cs}^+$  cations. Quantitative analysis returned the atomic ratio as  $\text{Au} : \text{S} : \text{Cs} = 1 : 0.68 : 0.76$ , consistent with completely  $\text{Cs}^+$ -deprotonated NC with the molecular formula of  $\text{Cs}_4\text{Ag}_{44}(\text{SPhCOOCs})_{30}$  (calculated atomic ratio of  $\text{Au} : \text{S} : \text{Cs} = 1 : 0.68 : 0.77$ , association of 4 additional  $\text{Cs}^+$  was for neutralization of 4 e- core charge<sup>27</sup>). In addition, the elemental maps of a typical octahedral SC (Figure 6.2c, up panel) show uniform distributions of Ag (red), sulfur (green), and Cs (blue) in the SC. Taken together, UV-vis spectroscopy and EDX measurements indicate the conservation of shape and size of  $\text{Ag}_{44}(\text{p-MBA})_{30}$  NCs in the octahedral SCs.

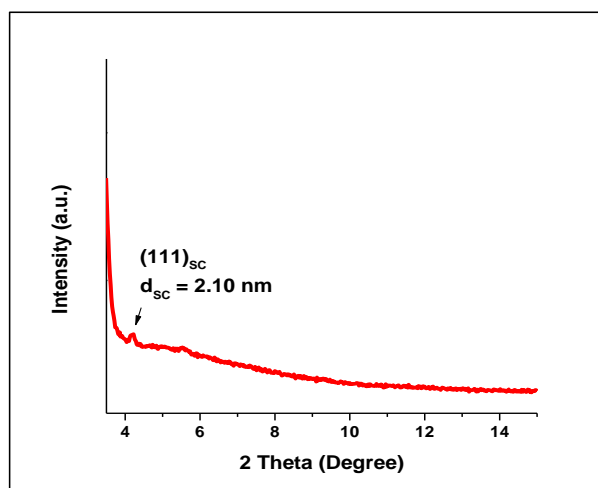


**Figure 6.3** Powder XRD pattern of octahedral  $\text{Ag}_{44}(\text{p-MBA})_{30}$  NC-SCs grown in a solution of  $f_{\text{DMSO}} = 0.5$  and  $[\text{Cs}^+] = 33$  mM. The peak at  $2\theta = 4.19^\circ$  was assigned to *f.c.c.*  $(111)_{\text{SC}}$  facets. Theoretical  $2\theta$  corresponding to *f.c.c.*  $(111)_{\text{SC}}$  could be estimated based on the reported packing diameter ( $D = 2.58$  nm) of  $\text{Ag}_{44}(\text{p-MBA})_{30}$  NCs in the SCs.<sup>27</sup> The  $D$  was transcribed into the lattice parameter  $a$  of a *f.c.c.* SC via the equation  $a = \sqrt{2}D$ . Since the X-ray source was Cu  $\text{K}_\alpha$  radiation ( $\lambda = 1.5405$  Å),  $2\theta$  corresponding to *f.c.c.*  $(111)_{\text{SC}}$  was calculated to be  $4.20^\circ$ , in good agreement with the measured value ( $2\theta = 4.19^\circ$ ).

In order to gain some insights into the crystallization process, we monitored the crystallization by following the NC concentration ( $[\text{NC}]$ ) as a function of the time of evaporation ( $t$ ). The characteristic absorbance of  $\text{Ag}_{44}(\text{p-MBA})_{30}$  NCs at  $\lambda = 645$  nm

(denoted as  $I$ ) was used as a proxy for  $[\text{NC}]$ . Figure 6.2d shows two sets of  $I$ - $t$  plots from crystallization solutions before (black line) and after (red line) centrifugation (5,000 rpm, 3 min) respectively. The purpose of centrifugation was to remove any small SCs suspended in the crystallization solution. The solutions before and after centrifugation both showed nearly time-invariant  $I$  values in the early stage of evaporation; forming plateaus in the  $I$ - $t$  plot. The  $I$  values before and after centrifugation are also close to each other. These observations indicate that the  $\text{Ag}_{44}(\text{p-MBA})_{30}$  NCs existed as discrete particles at this stage. After the plateau  $I$  started to decline exponentially with time and the  $I$  values before and after centrifugation also departed from each other more distinctively especially in the early stage of the decline ( $t = 14$  h). This signals the start of the formation of small SCs, as evidenced by the FESEM analysis (inset #1 of Figure 6.2d) at  $t = 14$  h where small octahedral SCs (several  $\mu\text{m}$  in size) were found. After  $t = 14$  h, the  $I$  values before and after centrifugation continued to decline but gradually approached each other again, suggesting the settling and the growth of SCs in size. Typical FETEM image corresponding to well-grown octahedral SCs is shown in the inset #2 of Figure 6.2d for ease of comparison.

The  $I$ - $t$  measurements suggest that crystallization probably occurred through a “nucleation-growth” process (Figure 6.4).<sup>231</sup> In the early stage of evaporation ( $t < 12$  h, Phase 0 in Route I of Figure 6.4), the change in solvent polarity was not sufficient to induce the crystallization of  $\text{Ag}_{44}(\text{p-MBA})_{30}$  NCs and hence the  $\text{Ag}_{44}(\text{p-MBA})_{30}$  NCs remained in the solution phase (the  $I$  plateau in the  $I$ - $t$  plot). However, when the decrease in polarity continued with time due to the evaporation of water, the solubility of  $\text{Ag}_{44}(\text{p-MBA})_{30}$  NCs ( $[\text{NC}]_s$ ) would eventually be exceeded and supersaturation of  $\text{Ag}_{44}(\text{p-MBA})_{30}$  NCs (as measured by  $S = [\text{NC}]/[\text{NC}]_s$ ) occurred in the solution. When



$S$  was high enough (the critical value,  $S_{\text{cri}}$ ) to overcome the energy barrier for nucleation, the nucleation of SCs was made possible. This is the nucleation phase of crystallization (Phase I in Route I of Figure 6.4). Since nucleation is usually complete within a short period of time, it is difficult to accurately identify the nucleation phase in the  $I$ - $t$  plot. However, based on the observation of extensive formation of small SCs at  $t = 14$  h, we expect the nucleation time ( $t_{\text{nuc}}$ ) to be between 12 and 14 h. The octahedral shape of these small SCs also suggests that the nuclei of SCs were also octahedral. After nucleation was the growth phase of SCs ( $t > t_{\text{nuc}}$ , Phase II in Route I of Figure 6.4) where SCs grew by uniform deposition of newly precipitated NCs on the surface of the growing nuclei. The depletion of discrete  $\text{Ag}_{44}(\text{p-MBA})_{30}$  NCs was more gradual in the growth phase, as shown by the decay of  $I$  at  $t > t_{\text{nuc}}$ .

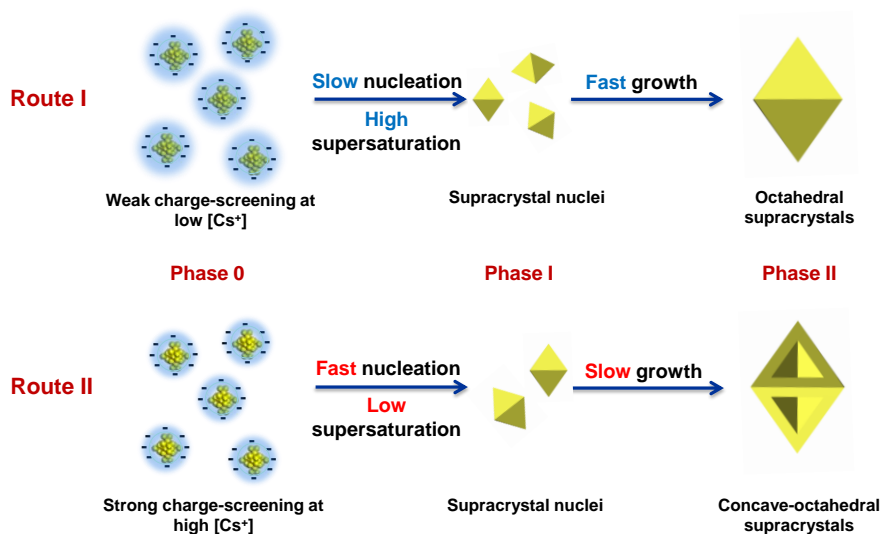


**Figure 6.4** Schematic illustration of the formation of octahedral (Route I) and concave-octahedral (Route II)  $\text{Ag}_{44}(\text{p-MBA})_{30}$  NC supracrystals.

### 6.3.2 Fabrication of Concave-Octahedral $\text{Ag}_{44}(\text{p-MBA})_{30}$ NC-SCs

With the above understanding it should be possible to modify the shape of SCs by manipulating the kinetics of their growth. We learn from the synthesis of nanocrystals

that concave faces could be developed on a polyhedral nanocrystal by selectively depositing newly-formed atoms on the high curvature sites (edges and corners).<sup>232-234</sup> Selective deposition is facilitated by a low rate of generation of the depositing atoms.<sup>233-234</sup> We have applied the principle (a kinetic control strategy) to program the spatial arrangement of constituent nanocrystals in heterogeneous noble metal nanocrystals in our recent work.<sup>235-236</sup> We expect the strategy to also work for the shape-engineering of  $\text{Ag}_{44}(\text{p-MBA})_{30}$  NC-SCs. The precipitation kinetics of  $\text{Ag}_{44}(\text{p-MBA})_{30}$  NCs in the growth solution should be the equivalence of the atom generation kinetics in nanocrystal synthesis key for shape-engineering. Since deprotonated  $\text{Ag}_{44}(\text{p-MBA})_{30}$  NCs carry a high charge (34 e<sup>-</sup> per NC, where 30 e<sup>-</sup> are from the deprotonation of *p*-MBA ligands and 4 e<sup>-</sup> are from the charge in the core),<sup>27</sup> we hypothesized that the precipitation kinetics of  $\text{Ag}_{44}(\text{p-MBA})_{30}$  NCs could therefore be manipulated by the selective screening of the  $\text{Ag}_{44}(\text{p-MBA})_{30}$  NC's charge.

We therefore carried out the crystallization of  $\text{Ag}_{44}(\text{p-MBA})_{30}$  NCs under a strong charge-screening environment created by elevating  $[\text{Cs}^+]$  while keeping other conditions intact. As shown in Figure 6.5a, the shape of  $\text{Ag}_{44}(\text{p-MBA})_{30}$  NC-SCs changed from octahedron to concave-octahedron after elevating  $[\text{Cs}^+]$  from 33 mM to 66 mM. These concave-octahedral SCs were morphologically similar to octahedral SCs except for a distinct depression on each face and a slightly larger size (average size = 34.15  $\mu\text{m}$ , the histogram of size distribution is shown in the inset (top) of Figure 6.5a). The chemical identity of concave-octahedral SCs was similarly characterized by UV-vis spectroscopy and EDX elemental analysis. The redissolved SCs (in 66 mM CsOH aqueous solution) showed identical UV-vis absorption features (Figure 6.5b) as those of discrete  $\text{Ag}_{44}(\text{p-MBA})_{30}$  NCs (Figure 6.1a). Elemental analysis (Figure 6.5c, top panel) also confirmed the uniform distribution of Ag (red), S (green) and Cs (blue)

throughout the concave-octahedral SC. All elements except Cu (from the copper grid in EDX analysis) (Figure 6.5c, bottom panel) could be assigned to  $\text{Ag}_{44}(\text{p-MBA})_{30}$  NCs and  $\text{Cs}^+$  cations.

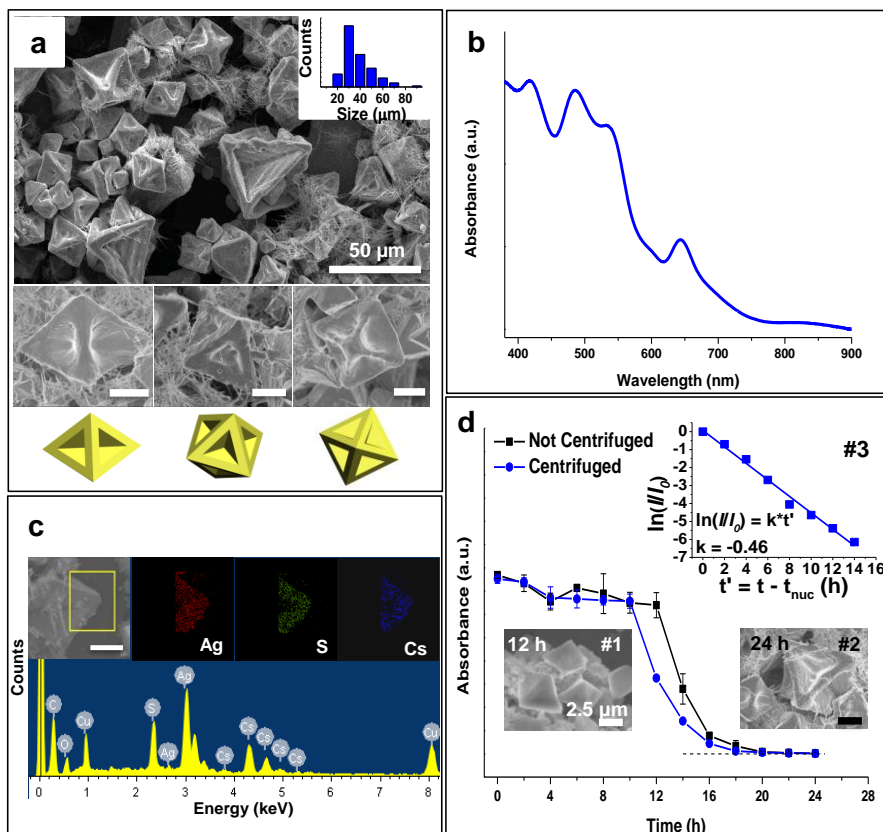


**Figure 6.5** SEM image, (b) UV-vis absorption spectrum, and (c) EDX elemental analysis of concave-octahedral supracrystals grown at  $[\text{Cs}^+] = 66 \text{ mM}$  and  $f_{\text{DMSO}} = 0.5$ ; and (d) UV-vis absorbance at  $\lambda = 645 \text{ nm}$  ( $I$ ) of the crystallization solution before (black line) and after (blue line) centrifugation plotted against  $t$ . The top inset in (a) shows the size histogram of supracrystals, while the bottom insets in (a) show the FESEM images and schematic illustrations of supracrystals viewed from 3 different directions. The upper and lower panels in (c) are elemental maps and EDX spectrum, respectively. Insets #1-2 in (d) show the FESEM images of supracrystals obtained at different  $t$ , and inset #3 shows the fit of a kinetic model for the precipitation reaction of  $\text{Ag}_{44}(\text{p-MBA})_{30}$  NCs, where  $t_{\text{nuc}} = 10 \text{ h}$  was used in the fitting. All scale bars in the EM images are  $10 \mu\text{m}$  unless indicated otherwise.

The  $I$ - $t$  plots in Figure 6.5d suggest that the growth of concave-octahedral SCs was dependent on charge-screening-assisted (or  $\text{Cs}^+$ -assisted) nucleation and growth. The  $I$ - $t$  plots of concave-octahedral SCs before and after centrifugation are visually similar to those of octahedral SCs but there are a few important differences. The most noticeable difference is the earlier onset of the divergence of  $I$  before and after centrifugation ( $t = 12$  h for the concave-octahedral SCs vs 14 h for the octahedral SCs). This is suggestion that the nucleation of concave-octahedral SCs was kinetically more facile (a  $t_{\text{nuc}}$  between 10-12 h) caused most likely by the stronger charge-screening at  $[\text{Cs}^+] = 66$  mM. As shown in Route II of Figure 6.4 (Phase 0), the more compressed double layer of  $\text{Ag}_{44}(\text{p-MBA})_{30}$  NC at  $[\text{Cs}^+] = 66$  mM increased the approach of neighboring NCs and hence the tendency for aggregation (nucleation). The relative lowering of the energy barrier of nucleation enabled nucleation to occur at a lower  $S_{\text{cri}}$ , which translated to a shorter time of evaporation (Phase I in Route II of Figure 6.4). A direct consequence of the precipitation of  $\text{Ag}_{44}(\text{p-MBA})_{30}$  NCs at lower  $S_{\text{cri}}$  was a slower precipitation kinetics (Phase II in Route II of Figure 6.4). This was confirmed by the analysis of the kinetics of decay of the  $I$  profile during the growth phases of both octahedral and concave-octahedral SCs (inset #3 of Figure 6.2d and 6.5d respectively).  $I$  after centrifugation was used in the kinetic analysis since it is a more accurate measure of  $[\text{NC}]$ . In both cases, the exponential decay of  $I$  followed a *pseudo*-1<sup>st</sup> order kinetics ( $\ln(I/I_0) = k \times (t - t_{\text{nuc}})$ , where  $k$  is the specific rate constant and  $I_0$  denotes the absorbance at  $t_{\text{nuc}}$ ). The calculated  $k$  values were 0.54 (with a coefficient of determination ( $R^2$ ) of 0.993) and 0.46 ( $R^2 = 0.989$ ) for the growth of octahedral SCs (inset #3 of Figure 6.2d) and the growth of concave-octahedral SCs (inset #3 of Figure 6.5d) respectively, confirming the slower intrinsic kinetics for the precipitation of  $\text{Ag}_{44}(\text{p-MBA})_{30}$  NCs. The slower rate of precipitation promoted the preferential

deposition of newly precipitated  $\text{Ag}_{44}(\text{p-MBA})_{30}$  NCs onto the corners and edges of pre-existing nuclei to form the concave-octahedral SCs. The parallelism between the kinetic control of selective deposition in the synthesis of SCs and the kinetic control of selective deposition in the synthesis of concave-polyhedral nanocrystals is therefore established.<sup>233-234</sup>

The corner/edge-selective deposition on octahedral SCs was also validated by FESEM analysis. The size and morphology of small SCs obtained at  $t = 12$  h, when the  $I$  values before and after centrifugation began to diverge, were examined by FETEM (inset #1 of Figure 6.5d). These small SCs were octahedral (several  $\mu\text{m}$  in size) with slightly concave faces. The extent of depression in the faces was markedly lower than that of the fully-developed concave-octahedral SCs (inset #2 of Figure 6.5d). This is a good indication that the face-concavity of concave-octahedral SCs was developed by the selective deposition of newly precipitated  $\text{Ag}_{44}(\text{p-MBA})_{30}$  NCs on the corners and edges of octahedral nuclei.

### 6.3.3 The Operating Regions of Shape-Tailorable Crystallization of $\text{Ag}_{44}(\text{p-MBA})_{30}$ NCs

It should be mentioned that the charge-screening-assisted (or  $\text{Cs}^+$ -assisted) nucleation and growth mechanism requires a suitably low  $S$  value in the starting solution to take effect. The  $S$  value in starting solution could be controlled by  $f_{\text{DMSO}}$ . We found that octahedral SCs were the only crystallization product throughout a broad  $[\text{Cs}^+]$  range of 16.5-99 mM (Figure 6.6b-j and f-m) at  $f_{\text{DMSO}} = 0.6$  ( $> 0.5$ ,  $f_{\text{DMSO}} = 0.5$  was used in this study to produce both octahedral and concave-octahedral SCs). An initially high  $S$  value in the starting solution could easily transcend the range of  $S$

suitable for corner/edge-selective deposition. In such cases, the precipitation kinetics was fast regardless of the value of  $[Cs^+]$ , favoring the formation of octahedral SCs.

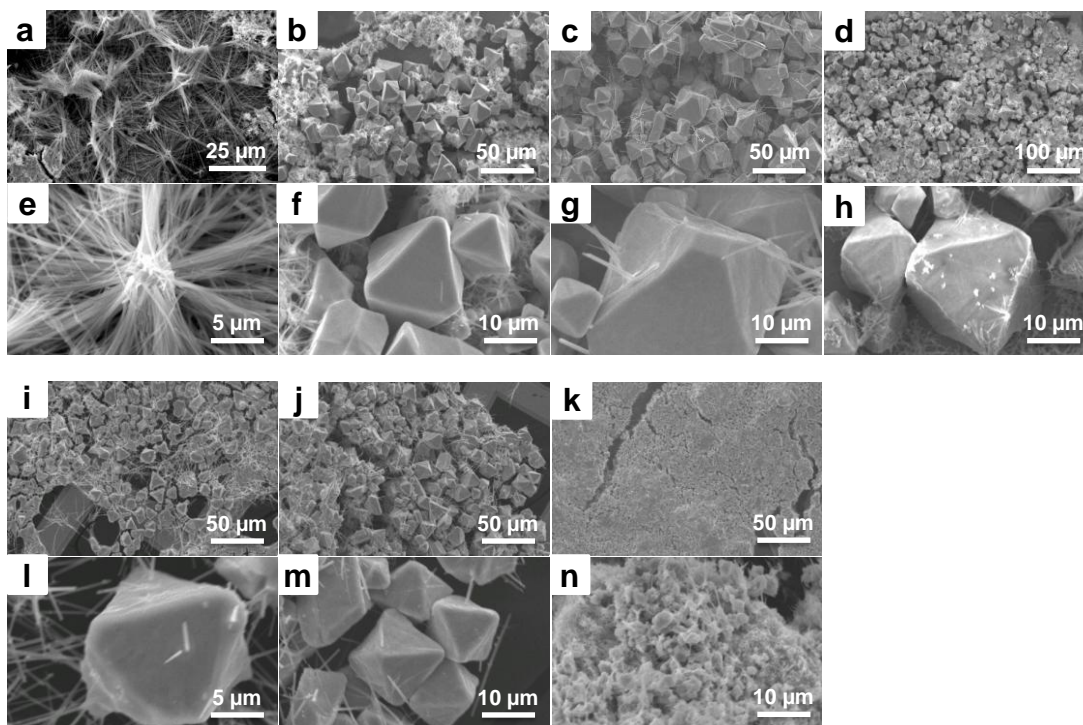


**Figure 6.6** SEM images of assembled/crystallized  $Ag_{44}(p-MBA)_{30}$  NCs at  $f_{DMSO} = 0.6$  and  $[Cs^+] = 8.25$  mM (a, e), 16.5 mM (b, f), 33 mM (c, g), 66 mM (d, h), 82.5 mM (i, l), 99 mM (j, m) and 132 mM (k, n). (a-d, i-k) and (e-h, l-n) are low and high magnification views, respectively.

In addition, it was found that  $[Cs^+]$  should be within a certain range of values for crystallization to occur. Extreme  $[Cs^+]$  values (too high or too low) spoiled the crystallization process. For example, at a very high  $[Cs^+]$  of 132 mM (at  $f_{DMSO} = 0.6$ ), the NCs were not soluble in the starting solution at ambient conditions. The very strong charge-screening effects led the NCs to aggregate randomly into an amorphous film (see morphology in Figure 6.6k and n). The amorphous film is highly soluble in water. Their UV-vis spectrum (Figure 6.7, black line) shows absorption features characteristic of discrete  $Ag_{44}(p-MBA)_{30}$  NCs (Figure 6.1a), suggesting that the size and structure of  $Ag_{44}(p-MBA)_{30}$  NCs are preserved in the amorphous film.

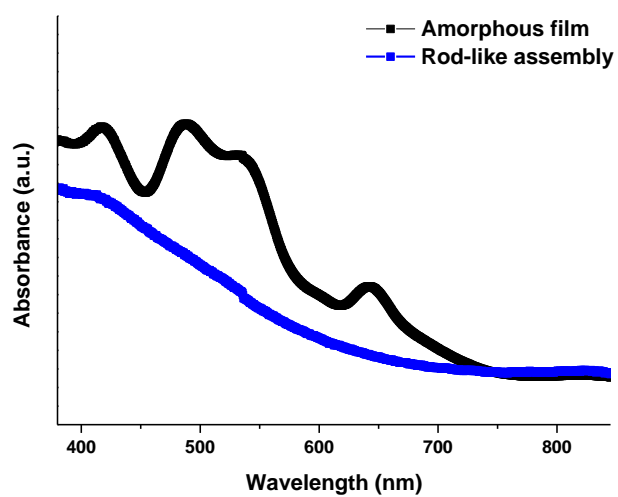


**Figure 6.7** UV-vis absorption spectra of a typical amorphous film (black line) and a typical rod-like assembly (blue line) redispersed in 66 mM CsOH aqueous solution.

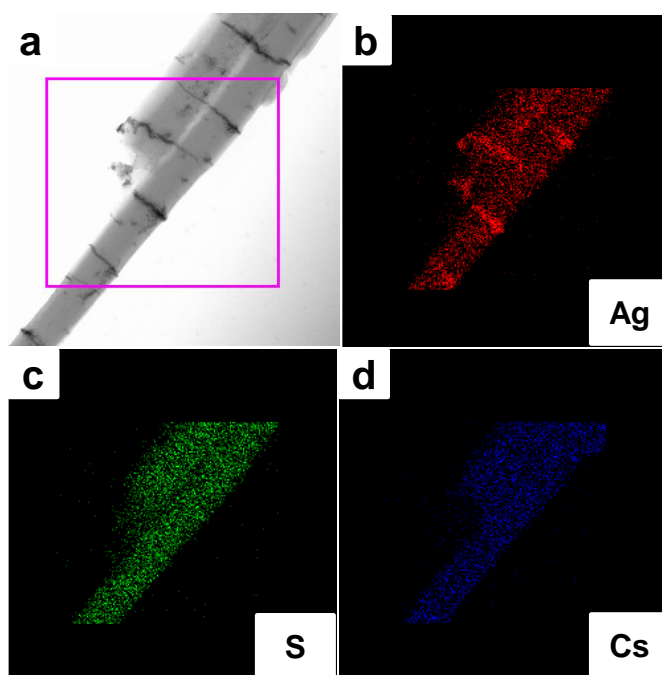


**Figure 6.8** STEM image (a) and elemental maps of Ag (b), S (c), and (d) Cs in the rod-like assembly.

At the other extreme of a very low  $[\text{Cs}^+]$  (8.25 mM), a rod-like assembly of NCs was observed (Figure 6.6a and e). The rod-like assemblies are not soluble in aqueous solution and their aqueous dispersion displays a featureless absorption spectrum typical of the decomposition of  $\text{M}_n(\text{SR})_m$  NCs into  $\text{M}(\text{I})\text{-SR}$  complexes.<sup>75,139,216,237</sup> This observation suggests that the rod-like assemblies are likely packed  $\text{Ag}(\text{I})\text{-}(p\text{-MBA})$  complexes (the decomposition products of  $\text{Ag}_{44}(p\text{-MBA})_{30}$  NCs.). The hypothesis was verified by STEM and EDX elemental analysis shown in Figure 6.8. According to the STEM (Figure 6.8a) and EDX (Figure 6.8b-d) results, the rod-like assembly may be described better as a “bamboo-like” assembly where  $\text{Ag}(0)$  nodes decorate the aligned stems of  $\text{Ag}(\text{I})\text{-}(p\text{-MBA})$  complexes.  $\text{Cs}^+$  was assimilated in the aligned  $\text{Ag}(\text{I})\text{-}(p\text{-MBA})$  complexes for purpose of charge neutrality. The formation of bamboo-like pattern could be due to the phase-separation of  $\text{Ag}(0)$  and  $\text{Ag}(\text{I})\text{-}(p\text{-MBA})$  complexes released from the decomposition of  $\text{Ag}_{44}(p\text{-MBA})_{30}$  NCs. We posit that the decomposition of  $\text{Ag}_{44}(p\text{-MBA})_{30}$  NCs released  $\text{Ag}(0)$  from the NC core, and  $\text{Ag}(\text{I})\text{-}(p\text{-MBA})$  complexes from the NC protecting shell in  $\text{O}_2$ -free environment. The aggregation of  $\text{Ag}(0)$  formed the nodes and the assembly of  $\text{Ag}(\text{I})\text{-}(p\text{-MBA})$  complexes formed the stems in the bamboo-like assembly. The decomposition of  $\text{Ag}_{44}(p\text{-MBA})_{30}$  NCs at low  $[\text{Cs}^+]$  ( $\text{Cs}^+$  provided by  $\text{CsOH}$  dissociation) could be due to their instability in the reduced pH (Figure 6.9) environment not amped up by  $\text{CsOH}$ . It should be mentioned that a similar alignment of  $\text{Au}(\text{I})\text{-SR}$  complexes into 1D assembly has been observed before.<sup>238</sup>



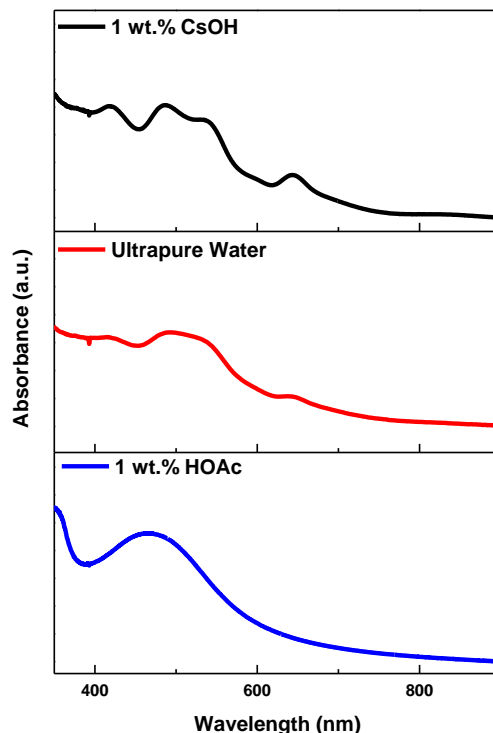


**Figure 6.9** UV-vis absorption spectra of  $\text{Ag}_{44}(\text{p-MBA})_{30}$  NCs in 1 wt.% CsOH ( $[\text{CsOH}] = 66 \text{ mM}$ ) aqueous solution (black line), in ultrapure water (red line), and in 1 wt.% HOAc aqueous solution (blue line). The fading of the absorption features of pure  $\text{Ag}_{44}(\text{p-MBA})_{30}$  NCs from the top to the bottom panels suggests the decreased stability of as-prepared  $\text{Ag}_{44}(\text{p-MBA})_{30}$  NCs in progressively more acidic solutions.

We have also undertaken a preliminary survey of the operating regions for the shape-engineering of  $\text{Ag}_{44}(\text{p-MBA})_{30}$  NC-SCs in the DMSO/water dual-solvent system. We mapped out the  $[\text{Cs}^+]$ - $f_{\text{DMSO}}$  space since these two parameters have the most influence on SC formation (Figure 6.10). SEM images corresponding to each dotted point in the diagrams of Figures 6.2, 6.5, 6.6 and 6.11-6.15 were taken. The diagram constructed as such (Figure 6.10) can be divided into four regions. Two of them are suitable for SC formation, *i.e.*, the upper-left region (II) for concave-octahedral SCs and the middle valley region (III) for the octahedral SCs. A loose but simple rule of thumb for SC shape-engineering is that high  $[\text{Cs}^+]$  and low  $f_{\text{DMSO}}$  favor the formation of concave-octahedral SCs, and the reverse condition low  $[\text{Cs}^+]$  and high

$f_{\text{DMSO}}$  favor the formation of octahedral SCs. On the other hand, experimental settings falling into the other two regions (region (I) and (IV)) would not produce SCs. Region (I) is mainly due to the low stability of  $\text{Ag}_{44}(\text{p-MBA})_{30}$  NCs in the CsOH-deficient low pH environment as discussed before. In this region,  $\text{Ag}_{44}(\text{p-MBA})_{30}$  NCs would readily decompose. The alignment of the fragments of decomposed  $\text{Ag}_{44}(\text{p-MBA})_{30}$  NCs gives rise to rod-like assemblies in this region. Region (IV) is defined by the solubility limit of  $\text{Ag}_{44}(\text{p-MBA})_{30}$  NCs in the starting solution at ambient conditions where solubility is limited by either a strong charge-screening effect (due to high  $[\text{Cs}^+]$ ) or the low polarity of solvent (high  $f_{\text{DMSO}}$ ). The fast aggregation of  $\text{Ag}_{44}(\text{p-MBA})_{30}$  NCs in this region results in the formation of an amorphous film.

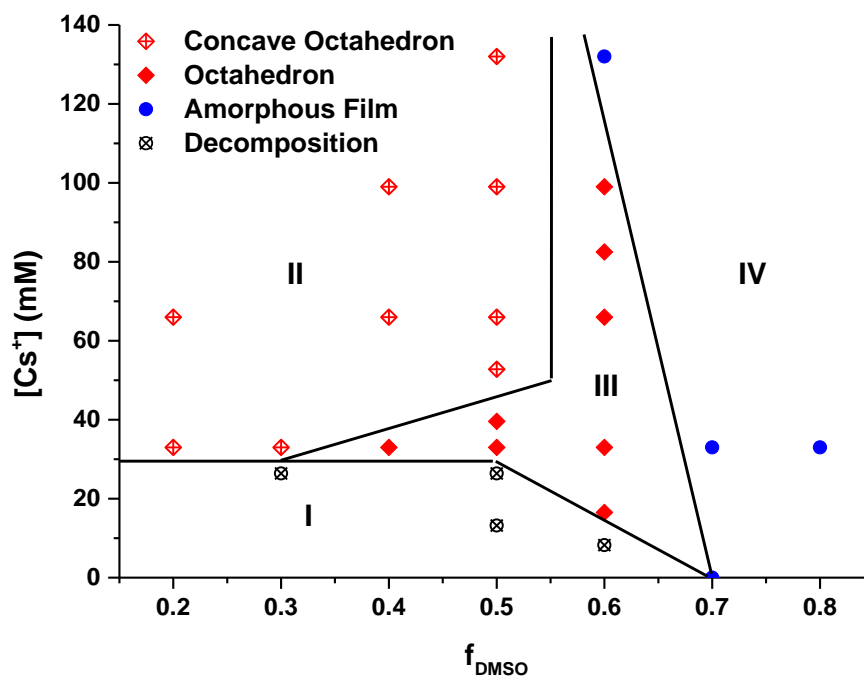


**Figure 6.10** The operating regions of shape-tailorable crystallization of  $\text{Ag}_{44}(\text{p-MBA})_{30}$  NCs in mixtures of DMSO/water with varied  $f_{\text{DMSO}}$  and  $[\text{Cs}^+]$ .

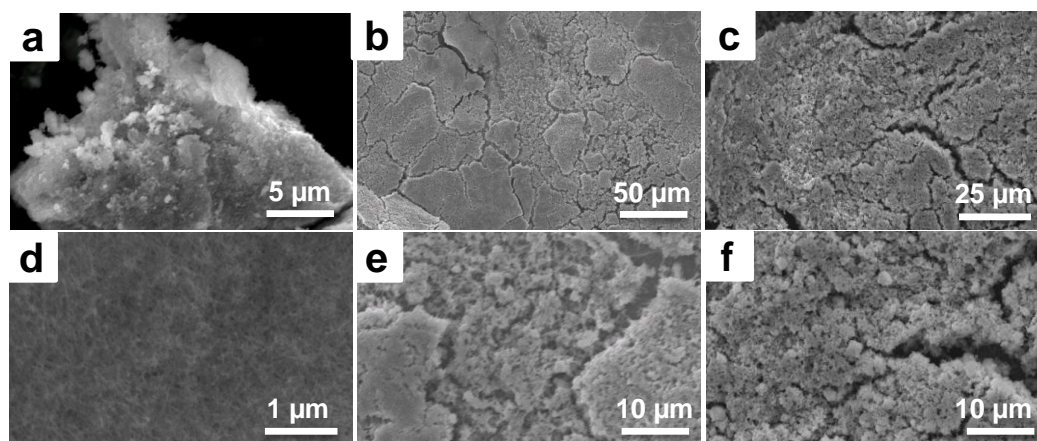


**Figure 6.11** SEM images of assembled/crystallized  $\text{Ag}_{44}(\text{p-MBA})_{30}$  NCs at  $f_{\text{DMSO}} = 0.7$  (a-b, d-e) and 0.8 (c, f).  $[\text{Cs}^+] = 0$  mM in (a, d) and 33 mM in (b-c, e-f) respectively. (a-c) and (d-f) are low and high magnification views, respectively.

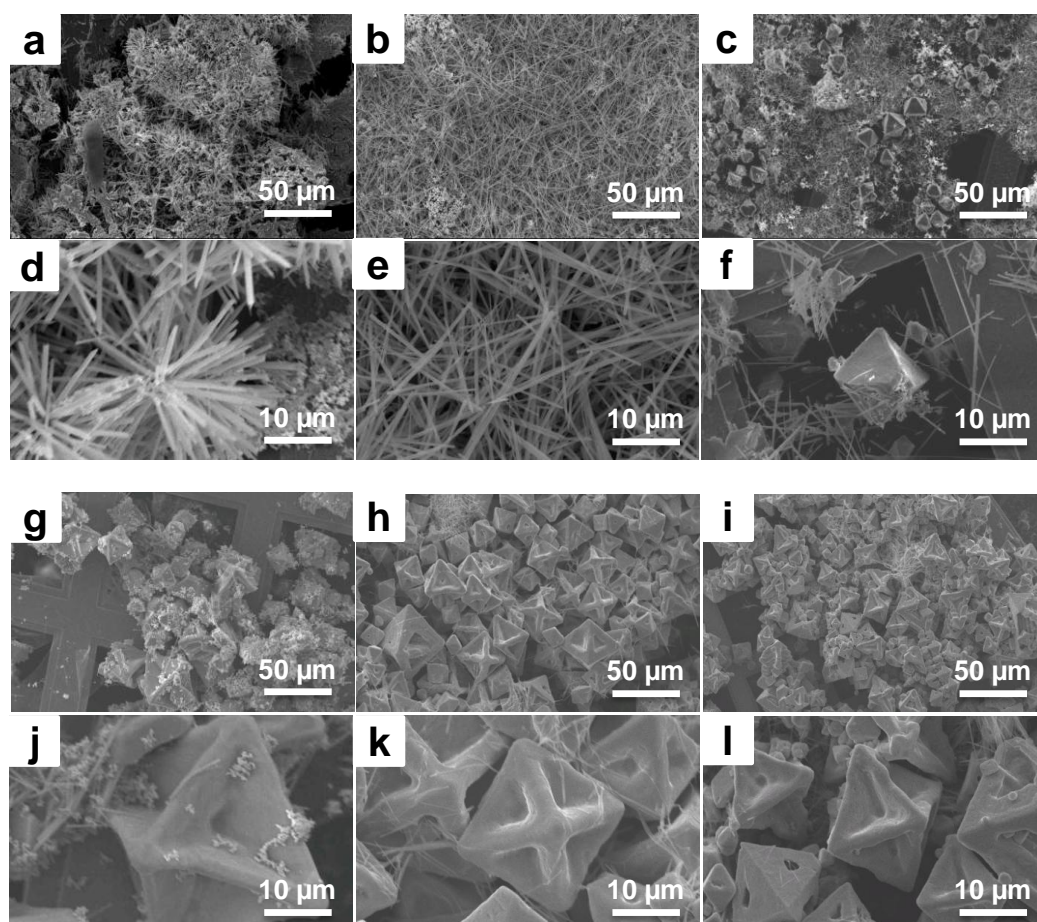


**Figure 6.12** SEM images of assembled/crystallized  $\text{Ag}_{44}(\text{p-MBA})_{30}$  NCs at  $f_{\text{DMSO}} = 0.5$  and at  $[\text{Cs}^+] = 13.2$  mM (a, d), 26.4 mM (b, e), 39.6 mM (c, f), 52.8 mM (g, j), 99 mM (h, k) and 132 mM (i, l). (a-c, g-i) and (d-f, j-l) are low and high magnification views, respectively.

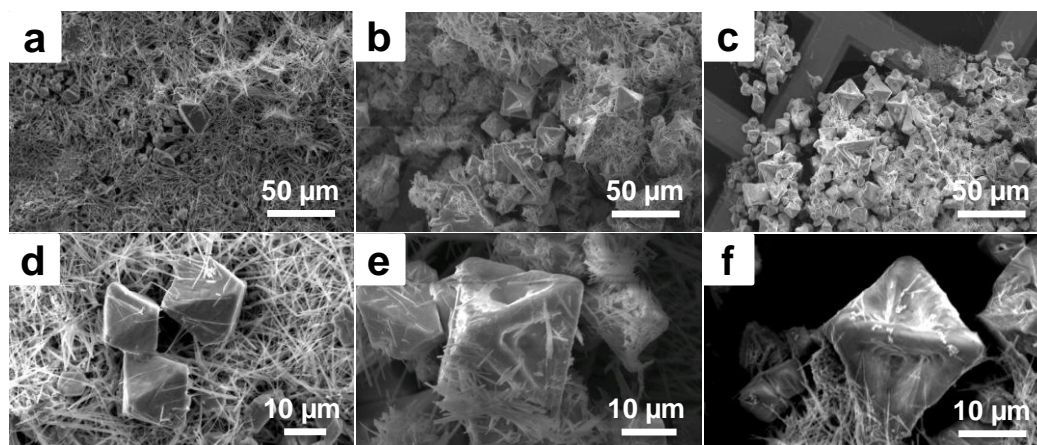


**Figure 6.13** SEM images of assembled/crystallized  $\text{Ag}_{44}(\text{p-MBA})_{30}$  NCs at  $f_{\text{DMSO}} = 0.4$  and  $[\text{Cs}^+] = 33$  mM (a, d), 66 mM (b, e), and 99 mM (c, f). (a-c) and (d-f) are low and high magnification views, respectively.

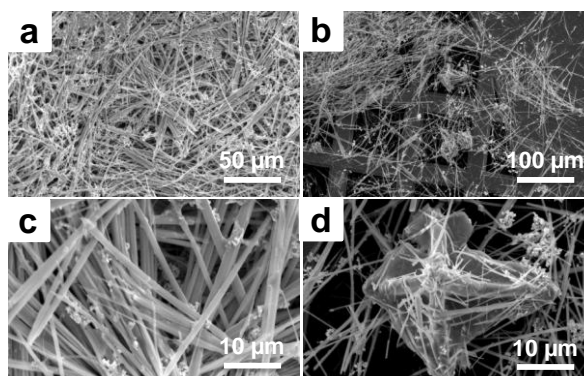


**Figure 6.14** SEM images of assembled/crystallized  $\text{Ag}_{44}(\text{p-MBA})_{30}$  NCs at  $f_{\text{DMSO}} = 0.3$  and  $[\text{Cs}^+] = 26.4$  mM (a, c) and 33 mM (b, d). (a-b) and (c-d) are low and high magnification views, respectively.

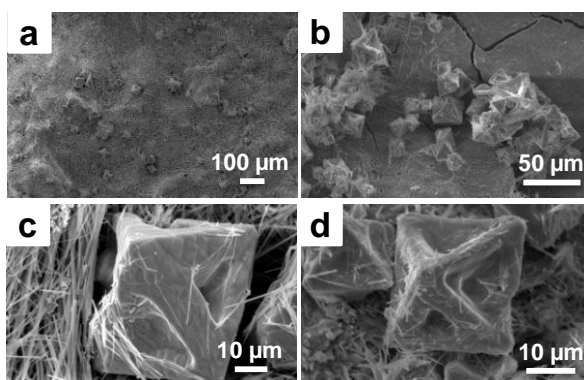


**Figure 6.15** SEM images of assembled/crystallized  $\text{Ag}_{44}(\text{p-MBA})_{30}$  NCs at  $f_{\text{DMSO}} = 0.2$  and  $[\text{Cs}^+] = 33$  mM (a, c) and 66 mM (b, d). (a-b) and (c-d) are low and high magnification views, respectively.

## 6.4 Conclusion

In summary, we have developed a simple and reproducible counterion-assisted atomic-mimetic protocol for packing  $\text{Ag}_{44}(\text{p-MBA})_{30}$  into both octahedral and concave octahedral SCs. The formation of highly symmetric *f.c.c.* octahedral SCs was promoted by the atom-like features of  $\text{Cs}^+$ -deprotonated  $\text{Ag}_{44}(\text{p-MBA})_{30}$  NCs, such as uniformity of size, *pseudo*-spherical morphology, rigid surface, and non-directional bonding. The charge screening effect of  $[\text{Cs}^+]$ , which altered the double layer characteristics of deprotonated  $\text{Ag}_{44}(\text{p-MBA})_{30}$  NCs, was highly effective in tailoring the growth kinetics of SCs. Through the delicate control of the growth kinetics we were able to create concavity in the exposed faces of the octahedral nuclei to form concave-octahedral SCs. We have also mapped out the operating regions in the  $[\text{Cs}^+]$ - $f_{\text{DMSO}}$  space to guide the shape-tailorable crystallization of  $\text{Ag}_{44}(\text{p-MBA})_{30}$  NCs. To the best of our knowledge, this is the first report on systematizing the shape-engineering of NC-SCs. The simplicity and good experimental reproducibility suggest that the counterion-assisted dual-solvent approach may also be useful for the crystallization of other noble metal NCs.

---

# CHAPTER 7 CONCLUSIONS AND RECOMMENDATIONS

## 7.1 Conclusions

Through this thesis effort, we have developed ionic, molecular, and atomic mimetic strategies for the self-assembly of noble metal (*e.g.*, Au or Ag) nanoclusters (*i.e.*, NM-NCs or  $M_n(SR)_m$  NCs) into hierarchical structures with variable sizes, morphologies, symmetries and structural orderliness. NM-NCs were made into ionic mimetic, molecular mimetic (amphiphile-mimetic), and atomic mimetic nanomaterials by rational surface modifications, and the corresponding ion-like, amphiphile-like, and hard-sphere-like behaviors were used to control the self-assembly of NM-NCs into ordered structures in varying degrees of long range order. Amorphous monodisperse colloidal spheres, bilayer-based lamellar structures with regular interlayer packing (1D ordered), and single-crystalline supracrystals (SCs, 3D ordered) were formed by ionic mimetic, amphiphile-mimetic and atomic mimetic self-assembly of the NM-NCs, respectively.

The major findings in this PhD study may be summarized briefly as follows:

- 1) High monodispersity, the enabling property for NC self-assembly, could be achieved by the deliberate control of the kinetics of NC formation. Phase equilibrium (*e.g.*, equilibrium partition between immiscible solvents, and aggregation-dissociation equilibrium) is a very effective scheme for kinetic control. The synthesis of monodisperse and atomically precise  $Au_{15}(SG)_{13}$ , and  $Au_{18}(SG)_{14}$  NCs, where SG is glutathione ligand, in Chapter 3 was based on the combination of two equilibria. A mild and unvarying reducing power was

maintained by the equilibrium partition of a mild reductant, borane *tert*-butylamine complex (TBAB) between an organic solvent and the aqueous phase. At the same time a slow and sustainable supply of Au precursor was made possible by the aggregation-dissociation equilibrium between free and aggregated Au(I)-SG complexes. The mild and constant reduction environment generated as such was able to produce monodisperse and atomically precise Au<sub>15</sub>(SG)<sub>13</sub> or Au<sub>18</sub>(SG)<sub>15</sub> NCs. We also demonstrated that the pH-sensitive aggregation-dissociation equilibrium of Au(I)-SG complexes could be used to tailor the NC size.

- 2) Chapter 4 demonstrates that ion-like structural features (*e.g.*, small size, uniform structure, and high charge density) and ion-like behaviors could also be used to drive self-assembly. This was done by imparting charges to the M<sub>n</sub>(SR)<sub>m</sub> NCs followed by ionic-crosslinking with bridging counterions. Hence negatively charged M<sub>n</sub>(SR)<sub>m</sub> NCs (*e.g.*, Au<sub>29-43</sub>(SG)<sub>27-37</sub>, Au<sub>15</sub>(SG)<sub>13</sub>, and Ag<sub>16</sub>(SG)<sub>9</sub> NCs) were used as supramolecular ions and assembled into monodisperse colloidal spheres by divalent cations (*e.g.*, Zn<sup>2+</sup> and Cd<sup>2+</sup>). The formation of monodisperse colloidal spheres, which is characteristically different from the random aggregation of large NM-NPs by counter ions, could be regarded as a first attempt (albeit not a very successful one) to mimic the formation of ionic crystals by normal ions. However, it has to be mentioned that the spherical NC-assemblies are amorphous (no regular spacing in the packing, *d*). The large size difference between negatively charged M<sub>n</sub>(SR)<sub>m</sub> NCs (of the order of ~1 nm) and counter cations (of the order of ~1 Å) could be a reason. The negatively charged M<sub>n</sub>(SR)<sub>m</sub> NCs also exhibited step-like self-assembly behavior – self-assembly only occurred when the solubility product (K<sub>sp</sub>)

between the carboxylate ions on the NC surface and the divalent cations was exceeded. A strong interaction between the close-packed NCs also resulted in luminescence enhancement, demonstrating the ability of self-assembly to modify NC properties.

- 3) Amphiphilicity could also be used to promote self-assembly of amphiphile-like NM-NCs into regular stacked lamellar structures (Chapter 5). By covering the surface of hydrophilic  $\text{Au}_{25}(\text{MHA})_{18}$  NCs (MHA is 6-mercaptohexanoic acid) with about half of a monolayer of hydrophobic cetyltrimethylammonium ( $\text{CTA}^+$ ), amphiphilic  $\text{Au}_{25}(\text{MHA})_{18}@x\text{CTA}$  NCs ( $x = 6-9$ , where  $x$  is the number of  $\text{CTA}^+$  per NC) were formed. Due to the coexistence of flexible hydrophilic MHA and hydrophobic  $\text{MHA}\cdots\text{CTA}$  ligands in comparable amounts on the NC surface,  $\text{Au}_{25}(\text{MHA})_{18}@x\text{CTA}$  NCs ( $x = 6-9$ ) were able to vary their polarity according to the medium polarity to exhibit good amphiphilicity. This medium-induced polarity modulation mechanism enabled  $\text{Au}_{25}(\text{MHA})_{18}@x\text{CTA}$  NCs ( $x = 6-9$ ) to precipitate out in a surfactant-like configuration (hydrophilic and hydrophobic moieties localized on opposite ends) in a very polar solvent (*e.g.*, dimethylsulfoxide, DMSO). The precipitated surfactant-like NCs then self-assembled into lamellar structures containing regularly stacked NC bi-layers at the liquid-air interface, in analogy to the formation of the lamellar phase (the liquid crystal phase) of common surfactants. The amphiphilicity also imparted the NCs with very good solubility in a wide range of solvents with markedly different polarities, which should increase the versatility of NC-based materials in applications.
- 4) Monodisperse  $\text{M}_n(\text{SR})_m$  NCs with a rigid surface and non-directional bonding habits (supramolecular atoms) are hard-sphere-like, and could form 3D ordered



SCs by depletion forces (entropy effect). Chapter 6 shows that the deprotonation of *p*-mercaptobenzoic acid (*p*-MBA) ligands by  $\text{Cs}^+$  (from  $\text{CsOH}$ ) could suppress the formation of directional hydrogen-bonds between the NCs, thereby eliminating the directional bonding between  $\text{Ag}_{44}(\text{p-MBA})_{30}$  NCs. The lack of a directional bonding habit, together with a uniform size, *pseudo*-spherical geometry and a rigid surface (due to the rigidity of the *p*-MBA ligand); rendered the  $\text{Ag}_{44}(\text{p-MBA})_{30}$  NCs as hard-sphere-like supramolecular atoms, and the formation of closely-packed *f.c.c.* octahedral SCs by depletion forces. Kinetics investigation revealed that the self-assembly (or crystallization) followed a  $\text{Cs}^+$ -assisted nucleation and growth mechanism. Such mechanism also provided a means to shape the  $\text{Ag}_{44}(\text{p-MBA})_{30}$  NC-SCs. Fast nucleation and slow growth, made possible by high  $\text{Cs}^+$  concentration, were found to produce concave-octahedral  $\text{Ag}_{44}(\text{p-MBA})_{30}$  NC-SCs selectively. The ability to produce NC-SCs with tailorable shapes could easily expand the NC-SC library for basic and applied research.

## 7.2 Recommendations for Future Work

### 1) Synthesis of other $\text{M}_n(\text{SR})_m$ NCs by the two-phase approach in this project

Despite the great efforts to promote the direct synthesis of NCs without separation, there still exist synthetic gaps for several  $\text{M}_n(\text{SR})_m$  NC sizes. For example, several  $\text{Au}_n(\text{SR})_m$  NCs (*e.g.*,  $(n\ m) = (33\ 22)$ ,<sup>8</sup>  $(40\ 24)$ <sup>127</sup> and  $(55\ 31)$ <sup>128</sup>) have been isolated by physical means (*e.g.*, electrophoresis and liquid chromatography), but the direct and scalable synthesis of these  $\text{Au}_n(\text{SR})_m$  NCs is still lacking. This is most probably due to their less-stable nature (in comparison with the exceptional stability of sizes such as  $(n\ m) = (25\ 18)$ ,  $(38\ 24)$ , and  $(144$

60)), which renders the common stability-based “size-focusing” method (see §2.2.2 for more details) ineffective for the synthesis of metastable  $\text{Au}_n(\text{SR})_m$  NCs.<sup>131</sup> The two-phase approach in Chapter 2, which depends more on kinetics control rather than the intrinsic stability of the  $\text{Au}_n(\text{SR})_m$  NCs, could be a good alternative for synthesis of metastable NCs. There will of course be challenges ahead such as the search for the specific, deliberate control of the experimental parameters (*e.g.*, pH, temperature, solvent polarity, and the type and amount of thiol used).

## 2) Increasing the structural orderliness in ionic-mimetic self-assembly

It is worth recalling that the colloidal spheres in Chapter 4, which were formed by ionic mimetic self-assembly of negatively charged  $\text{M}_n(\text{SR})_m$  NCs, were amorphous. We attributed the absence of a higher structural order to the large size-difference between negatively charged  $\text{M}_n(\text{SR})_m$  NCs and the counter cations. Hence, one possible way to increase the structural order of these NC-assemblies is to replace the small counter cations with positively charged  $\text{M}_n(\text{SR})_m$  NC of comparable sizes. A similar concept has earlier been used by Grzybowski and co-workers for the preparation of NP-SCs, where similarly-sized but oppositely-charged Au and Ag NPs were assembled into diamond-like SCs.<sup>239</sup> However, several technical challenges have to be addressed before one can validate/invalidate this hypothesis; for example, the lack of synthesis methods for positively charged  $\text{M}_n(\text{SR})_m$  NCs in similar size and monodispersity.

## 3) Crystallization of other $\text{M}_n(\text{SR})_m$ NCs by the atomic-mimetic self-assembly approach

Crystallization of  $\text{M}_n(\text{SR})_m$  NCs poses the greatest technical challenge to the current state of NC research. The atomic mimetic self-assembly method in Chapter 6 was shown to be able to form single-crystalline  $\text{Ag}_{44}(p\text{-MBA})_{30}$  NC-SCs, based

only on the hard-sphere-like structural features of the latter (*e.g.*, monodisperse size, *pseudo*-spherical geometry, rigid surface, and non-directional bonding habit). Thus, it is possible that the atomic mimetic method may be readily extended to the crystallization of other  $M_n(SR)_m$  NCs with similar hard-sphere-like features. Our preliminary results indicated that  $Au_{44}(p\text{-MBA})_{26}$  NCs could be crystallized via a similar atomic mimetic method (data not shown). The optimization of the crystallization conditions for  $Au_{44}(p\text{-MBA})_{26}$  NCs is still under way. In addition, the atomic-mimetic crystallization approach could also be used to engineer the shape of  $M_n(SR)_m$  NC-SCs. This is yet another way to greatly expand the  $M_n(SR)_m$  NC-SCs library for basic research and application explorations.

## REFERENCES

- (1) Whetten, R. L.; Khoury, J. T.; Alvarez, M. M.; Murthy, S.; Vezmar, I.; Wang, Z. L.; Stephens, P. W.; Cleveland, C. L.; Luedtke, W. D.; Landman, U. *Adv. Mater.* **1996**, *8*, 428.
- (2) Jin, R. *Nanoscale* **2010**, *2*, 343.
- (3) Lu, Y.; Chen, W. *Chem. Soc. Rev.* **2012**, *41*, 3594.
- (4) Yu, Y.; Yao, Q.; Luo, Z.; Yuan, X.; Lee, J. Y.; Xie, J. *Nanoscale* **2013**, *5*, 4606.
- (5) Schmid, G. *Chem. Soc. Rev.* **2008**, *37*, 1909.
- (6) Bartlett, P. A.; Bauer, B.; Singer, S. J. *J. Am. Chem. Soc.* **1978**, *100*, 5085.
- (7) Zheng, J.; Nicovich, P. R.; Dickson, R. M. *Annu. Rev. Phys. Chem.* **2007**, *58*, 409.
- (8) Negishi, Y.; Nobusada, K.; Tsukuda, T. *J. Am. Chem. Soc.* **2005**, *127*, 5261.
- (9) Yuan, X.; Luo, Z.; Yu, Y.; Yao, Q.; Xie, J. *Chem. Asian J.* **2013**, *8*, 858.
- (10) Yuan, X.; Luo, Z.; Zhang, Q.; Zhang, X.; Zheng, Y.; Lee, J. Y.; Xie, J. *ACS Nano* **2011**, *5*, 8800.
- (11) Luo, Z.; Yuan, X.; Yu, Y.; Zhang, Q.; Leong, D. T.; Lee, J. Y.; Xie, J. *J. Am. Chem. Soc.* **2012**, *134*, 16662.
- (12) Yu, Y.; Luo, Z.; Chevrier, D. M.; Leong, D. T.; Zhang, P.; Jiang, D.-e.; Xie, J. *J. Am. Chem. Soc.* **2014**, *136*, 1246.
- (13) Shang, L.; Dong, S. J.; Nienhaus, G. U. *Nano Today* **2011**, *6*, 401.
- (14) Chen, S.; Ingram, R. S.; Hostetler, M. J.; Pietron, J. J.; Murray, R. W.; Schaaff, T. G.; Khoury, J. T.; Alvarez, M. M.; Whetten, R. L. *Science* **1998**, *280*, 2098.
- (15) Chen, S.; Murray, R. W.; Feldberg, S. W. *J. Phys. Chem. B* **1998**, *102*, 9898.
- (16) Yamazoe, S.; Koyasu, K.; Tsukuda, T. *Acc. Chem. Res.* **2013**, *47*, 816.
- (17) Li, G.; Jin, R. *Acc. Chem. Res.* **2013**, *46*, 1749.
- (18) Chen, Y.-S.; Choi, H.; Kamat, P. V. *J. Am. Chem. Soc.* **2013**, *135*, 8822.
- (19) Chen, Y.-S.; Kamat, P. V. *J. Am. Chem. Soc.* **2014**, *136*, 6075.
- (20) Luo, Z.; Zheng, K.; Xie, J. *Chem. Commun.* **2014**, *50*, 5143.
- (21) Jin, R.; Zhu, Y.; Qian, H. *Chem. Eur. J.* **2011**, *17*, 6584.
- (22) Udayabhaskararao, T.; Pradeep, T. *J. Phys. Chem. Lett.* **2013**, *4*, 1553.
- (23) Pei, Y.; Zeng, X. C. *Nanoscale* **2012**, *4*, 4054.
- (24) Jadzinsky, P. D.; Calero, G.; Ackerson, C. J.; Bushnell, D. A.; Kornberg, R. D. *Science* **2007**, *318*, 430.
- (25) Zhu, M.; Aikens, C. M.; Hollander, F. J.; Schatz, G. C.; Jin, R. *J. Am. Chem. Soc.* **2008**, *130*, 5883.
- (26) Heaven, M. W.; Dass, A.; White, P. S.; Holt, K. M.; Murray, R. W. *J. Am. Chem. Soc.* **2008**, *130*, 3754.
- (27) Desireddy, A.; Conn, B. E.; Guo, J.; Yoon, B.; Barnett, R. N.; Monahan, B. M.; Kirschbaum, K.; Griffith, W. P.; Whetten, R. L.; Landman, U.; Bigioni, T. P. *Nature* **2013**, *501*, 399.
- (28) Yang, H.; Wang, Y.; Huang, H.; Gell, L.; Lehtovaara, L.; Malola, S.; Häkkinen, H.; Zheng, N. *Nat. Commun.* **2013**, *4*, 2422.
- (29) Zeng, C.; Qian, H.; Li, T.; Li, G.; Rosi, N. L.; Yoon, B.; Barnett, R. N.; Whetten, R. L.; Landman, U.; Jin, R. *Angew. Chem. Int. Ed.* **2012**, *51*, 13114.
- (30) Malola, S.; Lehtovaara, L.; Enkovaara, J.; Häkkinen, H. *ACS Nano* **2013**, *7*, 10263.

- (31) Qian, H.; Zhu, Y.; Jin, R. *Proc. Natl. Acad. Sci. U. S. A.* **2012**, *109*, 696.
- (32) Jiang, D.-e. *Nanoscale* **2013**, *5*, 7149.
- (33) Crasto, D.; Malola, S.; Brososky, G.; Dass, A.; Häkkinen, H. *J. Am. Chem. Soc.* **2014**, *136*, 5000.
- (34) Negishi, Y.; Iwai, T.; Ide, M. *Chem. Commun.* **2010**, *46*, 4713.
- (35) Mathew, A.; Natarajan, G.; Lehtovaara, L.; Häkkinen, H.; Kumar, R. M.; Subramanian, V.; Jaleel, A.; Pradeep, T. *ACS Nano* **2013**, *8*, 139.
- (36) Tracy, J. B.; Kalyuzhny, G.; Crowe, M. C.; Balasubramanian, R.; Choi, J.-P.; Murray, R. W. *J. Am. Chem. Soc.* **2007**, *129*, 6706.
- (37) Parker, J. F.; Weaver, J. E. F.; McCallum, F.; Fields-Zinna, C. A.; Murray, R. W. *Langmuir* **2010**, *26*, 13650.
- (38) Dass, A. *J. Am. Chem. Soc.* **2009**, *131*, 11666.
- (39) Toikkanen, O.; Ruiz, V.; Rönholm, G.; Kalkkinen, N.; Liljeroth, P.; Quinn, B. M. *J. Am. Chem. Soc.* **2008**, *130*, 11049.
- (40) Levi-Kalisman, Y.; Jadzinsky, P. D.; Kalisman, N.; Tsunoyama, H.; Tsukuda, T.; Bushnell, D. A.; Kornberg, R. D. *J. Am. Chem. Soc.* **2011**, *133*, 2976.
- (41) Negishi, Y.; Sakamoto, C.; Ohyama, T.; Tsukuda, T. *J. Phys. Chem. Lett.* **2012**, *3*, 1624.
- (42) Kauffman, D. R.; Alfonso, D.; Matranga, C.; Qian, H.; Jin, R. *J. Phys. Chem. C* **2013**, *117*, 7914.
- (43) Tracy, J. B.; Crowe, M. C.; Parker, J. F.; Hampe, O.; Fields-Zinna, C. A.; Dass, A.; Murray, R. W. *J. Am. Chem. Soc.* **2007**, *129*, 16209.
- (44) Niihori, Y.; Matsuzaki, M.; Pradeep, T.; Negishi, Y. *J. Am. Chem. Soc.* **2013**, *135*, 4946.
- (45) Grzelczak, M.; Vermant, J.; Furst, E. M.; Liz-Marzán, L. M. *ACS Nano* **2010**, *4*, 3591.
- (46) Grzybowski, B. A.; Wilmer, C. E.; Kim, J.; Browne, K. P.; Bishop, K. J. M. *Soft Matter* **2009**, *5*, 1110.
- (47) Pileni, M. P. *J. Phys. Chem. B* **2001**, *105*, 3358.
- (48) Pileni, M. P. *Acc. Chem. Res.* **2008**, *41*, 1799.
- (49) Gao, Y.; Tang, Z. Y. *Small* **2011**, *7*, 2133.
- (50) Lee, J.; Govorov, A. O.; Dulka, J.; Kotov, N. A. *Nano Lett.* **2004**, *4*, 2323.
- (51) Courty, A.; Mermet, A.; Albouy, P. A.; Duval, E.; Pileni, M. P. *Nat. Mater.* **2005**, *4*, 395.
- (52) Murray, C. B.; Kagan, C. R.; Bawendi, M. G. *Annu. Rev. Mater. Sci.* **2000**, *30*, 545.
- (53) Bishop, K. J. M.; Wilmer, C. E.; Soh, S.; Grzybowski, B. A. *Small* **2009**, *5*, 1600.
- (54) Macfarlane, R. J.; Jones, M. R.; Lee, B.; Auyeung, E.; Mirkin, C. A. *Science* **2013**, *341*, 1222.
- (55) Brust, M.; Schiffrin, D. J.; Bethell, D.; Kiely, C. J. *Adv. Mater.* **1995**, *7*, 795.
- (56) Mirkin, C. A.; Letsinger, R. L.; Mucic, R. C.; Storhoff, J. J. *Nature* **1996**, *382*, 607.
- (57) Das, A.; Li, T.; Nobusada, K.; Zeng, C.; Rosi, N. L.; Jin, R. *J. Am. Chem. Soc.* **2013**, *135*, 18264.
- (58) Kumara, C.; Aikens, C. M.; Dass, A. *J. Phys. Chem. Lett.* **2014**, 461.
- (59) Zeng, C.; Li, T.; Das, A.; Rosi, N. L.; Jin, R. *J. Am. Chem. Soc.* **2013**, *135*, 10011.
- (60) Qian, H.; Eckenhoff, W. T.; Zhu, Y.; Pintauer, T.; Jin, R. *J. Am. Chem. Soc.* **2010**, *132*, 8280.

- (61) Heinecke, C. L.; Ni, T. W.; Malola, S.; Mäkinen, V.; Wong, O. A.; Häkkinen, H.; Ackerson, C. J. *J. Am. Chem. Soc.* **2012**, *134*, 13316.
- (62) Wang, F.; Zhang, X.; Zhang, Z.; He, C. *J. Mater. Chem.* **2011**, *21*, 15167.
- (63) Wu, Z.; Dong, C.; Li, Y.; Hao, H.; Zhang, H.; Lu, Z.; Yang, B. *Angew. Chem. Int. Ed.* **2013**, *52*, 9952.
- (64) Yoon, B.; Luedtke, W. D.; Barnett, R. N.; Gao, J.; Desiredy, A.; Conn, B. E.; Bigioni, T.; Landman, U. *Nat. Mater.* **2014**, *13*, 807.
- (65) Zhang, Q.; Xie, J.; Yang, J.; Lee, J. Y. *ACS Nano* **2008**, *3*, 139.
- (66) Bakr, O. M.; Amendola, V.; Aikens, C. M.; Wenseleers, W.; Li, R.; Dal Negro, L.; Schatz, G. C.; Stellacci, F. *Angew. Chem. Int. Ed.* **2009**, *48*, 5921.
- (67) Ingram, R. S.; Hostetler, M. J.; Murray, R. W.; Schaaff, T. G.; Khoury, J. T.; Whetten, R. L.; Bigioni, T. P.; Guthrie, D. K.; First, P. N. *J. Am. Chem. Soc.* **1997**, *119*, 9279.
- (68) Shiang, Y.-C.; Huang, C.-C.; Chen, W.-Y.; Chen, P.-C.; Chang, H.-T. *J. Mater. Chem.* **2012**, *22*, 12972.
- (69) Diez, I.; Ras, R. H. A. *Nanoscale* **2011**, *3*, 1963.
- (70) Zhu, Y.; Qian, H.; Drake, B. A.; Jin, R. *Angew. Chem. Int. Ed.* **2010**, *49*, 1295.
- (71) Zhu, Y.; Qian, H.; Jin, R. *J. Mater. Chem.* **2011**, *21*, 6793.
- (72) Tsukuda, T. *B. Chem. Soc. Jpn.* **2012**, *85*, 151.
- (73) Stampelcoskie, K. G.; Chen, Y.-S.; Kamat, P. V. *J. Phys. Chem. C* **2013**, *118*, 1370.
- (74) Huang, C.-C.; Yang, Z.; Lee, K.-H.; Chang, H.-T. *Angew. Chem. Int. Ed.* **2007**, *46*, 6824.
- (75) Yuan, X.; Tay, Y.; Dou, X.; Luo, Z.; Leong, D. T.; Xie, J. *Anal. Chem.* **2012**, *85*, 1913.
- (76) Nie, X.; Qian, H.; Ge, Q.; Xu, H.; Jin, R. *ACS Nano* **2012**, *6*, 6014.
- (77) Zhang, Q.; Xie, J.; Yu, Y.; Lee, J. Y. *Nanoscale* **2010**, *2*, 1962.
- (78) Kubo, R.; Kawabata, A.; Kobayashi, S. *Annu. Rev. Mater. Sci.* **1984**, *14*, 49.
- (79) Qian, H.; Zhu, Y.; Jin, R. *ACS Nano* **2009**, *3*, 3795.
- (80) Häkkinen, H. *Nat. Chem.* **2012**, *4*, 443.
- (81) Krommenhoek, P. J.; Wang, J.; Hentz, N.; Johnston-Peck, A. C.; Kozek, K. A.; Kalyuzhny, G.; Tracy, J. B. *ACS Nano* **2012**, *6*, 4903.
- (82) Nishigaki, J.-i.; Tsunoyama, R.; Tsunoyama, H.; Ichikuni, N.; Yamazoe, S.; Negishi, Y.; Ito, M.; Matsuo, T.; Tamao, K.; Tsukuda, T. *J. Am. Chem. Soc.* **2012**, *134*, 14295.
- (83) Crasto, D.; Dass, A. *J. Phys. Chem. C* **2013**, *117*, 22094.
- (84) Alvarez, M. M.; Khoury, J. T.; Schaaff, T. G.; Shafigullin, M.; Vezmar, I.; Whetten, R. L. *Chem. Phys. Lett.* **1997**, *266*, 91.
- (85) Tsunoyama, H.; Nickut, P.; Negishi, Y.; Al-Shamery, K.; Matsumoto, Y.; Tsukuda, T. *J. Phys. Chem. C* **2007**, *111*, 4153.
- (86) Zeng, C.; Liu, C.; Pei, Y.; Jin, R. *ACS Nano* **2013**.
- (87) Zhu, M.; Lanni, E.; Garg, N.; Bier, M. E.; Jin, R. *J. Am. Chem. Soc.* **2008**, *130*, 1138.
- (88) Dharmaratne, A. C.; Krick, T.; Dass, A. *J. Am. Chem. Soc.* **2009**, *131*, 13604.
- (89) Qian, H.; Jin, R. *Nano Lett.* **2009**, *9*, 4083.
- (90) Liu, Y.; Tsunoyama, H.; Akita, T.; Xie, S.; Tsukuda, T. *ACS Catal.* **2010**, *1*, 2.
- (91) Alvarez, M. M.; Khoury, J. T.; Schaaff, T. G.; Shafigullin, M. N.; Vezmar, I.; Whetten, R. L. *J. Phys. Chem. B* **1997**, *101*, 3706.
- (92) Hu, M.; Chen, J.; Li, Z.-Y.; Au, L.; Hartland, G. V.; Li, X.; Marquez, M.; Xia, Y. *Chem. Soc. Rev.* **2006**, *35*, 1084.

- (93) Youngblood, W. J.; Lee, S.-H. A.; Maeda, K.; Mallouk, T. E. *Acc. Chem. Res.* **2009**, *42*, 1966.
- (94) Li, L.; Yang, X.; Gao, J.; Tian, H.; Zhao, J.; Hagfeldt, A.; Sun, L. *J. Am. Chem. Soc.* **2011**, *133*, 8458.
- (95) Habeeb Muhammed, M.; Ramesh, S.; Sinha, S.; Pal, S.; Pradeep, T. *Nano Res.* **2008**, *1*, 333.
- (96) Xie, J.; Zheng, Y.; Ying, J. Y. *J. Am. Chem. Soc.* **2009**, *131*, 888.
- (97) Dou, X.; Yuan, X.; Yu, Y.; Luo, Z.; Yao, Q.; Leong, D. T.; Xie, J. *Nanoscale* **2013**, *6*, 157.
- (98) Yuan, X.; Setyawati, M. I.; Tan, A. S.; Ong, C. N.; Leong, D. T.; Xie, J. *NPG Asia Mater.* **2013**, *5*, e39.
- (99) Zhou, C.; Sun, C.; Yu, M.; Qin, Y.; Wang, J.; Kim, M.; Zheng, J. *J. Phys. Chem. C* **2010**, *114*, 7727.
- (100) Yu, M.; Zhou, C.; Liu, J.; Hankins, J. D.; Zheng, J. *J. Am. Chem. Soc.* **2011**, *133*, 11014.
- (101) Muhammed, M. A. H.; Verma, P. K.; Pal, S. K.; Kumar, R. C. A.; Paul, S.; Omkumar, R. V.; Pradeep, T. *Chem. Eur. J.* **2009**, *15*, 10110.
- (102) Rao, T. U. B.; Nataraju, B.; Pradeep, T. *J. Am. Chem. Soc.* **2010**, *132*, 16304.
- (103) Shang, L.; Azadfar, N.; Stockmar, F.; Send, W.; Trouillet, V.; Bruns, M.; Gerthsen, D.; Nienhaus, G. U. *Small* **2011**, *7*, 2614.
- (104) Huang, C.-C.; Hung, Y.-L.; Shiang, Y.-C.; Lin, T.-Y.; Lin, Y.-S.; Chen, C.-T.; Chang, H.-T. *Chem. Asian J.* **2010**, *5*, 334.
- (105) Wu, Z.; Wang, M.; Yang, J.; Zheng, X.; Cai, W.; Meng, G.; Qian, H.; Wang, H.; Jin, R. *Small* **2012**, *8*, 2028.
- (106) Xie, J.; Zheng, Y.; Ying, J. Y. *Chem. Commun.* **2010**, *46*, 961.
- (107) Yuan, X.; Yeow, T. J.; Zhang, Q.; Lee, J. Y.; Xie, J. *Nanoscale* **2012**, *4*, 1968.
- (108) Chaki, N. K.; Negishi, Y.; Tsunoyama, H.; Shichibu, Y.; Tsukuda, T. *J. Am. Chem. Soc.* **2008**, *130*, 8608.
- (109) Andres, R. P.; Bein, T.; Dorogi, M.; Feng, S.; Henderson, J. I.; Kubiak, C. P.; Mahoney, W.; Osifchin, R. G.; Reifengerger, R. *Science* **1996**, *272*, 1323.
- (110) Lee, D.; Donkers, R. L.; Wang, G.; Harper, A. S.; Murray, R. W. *J. Am. Chem. Soc.* **2004**, *126*, 6193.
- (111) Kwak, K.; Lee, D. *J. Phys. Chem. Lett.* **2012**, *3*, 2476.
- (112) Negishi, Y.; Chaki, N. K.; Shichibu, Y.; Whetten, R. L.; Tsukuda, T. *J. Am. Chem. Soc.* **2007**, *129*, 11322.
- (113) Zhu, M.; Eckenhoff, W. T.; Pintauer, T.; Jin, R. *J. Phys. Chem. C* **2008**, *112*, 14221.
- (114) Zhu, Y.; Qian, H.; Zhu, M.; Jin, R. *Adv. Mater.* **2010**, *22*, 1915.
- (115) Zhu, Y.; Qian, H.; Jin, R. *Chem. Eur. J.* **2010**, *16*, 11455.
- (116) Wu, Z.; Jiang, D.-e.; Mann, A. K. P.; Mullins, D. R.; Qiao, Z.-A.; Allard, L. F.; Zeng, C.; Jin, R.; Overbury, S. H. *J. Am. Chem. Soc.* **2014**, *136*, 6111.
- (117) Xie, S.; Tsunoyama, H.; Kurashige, W.; Negishi, Y.; Tsukuda, T. *ACS Catal.* **2012**, *2*, 1519.
- (118) Liu, Y.; Tsunoyama, H.; Akita, T.; Tsukuda, T. *Chem. Commun.* **2010**, *46*, 550.
- (119) Brust, M.; Walker, M.; Bethell, D.; Schiffrin, D. J.; Whyman, R. *J. Chem. Soc., Chem. Commun.* **1994**, 801.
- (120) Schaaff, T. G.; Shafiqullin, M. N.; Khoury, J. T.; Vezmar, I.; Whetten, R. L.; Cullen, W. G.; First, P. N.; Gutiérrez-Wing, C.; Ascensio, J.; Jose-Yacamán, M. J. *J. Phys. Chem. B* **1997**, *101*, 7885.

- (121) Hostetler, M. J.; Wingate, J. E.; Zhong, C.-J.; Harris, J. E.; Vachet, R. W.; Clark, M. R.; Londono, J. D.; Green, S. J.; Stokes, J. J.; Wignall, G. D.; Glish, G. L.; Porter, M. D.; Evans, N. D.; Murray, R. W. *Langmuir* **1998**, *14*, 17.
- (122) Kumar, S.; Bolan, M. D.; Bigioni, T. P. *J. Am. Chem. Soc.* **2010**, *132*, 13141.
- (123) Guo, J.; Kumar, S.; Bolan, M.; Desireddy, A.; Bigioni, T. P.; Griffith, W. P. *Anal. Chem.* **2012**, *84*, 5304.
- (124) Dance, I. G.; Fisher, K. J.; Banda, R. M. H.; Scudder, M. L. *Inorg. Chem.* **1991**, *30*, 183.
- (125) Schaaff, T. G.; Knight, G.; Shafiqullin, M. N.; Borkman, R. F.; Whetten, R. L. *J. Phys. Chem. B* **1998**, *102*, 10643.
- (126) Tsunoyama, H.; Negishi, Y.; Tsukuda, T. *J. Am. Chem. Soc.* **2006**, *128*, 6036.
- (127) Qian, H.; Zhu, Y.; Jin, R. *J. Am. Chem. Soc.* **2010**, *132*, 4583.
- (128) Qian, H.; Jin, R. *Chem. Commun.* **2011**, *47*, 11462.
- (129) Jimenez, V. L.; Leopold, M. C.; Mazzitelli, C.; Jorgenson, J. W.; Murray, R. W. *Anal. Chem.* **2002**, *75*, 199.
- (130) Shichibu, Y.; Negishi, Y.; Tsukuda, T.; Teranishi, T. *J. Am. Chem. Soc.* **2005**, *127*, 13464.
- (131) Jin, R.; Qian, H.; Wu, Z.; Zhu, Y.; Zhu, M.; Mohanty, A.; Garg, N. *J. Phys. Chem. Lett.* **2010**, *1*, 2903.
- (132) Shichibu, Y.; Negishi, Y.; Tsunoyama, H.; Kanehara, M.; Teranishi, T.; Tsukuda, T. *Small* **2007**, *3*, 835.
- (133) Schaaff, T. G.; Whetten, R. L. *J. Phys. Chem. B* **1999**, *103*, 9394.
- (134) Qian, H.; Jin, R. *Chem. Mater.* **2011**, *23*, 2209.
- (135) Thumu, U. B. R.; Bootharaju, M. S.; Pradeep, T. *Nanoscale* **2013**, *5*, 9404.
- (136) Chakraborty, I.; Govindarajan, A.; Erusappan, J.; Ghosh, A.; Pradeep, T.; Yoon, B.; Whetten, R. L.; Landman, U. *Nano Lett.* **2012**, *12*, 5861.
- (137) Walter, M.; Akola, J.; Lopez-Acevedo, O.; Jadzinsky, P. D.; Calero, G.; Ackerson, C. J.; Whetten, R. L.; Gronbeck, H.; Hakkinen, H. *Proc. Natl. Acad. Sci. U. S. A.* **2008**, *105*, 9157.
- (138) Maity, P.; Xie, S.; Yamauchi, M.; Tsukuda, T. *Nanoscale* **2012**, *4*, 4027.
- (139) Wu, Z.; Suhan, J.; Jin, R. *J. Mater. Chem.* **2009**, *19*, 622.
- (140) Qian, H.; Zhu, M.; Andersen, U. N.; Jin, R. *J. Phys. Chem. A* **2009**, *113*, 4281.
- (141) Wu, Z.; MacDonald, M. A.; Chen, J.; Zhang, P.; Jin, R. *J. Am. Chem. Soc.* **2011**, *133*, 9670.
- (142) Zhu, M.; Qian, H.; Jin, R. *J. Am. Chem. Soc.* **2009**, *131*, 7220.
- (143) Zhu, M.; Qian, H.; Jin, R. *J. Phys. Chem. Lett.* **2010**, *1*, 1003.
- (144) Zeng, C.; Chen, Y.; Li, G.; Jin, R. *Chem. Mater.* **2014**, *26*, 2635.
- (145) Li, G.; Zeng, C.; Jin, R. *J. Am. Chem. Soc.* **2014**, *136*, 3673.
- (146) Wu, Z.; Lanni, E.; Chen, W.; Bier, M. E.; Ly, D.; Jin, R. *J. Am. Chem. Soc.* **2009**, *131*, 16672.
- (147) Negishi, Y.; Arai, R.; Niihori, Y.; Tsukuda, T. *Chem. Commun.* **2011**, *47*, 5693.
- (148) Qingbo, Z.; Jim Yang, L.; Jun, Y.; Chris, B.; Jixuan, Z. *Nanotechnology* **2007**, *18*, 245605.
- (149) Woodcock, L. V. *Nature* **1997**, *385*, 141.
- (150) Auyeung, E.; Li, T.; Senesi, A. J.; Schmucker, A. L.; Pals, B. C.; de la Cruz, M. O.; Mirkin, C. A. *Nature* **2014**, *505*, 73.
- (151) Shevchenko, E. V.; Talapin, D. V.; Murray, C. B.; O'Brien, S. *J. Am. Chem. Soc.* **2006**, *128*, 3620.
- (152) Shevchenko, E. V.; Talapin, D. V.; Kotov, N. A.; O'Brien, S.; Murray, C. B. *Nature* **2006**, *439*, 55.



- (153) Gao, Y. *J. Phys. Chem. C* **2013**, *117*, 8983.
- (154) Sinnokrot, M. O.; Valeev, E. F.; Sherrill, C. D. *J. Am. Chem. Soc.* **2002**, *124*, 10887.
- (155) Steiner, T. *Angew. Chem. Int. Ed.* **2002**, *41*, 48.
- (156) Hunter, C. A.; Sanders, J. K. M. *J. Am. Chem. Soc.* **1990**, *112*, 5525.
- (157) Burley, S.; Petsko, G. *Science* **1985**, *229*, 23.
- (158) Askew, B.; Ballester, P.; Buhr, C.; Jeong, K. S.; Jones, S.; Parris, K.; Williams, K.; Rebek, J. *J. Am. Chem. Soc.* **1989**, *111*, 1082.
- (159) Claessens, C. G.; Stoddart, J. F. *J. Phys. Org. Chem.* **1997**, *10*, 254.
- (160) Aakeroy, C. B.; Seddon, K. R. *Chem. Soc. Rev.* **1993**, *22*, 397.
- (161) Desiraju, G. R. *J. Am. Chem. Soc.* **2013**, *135*, 9952.
- (162) Schaaff, T. G.; Whetten, R. L. *J. Phys. Chem. B* **2000**, *104*, 2630.
- (163) Negishi, Y.; Takasugi, Y.; Sato, S.; Yao, H.; Kimura, K.; Tsukuda, T. *J. Am. Chem. Soc.* **2004**, *126*, 6518.
- (164) Fields-Zinna, C. A.; Sampson, J. S.; Crowe, M. C.; Tracy, J. B.; Parker, J. F.; deNey, A. M.; Muddiman, D. C.; Murray, R. W. *J. Am. Chem. Soc.* **2009**, *131*, 13844.
- (165) Yuan, X.; Yu, Y.; Yao, Q.; Zhang, Q.; Xie, J. *J. Phys. Chem. Lett.* **2012**, *3*, 2310.
- (166) Jiang, D.-e.; Chen, W.; Whetten, R. L.; Chen, Z. *J. Phys. Chem. C* **2009**, *113*, 16983.
- (167) Tlahuice, A.; Garzon, I. L. *Phys. Chem. Chem. Phys.* **2012**, *14*, 3737.
- (168) Pei, Y.; Gao, Y.; Shao, N.; Zeng, X. C. *J. Am. Chem. Soc.* **2009**, *131*, 13619.
- (169) Lee, D.; Donkers, R. L.; DeSimone, J. M.; Murray, R. W. *J. Am. Chem. Soc.* **2003**, *125*, 1182.
- (170) Wu, Z.; Jin, R. *Nano Lett.* **2010**, *10*, 2568.
- (171) Zheng, N.; Fan, J.; Stucky, G. D. *J. Am. Chem. Soc.* **2006**, *128*, 6550.
- (172) Staubitz, A.; Robertson, A. P. M.; Sloan, M. E.; Manners, I. *Chem. Rev.* **2010**, *110*, 4023.
- (173) Martin, M. N.; Li, D.; Dass, A.; Eah, S.-K. *Nanoscale* **2012**, *4*, 4091.
- (174) Pirie, N. W.; Pinhey, K. G. *J. Biol. Chem.* **1929**, *84*, 321.
- (175) Yao, Q.; Yu, Y.; Yuan, X.; Yu, Y.; Xie, J.; Lee, J. Y. *Small* **2013**, *9*, 2696.
- (176) Yu, Y.; Luo, Z.; Yu, Y.; Lee, J. Y.; Xie, J. *ACS Nano* **2012**, *6*, 7920.
- (177) van Herrikhuyzen, J.; Janssen, R. A. J.; Meijer, E. W.; Meskers, S. C. J.; Schenning, A. P. H. J. *J. Am. Chem. Soc.* **2005**, *128*, 686.
- (178) Park, J.; Joo, J.; Kwon, S. G.; Jang, Y.; Hyeon, T. *Angew. Chem. Int. Ed.* **2007**, *46*, 4630.
- (179) Templeton, A. C.; Zamborini, F. P.; Wuelfing, W. P.; Murray, R. W. *Langmuir* **2000**, *16*, 6682.
- (180) Kim, Y.; Johnson, R. C.; Hupp, J. T. *Nano Lett.* **2001**, *1*, 165.
- (181) Schmidbaur, H.; Schier, A. *Chem. Soc. Rev.* **2008**, *37*, 1931.
- (182) Ito, H.; Saito, T.; Oshima, N.; Kitamura, N.; Ishizaka, S.; Hinatsu, Y.; Wakeshima, M.; Kato, M.; Tsuge, K.; Sawamura, M. *J. Am. Chem. Soc.* **2008**, *130*, 10044.
- (183) Valeur, B. *Molecular Fluorescence: Principles and Applications*; Wiley-VCH: Weinheim, Germany, 2002.
- (184) Hong, Y.; Lam, J. W. Y.; Tang, B. Z. *Chem. Soc. Rev.* **2011**, *40*, 5361.
- (185) Choi, S.; Dickson, R. M.; Yu, J. *Chem. Soc. Rev.* **2012**, *41*, 1867.
- (186) Yuan, X.; Zhang, B.; Luo, Z.; Yao, Q.; Leong, D. T.; Yan, N.; Xie, J. *Angew. Chem. Int. Ed.* **2014**, *53*, 4623.
- (187) Kwak, K.; Kumar, S. S.; Pyo, K.; Lee, D. *ACS Nano* **2013**, *8*, 671.

- (188) Zubarev, E. R.; Xu, J.; Sayyad, A.; Gibson, J. D. *J. Am. Chem. Soc.* **2006**, *128*, 4958.
- (189) Andala, D. M.; Shin, S. H. R.; Lee, H.-Y.; Bishop, K. J. M. *ACS Nano* **2012**, *6*, 1044.
- (190) Uzun, O.; Hu, Y.; Verma, A.; Chen, S.; Centrone, A.; Stellacci, F. *Chem. Commun.* **2008**, 196.
- (191) Nikolic, M. S.; Olsson, C.; Salcher, A.; Kornowski, A.; Rank, A.; Schubert, R.; Frömsdorf, A.; Weller, H.; Förster, S. *Angew. Chem. Int. Ed.* **2009**, *48*, 2752.
- (192) Pearce, T. R.; Waybrant, B.; Kokkoli, E. *Chem. Commun.* **2013**, *50*, 210.
- (193) Luo, X.; Wu, S.; Liang, Y. *Chem. Commun.* **2002**, 492.
- (194) Israelachvili, J. N.; Mitchell, D. J.; Ninham, B. W. *J. Chem. Soc., Faraday Trans. 2* **1976**, *72*, 1525.
- (195) Daniel, M.-C.; Astruc, D. *Chem. Rev.* **2003**, *104*, 293.
- (196) Edmonds, W. F.; Li, Z.; Hillmyer, M. A.; Lodge, T. P. *Macromolecules.* **2006**, *39*, 4526.
- (197) Jakobs, R. T. M.; van Herrikhuyzen, J.; Gielen, J. C.; Christianen, P. C. M.; Meskers, S. C. J.; Schenning, A. P. H. J. *J. Mater. Chem.* **2008**, *18*, 3438.
- (198) Zubarev, E. R.; Xu, J.; Sayyad, A.; Gibson, J. D. *J. Am. Chem. Soc.* **2006**, *128*, 15098.
- (199) Yamamoto, S.; Maruyama, Y.; Hyodo, S.-a. *J. Chem. Phys.* **2002**, *116*, 5842.
- (200) Carmona-Ribeiro, A. M. *Chem. Soc. Rev.* **1992**, *21*, 209.
- (201) Song, J.; Cheng, L.; Liu, A.; Yin, J.; Kuang, M.; Duan, H. *J. Am. Chem. Soc.* **2011**, *133*, 10760.
- (202) van Herrikhuyzen, J.; Portale, G.; Gielen, J. C.; Christianen, P. C. M.; Sommerdijk, N. A. J. M.; Meskers, S. C. J.; Schenning, A. P. H. J. *Chem. Commun.* **2008**, 697.
- (203) Yang, H.; Wang, Y.; Yan, J.; Chen, X.; Zhang, X.; Häkkinen, H.; Zheng, N. *J. Am. Chem. Soc.* **2014**, *136*, 7197.
- (204) Yao, Q.; Luo, Z.; Yuan, X.; Yu, Y.; Zhang, C.; Xie, J.; Lee, J. Y. *Sci. Rep.* **2014**, *4*, 3848.
- (205) Pradhan, S.; Xu, L.; Chen, S. *Adv. Funct. Mater.* **2007**, *17*, 2385.
- (206) Woehle, G. H.; Warner, M. G.; Hutchison, J. E. *J. Phys. Chem. B* **2002**, *106*, 9979.
- (207) Dass, A.; Stevenson, A.; Dubay, G. R.; Tracy, J. B.; Murray, R. W. *J. Am. Chem. Soc.* **2008**, *130*, 5940.
- (208) Templeton, A. C.; Hostetler, M. J.; Warmoth, E. K.; Chen, S.; Hartshorn, C. M.; Krishnamurthy, V. M.; Forbes, M. D. E.; Murray, R. W. *J. Am. Chem. Soc.* **1998**, *120*, 4845.
- (209) Tiddy, G. J. T. *Phys. Rep.* **1980**, *57*, 1.
- (210) Svenson, S. *Curr. Opin. Colloid Interface Sci.* **2004**, *9*, 201.
- (211) Szoka, F.; Papahadjopoulos, D. *Annu. Rev. Biophys. Bioeng.* **1980**, *9*, 467.
- (212) Chen, F.; Xu, G.-Q.; Hor, T. S. A. *Mater. Lett.* **2003**, *57*, 3282.
- (213) Cheng, W.; Dong, S.; Wang, E. *Langmuir* **2003**, *19*, 9434.
- (214) Li, Z.; Zhang, J.; Du, J.; Han, B.; Mu, T.; Gao, Y.; Liu, Z. *Mater. Chem. Phys.* **2005**, *91*, 40.
- (215) Pashley, R. M.; McGuiggan, P. M.; Horn, R. G.; Ninham, B. W. *J. Colloid Interface Sci.* **1988**, *126*, 569.
- (216) Zhu, M.; Chan, G.; Qian, H.; Jin, R. *Nanoscale* **2011**, *3*, 1703.
- (217) Kauffman, D. R.; Alfonso, D.; Matranga, C.; Li, G.; Jin, R. *J. Phys. Chem. Lett.* **2012**, *4*, 195.

- (218) Xia, Y.; Xiong, Y.; Lim, B.; Skrabalak, S. E. *Angew. Chem. Int. Ed.* **2009**, *48*, 60.
- (219) Tao, A. R.; Habas, S.; Yang, P. *Small* **2008**, *4*, 310.
- (220) Jun, Y.-w.; Choi, J.-s.; Cheon, J. *Angew. Chem. Int. Ed.* **2006**, *45*, 3414.
- (221) Yu, Y.; Zhang, Q.; Liu, B.; Lee, J. Y. *J. Am. Chem. Soc.* **2010**, *132*, 18258.
- (222) Busbee, B. D.; Obare, S. O.; Murphy, C. J. *Adv. Mater.* **2003**, *15*, 414.
- (223) Yin, Y.; Erdonmez, C.; Aloni, S.; Alivisatos, A. P. *J. Am. Chem. Soc.* **2006**, *128*, 12671.
- (224) Xie, J.; Lee, J. Y.; Wang, D. I. C.; Ting, Y. P. *ACS Nano* **2007**, *1*, 429.
- (225) Yin, Y.; Lu, Y.; Sun, Y.; Xia, Y. *Nano Lett.* **2002**, *2*, 427.
- (226) Lanci, C. J.; MacDermaid, C. M.; Kang, S.-g.; Acharya, R.; North, B.; Yang, X.; Qiu, X. J.; DeGrado, W. F.; Saven, J. G. *Proc. Natl. Acad. Sci. U. S. A.* **2012**, *109*, 7304.
- (227) Compton, O. C.; Osterloh, F. E. *J. Am. Chem. Soc.* **2007**, *129*, 7793.
- (228) Goubet, N.; Richardi, J.; Albouy, P.-A.; Pileni, M.-P. *Adv. Funct. Mater.* **2011**, *21*, 2693.
- (229) Harkness, K. M.; Tang, Y.; Dass, A.; Pan, J.; Kothalawala, N.; Reddy, V. J.; Cliffel, D. E.; Demeler, B.; Stellacci, F.; Bakr, O. M.; McLean, J. A. *Nanoscale* **2012**, *4*, 4269.
- (230) Oosawa, F.; Asakura, S. *J. Chem. Phys.* **1954**, *22*, 1255.
- (231) LaMer, V. K.; Dinigar, R. H. *J. Am. Chem. Soc.* **1950**, *72*, 4847.
- (232) Zhang, H.; Jin, M.; Xia, Y. *Angew. Chem. Int. Ed.* **2012**, *51*, 7656.
- (233) Jin, M.; Zhang, H.; Xie, Z.; Xia, Y. *Angew. Chem. Int. Ed.* **2011**, *50*, 7850.
- (234) Lu, C.-L.; Prasad, K. S.; Wu, H.-L.; Ho, J.-a. A.; Huang, M. H. *J. Am. Chem. Soc.* **2010**, *132*, 14546.
- (235) Yu, Y.; Zhang, Q.; Xie, J.; Lee, J. Y. *Nat. Commun.* **2013**, *4*, 1454.
- (236) Yu, Y.; Zhang, Q.; Yao, Q.; Xie, J.; Lee, J. Y. *Chem. Mater.* **2013**, *25*, 4746.
- (237) Su, W.; Cao, R.; Hong, M.; Wong, W.-T.; Lu, J. *Inorg. Chem. Commun.* **1999**, *2*, 241.
- (238) Zhang, Y. X.; Zeng, H. C. *Adv. Mater.* **2009**, *21*, 4962.
- (239) Kalsin, A. M.; Fialkowski, M.; Paszewski, M.; Smoukov, S. K.; Bishop, K. J. M.; Grzybowski, B. A. *Science* **2006**, *312*, 420.

## PUBLICATIONS

1. Yao Q., Yu Y., Yuan X., Yu Y., Zhao D., Xie J., Lee J. Y., Counterion-Assisted Shaping of Nanocluster Supracrystals. *Angew. Chem. Int. Ed.* **2015**, *54*, 184-189.
2. Yao Q., Yuan X., Yu Y., Yu Y., Xie J., Lee J. Y., Introducing Amphiphilicity to Noble Metal Nanoclusters via Phase-Transfer Driven Ion-Pairing Reaction. *J. Am. Chem. Soc.* **2015**, *137*, 2128-2136.
3. Yao, Q.; Luo, Z.; Yuan, X.; Yu, Y.; Zhang, C.; Xie, J.; Lee, J. Y., Assembly of Nanoions via Electrostatic Interactions: Ion-Like Behavior of Charged Noble Metal Nanoclusters. *Sci. Rep.* **2014**, *4*, 3848.
4. Yao, Q.; Yu, Y.; Yuan, X.; Yu, Y.; Xie, J.; Lee, J. Y., Two-Phase Synthesis of Small Thiolate-Protected Au<sub>15</sub> and Au<sub>18</sub> Nanoclusters. *Small* **2013**, *9*, 2696-2701.
5. Yu, Y.†; Yao, Q.†; Luo, Z.; Yuan, X.; Lee, J. Y.; Xie, J., Precursor Engineering and Controlled Conversion for the Synthesis of Monodisperse Thiolate-Protected Metal Nanoclusters. *Nanoscale* **2013**, *5*, 4606-4620. (†Jointed First-Authorship)
6. Yuan, X.; Yao, Q.; Yu, Y.; Luo, Z.; Xie, J., Novel Synthetic Strategies for Thiolate-Protected Au and Ag Nanoclusters: Towards Atomic Precision and Strong Luminescence. *RSC Book "Functional Nanometer-Sized Clusters of Transition Metals: Synthesis, Properties and Applications"* **2014**, 131-167. (Invited Book Chapter)
7. Yu Y.; Zhang Q.; Yao Q.; Xie J.; Lee J. Y. Architectural Design of Heterogeneous Metallic Nanocrystals — Principles and Processes. *Acc. Chem. Res.* **2014**, *47*, 3530-3540.
8. Yu, Y.; Zhang, Q.; Yao, Q.; Zhan, Y.; Lu, M.; Yang, L.; Xu, C.; Xie, J.; Lee, J. Y., Learning from Nature: Introducing an Epiphyte-Host Relationship in the Synthesis of Alloy Nanoparticles by Co-Reduction Methods. *Chem. Commun.* **2014**, *50*, 9765-9768.
9. Xia, H.; Xiong, W.; Lim, C. K.; Yao, Q.; Wang, Y.; Xie, J., Hierarchical TiO<sub>2</sub>-B Nanowire@ $\alpha$ -Fe<sub>2</sub>O<sub>3</sub> Nanothorn Core-Branch Arrays as Superior Electrodes for Lithium-Ion Microbatteries. *Nano Res.* **2014**, *7*, 1797-1808.
10. Dou, X.; Yuan, X.; Yao, Q.; Luo, Z.; Zheng, K.; Xie, J., Facile Synthesis of Water-Soluble Au<sub>25-x</sub>Ag<sub>x</sub> Nanoclusters Protected by Mono- and Bi-Thiolate Ligands. *Chem. Commun.* **2014**, *50*, 7459-7462.
11. Yuan, X.; Zhang, B.; Luo, Z.; Yao, Q.; Leong, D. T.; Yan, N. and Xie, J., Balancing the Rate of Cluster Growth and Etching for Gram-scale Synthesis of

- Mono-, Bi- and Multi-Thiolate-Protected Au<sub>25</sub> Nanoclusters with Atomic Precision. *Angew. Chem. Int. Ed.* **2014**, *53*, 4623-4627.
12. Liu, H.; Ye, F.; Yao, Q.; Cao, H.; Xie, J.; Lee, J. Y.; Yang, J., Stellated Ag-Pt Bimetallic Nanoparticles: an Effective Platform for Catalytic Activity Tuning. *Sci. Rep.* **2014**, *4*, 3969.
13. Yu, Y.; Yao, Q.; Cheng, K.; Yuan, X.; Luo, Z.; Xie, J., Solvent Controls the Formation of Au<sub>29</sub>(SR)<sub>20</sub> Nanoclusters in the CO-Reduction Method. *Part. Part. Syst. Char.* **2014**, *31*, 652-656.
14. Dou, X.; Yuan, X.; Yu, Y.; Luo, Z.; Yao, Q.; Leong, D. T.; Xie, J., Lighting up Thiolated Au@Ag Nanoclusters via Aggregation-Induced Emission. *Nanoscale* **2013**, *6*, 157-161.
15. Yu, Y.; Chen, X.; Yao, Q.; Yu, Y.; Yan, N.; Xie, J., Scalable and Precise Synthesis of Thiolated Au<sub>10-12</sub>, Au<sub>15</sub>, Au<sub>18</sub>, and Au<sub>25</sub> Nanoclusters via pH Controlled CO Reduction. *Chem. Mater.* **2013**, *25*, 946-952.
16. Yu, Y.; Zhang, Q.; Yao, Q.; Xie, J.; Lee, J. Y., Guiding Principles in the Galvanic Replacement Reaction of an Underpotentially Deposited Metal Layer for Site-Selective Deposition and Shape and Size Control of Satellite Nanocrystals. *Chem. Mater.* **2013**, *25*, 4746-4756.
17. Yuan, X.; Yao, Q.; Yu, Y.; Luo, Z.; Dou, X.; Xie, J., Traveling through the Desalting Column Spontaneously Transforms Thiolated Ag Nanoclusters from Nonluminescent to Highly Luminescent. *J. Phys. Chem. Lett.* **2013**, *4*, 1811-1815.
18. Yuan, X.; Luo, Z.; Yu, Y.; Yao, Q.; Xie, J., Luminescent Noble Metal Nanoclusters as an Emerging Optical Probe for Sensor Development. *Chem. Asian. J.* **2013**, *8*, 858-871.
19. Fang, C.; Toh, X. N.; Yao, Q.; Julius, D.; Hong, L.; Lee, J. Y., Semi-Interpenetrating Polymer Network Proton Exchange Membranes with Narrow and Well-Connected Hydrophilic Channels. *J. Power Sources* **2013**, *226*, 289-298.
20. Yuan, X.; Yu, Y.; Yao, Q.; Zhang, Q.; Xie, J., Fast Synthesis of Thiolated Au<sub>25</sub> Nanoclusters via Protection-Deprotection Method. *J. Phys. Chem. Lett.* **2012**, *3*, 2310-2314.